Global infrasound observations and their relation to atmospheric tides and mountain waves

Patrick Hupe

München 2018

Global infrasound observations and their relation to atmospheric tides and mountain waves

Patrick Hupe

Dissertation
an der Fakultät für Physik
der Ludwig–Maximilians–Universität
München

vorgelegt von
Patrick Hupe
aus Gehrden (Region Hannover)

München, den 19.12.2018

Erstgutachter: Prof. Dr. Markus Rapp
Zweitgutachter: HDR Dr. Alexis Le Pichon
Tag der mündlichen Prüfung: 20.02.2019

Zusammenfassung

Niederfrequenter Schall (Infraschall) kann aufgrund geringer Dämpfung — je nach Zustand der Atmosphäre — Distanzen von wenigen hundert bis einigen tausend Kilometern zurücklegen. Diese Eigenschaft wird zur Registrierung atmosphärischer Explosionen genutzt: Nachdem das Kernwaffenteststoppabkommen (CTBT) von den Vereinten Nationen im Jahr 1996 zur Unterzeichnung aufgelegt worden war, wurde ein globales Messnetz (IMS) konzipiert, das in der Lage sein soll, Explosionen mit einer Ladungsstärke von mindestens einer Kilotonne TNT-Äquivalent weltweit zu detektieren. Sechzig Infraschallstationen des IMS registrieren entsprechende Druckschwankungen in Größenordnungen von 10^{-3} Pa bis 10 Pa. Diese Arbeit befasst sich mit der Bestimmung von natürlichen atmosphärischen Wellen verschiedener Skalen aus den barometrischen Datensätzen des IMS-Infraschallmessnetzes. Der Schwerpunkt liegt auf dem niederfrequenten Teil des registrierten Spektrums von Infraschallwellen, d. h. Perioden von 2 s bis 100 s.

Zunächst wird gezeigt, dass sich die hohe Präzision der barometrischen Daten und die weltweite Verteilung der IMS-Stationen eignen, ein breites Spektrum atmosphärisch-dynamischer Phänomene zu quantifizieren. Auffällig sind dabei die atmosphärischen Gezeiten, die deutlich bei Perioden von 24 h, 12 h und 8 h nachweisbar sind. Die geografische und saisonale Variabilität dieser speziellen, großskaligen Form von atmosphärischen Schwerewellen werden mit dem IMS-Infraschallmessnetz akkurat erfasst.

Die spektrale Analyse der differentiellen Druckdaten hebt zusätzlich zu Gezeiten auch einen kurzperiodischen Bereich hervor. Es handelt sich um kohärente Strukturen, genannt Mikrobarome, die nahezu permanent durch Interaktion gegenläufiger ozeanischer Wellen entstehen und weltweit als Infraschall mit Perioden von 2 s bis 10 s registriert werden. Die Wind- und Temperaturverteilung der mittleren Atmosphäre bestimmt die Detektierbarkeit der Signale, ist in Wettermodellen oft jedoch nicht präzise wiedergegeben. Zur Quantifizierung von Modellunsicherheiten wurden an der Infraschallstation IS26 im bayerischen Wald mithilfe eines Lidars Temperaturprofile im Höhenbereich von 20 km bis 90 km gemessen. Unter Verwendung eines Quellenmodells sowie einer atmosphärischen Dämpfungsrelation ließen sich die Unsicherheiten erstmalig in Mikrobaromamplituden übertragen. Dies ermöglichte bis zu 97 % der Detektionen hinsichtlich ihrer Variabilität in Ursprungsrichtung und Amplitude zu erklären.

Mikrobarome und Gezeitenwellen unterscheiden sich aufgrund der verschiedenen Skalen in ihrer rücktreibenden Druckkraft bzw. Schwerkraft. Atmosphärische Schwerewellen kennzeichnen einen breiten Spektralbereich zwischen Infraschall und den Gezeiten. Orografische Infraschallwellen (engl. *Mountain-associated Waves*, MAWs), deren Entstehungsmechanismus bislang nicht abschließend erforscht worden ist, wurden hier auf einen Zusammenhang mit orografischen Schwerewellen untersucht. MAWs sind ähnlich wie Mikrobarome kohärente Strukturen, die mit Perioden von 10 s bis 100 s über Distanzen von tausenden Kilometern detektiert werden können. Die IMS-Daten ermöglichten im Rahmen dieser Arbeit erstmals eine globale Analyse der MAWs. Mittels Kreuzpeilung konnten globale Quellregionen dieses Phänomens monatsweise bestimmt werden. Es wird gezeigt, dass MAWs mit troposphärischen Winden korrelieren. Diese allein erklären jedoch nicht die saisonale Variabilität in MAW-Detektionen. Mögliche weitere in der Entstehung von MAWs relevante Prozesse werden diskutiert, zum Beispiel das Brechen orografischer Schwerewellen. Ein Vergleich mit aus Satellitendaten bestimmten orografischen Quellregionen von Schwerewellen deutet darauf hin, dass diese mit denen von MAWs übereinstimmen

— und zwar auch in Regionen, in denen die vertikale Ausbreitung von Schwerewellen durch ein Windminimum in der Stratosphäre unterdrückt wird. Wenn sich das Wellenbrechen in weiteren Studien als primäre Anregung orografischer Infraschallwellen bestätigt, kann das Auftreten von orografischen Schwerewellen global mit dem IMS-Infraschallnetzwerk abgeleitet werden.

Abstract

Infrasound can propagate through the atmosphere over distances of hundreds to thousands of kilometers as a result of low absorption, depending on the state of the atmosphere. This property is utilized to record atmospheric explosions. Following the opening by the United Nations of the Comprehensive Nuclear-Test-Ban Treaty for signature in 1996, the International Monitoring System (IMS) was designed in order to detect explosions with a minimum yield of one kiloton of TNT equivalent worldwide. Sixty IMS infrasound stations have since been recording corresponding pressure fluctuations of the order of 10^{-3} Pa to 10 Pa. This thesis reports on the determination of atmospheric waves, on different scales, from the barometric datasets of the IMS infrasound network. The focus was on the low-frequency part of the recorded spectrum of infrasonic waves, i.e., periods of 2 s to 100 s.

The high precision of the barometric data and the worldwide distribution of the IMS stations were utilized to characterize a broad spectrum of atmospheric-dynamic phenomena. Dominant features include the thermal atmospheric tides, which are clearly distinguished at periods of 24 h, 12 h and 8 h in spectral analyses. The IMS infrasound network allowed the accurate characterization of the geographic and seasonal variability of this specific large-scale type of atmospheric gravity wave.

In addition to these tides, spectral analysis of the differential pressure data also highlights a short-period range (2–10 s). This reflects coherent structures — microbaroms — that almost permanently produce infrasound detections worldwide. Microbaroms originate from the interaction of opposing ocean surface waves. The distribution of winds and temperature in the middle atmosphere determines the detectability of such signals. In weather models, however, the middle atmosphere is only represented to a limited extent. To quantify model uncertainties, temperature profiles in the altitude range of 20 km to 90 km were measured at infrasound station IS26 in Germany using a mobile lidar system. Combining a source model with an atmospheric attenuation relation allowed the transfer of these uncertainties into microbarom amplitudes for the first time. These explained up to 97 % of the detections, in terms of their variability in origin and amplitude.

Microbaroms and tidal waves differ in their restoring force — namely, pressure and buoyancy — due to their different scales. Atmospheric gravity waves reflect a broad spectral range between infrasound and the tides. A relation between orographic gravity waves and infrasonic mountain-associated waves (MAWs), of which the source generation mechanism has not yet been fully explored, was investigated here. Similarly to microbaroms, MAWs are coherent structures at periods of 10 s to 100 s that can propagate over distances of thousands of kilometers. The IMS data, for the first time, enabled a global analysis of MAWs. A cross-bearing method determined global source regions of this phenomenon on a monthly basis. It is shown that the MAWs correlate with tropospheric winds; however, the latter are not sufficient to explain the seasonal variability in MAW detections. Further possible processes being involved in the excitation of MAWs are discussed, including breaking orographic gravity waves. The comparison with gravity wave source regions, derived from satellite data, suggests that MAW source regions match those of orographic gravity waves, even when vertically propagating gravity waves are filtered due to a stratospheric wind minimum causing the waves to break. If this process, in future studies, turns out to induce the MAWs, their occurrence detected by the IMS infrasound network can allow monitoring orographic gravity wave activity globally.

Publications

Parts of this thesis have been published in the following peer-reviewed open-access articles which are both distributed under the Creative Commons Attribution 4.0 License (CC BY 4.0):

- Hupe et al., 2018:

  Hupe, P., L. Ceranna, and C. Pilger (2018) Using barometric time series of the IMS infrasound network for a global analysis of thermally induced atmospheric tides. *Atmos. Meas. Tech.*, **11**(4), 2027–2040, doi:10.5194/amt-11-2027-2018.

  Patrick Hupe prepared and revised the manuscript and performed the data processing and analyses with support from Lars Ceranna and Christoph Pilger. Lars Ceranna supervised the project. All authors discussed the results and thereby contributed to the final version of the manuscript.

- Hupe et al., 2019:

  Hupe, P., L. Ceranna, C. Pilger, M. De Carlo, A. Le Pichon, B. Kaifler, and M. Rapp (2018) Assessing middle atmosphere weather models using infrasound detections from microbaroms. *Geophys. J. Int.*, **216**(3), 1761–1767, doi:10.1093/gji/ggy520.

  Patrick Hupe performed the data analyses and computations, produced the figures and wrote the manuscript. The conceptual ideas for this study were initiated by Alexis Le Pichon and Lars Ceranna. Patrick Hupe, Lars Ceranna, Christoph Pilger, Marine De Carlo, and Alexis Le Pichon contributed to microbarom data interpretation. Bernd Kaifler developed the CORAL system, operated it during the campaign and processed the measurements. All authors critically reviewed and improved the manuscript. Markus Rapp and Alexis Le Pichon supervised Patrick Hupe's PhD project.

Additionally, single paragraphs or figures of this thesis will be found in the following peer-reviewed book chapters, to be published in January 2019 and available online since October 2018:

- Ceranna et al., 2019:

  Ceranna, L., R. S. Matoza, P. Hupe, A. Le Pichon, and M. Landès (2019) Systematic Array Processing of a Decade of Global IMS Infrasound Data. *In* Le Pichon, A., E. Blanc, and A. Hauchecorne (eds.): *Infrasound Monitoring for Atmospheric Studies — Challenges in Middle-Atmosphere Dynamics and Societal Benefits*, pp. 471–482. Springer, Dordrecht, the Netherlands. ISBN 978-3-319-75138-2, doi:10.1007/978-3-319-75140-5_13.

  Patrick Hupe contributed to this chapter by producing figures and by reprocessing the IMS infrasound data set at the BGR.

- Blanc et al., 2019:

  Blanc, E., K. Pol, A. Le Pichon, A. Hauchecorne, P. Keckhut, G. Baumgarten, J. Hildebrand, J. Höffner, G. Stober, R. Hibbins, P. Espy, M. Rapp, B. Kaifler, L. Ceranna, P. Hupe, J. Hagen, R. Rüfenacht, N. Kämpfer, and P. S. M. Smets (2019) Middle Atmosphere Variability and Model Uncertainties as Investigated in the Framework of the ARISE Project. *In* Le Pichon, A., E. Blanc, and A. Hauchecorne (eds.): *Infrasound Monitoring for Atmospheric Studies — Challenges in Middle-Atmosphere Dynamics and Societal Benefits*, pp. 845–888. Springer, Dordrecht, the Netherlands. ISBN 978-3-319-75138-2, doi:10.1007/978-3-319-75140-5_28.

  Patrick Hupe contributed to section 3 of this chapter by writing parts of the text and providing a figure on lidar and ECMWF data comparisons. Moreover, setting up a configuration for the automatic detection of gravity waves and performing the reprocessing of IMS infrasound data were subject to his work at the BGR.

Contents

1 Introduction

1.1 Waves in the atmosphere

Waves of different spatial and temporal scales play a key role in atmospheric dynamics because they transport energy and momentum. In the middle atmosphere, including the stratosphere (from approximately 12–50 km) and the mesosphere (approximately 50–90 km), transported momentum can modify circulation patterns when waves break (e.g., Holton, 1983). Following Baldwin and Dunkerton (2001), there is robust evidence that such modifications, in turn, affect tropospheric circulation systems and, thus, weather. An example is the dissipation of planetary waves (PWs), which induces sudden stratospheric warming (SSW) events (Matsuno, 1971).

PWs, or Rossby waves, are characterized by wavelengths of thousands of kilometers and periods of days to several weeks (Rossby, 1939). They are caused by barotropic and baroclinic instabilities, which amplify the relative vorticity of the tropospheric jet-stream (at around 10 km altitude). The combined effect of relative vorticity and the Coriolis force (caused by the Earth's rotation) varies with latitude, making the potential vorticity gradient the restoring force of PWs. This results in the typically meandering jet-stream, especially in the Northern Hemisphere (e.g., Rhines, 2015). Upward-propagating and breaking PWs transfer momentum into the middle atmosphere, resulting in a deceleration and reversal of the prevailing strong westerly winds, which are known as the polar vortex (in the winter stratosphere). Associated with the weakening or even splitting polar vortex, the polar stratospheric temperatures increase (Limpasuvan et al., 2004). Charlton and Polvani (2007) found that vortex splits happened in 46 % of the SSW events between 1957 and 2002. Modification of the predominant circulation pattern causes surface temperature anomalies for several days to weeks (Kodera et al., 2013; Butler et al., 2017).

Another important type of atmospheric wave is the gravity wave (GW). GWs are induced by the vertical displacement of air parcels in a stably stratified atmosphere, with the restoring force being buoyancy (e.g., Nappo, 2012). A general GW solution can be obtained from the linearized fundamental conservation equations (momentum, mass and energy) for fluids (e.g., Fritts and Alexander, 2003). GW sources include deep convection, polar fronts, jet-stream instabilities, geostrophic adjustment and orography (e.g., Fritts and Alexander, 2003; Plougonven and Zhang, 2014). Due to the variety of potential sources, GWs are characterized by different spatial and temporal scales, ranging from a few to thousands of kilometers and several minutes up to 24 h, respectively (Fritts and Alexander, 2003). These temporal limitations reflect the Brunt–Väisälä frequency (N_B) and the Coriolis parameter.

The special interest here is the orographic GW, which is excited by the flow over mountain ranges. Therefore, 'mountain wave' is a common term for this type of GW (e.g., Kaifler et al., 2015). (Note that, in this thesis, the term 'orographic GW' is used to clearly distinguish between GWs and the acoustic waves described in Section 1.4.) Orographic GWs are characterized by low or zero horizontal phase velocities (Fritts and Alexander, 2003). Their wavelengths depend on the horizontal wind speed and N_B (Scorer, 1949). Mountain height additionally determines the amplitude, as well as the energy and momentum that can be transported into the stratosphere and mesosphere (Gill, 1982; Holton, 1983). GWs break at altitudes where their amplitudes grow so large that they become unstable (e.g., Nappo, 2012). GWs also break at altitudes where the background flow equals the horizontal phase speed of the waves; when approaching such critical levels, the vertical wavelength reduces and the shear tends to increase, causing the wave to break because of dynamic instability (Dörnbrack et al., 1995; Fritts and Alexander, 2003; Nappo, 2012). This is known as critical level filtering. For orographic GWs, critical levels occur at altitudes where the background flow is zero (Alexander et al., 2010).

A special type of GW is the atmospheric thermal tide. This acts on larger scales than the aforementioned types of GWs and is subject to the Earth's rotation (Oberheide et al., 2015). Atmospheric tides are global oscillations with periods of 24 h, 12 h and other fractions of the solar day, which are induced by insolation. Whilst PWs and other GWs are generally launched in the troposphere or lower stratosphere, atmospheric tides can be excited at different altitudes due to the subsequent absorption of solar radiation, for instance, by ozone in the stratosphere (Butler and Small, 1963) or by water vapor in the troposphere (Whiteman and Bian, 1996). Further information on atmospheric tides is given in Chapter 4, in which solar tides are derived from infrasound observations.

Upward wave propagation results in increasing wave amplitudes due to decreasing density with altitude, provided that no dissipation occurs such that their energy is conserved. PWs, GWs and tides can be measured, for instance, as oscillations or perturbations in temperature and winds with respect to the background conditions; however, routine measurements of temperature and winds are sparse in the middle atmosphere (e.g., Baumgarten, 2010, fig. 1). For this reason, numerical weather prediction (NWP) models only represent dynamic processes to a limited extent (Charlton-Perez et al., 2013). A better understanding of middle atmosphere dynamics is essential for improving NWP models (e.g., Tripathi et al., 2014). Consequently, techniques for observing the middle atmosphere have been continuously enhanced, including light detection and ranging (lidar) instruments, radar systems, satellite instruments and newly developed prototypes, such as wind radiometers (Rüfenacht et al., 2014; Hagen et al., 2018). Moreover, Le Pichon et al. (2015) demonstrated that lidar and infrasound are reasonable remote sensing combinations for assessing middle atmosphere dynamics.

1.2 Infrasound in the atmosphere

Sound waves, including audible sound and infrasound, propagate as longitudinal waves through gases and liquids. They induce the compression and rarefaction of a medium, which can be recorded as pressure deviations from the equilibrium. A restoring force proportional to the pressure disturbance resets the medium to its initial state; thus, acoustic waves are also known as pressure waves, as opposed to GWs, in which the restoring force is buoyancy. The upper frequency limit of infrasound is about 20 Hz — the approximate threshold of human-audible sound. The temperature-dependent acoustic cut-off frequency (N_A) denotes the lower limit (Fig. 1.1) — approximately 3.3 mHz at 20°C. Below N_A down to N_B, both buoyancy and pressure act as restoring forces. This intermediate frequency range varies with altitude and is associated with so-called acoustic-GWs (Gossard and Hooke, 1975).

According to De Groot-Hedlin et al. (2010), the atmosphere can be considered to be a low-pass filter. In contrast to audible sound, infrasound can propagate over thousands of kilometers (Sutherland and Bass, 2004; Evers and Haak, 2010). This feature is amplified by atmospheric waveguides between the ground and the tropopause, the stratopause or the temperature inversion in the lower thermosphere (Drob et al., 2003). The Earth's surface serves as an almost flat wave reflector; however, non-linear dissipation and absorption in the thermosphere effectively constrain the ground-to-thermosphere duct to a few hundreds of kilometers only (Sutherland and Bass, 2004). The ground-to-stratosphere duct is the most important one for acoustic energy transport regarding long-distance infrasound propagation, but its presence is sensitive to the strength and direction of stratospheric winds (Drob et al., 2003). The theory behind this is addressed in Chapter 3.

The essential role of stratospheric winds for infrasound propagation has encouraged several studies using natural infrasound sources. Ambient low-frequency infrasound, with frequencies of 0.1 Hz to 0.5 Hz, is quasi-continuously radiated from wide areas of the oceans (Donn and Rind, 1971). It originates from the non-linear interaction of ocean waves travelling in nearly opposite directions at the surface (Brekhovskikh et al., 1973; Waxler and Gilbert, 2006). These so-called microbaroms are globally detected at infrasound stations, and clearly undergo a seasonal cycle related to the stratospheric winds (e.g., Landès et al., 2014; Ceranna et al., 2019). Consequently, this ambient source has been used to probe and monitor the middle atmosphere winds (Garcés et al., 2004; Le Pichon et al., 2006, 2015; Smets, 2018). Infrasound detections from microbaroms are discussed in Chapter 5.

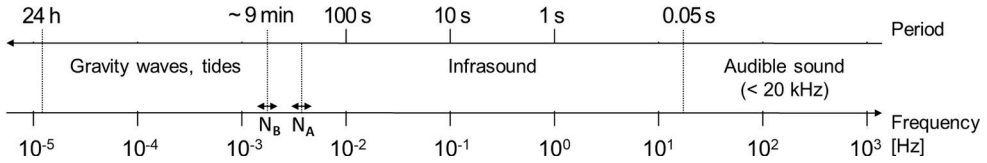

Figure 1.1: Frequency and period range of (infra)sound and gravity waves. N_A is the acoustic cut-off frequency; and N_B is the Brunt–Väisälä frequency, denoting the lower period limit of atmospheric gravity waves.

Lalande et al. (2012) proposed that infrasound inversions can improve the characterization of the upper atmosphere. SSW events have also been the subject of such studies (e.g., Assink et al., 2014b), given the nature of their stratospheric wind reversals; for instance, Evers and Siegmund (2009) and Smets and Evers (2014) evaluated the life-cycle of SSW events using microbarom detections in infrasound recordings. Further natural, but relatively event-like, infrasound sources, such as volcanoes (Matoza et al., 2011; Assink et al., 2014a; Matoza and Fee, 2018) or fireballs (e.g., Le Pichon et al., 2013; Pilger et al., 2015), have been analyzed in studies addressing the infrasound network detection capability of the International Monitoring System (IMS). The IMS network capability is a crucial concern for globally monitoring compliance with the Comprehensive Nuclear-Test-Ban Treaty (CTBT).

1.3 The infrasound network of the IMS

This section partly consists of literal excerpts from Hupe et al. (2018).

The aim of the CTBT and the Preparatory Commission (PrepCom) of the CTBT Organization (CTBTO) is to ban nuclear explosions underground, under water and in the atmosphere (CTBTO PrepCom, 2017). Seismology, hydroacoustics and infrasound are the corresponding waveform technologies used to detect, locate and characterize even small explosions of at least 1 kt TNT-equivalent. Complementary radionuclide stations support the IMS technologies, enabling the identification of explosions of a chemical or nuclear nature, the latter of which is a treaty violation. The IMS was designed to monitor compliance with the CTBT in the late 1990s.

The infrasound technology had already been used to detect significant nuclear explosions in the atmosphere before the United Nations presented the CTBT for signature in 1996 (Christie and Campus, 2010). The IMS infrasound network is supposed to consist of 60 stations, which are more uniformly distributed (Fig. 1.2) than were previous smaller networks (Blanc et al., 2010). The average separation distance of adjacent stations is around 2,000 km (Le Pichon et al., 2012; Hedlin and Walker, 2012). As of the end of August 2018, 51 stations have been certified (Fig. 1.3) by the CTBTO PrepCom and are in almost permanent operation. Another nine sites are under construction or still remain in the process of planning (CTBTO PrepCom, 2018).

Explosions in the Earth's atmosphere produce infrasound that can be recorded by highly sensitive pressure sensors — microbarometers — at considerable distance from the source. Each IMS infrasound station is constructed as an array, consisting of at least four microbarometers with a flat response from 0.01 Hz to 8 Hz. These sensors record differential pressure with a sensitivity down to 1 mPa. To enhance the signal-to-noise ratio (SNR) of detections in a noisy environment, the sensors are equipped with acoustic filters (Hedlin et al., 2003; Alcoverro and Le Pichon, 2005). These ensure a reduction in local noise — in particular, pressure disturbances induced by small-scale turbulence — and they are most efficient at frequencies above 0.5 Hz (Alcoverro and Le Pichon, 2005).

Altogether, each array serves as an acoustic antenna that provides an indication of the direction and apparent wave velocity of a passing coherent signal. The majority of stations are equipped with MB2000 and MB2005 microbarometer sensors. Their differential

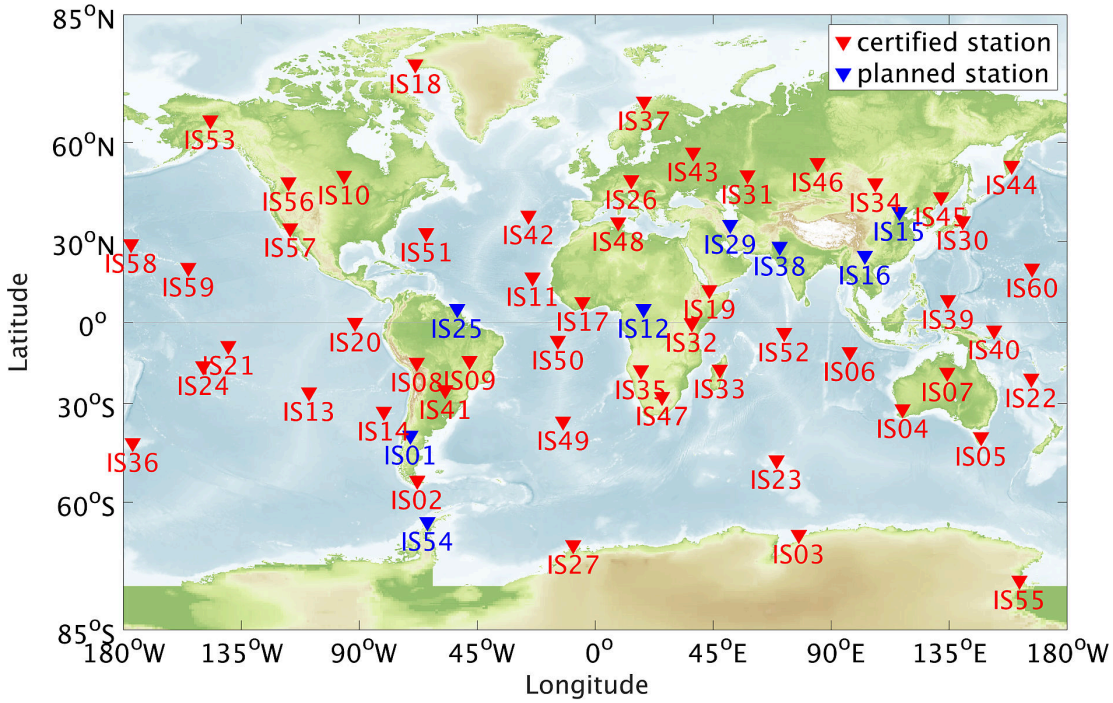

Figure 1.2: Station map of the IMS infrasound network as part of the CTBT verification regime. Each red triangle represents a certified array (August 2018), blue triangles depict planned sites, as far as the locations are already known.

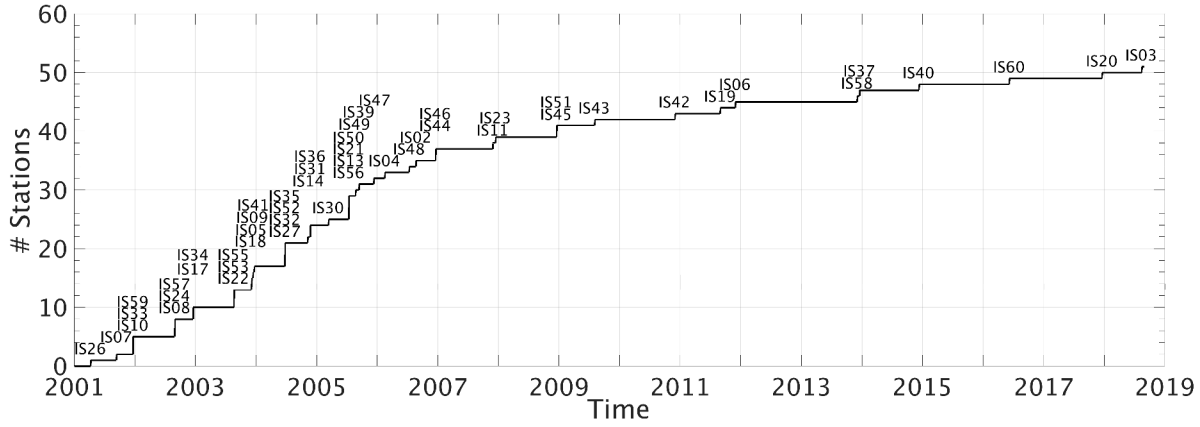

Figure 1.3: The number of certified stations that are part of the IMS (as of August 2018, according to CTBTO PrepCom, 2018) has significantly increased since the initial installations in the last 18 years. Note that short interruptions, followed by re-certifications — for example, after sensor replacement — are not considered.

pressure channels operate at a bandwidth of 0.01 Hz to 27 Hz and at a sampling rate of 20 Hz (MARTEC, 2006). In addition, these sensors record absolute air pressure at a sampling rate of 1 Hz (Ponceau and Bosca, 2010). This channel allows for measuring fluctuations, with frequencies ranging from direct current to 40 Hz (MARTEC, 2006); hence, measurements reflect atmospheric dynamics on different scales. In Chapter 4, the absolute pressure data of several stations are used to produce a global comparison of atmospheric tides. Following MARTEC (2006), the sensors' electronic noise amounts to 2 mPa ($2 \cdot 10^{-3}$ Pa), which is negligibly small in terms of atmospheric dynamics values that are commonly measured in the range of Pa to hPa. At the majority of stations, further equipment comprises meteorological sensors for wind speed, wind direction and temperature. Some stations have already been equipped with a new generation of microbarometer sensors, named MB3a. These feature further reduced sensor electronic noise (SeismoWave, 2014).

All certified IMS stations are subject to the calibration standards of the CTBTO PrepCom. National operators ensure station functionality and data quality. Satellite-based data transmission to the International Data Center (IDC) in Vienna is established through the Global Communications Infrastructure. At the IDC, all data are routinely processed to automatically detect explosive events in the atmosphere (Brachet et al., 2010; Marty, 2019). Chapter 2 describes an array processing method to detect correlated signals. National Data Centers (NDCs), such as the German Federal Institute for Geosciences and Natural Resources (BGR), can obtain IMS data for national duties, such as governmental consultation (Pilger et al., 2017), or for research purposes regarding infrasound propagation and source studies.

1.4 Mountain-associated infrasonic waves (MAWs)

A natural infrasound phenomenon, which has not been of much interest in terms of the CTBT, was first reported as very low frequency waves, as observed in North America (Cook, 1969). These waves possess periods of between 10 s and 100 s. According to Campbell and Young (1963), auroral activity was known to produce sound in this frequency range (see also Wilson et al., 2010), but the unfamiliar phenomenon mentioned by Cook (1969) was, as a result of triangulation, apparently linked to mountainous regions (Larson et al., 1971). Therefore, these acoustic waves are known as mountain-associated sound (Chimonas, 1977) or, more commonly, as MAWs. Figure 1.4 shows a typical example of coherent waveforms that were recorded at IMS infrasound station IS02 during a MAW event.

Larson et al. (1971) observed amplitudes of 0.05 Pa to 0.7 Pa at three sites in the USA — in Alaska, Colorado and Idaho. They found a daily variation in the number of detections, and considered local noise to be the reason. The annual cycle of MAW detections, showing maxima in winter months, seemed well correlated with zonal wind and eddy kinetic energy. As a result, Larson et al. (1971) postulated that wind speeds of at least $20\,\mathrm{m\,s^{-1}}$ at the 500 hPa level, and the corresponding wind direction perpendicular to the mountain range, were essential for MAW occurrence. They considered source mechanisms, such as atmospheric turbulence (as did Meecham, 1971) or spontaneous acoustic emissions

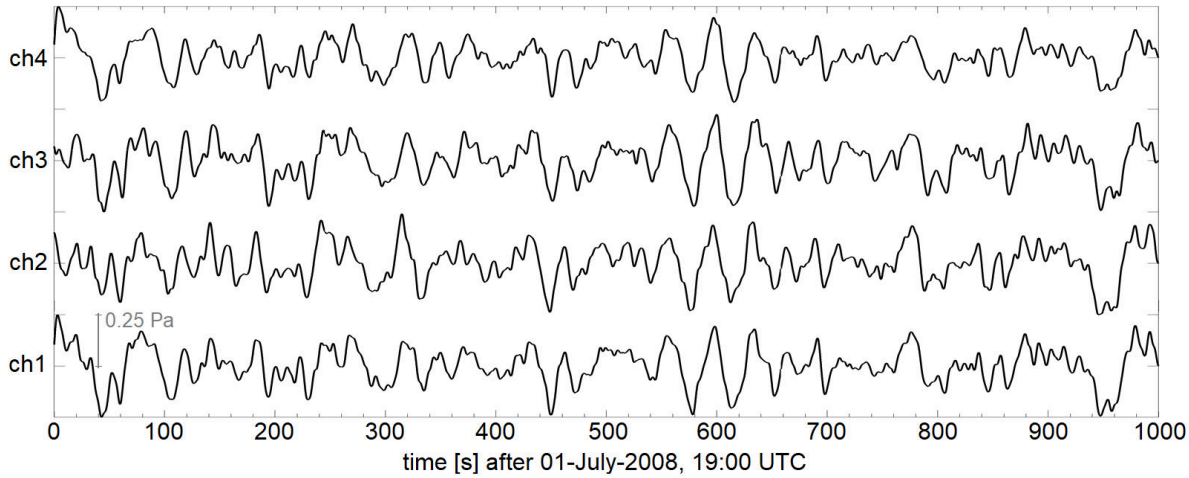

Figure 1.4: The bandpass-filtered waveforms (0.01–0.1 Hz) were recorded at the southern tip of South America. Four sensors, as part of IS02, show typical MAW signals. The waveforms are offset by 0.5 Pa. The array has an aperture of almost 2 km (an overview of IMS infrasound array configurations is given by Gibbons et al., 2015). The correlation coefficients for all pairs of the shown waveforms range from 0.85 to 0.96.

from vortex shedding, similar to the cause of Kármán vortex streets. Larson et al. (1971) supposed a more complex mechanism, based on the aerodynamic sound theory of Chanaud (1970), who suggested feedback mechanisms in addition to spontaneous sound emissions. The acoustic energy feedback could have been triggered by reflection at the ground or in particular atmospheric layers, such as the tropopause, as well as by interaction with surrounding obstacles (Larson et al., 1971). This would result in a reinforcement of the sound-producing flow or would otherwise disturb the initial sound field.
Based upon a mathematical, idealized two-dimensional approach, Chimonas (1977) investigated the idea of MAW production by non-acoustic waves in the same period domain interacting with terrain irregularities. His conclusion was that the scattering of wind oscillations with low phase velocity (i.e., in the order of the mean flow) to modes with high phase velocity (i.e., sound) at terrain irregularities could be the mechanism of "at least part of the infrasound signal" (Chimonas, 1977, p. 806).

An observational analysis by Bedard (1978), using sensors in the Rocky Mountains (USA), proved the pioneering hypothesis of Larson et al. (1971) regarding the annual cycle in detections. He consulted aircraft observations to support the theory of air turbulence being a source of MAWs. A conclusion was that the lee of the continental divide was a "preferred source region for infrasound" (Bedard, 1978, p. 1014). Remarkably, Rockway et al. (1974) had wondered whether the effect of atmospheric conditions on the propagation of MAWs had been underestimated in previous theories. They assessed the possible source mechanism by performing ray-tracing, based upon source regions along the Pacific Coast and in the Rocky Mountains, as determined by Larson et al. (1971). Indeed, winds affecting propagation conditions turned out to be the primary reason for the seasonal occurrence of

MAW detections. Rockway et al. (1974) concluded that propagation conditions need to be well understood in order to be able to identify possible source generation mechanisms, and suggested that emphasis be placed on the spectrum of signals. The latter was done by Thomas et al. (1974), again for measurements in the Rocky Mountains. Concerning the most likely source mechanisms, they studied the power spectra of eight MAW events towards mean-shear and isotropic turbulence. Following Meecham and Ford (1958) and Meecham (1971), respectively, the slopes of these spectra differ. From three considered sources — the jet-stream, lee waves (both associated with mean-shear turbulence) and wake turbulence (isotropic) — the observed power spectra best fit the isotropic theory, which made wake turbulence "a likely cause of MAW signals" (Thomas et al., 1974, p. 1397). They also noted that, if breaking lee waves were a source, MAWs would be associated with long and high mountain chains, rather than with isolated peaks, as has been observed in such studies so far.

The first published analysis beyond just North America was based on an infrasound network consisting of seven arrays located between Alaska and Argentina, plus one located in Israel (Greene and Howard, 1975). Each array was equipped with four microbarometers. In one year of data collection, many MAW signals were located between Colorado and Alaska in the Northern Hemisphere and along the southern part of the Andes in the Southern Hemisphere. Greene and Howard (1975) pointed out that much fewer detections were associated with the northern part of the Andes, concluding that acoustic radiation must depend on topography, single mountains or combined meteorological and topographic conditions.

Since then, however, the exact source mechanism has remained unclear, and published studies have become rare. Chunchuzov (1994) took up the theoretical approach again on the potential aerodynamic generation mechanism of MAWs due to wave scattering, as modeled by Chimonas (1977). More precisely, Chunchuzov (1994) proposed a generation model of non-stationary mountain waves that involve acoustic modes. The theory of non-stationary waves assumed that the wind velocities of the mean flow are subject to turbulent inhomogeneities and, therefore, continuously fluctuate. Perturbations induced by mountains are consequently non-stationary, which allows them to propagate in a stably stratified atmosphere (Chunchuzov, 1994), as opposed to the classical (stationary) GWs induced by orography. In addition to internal GWs, the non-stationary mountain wave model allowed the generation of acoustic impulses by "strong wind gusts among the wind fluctuations near the mountain" (Chunchuzov, 1994, p. 2205). The single acoustic impulses would propagate in atmospheric wave guides, whereas the remotely detected infrasound signal would be a superposition of each gust's impulse. It was concluded that this possible infrasound generation mechanism was analogous to the effective dipole radiation.

While the GW features of non-stationary mountain waves have been further investigated (e.g., Gavrilov, 1997; Hills and Durran, 2012), further investigations and reports on the infrasonic MAWs have been rare. Admittedly, McKisic (1997), who provided a review of infrasound observations, including MAWs, referred to Hauf et al. (1996), who recorded air pressure within a local microbarometer network in southern Germany at time scales of 2 s to 30 min. Signatures of between 0.02 Hz and 0.1 Hz, however, were "not correlated at the

different sensor locations" (Hauf et al., 1996, p. 1019). The corresponding power spectrum was associated with turbulence locally induced by wind. Since their actual focus was on GWs, detailed study of these signatures was not pursued.
Nishida et al. (2005) reported on observations of local MAWs in Japan. They used an experimental array consisting of 28 microbarometers, which were separated by about 500 m, and operated for 1.5 years.

Renewed interest arose from the opportunity to study low-frequency barometric fluctuations at remote sites around the globe, using the IMS infrasound network. Wilson et al. (2010) analyzed MAW detections at two stations. At IS53 in Alaska, they noticed three dominant directions of MAW arrivals, mainly detected during winter. Each direction was associated with a mountain range or peninsula within hundreds of kilometers of the sensors. They observed MAW events that exhibited a drift in the source direction over time. Wilson et al. (2010) associated this eastward shift with severe winter storms passing by. Similarly, they found dominant directions at IS55 in Antarctica. They postulated that the different waveform characteristics of selected events were related to the distance of the sources, assuming that more distant mountain ranges resulted in lower frequencies than nearer sources. The source localization, however, was seemingly based on topographic features and the exclusion principle. Without taking additional stations into consideration, triangulation methods for an exact source localization were not applicable.
More recent infrasound observations have attempted to provide a global view of MAWs (Blanc et al., 2018; Ceranna et al., 2019), using the IMS infrasound network, which is what led to the initiation of this research.

1.5 Hypothesis and research objectives

In past decades, reports on MAW observations have been rare, but the IMS infrasound network has provided an opportunity to renew research efforts on MAWs. The proposed source generation mechanisms in the 1970s were based upon measurements with regional sets of microbarometers, and Rockway et al. (1974) remarked that the generation mechanism was difficult to clarify, since infrasound detections of MAWs were subject to atmospheric variability. Larson et al. (1971) proposed, however, that the occurrence of MAWs correlated with high wind speeds at the 500 hPa level and a flow perpendicular to the mountain chains in North America. Chunchuzov (1994) considered the interaction of a non-stationary flow with mountains as a possible source of MAWs.
It is known from Gill (1982) and Nappo (2012), for instance, that GWs also require certain tropospheric wind conditions in order to be launched at orographic terrain, and to propagate into the middle atmosphere. Kaifler et al. (2015) reported that, on the one hand, strong stratospheric GW potential energy was observed over New Zealand when moderate to strong tropospheric winds, perpendicular to the mountain range, occurred; on the other hand, their observations showed that moderate to weak winds triggered large GW amplitudes in the mesosphere.

To better understand the physical origin of MAWs, their global occurrence is analyzed in detail here, and compared with tropospheric winds and GWs observed at stratospheric altitudes. The following hypothesis is assessed in this thesis:

Global infrasound observations allow identifying the source regions and the temporal variability of infrasonic MAWs. MAWs and orographic GWs share common physical conditions required for their excitation; therefore, infrasound observations are a suitable indirect method to monitor orographic GWs sources on a global scale.

The MAW observations have also been compared with the tropospheric wind conditions. Depending on its outcome, an agreement in the seasonal and spatial variation of both wave phenomena could be indicative of the source generation mechanism of MAWs. The following questions serve as a guide through this thesis:

I Does the station coverage of the IMS infrasound network allow the study of atmospheric wave phenomena on a global scale?

II Do NWP models appropriately reflect middle atmosphere variability in order to allow the explanation of infrasound detections by propagation modeling?

III Will a global analysis of MAW detections, using the IMS infrasound network, improve the understanding of MAW occurrence, compared to the findings on MAWs from the 1970s?

For the determination of MAW source regions (**III**), a cross-bearing method was elaborated. This method is described in Chapter 2, alongside an overview of infrasound data processing techniques, and the further data and methods used throughout this thesis. Chapter 3 deals with the theory of infrasound propagation and the role of the atmosphere. Chapter 4 demonstrates the potential of the IMS infrasound network in the global study of spatial and temporal variability of atmospheric tides, as seen in barometric recordings (**Question I**). Infrasound detections of a single IMS station are used to address **Question II** in Chapter 5. Lidar measurements and microbarom detections at the German IS26 allowed an estimation of the effects of middle atmosphere variability, and the related NWP model uncertainties, on propagation modeling. The results are relevant in the context of the CTBT, and also for the interpretation of MAW variability. In Chapter 6, the global infrasound network is used to characterize the seasonal variation in MAW detections, and to determine monthly source regions. Two MAW hotspots in the Southern Hemisphere are analyzed in detail to address **Question III**. This includes the validation of propagation conditions from these hotspots, using ray-tracing, and their tropospheric source conditions.

Furthermore, monthly MAW source regions are compared with stratospheric GW parameter climatologies derived from satellite data, and the possible source generation mechanism of MAWs is briefly discussed. Chapter 7 provides conclusions on the findings, with regard to the hypothesis. Further steps are outlined in Chapter 8.

2 | Datasets and methods

This thesis is generally based on data from the IMS infrasound network. A couple of additional observation technologies and datasets were used for comparison and validation purposes. In this chapter, methods are presented for obtaining coherent signal detections from infrasound data, and atmospheric data are introduced for modeling infrasound propagation. These data and methods are the subject of analyses throughout the thesis. Further technologies and datasets are, if applicable, briefly introduced in the respective chapters.

2.1 Infrasound data processing

The differential pressure data routinely sent to the IDC for data processing stress the huge storage capacities of the NDCs. The German IS26 in the Bavarian Forest, for instance, was installed in 1999, and IS27 at Neumayer Station in Antarctica has been operating since 2003. These arrays consist of eight and nine sensors, respectively, each recording at a sampling rate of 20 Hz. For IS26, this amounts to 576,000 samples per hour, or 13,824,000 samples per day. In addition, the original waveform data of all other IMS infrasound stations are archived at the BGR. To extract the relevant information from the large datasets, the following array processing algorithm was applied to the original waveform datasets for the automatic determination of wave parameters.

2.1.1 The Progressive Multi-Channel Correlation (PMCC) method

Cansi (1995) developed the PMCC algorithm to distinguish coherent signals from incoherent noise. He initially used 10 linearly-spaced frequency bands, between 0.01 Hz and 5 Hz. Since then, the PMCC algorithm has been enhanced by Le Pichon et al. (2010), who relied on a variable window length and 15 logarithmically-spaced frequency bands (similar to those in Fig. 2.1(a)) for more efficient computations (Ceranna et al., 2019).

The PMCC algorithm detects coherent acoustic energy at successive element triplets within an array, using bandpass filters, cross-correlation functions and time delays between sensors (Cansi, 1995). Thresholds apply for the maximum time delay to be considered as a coherent signal. An example of a wavefront arrival at an element triplet is given in Fig. 2.2. The time delays (e.g., Δt_{12}) and distances (e.g., r_{12}) among the sensors allow the PMCC algorithm to determine the apparent phase velocity (v_{app}) and the direction of origin, that

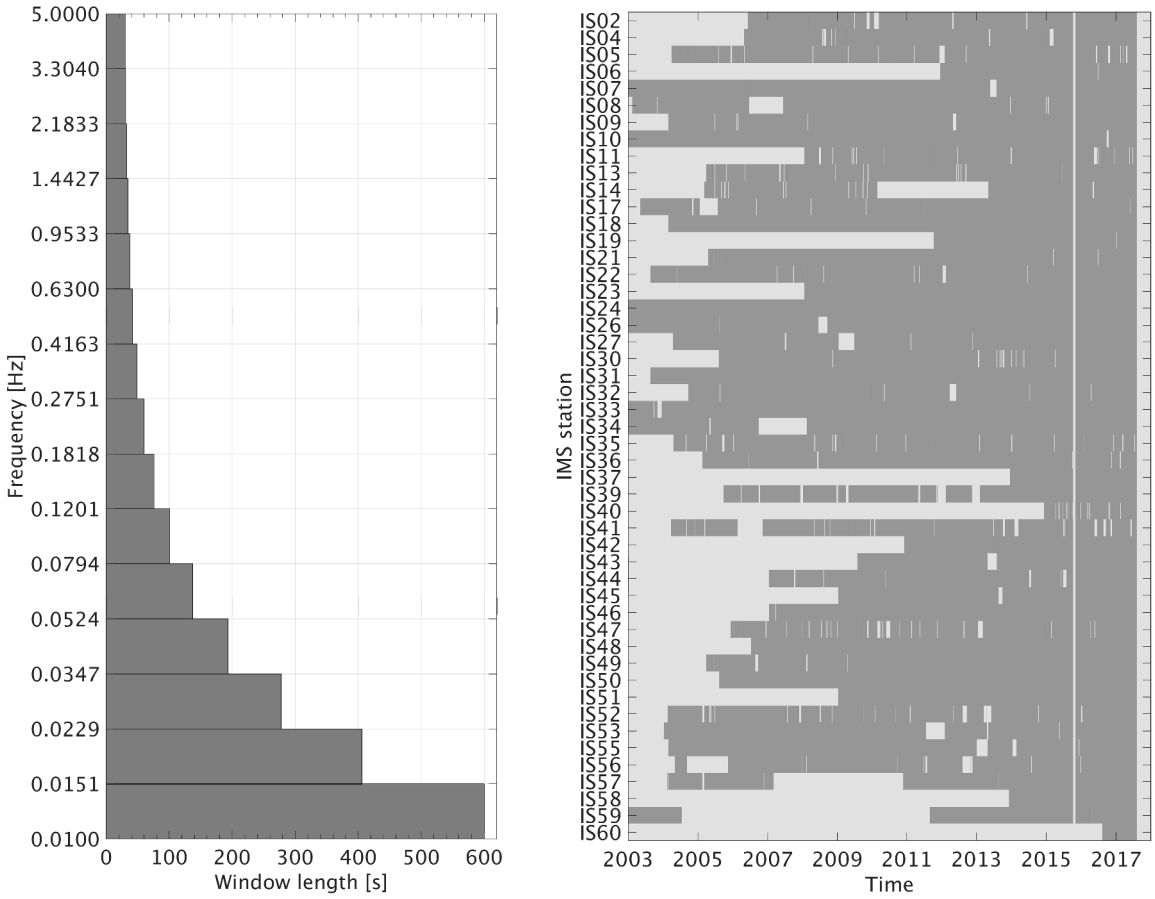

(a) Latest PMCC configuration.

(b) Data availability.

Figure 2.1: The standard PMCC configuration is based on 15 logarithmically-spaced frequency bands with varying time windows (a). The daily data availability (dark gray) at the German NDC (b) shows almost continuous operation of the IMS infrasound stations. The latest data retrieval from the IDC was in 2017. At the time of writing, data from end-2015 were subject to reprocessing.

is, the back-azimuth, β (as opposed to the propagation direction, α). Note that v_{app} refers to the apparent wavefront velocity in the x–y domain. If the wavefront is inclined — when the vector normal to the wavefront ($\hat{\boldsymbol{n}}$) has a vertical component (e.g., when arriving from higher altitudes) — the apparent phase velocity provided by the PMCC will be greater than the actual phase velocity (e.g., Evers, 2008).

The PMCC algorithm performs a calculation for each frequency band and time window. Each detected arrival is recorded as a pixel, and attributed with a frequency, time, back-azimuth and apparent velocity. Pixels are clustered into families if they exhibit similar wavefront parameters (in particular, β and v_{app}) in an evaluated time–frequency domain (e.g., Brachet et al., 2010). It is assumed that these belong to the same signal and event;

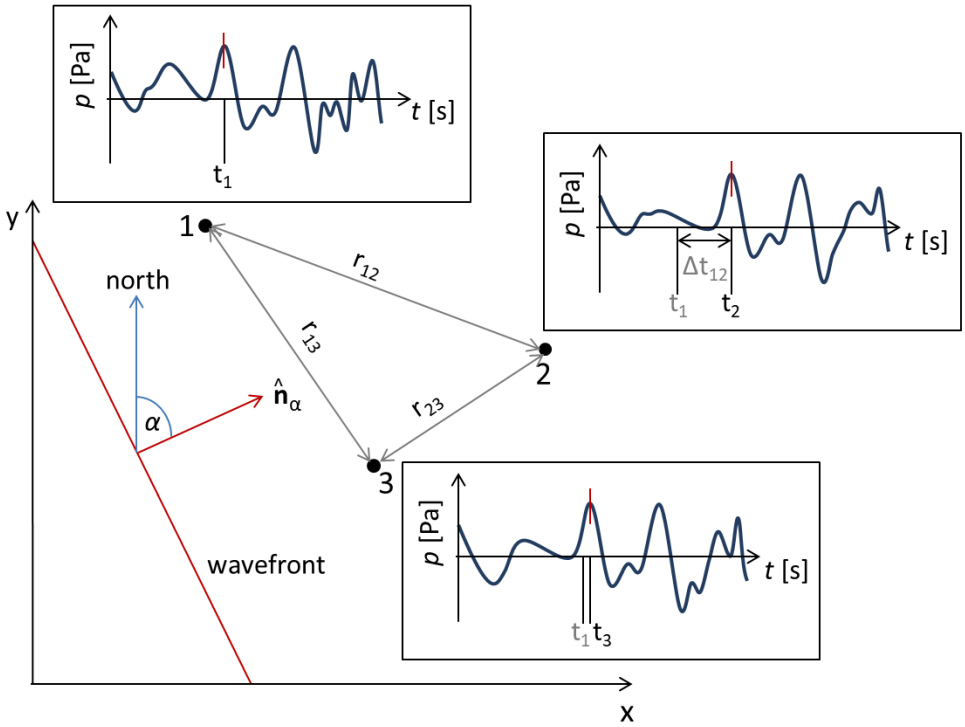

Figure 2.2: Schematic, two-dimensional illustration of a wavefront passing an array of infrasound sensors in the x-y domain. The unit vector normal to the wavefront ($\hat{\boldsymbol{n}}_\alpha$) denotes the propagation direction (α, respective to north). In bandpass-filtered pressure recordings (p) the arrival times (t_1, t_2, t_3) of the wavefront amplitude are marked by the red line.

thus, the family size is a measure of the dominance of an event (e.g., in terms of duration). The PMCC algorithm disregards those arrivals that are not associated with the dominant family in a given time window and frequency band (Cansi, 1995).

A Fisher correlation analysis in the time domain (e.g., Fisher, 1992) — which actually is an alternative method to PMCC — produces a Fisher ratio (F). Melton and Bailey (1957) first introduced the F-detector to analyze coherent signals within uncorrelated noise. F compares the variance of noise plus the coherent signal with the variance of noise; hence, for uncorrelated noise only, F equals one, exceeding one when a coherent signal is recorded. In the latter case, a relation between F and the SNR is provided, following Melton and Bailey (1957):

$$F = N_{array} \cdot SNR^2 + 1 \ , \tag{2.1}$$

where N_{array} is the number of array elements contributing to the analysis. As a threshold, Olson (2004) statistically tested that, for $F > 3$, the recorded signal will contain a coherent signal with a confidence level of 99 %.

All detected events using the PMCC algorithm are stored in bulletins, which are also archived at the BGR. These detection lists contain, inter alia, the following parameters:

- Time of arrival (start, and end or duration)
- Frequency (min, max, central)
- Root-mean-square (RMS) amplitude
- β and its standard deviation (σ)
- v_{app} and σ
- Family size
- Correlation accuracy
- Peak-to-peak amplitude
- Fisher ratio (F)

For this study, all waveform data from the IMS infrasound network, which were obtained from the IDC for the time period January 2003 to July 2017, were reprocessed using the configuration shown in Fig. 2.1(a). This consumed an equivalent total central processing unit time of approximately 13 years. The resulting data availability at the German NDC is shown in Fig. 2.1(b).

The large number of infrasound detections provided by the bulletins can be categorized into three main frequency domains. In the context of the CTBT, the most important detections cover frequencies between 0.1 Hz and 0.5 Hz. This is the dominant range of PMCC detections, equivalent to periods of $\leq$10 s and $\geq$2 s, respectively. Atmospheric explosions, meteorites and microbaroms occur in this frequency band (Ceranna et al., 2019, and references therein), the latter of which are assessed in Chapter 5. Frequencies between 0.5 Hz and 5 Hz are associated with transient natural signals, such as volcanoes, or man-made disturbances, such as mining (Le Pichon et al., 2008; Pilger et al., 2018). The detected signals with frequencies below 0.1 Hz are generally of natural origin, and include auroras and the MAWs (Wilson et al., 2010), the latter of which are analyzed in Chapter 6. Hardly any detections are obtained below 0.01 Hz using the standard PMCC configuration. Here, the transition from acoustic waves to gravity waves is marked by the acoustic cut-off frequency and the Brunt–Väisälä frequency, respectively.

2.1.2 Adjusting the PMCC algorithm for GWs

An adjustment of the PMCC configuration towards lower frequencies is currently not the primary purpose, in terms of the CTBT. Nevertheless, it would be a bonus for atmospheric studies if such a global network was capable of monitoring GWs. Marty et al. (2010) has already demonstrated that GWs are represented in the power spectral density (PSD) functions of the IMS pressure recordings. The detection of GWs at a single infrasound station, IS17 in Ivory Coast, has clearly exhibited the geographical variation of deep convection associated with the Intertropical Convergence Zone (Blanc et al., 2018).

To allow automatic detection of GWs using the PMCC, the frequency bands and window lengths were modified. Initially, 10 frequency bands were considered, in order to limit

the processing time. Compared to the standard PMCC configuration, the detections were significantly reduced, only covering the lower period scales (up to 3 h) of the GWs. This limitation is a result of the IMS array apertures, which are generally of the order of 1 km to 3 km (Christie and Campus, 2010; Evers and Haak, 2010); hence, longer wavelengths and larger period scales up to 24 h are technically omitted. Chapter 6 provides an overview of GW detections using the PMCC algorithm.

2.1.3 Cross-bearing method for source localization

The back-azimuth given in the detection lists provides the direction of origin of a detected source. The time delay between coherent signals at an array's sensors provides the apparent phase velocity. With this information from at least two different arrays, a likely source region can be estimated. The more stations that contribute, the more precise is the localization — essential in the CTBT context, when verifying nuclear tests using IMS technologies. Natural ambient noise, however, such as microbaroms and MAWs, is a two-dimensional, quasi-continuous signal, rather than a sudden point-like explosion (Landès et al., 2012). Moreover, the detectability of specific events at different stations depends on the propagation conditions between the source and the station, as elaborated upon in Chapter 3. For these reasons, common methods using the onset times of at least two different stations (e.g., Le Pichon et al., 2008) are not applicable to arriving wave trains of MAWs. Instead, the dominant back-azimuth of a station in a defined time period is used for the cross-bearing approach. A combination of three stations is required for a solid localization of a signal's origin. The cross-bearing method used here is, in principle, similar to the one of Landès et al. (2012), which was used for locating microbarom source regions.

Since a detected back-azimuth (β) is fraught with uncertainty, due to array response, outage of a single sensor, or wind conditions along the propagation path (e.g., Le Pichon et al., 2005b), a general standard deviation of $\pm 5^\circ$ is added. This results in an azimuthal sector of 10° width. Landès et al. (2012) assumed a maximum propagation range of 10,000 km for microbaroms. In this thesis, this is assumed to be applicable to MAWs as well, since atmospheric attenuation in such low-frequency domains is generally low, as pointed out in Chapter 3.

Instead of a pixel-based polygon overlap (Landès et al., 2012), the following method was chosen. For each three-station set, all conceivable combinations of three rays (one per station), with azimuths of (i) $\beta - 5^\circ$, (ii) β or (iii) $\beta + 5^\circ$ were projected along the great circle paths, amounting to $3^3 = 27$ combinations. A maximum of three intersection points were calculated for each of these three-station combinations. Figure 2.3 demonstrates the procedure (a) schematically, and (b) using IMS station locations shown on a Mollweide projection.

If three intersection points were found, all of the rays in a three-station combination will intersect, and the longitudinal and latitudinal means will determine the coordinates of the combination's final location (Fig. 2.3). If only two intersection points were required, the method would consequently result in more, but maybe less accurate, localizations. This option may, however, be worth considering in regions with limited station coverage.

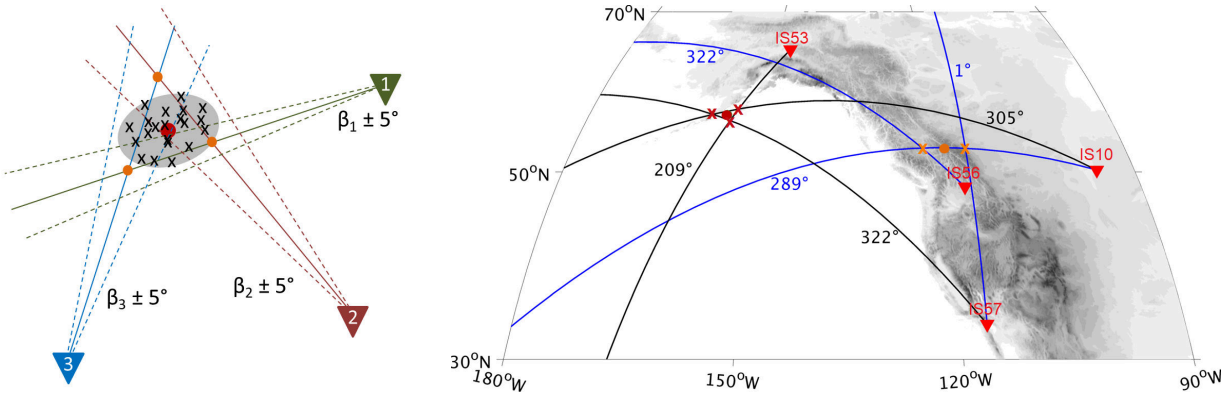

(a) Schematic illustration of the cross-bearing approach.

(b) Two different three-station combinations, depicted in black and blue, in North America.

Figure 2.3: The cross-bearing method is demonstrated by two examples. (a) A fictive combination of three stations is shown schematically. The stations' dominant back-azimuths are depicted by solid lines, the dashed lines depict the 5° uncertainties. For the main back-azimuths, the intersection points (orange circles) are shown, from which the final location (red circle) is derived. For all other combinations, the black crosses mark the final locations. The gray-shaded polygon ultimately highlights the likely source region of a signal detected at all stations. (b) Bearings along the great circle were applied to four IMS stations, shown on a Mollweide projection. One station combination is depicted by blue lines and another by black lines (without uncertainties). Only two intersection points (orange crosses) exist for the blue combination. The median point would be the orange circle, which in this case could be quite accurate, due to the short distance. It is also possible that the stations' back-azimuths represent different sources, however. To overcome this, it is required that three intersection points are found. The black combination fulfills this requirement (red crosses); hence, the located source origin (red circle) is probably more accurate.

Localizations based on one intersection point are generally neglected, since this is, in fact, a two-station combination, which is too prone to uncertainties when allowing a range of 10,000 km.

Another source of uncertainty might be a station combination in which at least one pair of back-azimuths points either in the same (one alongside the other) or opposite (towards each other) direction(s). Here, the triangulation method does not necessarily fail, but only slight deviations in the back-azimuths can cause significant horizontal shifts in the intersection point coordinates. Therefore, such combinations, with $\beta_1 - \beta_2 = \pm 10°$, are excluded. The cross-bearing method was applied to determining global MAW source regions (Chapter 6).

2.2 Atmospheric models of the European Center for Medium-Range Weather Forecasts (ECMWF)

The datasets of the ECMWF are often referred to not only in terms of forecast data, but also for comparisons with observational data and their validation. Moreover, they serve as input for infrasound propagation modeling. The ECMWF provides both reanalysis and operational datasets on a global scale. Among these services are ERA-interim and the high-resolution (HRES) atmospheric model analysis, which is provided by the Integrated Forecasting System (IFS). ERA-interim reanalyzes the atmosphere back to 1979 (Dee et al., 2011). Meteorological fields are available each 6 h at 60 vertical levels up to 0.1 hPa; the spatial resolution is 80 km (Berrisford et al., 2011). In this thesis, generally, the HRES operational analysis was focused on when referring to ECMWF data. HRES analysis fields are available each 6 h on a 0.1° x 0.1° grid. The model's upper limit is 0.01 hPa (around 80 km); the evolution of the vertical resolution started with 60 levels, before 91 levels were introduced in 2006. Since 2013, the atmospheric fields have been given for 137 vertical levels (ECMWF, 2014). In the upper levels, sponge layers are included to filter the wave reflections necessary for ensuring model performance (e.g., Smets, 2018).

Below the sponge layers, the model assimilates different data, from ground-based measurements to satellite observations, in order to represent the atmospheric state as realistically as possible. Therefore, the HRES wind and temperature fields of the IFS are commonly used in the context of infrasound propagation modeling (e.g., Le Pichon et al., 2012; Landès et al., 2014). In Chapter 5, lidar temperature measurements and ECMWF data are compared in order to estimate the effect of NWP model uncertainties in infrasound propagation. The HRES data are also considered for evaluations and ray-tracing in Chapter 6.

2.3 Compact Rayleigh Autonomous Lidar (CORAL)

Rayleigh lidars have been used for temperature measurements in the stratosphere and mesosphere since the end of the 1970s (Hauchecorne and Chanin, 1980). The technology makes use of Rayleigh scattering — a laser beam that is vertically pulsed into the atmosphere is backscattered at air molecules. The number of photon detections correlates with the air density. Altitude determination is based upon the time delay of the detected photons. Assuming the ideal gas relation (see Chapter 3), temperature profiles can be derived (Hauchecorne and Chanin, 1980).

Lidars provide data at high temporal and vertical resolution, which is why they are a key instrument in studying GWs in the middle atmosphere (e.g., Baumgarten et al., 2017; Hildebrand et al., 2017). Methods for extracting GWs from lidar observations have been discussed by Ehard et al. (2015). Due to a lack of autonomously-operating lidar systems for studying middle atmosphere dynamics at very remote locations (Kaifler, 2018a), the mobile system, CORAL, was developed at the Institute of Atmospheric Physics of the Ger-

man Aerospace Center (DLR). CORAL is highly appropriate for temporary observations at remote locations, since it can be operated for "at least six months" (Kaifler, 2018a, p. 4) without service inspection and, if at all needed, by remote control. These features encouraged a study at the German IS26 in the Bavarian Forest (Fig. 2.4(a)), prior to CORAL being shipped to Rio Grande in Argentina. Since November 2017, it has been installed for long-term GW observations at the southern tip of South America, a well-known hotspot for orographic GWs (e.g., Hoffmann et al., 2013, 2016; Jewtoukoff et al., 2015). Its location is less than 100 km northwest of IS02 in Ushuaia (Argentina), which will again encourage comparisons with infrasound recordings.

CORAL measures the photon count of a monochromatic laser beam with a wavelength of 532 nm. Temperature profiles are retrieved between approximately 14 km and 95 km altitude (Kaifler, 2018a). The vertical and temporal resolutions are 900 m and 10 min, respectively. Observations are limited to clear-sky conditions at night. The mobile system is equipped with a precipitation sensor and an all-sky camera (Fig. 2.4(b)) for automatic start-up and shut-down.

The campaign at IS26 resulted in 485 h of observation between May and November 2016. Temperature data from these observations were used to quantify the bias in the ECMWF operational HRES analysis, and its effect on atmospheric infrasound propagation modeling, in Chapter 5. In November 2017, CORAL was installed in Argentina. During the first 10 months of operation, several GW events were observed. The duration of the campaign is scheduled to last at least two years (Kaifler, 2018a).

(a) Infrared picture showing CORAL operating at IS26 on 14 November 2016.

(b) CORAL's precipitation and wind sensors.

Figure 2.4: CORAL was autonomously operated at IS26 in the Bavarian Forest (a). It is equipped with meteorological sensors (b). No human assistance is needed for start-up and shut-down during clear-sky conditions at night.

2.4 A ray-tracer for modeling infrasound propagation

Ray-tracing is one of the common methods for modeling infrasound propagation in the atmosphere (e.g., Evers, 2008). In this thesis, the two-dimensional finite differences (2D-FD) ray-tracing software package of Margrave (2000) was used. This solves the scalar wave equation with variable (sound) velocity:

$$\nabla^2 p_a(x,z,t) = \frac{1}{c^2(x,z)} \frac{\partial^2}{\partial t^2} p_a(x,z,t) \tag{2.2}$$

Here c and p_a are the speed of sound and the acoustic pressure wave field, respectively. The Laplace operator is given by:

$$\nabla^2 = \frac{\partial^2}{\partial x^2} + \frac{\partial^2}{\partial z^2} \tag{2.3}$$

The 2D-FD ray-tracer was initially developed for seismological purposes, but it can also be adapted to enable high-frequency approximation for estimating sound propagation in the atmosphere (Koch and Pilger, 2018). As an example, Le Pichon et al. (2013) successfully modeled long-range ducting, on a global scale, for the low-frequency fireball event of Chelyabinsk (Pilger et al., 2015) using the 2D-FD ray-tracer.

Inputs to the ray-tracer are atmospheric analysis fields for calculating the sound velocity field (Chapter 3). For the purposes of this study, the following set-up was chosen. Along the great-circle propagation path between the source and the receiver, vertical profiles of temperature, meridional wind and zonal wind were given each 100 km. These were interpolated to a horizontal and vertical grid of 500 m x 500 m. The upper model limit was set to 140 km. The vertical profiles were monthly means of ECMWF operational HRES analysis fields of up to 78 km altitude. These were supplemented by climatological temperature and wind data from empirical models. Temperature and atmospheric composition were obtained from the Naval Research Laboratory (NRL) Mass Spectrometer Incoherent Scatter Extended (MSISE) model, as of 2000 (NRLMSISE-00), produced by Picone et al. (2002). Meridional and zonal winds were based upon the Horizontal Wind Model (HWM), as of 2007 (HWM07), developed by Drob et al. (2008).
Rays are shot at azimuthal intervals of 1°, using elevation angles of 1° (straight up) to 89° (almost horizontal) for sources at the surface; for elevated sources, the elevation angles are extended to 179° (straight down). Another input parameter is the source frequency (f), which is needed to account for the atmospheric attenuation of infrasound. The theory behind infrasound propagation in the atmosphere, and a modeled example, are given in the next chapter. Furthermore, the ray-tracer is relied upon in Chapter 6 to validate the propagation conditions for MAWs.

3 | Theory: Infrasound propagation in the atmosphere

As stated in Section 1.2, infrasound can propagate over long distances because of minor atmospheric attenuation at low frequencies (De Groot-Hedlin et al., 2010). The essential role of middle atmosphere dynamics on infrasound propagation is highlighted in this chapter.

3.1 Effective sound speed

The speed of sound (c) in gases and liquids is calculated using the Newton–Laplace formula,

$$c = \sqrt{\frac{K}{\rho}} \ , \tag{3.1}$$

where K denotes the bulk modulus and ρ is the density of the medium. Assuming air to be an ideal gas, and acoustic wave propagation an adiabatic process (i.e., without heat transfer), it is

$$K = \kappa\, p \ , \tag{3.2}$$

where $\kappa = c_p\, c_v^{-1}$ is the adiabatic exponent, defined by the ratio of heat capacities at constant pressure (c_p) and constant volume (c_v). κ is well approximated by 1.4. p is the pressure, which can be substituted by the ideal gas law,

$$p = \rho\, R_s\, T \ , \tag{3.3}$$

with the specific gas constant $R_s = 287\,\mathrm{J\,kg^{-1}\,K^{-1}}$ (for dry air), and T denotes the temperature. Eq. 3.1 can then be written as the adiabatic speed of sound (c_T):

$$c_T = \sqrt{\kappa\, R_s\, T} \approx 20.05\,\sqrt{T}\ (\mathrm{in\ m\,s^{-1}}) \tag{3.4}$$

Horizontal winds play an essential role in the atmospheric ducting of acoustic energy (Drob et al., 2003), as winds govern the advection and refraction of sound. The vertical wind component is negligible to the first order, since the vertical motions are very small compared to the horizontal ones (e.g., in the troposphere: $\|\boldsymbol{v}_z\| \approx 0.1\,\mathrm{m\,s^{-1}}$ and $\|\boldsymbol{v}_h\| \approx 10\,\mathrm{m\,s^{-1}}$), except in small-scale synoptic phenomena. In a stratified atmosphere, the effect

of wind on sound wave velocity can best be explained by introducing the effective sound speed, v_{eff} (e.g., Wilson, 2003; Evers, 2008; Smets, 2018):

$$v_{eff} = c_T + w_\alpha \approx 20.05\sqrt{T} + w_\alpha \quad (\text{in m s}^{-1}) \,, \tag{3.5}$$

where c_T is the adiabatic speed of sound (Eq. 3.4) and w_α is the along-path wind speed (positive in the azimuthal direction of propagation, α). w_α is obtained by projecting the horizontal wind vector, $\boldsymbol{v}_h$, in the direction of α using the unit vector normal to the wavefront, $\hat{\boldsymbol{n}}_\alpha$ (see Fig. 2.2). Defining α beginning at north (0°–360°) (clockwise), the projection is calculated according to:

$$w_\alpha = \hat{\boldsymbol{n}}_\alpha \cdot \boldsymbol{v}_h = \begin{pmatrix} \sin\alpha \\ \cos\alpha \end{pmatrix} \cdot \begin{pmatrix} u \\ v \end{pmatrix} = u \cdot \sin\alpha + v \cdot \cos\alpha \tag{3.6}$$

Equation 3.5 implies that tail winds (advection) increase the effective sound speed and head winds reduce it. An important characteristic of sound in this context is its gradual refraction at layers with a sound-speed gradient, following Snell's law, in principle.
Overall, sound waves bend towards layers with lower effective sound speed; thus, in the absence of wind (see Fig. 3.1), a positive (negative) vertical temperature or adiabatic sound-speed gradient itself causes downward (upward) sound refraction (left side of Eq. 3.5). Given a positive vertical gradient of horizontal wind speed, the refractive properties will depend on the propagation direction, as shown schematically in Fig. 3.2. For downwind propagating waves, wind speeds increasing with altitude cause a positive effective sound-speed gradient and, hence, downward refraction; vice versa, upwind propagating sound

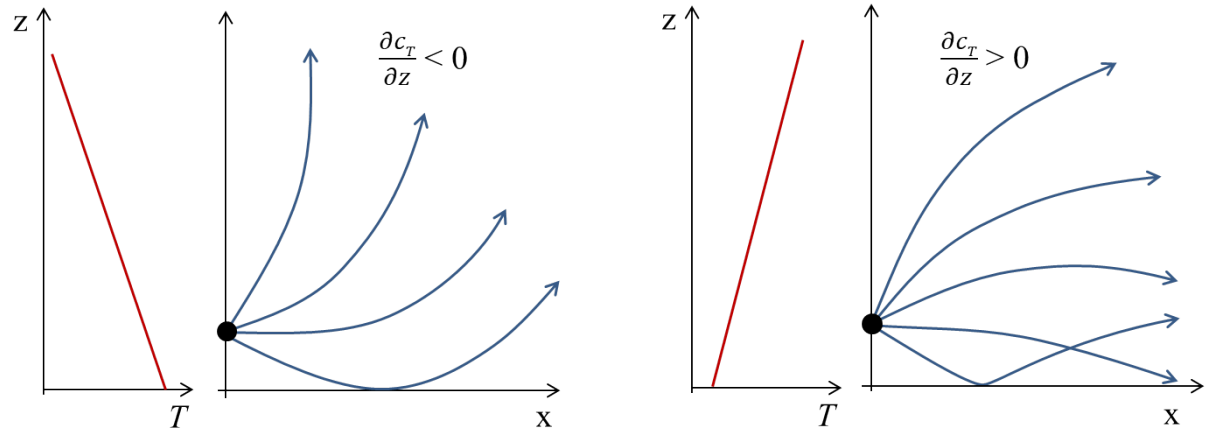

Figure 3.1: The principle of sound refraction due to a vertical temperature gradient (adiabatic speed of sound) is shown schematically. The temperature profiles are depicted in red. The fictive source (black circle) in the right-hand panels radiates sound in all directions. The effect of refraction (left – upward, right – downward) is depicted by the blue lines.

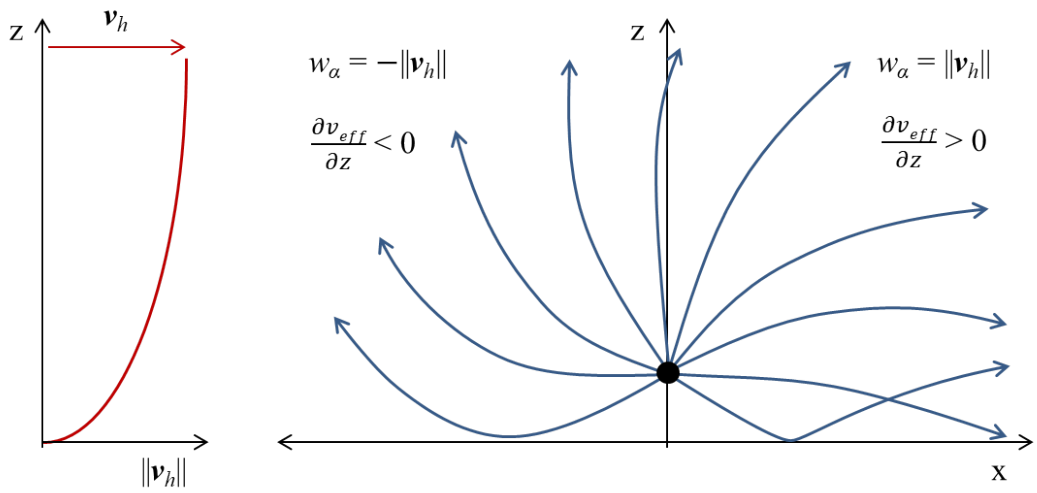

Figure 3.2: Similar to Fig. 3.1, but for a vertical gradient of horizontal wind speed. The horizontal wind speed profile is shown on the left, the wind direction is from left to right. The fictive source (black circle) in the right-hand panel radiates sound to in directions (upwind to the left, downwind to the right). The effect of refraction (left – upward, right – downward) depends on the sound propagation direction relative to the wind.

bends to higher altitudes due to the effectively decreasing sound speed caused by increasing tailwinds.

To estimate the combined effect of wind and temperature in a certain stratospheric layer, v_{eff} at altitude z is commonly compared to v_{eff} at the ground ($z_0 = 0\,\text{km}$) (e.g., Le Pichon et al., 2012), expressed as the effective sound speed ratio ($v_{eff-ratio}$):

$$v_{eff-ratio} = \frac{v_{eff,z}}{v_{eff,z_0}} \tag{3.7}$$

Downward refraction of an upward-propagating signal is likely when $v_{eff-ratio} \geq 1$. In the real atmosphere, three layers exist at which this condition can be fulfilled.

3.2 The role of the atmosphere

Adiabatic and effective sound speed vary with temperature and horizontal winds in terms of altitude, time and geographic location. Overall, four layers of the atmosphere are defined using the vertical temperature gradient. In the troposphere, temperature decreases up to altitudes of 10 km to 16 km; this is known as the tropopause, where temperature is almost constant. The layered stratosphere above this is characterized by a strong positive temperature gradient caused by the absorption of solar radiation in the ozone layer. The vertical extent of the stratosphere varies with season. Its upper limit, the stratopause, is given by a local maximum of the vertical temperature profile at around 40 km to 50 km

altitude. In the mesosphere, the temperature decreases to the absolute minimum of around -160°C, found at altitudes of between 85 km and 100 km above the summer pole. At mid-latitudes (Fig. 3.3(a)), the mesopause temperature amounts to −110°C in summer and −80°C in winter. Beyond the mesopause, temperature continuously increases in the thermospheric region, up to the exobase (at around 500 km), where temperature remains constant. This described structure of the atmosphere can be recognized in typical winter and summer vertical profiles for Central Europe, as shown in Fig. 3.3.

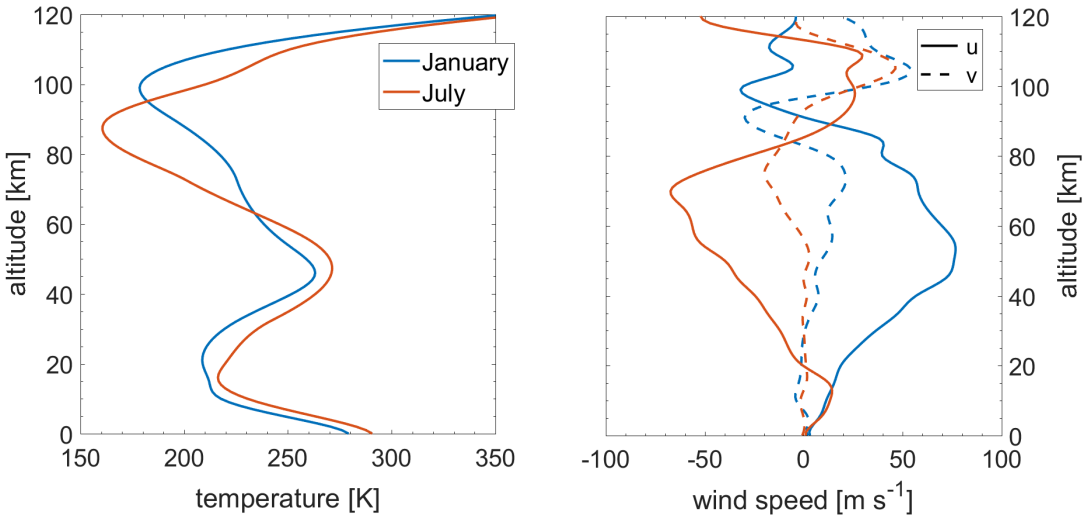

(a) Temperature. (b) Zonal (u) and meridional (v) winds.

Figure 3.3: The vertical structure of the atmosphere at 48.15°N and 11.75°E (Munich, Germany) is shown as a climatological mean for 15 January (blue) and 15 July (red). Data were obtained from the MSISE-00 and HWM07 empirical models.

Obviously, in the middle atmosphere the zonal wind speed is one magnitude higher than its meridional counterpart, and changes direction twice a year. This zonal wind pattern is called the stratospheric jet. It is at its maximum in an altitude region near the stratopause, at which location the temperature, and thus the adiabatic speed of sound, are relatively high. In the thermosphere, where the temperature gradient grows even greater, independently of the season, meridional winds become more relevant.

Using Eq. 3.6, the horizontal wind components are converted into along-path wind speed to calculate the effective sound speed (Eq. 3.5). In Fig. 3.4, the along-path wind speed is represented by the difference between effective and adiabatic sound speed, as shown for eastward and westward wave propagation. It is evident that the zonal wind significantly impacts the directional sound wave advection at the stratopause layer in summer and winter, while the adiabatic sound speed is on a comparable scale. During the reversal of the middle atmosphere circulation in the equinox months, the impact is weaker (e.g., in April). Since $v_{eff-ratio}$ has been introduced to estimate whether upward-propagating infrasonic waves are refracted downwards to the surface, a vertical line has been added

to the figures to indicate $v_{eff-ratio} = 1$. At altitudes where v_{eff} exceeds the line up to the maximum v_{eff}, sound waves can be assumed to bend downwards. Therefore, these altitudes are referred to as the turning heights of acoustic waves (e.g., Drob et al., 2013).

Acoustic waves adopt the characteristic effective sound speeds at the encountered turning heights as their apparent phase velocities (e.g., Wilson et al., 2010). Overall, thermospheric returns (from around 370 m s^{-1}) enable higher phase velocities than stratospheric returns (up to 400 m s^{-1}; see Fig. 3.4(d)); hence, the apparent phase velocity of a signal detected at the ground allows an estimation of the turning height and, thus, the relevant waveguide.

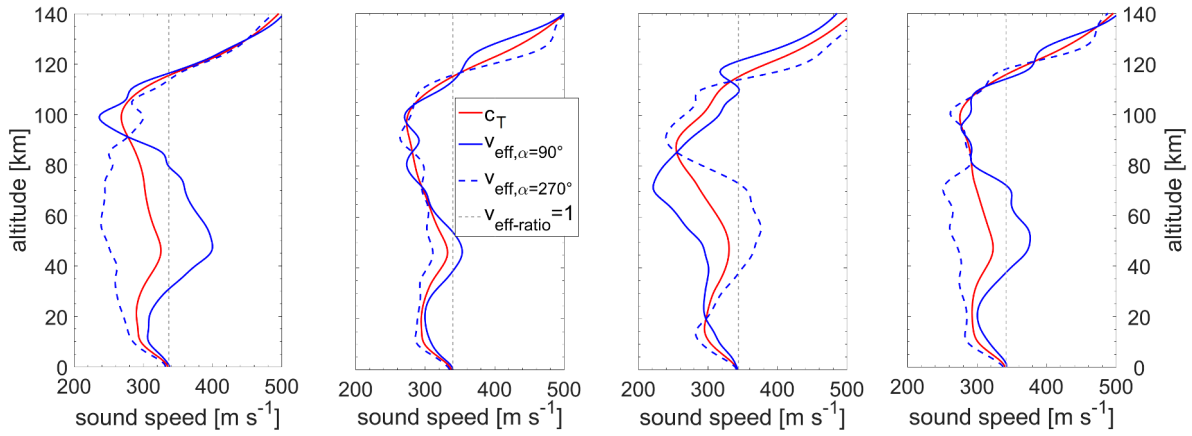

(a) January. (b) April. (c) July. (d) October.

Figure 3.4: Based upon the same datasets and location as in Fig. 3.3, the seasonal variations of adiabatic and effective sound speed are shown for eastward ($\alpha = 90°$, solid lines) and westward ($\alpha = 270°$, dashed lines) propagation.

3.2.1 Acoustic waveguides

The presence of a turning height implies the formation of an acoustic waveguide in the lower part of the atmosphere, if along-path propagation conditions are stable. Assuming the Earth's surface to be a nearly flat reflector, an infrasound signal could then be refracted and reflected multiple times, allowing its detection several hundreds of kilometers downwind from its source.

As could be expected from Fig. 3.3, the strong temperature increase in the thermosphere is only weakly affected by horizontal winds throughout the year (Fig. 3.4); hence, it favors a **ground-to-thermosphere waveguide** that exists almost independently of the propagation direction. The minimum turning height varies between 110 km and 120 km.

The **surface-to-stratopause waveguide** is highly variable with season, especially if the propagation direction has a zonal component. Turning heights can be found, if they

exist, between 40 km and 60 km, and even down to 30 km in winter (Fig. 3.4). Conditions for the stratospheric ducting of acoustic energy also vary with latitude. Zonal mean zonal wind speeds exhibit two extremes, of around $60\,\mathrm{m\,s^{-1}}$ to $70\,\mathrm{m\,s^{-1}}$, at the mid-latitudes during summer and winter (Fig. 3.5). The stratospheric circulation is opposed in both hemispheres; hence, wind speeds rapidly decrease to $0\,\mathrm{m\,s^{-1}}$ at the equator and the poles. Consequently, stratospheric ducting is most pronounced at mid-latitudes (Drob et al., 2003).

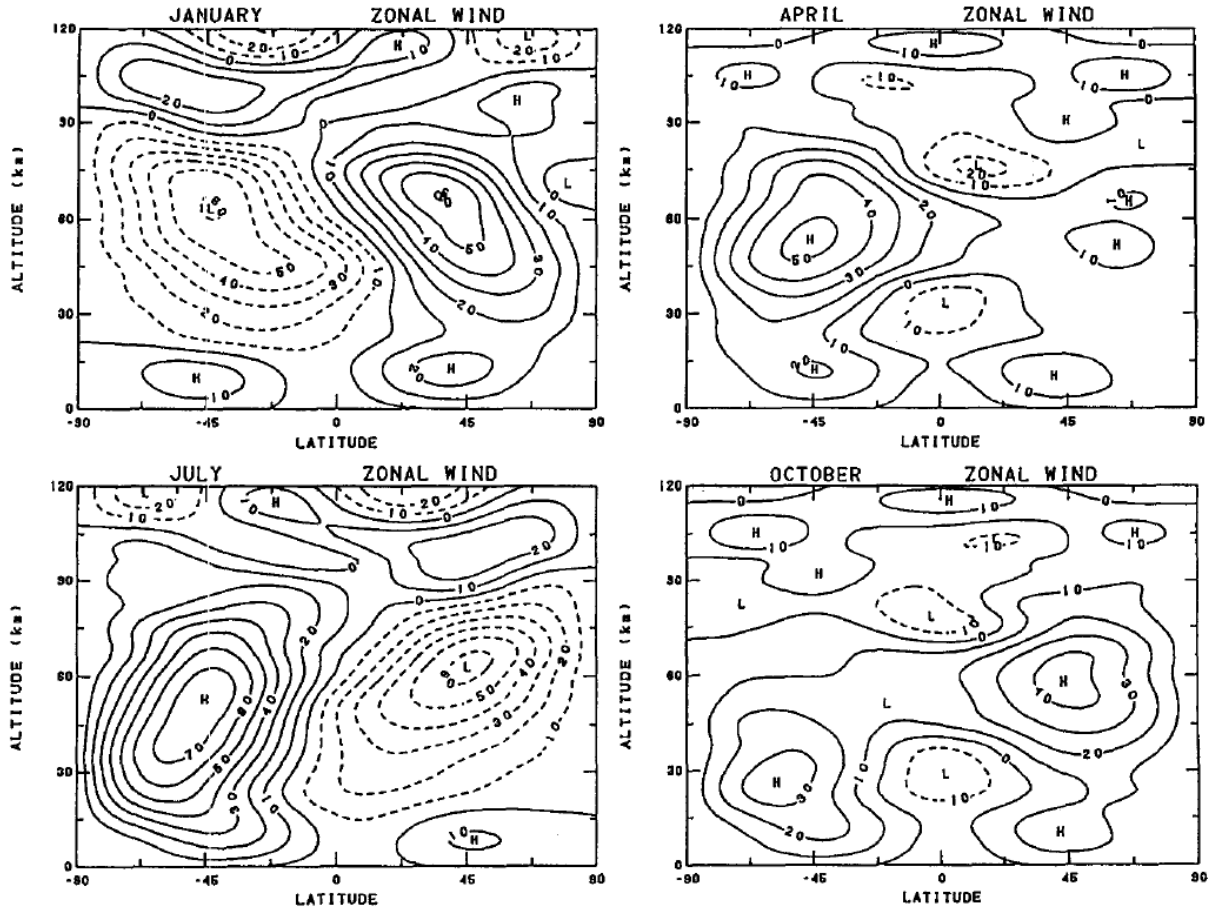

Figure 3.5: Contour plots of zonal mean zonal wind (in $\mathrm{m\,s^{-1}}$) for January, April, July and October (adapted from Hedin et al., 1996). The highest wind velocities can be found at the mid-latitudes at altitudes of between 30 km and 70 km. In the middle atmosphere circulation, eastward winds (solid lines) prevail in winter and westward winds (dashed lines) in summer. During the equinoctial months, the circulation pattern reverses.

Besides seasonal variability, waveguides are sensitive to changes in winds and temperature on shorter time scales from weeks to days. For example, SSW events can affect propagation conditions in the Northern Hemisphere when the polar vortex temporarily weakens, reverses or splits. In the latter case, the meridional wind component gains importance, in terms of stratospheric ducting. During SSW events, predominant propagation directions

are often suppressed, and opposite directions are favored (Smets and Evers, 2014). On time scales of hours, for instance, GW perturbations of middle atmosphere winds and temperature have the potential to affect refractivity (Chunchuzov and Kulichkov, 2019). This especially applies where stratospheric wind speeds are low, such that the $v_{eff-ratio}$ is close to one.

Obviously, the third conceivable waveguide — the **ground-to-troposphere waveguide** — cannot be anticipated in Fig. 3.4. Here, the effective sound speed decreases with altitude, independent of the propagation direction. This implies that infrasound bends upward in the lower atmosphere. As a result, an acoustic **shadow zone** evolves, in which signals are rarely detected. The extent of this varies between 100 km and 300 km from the source, depending on the source elevation and turning heights.
At the tropopause, the temperature gradient itself is not sufficient for refracting acoustic signals downward. Because of this, a tropospheric duct is either linked to a strong jet-stream, the wind speeds of which can be high enough to refract infrasound to the ground (Drob et al., 2003), or it is linked to a temperature inversion in the boundary layer near the surface (Evers, 2008). Compared to the stratospheric jets, the tropospheric jet-stream is spatially more constrained and temporarily more variable. Tropospheric ducting is consequently an exception rather than the rule, with ranges limited to around 750 km, according to Drob et al. (2003). They concluded that, if a tropospheric waveguide is present and not disturbed by topography, reduced geometric spreading and minor absorption favor detecting relatively high amplitudes within such a distance.

Figure 3.6 illustrates the sensitivity of infrasound propagation to middle atmosphere circulation for the conditions specific to January 2016. The surface bounces for ray-tracing simulations at 1°-intervals of α are based on the configuration of the 2D-FD ray-tracer introduced in Section 2.4. The potential source of microbaroms ($f = 0.25$ Hz) was set to 55.9°N and 3.6°E, in the North Sea ($z = 0$ m). The extent of the acoustic shadow zones between the source and the first bounces vary with propagation direction.

3.2.2 Infrasound attenuation

The attenuation of infrasonic waves in the atmosphere can be traced back to the transmission loss of acoustic energy for two main reasons. First, wave propagation is subject to the geometric spreading (A_s) of the wavefront. Following Crocker (1998), A_s (in decibels – dB) at a distance, r (in km), is described by

$$A_s(r) = 20 \cdot G \cdot \log_{10}\left(\frac{1}{r}\right) \quad [\text{dB}] \ , \tag{3.8}$$

respective to a reference distance of 1 km from the source. Parameter G describes the geometry, ranging from zero for plane wave propagation to one for spherical propagation. Second, atmospheric absorption dampens acoustic signals due to thermal conductivity, viscosity and molecular relaxation effects (Sutherland and Bass, 2004). Briefly summarized, these mechanisms are related to collisions among gas molecules, and air density, which is

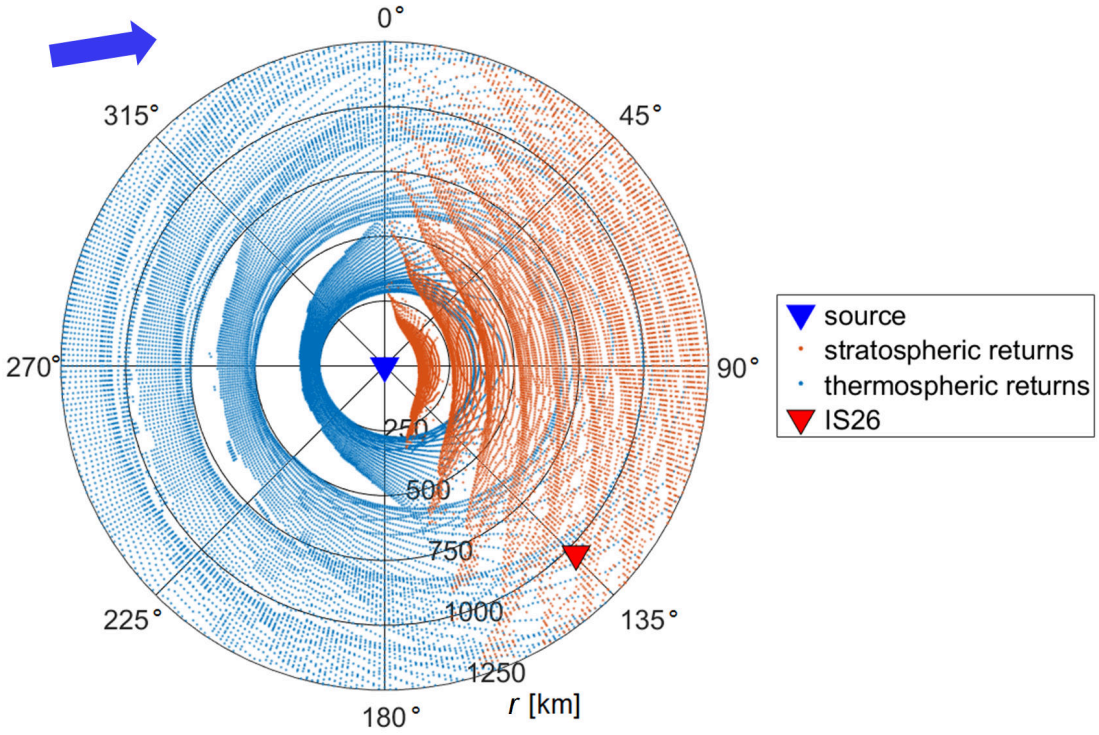

Figure 3.6: Surface bounces of ray-tracing simulations as a function of propagation direction (α) and distance (r) from the source (blue triangle). Blue and orange dots denote thermospheric and stratospheric returns, respectively. The latter are clearly related to the wind direction between 40 km and 60 km altitude (top left arrow, 261°).

maximum at the surface (1.2 kg m^{-3}) and decreases exponentially with altitude. The atmosphere is well mixed up to the turbopause, at around 100 km, with constant mixing ratios of molecular nitrogen (78 %), molecular oxygen (21 %) and argon (0.9 %). The remaining 0.1 % compose of various trace gases and aerosols. Based upon this homogeneously mixed layer, another level of classification divides the atmosphere into the homosphere and heterosphere. In the heterosphere (100–500 km), the density is very low ($\rho < 10^{-6}$ kg m^{-3}). The lack of turbulence, and the comparatively large molecular mean free path, which is proportional to the inverse of the density, results in molecular diffusion being the dominant mixing mechanism. Molecular diffusion results in stratification of the gases, with respect to their molecular weights. An attenuation model, proposed by Sutherland and Bass (2004), shows that the molecular attenuation coefficient significantly increases between around 90 km (10^{-4} km^{-1} at 0.1 Hz) and 120 km (10^{-2} km^{-1}) of altitude, due to the density decrease, whereas it is relatively low in the middle atmosphere (10^{-5} to 10^{-4} km^{-1}). Moreover, atmospheric absorption is proportional to the squared frequency. At 2 Hz, for instance, the attenuation coefficient is increased by two orders of magnitude compared to 0.1 Hz, whereas absorption becomes negligible at frequencies below 0.05 Hz — even in the lower thermosphere (Sutherland and Bass, 2004).

In summary, the surface-to-thermosphere waveguide, which is well established for most of the time, coincides with a strong attenuation of acoustic energy that is proportional to the squared frequency. Absorption and dissipation of acoustic energy cause the propagation range in this duct to be limited to less than 1,000 km, in general (Drob et al., 2003). Exceptions have only been observed at very low infrasonic frequencies ($f \leq 0.05$ Hz; i.e., comparable to MAWs), such as during the strong Chelyabinsk fireball event in February 2013 (Le Pichon et al., 2013; Pilger et al., 2015). Consequently, the surface-to-stratosphere waveguide is the most efficient infrasound ducting region, in terms of signal conservation and long-range propagation (Drob et al., 2003; Sutherland and Bass, 2004; Le Pichon et al., 2008; Landès et al., 2014).

3.3 Modeling example for Central Europe

The ray-tracing simulations shown in Fig. 3.6 represent the monthly mean propagation conditions for January 2016, based on the ECMWF operational HRES analysis fields, MSISE-00, and HWM07. In Fig. 3.7, the propagation to IS26 in southeastern Germany (48.85°N, 13.72°E), at a distance of 1,035 km, is shown, including atmospheric absorption at $f = 0.25$ Hz. Moreover, geometric spreading was considered using Eq. 3.8, with G (Crocker, 1998) set to 0.8, assuming that the non-linear interaction of ocean waves in opposite directions (Waxler and Gilbert, 2006) is neither a perfect point source ($G = 1$) nor a perfect line source ($G = 0.5$) of infrasound. The stronger the combined attenuation, the brighter the color of the ray. White-colored rays indicate that the signal is reduced by 80 dB, respective to a reference distance of 1 km from the source. The rays disappear when attenuation exceeds this threshold.

The graduated color-coding emphasizes the absorption of acoustic energy when the thermosphere is encountered for the first time, while attenuation, due to geometric spreading, is still relatively low (e.g., 38 dB at 250 km). Depending on the elevation angle, the turning height and, thus, attenuation, the downward refracted signal is barely detectable at the surface. After one or two bounces, signals from thermospheric ducts are usually considered to be undetectable (Sutherland and Bass, 2004).

Westerly zonal winds dominate the Northern Hemisphere stratosphere in January. Below the tropopause, a negative v_{eff} gradient leads to upward refraction of radiated sound. Between the tropopause and the stratopause, a positive v_{eff} gradient evolves; hence, sound is refracted back to the surface. The turning heights begin at around 27 km, individually depending on a ray's elevation angle. Smets (2018) proposed that elevations greater than 50° (here, from zenith) are needed for efficient downward refraction at the stratopause layer.

The shadow zone between the source and the first surface bounce from a stratospheric return extends to 160 km. Since the surface serves as a reflector, and the ground-to-stratosphere duct is stable along the propagation path, the signal is almost perfectly conserved when propagating downwind. As a result it is detected at IS26.

In July the signal needs to propagate upwind to be detected at the receiver. Since the

easterly winds effectively decrease the speed of sound with altitude, compared to the adiabatic sound speed, and because $v_{eff-ratio} < 1$, the sound waves pass the stratopause region towards higher altitudes. The shadow zone extends to 300 km until the first thermospheric return reaches the surface.
Note that, in reality, infrasound has been observed to penetrate modeled shadow zones (Hedlin and Walker, 2012, and references therein). Small-scale interactions of the acoustic wave field and, for instance, GWs have been assumed to cause scattering of the wavefront (e.g., Kulichkov, 2010), which is not properly resolved by the 2D-FD ray-tracer. The parabolic equation method turned out to be more realistic, in terms of modeling such features (Lingevitch et al., 2002; Norris et al., 2010; Gainville et al., 2010).

As seen in Fig. 3.5, middle atmospheric circulation reverses during spring and autumn. Consequently, during the equinoxes, the stratospheric jets are not as well established as during the solstices. This results in propagation conditions that yield values for $v_{eff-ratio}$ close to one, which is evident in April and October (Fig. 3.8). Not limited to the equinoxes, but more critical during these months, is the short-term variability in stratospheric temperature and winds. As stated above, such variability can be induced, for instance, by upward-propagating GWs. Such short-term temperature or wind perturbations are often not well resolved in atmospheric models, but can essentially modify the conditions for stratospheric ducting (Drob et al., 2013). Chapter 5 deals with such uncertainties in ECMWF temperature and wind profiles, and their impact on infrasound propagation. The objective was to explain the short-term variations in infrasound detection parameters of microbaroms, such as back-azimuth and amplitude.

3.4 Summary

Overall, infrasound propagation is strongly affected by atmosphere dynamics, which make it variable in time and space. Waveguides between the ground and the stratosphere or the lower thermosphere enable long-distance propagation of acoustic energy over hundreds to thousands of kilometers, whereas acoustic shadow zones can establish in the vicinity of a source. The presence of the ground-to-stratosphere waveguide in a specific propagation direction is mainly controlled by middle atmosphere circulation, as the strong jet-streams affect the effective sound speed. This waveguide generally ensures the best conservation of acoustic energy in the atmosphere, since absorption remains low below the mesopause, and significantly increases in the lower thermosphere. Waves with very low intrinsic frequencies, such as MAWs, are only weakly attenuated compared to higher frequencies.

Understanding atmospheric variability is a key issue for understanding a station's capability of detecting and — combined with other stations — locating explosive events, in the context of the CTBT. Background information on the detection capability of the IMS infrasound network is given in Appendix A.

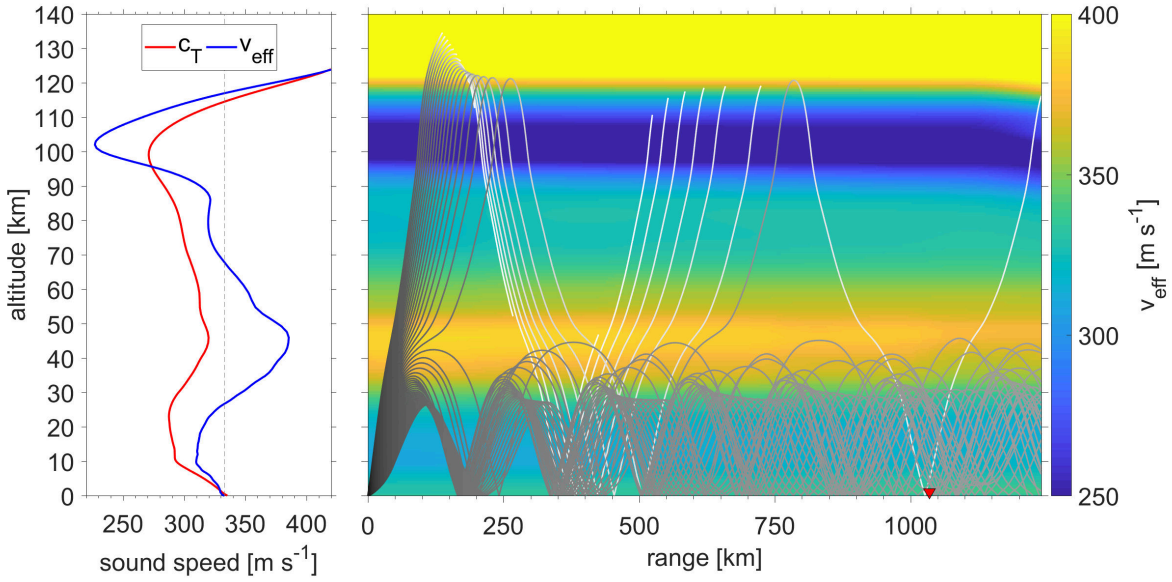

(a) January 2016.

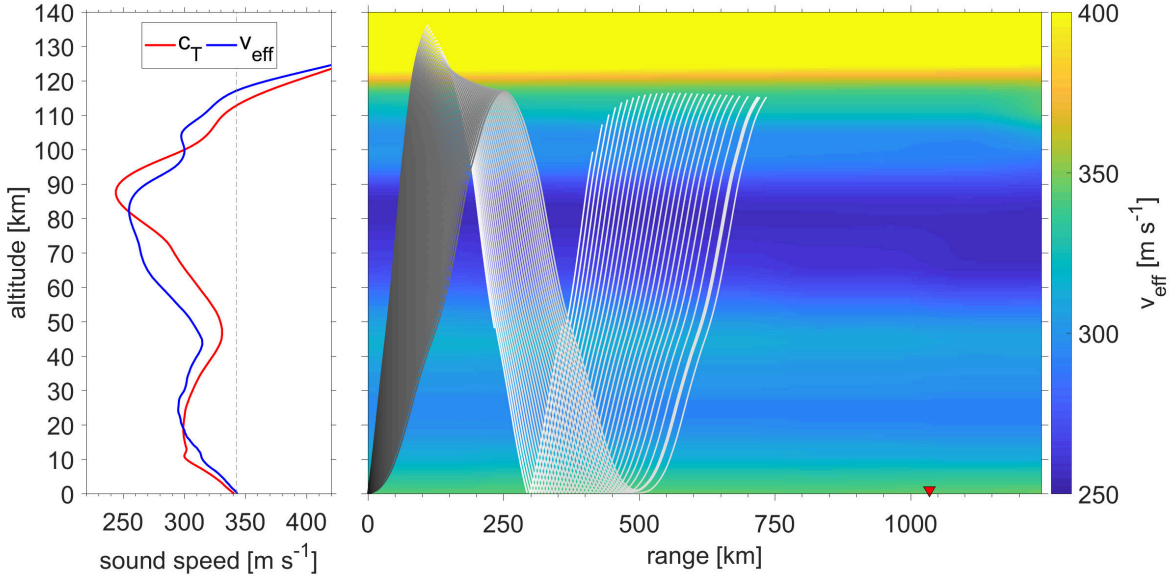

(b) July 2016.

Figure 3.7: Ray-tracing results for infrasound from a microbarom signal propagating towards IS26 in southeastern Germany (red triangle) are shown in the right-hand panels ($f = 0.25$ Hz, $\alpha = 134°$). The background mean effective sound speed in January (a) and July 2016 (b) is based upon operational ECMWF HRES analysis fields for up to 78 km; empirical climatological data are used beyond that. The adiabatic and effective sound speed profiles at the source are shown in the left-hand panels; the reference sound speed at the ground ($v_{eff-ratio} = 1$) is indicated by the dashed vertical line. The propagation path shown for January equals the situation shown in Fig. 3.6, but absorption is accounted for here.

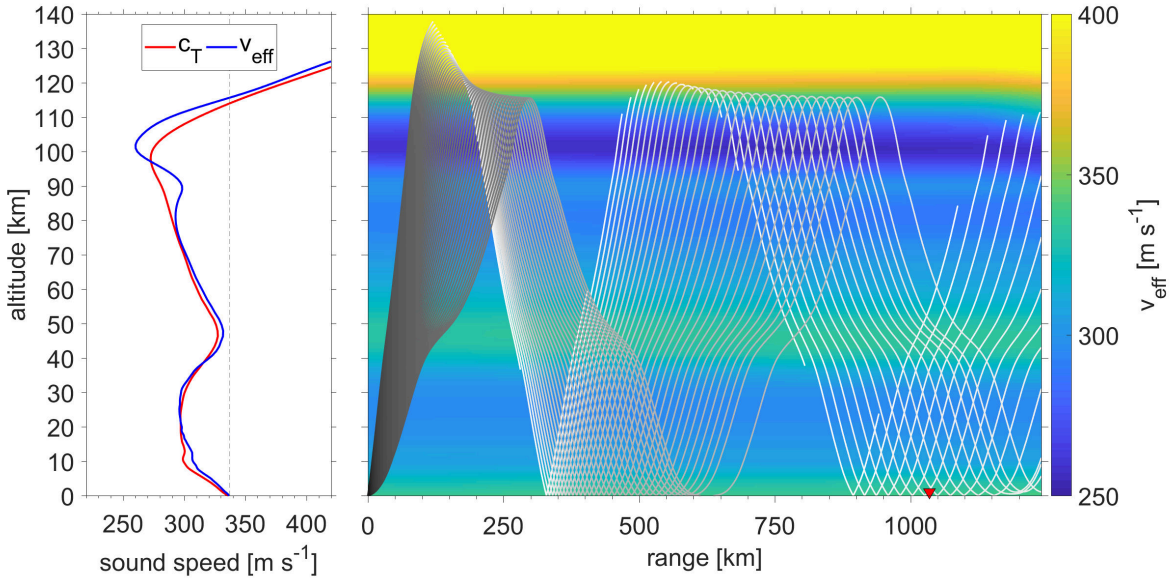

(a) April 2016.

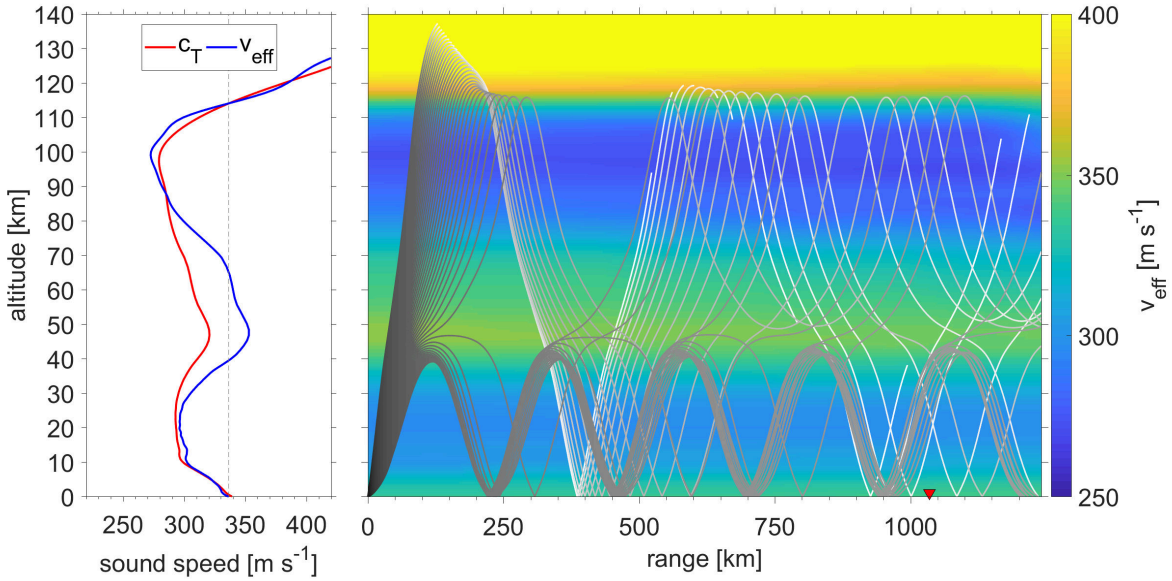

(b) October 2016.

Figure 3.8: Same as in Fig. 3.7, but for April and October 2016. In these months, the stratospheric circulation reversal towards summer and winter conditions, respectively, is advanced. $v_{eff-ratio}$ is, however, close to one in the upper stratosphere; hence, propagation conditions are prone to short-term variability in winds and temperature.

4 | Using the IMS infrasound network for global studies: Atmospheric tides

The potential of infrasound sensors for broadband measurements and the detection of atmospheric dynamics was identified by Blanc et al. (2010, 2018). Several studies have used infrasound measurements for investigating variations in the middle and upper atmosphere (e.g., Donn and Rind, 1972; Le Pichon et al., 2005a; Assink et al., 2012; Smets and Evers, 2014). Here, a methodology is described for systematically analyzing the geographic and temporal variability of the features of atmospheric dynamics, which relies on ground-based barometric data from the IMS infrasound network (Section 1.3). It particularly focuses on atmospheric thermal tides, a phenomenon observed all around the globe and in different layers of the atmosphere (Lindzen and Chapman, 1969; Oberheide et al., 2015). The study highlights manifold opportunities for using this dataset for research purposes due to its data accuracy and the uniform global distribution of the arrays (**Question I** of Section 1.5).

Significant parts of this chapter have been literally published by Hupe et al. (2018), entitled 'Using barometric time-series of the IMS infrasound network for a global analysis of thermally induced atmospheric tides'. All figures shown here are reproduced from that publication. For consistency in this thesis, minor text changes have been applied.

4.1 Overview of atmospheric tides

Tides can be traced to two excitation mechanisms (Chapman and Lindzen, 1970). One is gravitational forcing by the sun and the moon, which is commonly known to be the cause of the periodic rise and fall of sea level (ocean tides), the period of which is related to the lunar day (24 h and 50 min). Since the gravitational pull of the moon is considerably greater than that of the sun (e.g., Thomson, 1882; Lindzen and Chapman, 1969), the tidal signature in air pressure data should be related to the lunar day; however, the predominant tidal harmonics found in air pressure recordings are clearly related to the solar day (24 h). Therefore, a second excitation mechanism must exist; this is thermal forcing by the sun's radiation (Chapman and Lindzen, 1970). Unless otherwise stated, mentions of atmospheric

and solar tides in this chapter primarily imply the thermally-excited tides with periods related to the solar day. In particular, the focus is on the diurnal (24 h), semidiurnal (12 h) and terdiurnal tides (8 h), but also pressure oscillations with up to 9 cycles per day (cpd) can be identified by spectral analyses. The different harmonics result from periodic insolation absorption and latent heat release in various layers of the atmosphere (Forbes and Gillette, 1982). Non-linear wave interactions are considered to be another source of tidal harmonics, in particular, those below a period of 12 h (Moudden and Forbes, 2013).

In addition, the migrating and non-migrating components of the aforementioned tides must be differentiated between. The former propagate westward, following the apparent motion of the sun, while the latter do not (Chapman and Lindzen, 1970). When Haurwitz (1965) identified the non-migrating components in barometric recordings, he related them to the irregular distribution of land masses. Dai and Wang (1999) stated that the non-migrating tides can reach large amplitudes due to differences in sensible heat flux between land and sea. One prominent small-scale example causing a local (non-migrating) diurnal oscillation is the land–sea breeze pattern (Chapman and Lindzen, 1970). Insolation absorption by water vapor and ozone is considered to be the primary source of the migrating tides (Butler and Small, 1963; Chapman and Lindzen, 1970; Whiteman and Bian, 1996). Cloud effects, precipitation and latent heating are also considered to be a source of tidal variations, especially for the semidiurnal tide in the tropics (Dai and Wang, 1999). This study did not examine the different sources, but rather the characteristics of the various tides detected within a global network. The discussion focuses on the potential of the IMS infrasound network for geographic variability analyses in the context of the findings herein and previous studies on atmospheric tides. Whilst several of those studies have addressed the tidal effects and characteristics in the middle (e.g., Forbes, 1984) and upper (Forbes and Garrett, 1979; Forbes, 1990; Thayaparan, 1997; Zhao et al., 2005) atmosphere, this study concentrated on troposphere-based observations and theories (e.g., Haurwitz, 1956; Kertz, 1956; Dai and Wang, 1999).

4.2 Data selection and handling

From the 51 certified infrasound stations shown in Section 1.3, 17 sites were selected as the database for this study (Fig. 4.1). The selection accounted for various aspects, one of which was data availability. Most of the microbarometers record absolute pressure, but the time-series cover non-uniform periods. This has resulted from the subsequent installation and certification of new sites since the CTBTO initiated the design of the IMS (see Chapter 1.3). Selection of the stations was also aimed at a uniform geographic distribution, with limited periods of missing data.

The sampling rate of absolute air pressure data is generally 1 Hz; at some stations, recordings of 20 Hz are available. Taking into account that significant air pressure changes take several minutes to hours, rather than seconds, choosing a temporal resolution of 1 min seemed sufficient for this study, and reduced the enormous amount of data. As a consequence of the very different topographic locations of the global infrasound arrays —

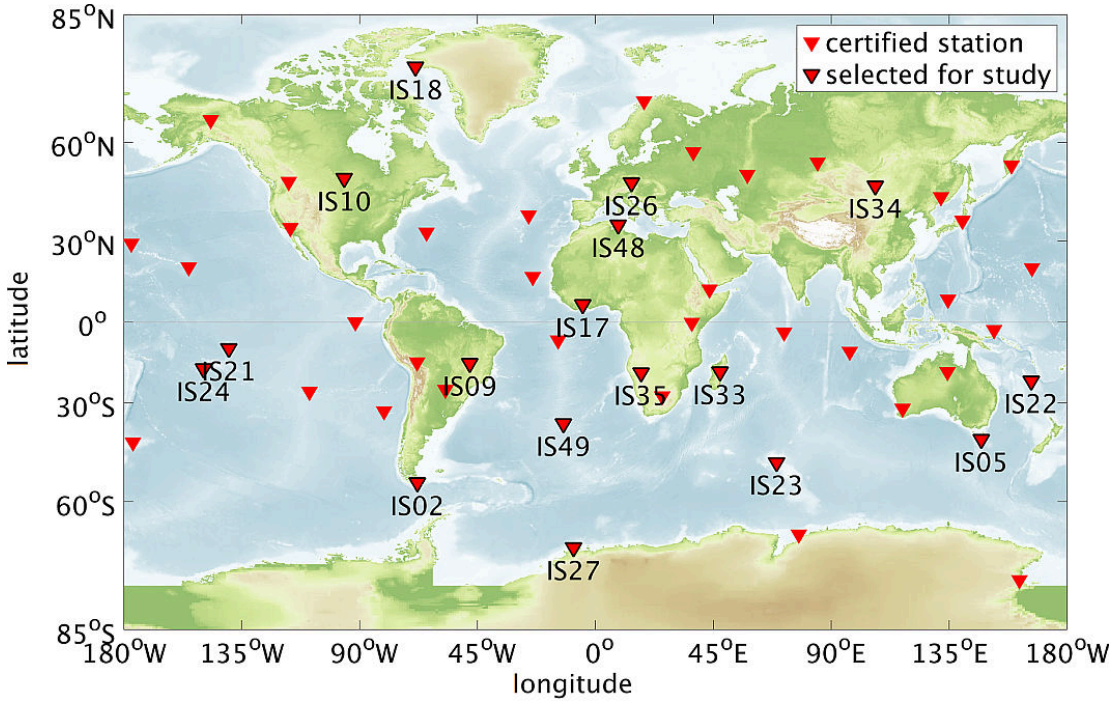

Figure 4.1: Each red triangle represents a certified IMS infrasound array (August 2018). The stations labeled supplied the database for this chapter. Reproduced and updated from Hupe et al. (2018).

for instance, IS27 in Antarctica and IS17 in Ivory Coast — the barometric time-series naturally differ from each other. For reasons of comparability, and due to the fact that the recorded air pressure is not reduced to mean sea level, air pressure fluctuations around the annual mean were considered. For this purpose, the respective annual mean was subtracted from the annual datasets, resulting in fluctuations around zero.

In the case of multiple recordings per array, the aforementioned procedure was adapted to each element's time-series. Following this, as schematically illustrated in Fig. 4.2, the median of the mean-free recordings was extracted. Overall, this resulted in only one record per station, and diminished the problem of temporarily missing data at a single sensor.

Nonetheless, the majority of stations only provided one dataset of absolute air pressure, corresponding to one sensor. As a consequence, supplementing errors that occurred, or missing data, was beyond the realm of possibility. Therefore, obviously erroneous values were handled as missing data; this included values that deviated from the mean by more than four times the standard deviation. Such outliers were additionally examined based on their plausibility; for example, hurricanes can cause large natural pressure deviations when passing an infrasound array. Figure 4.3 provides an overview of the availability of absolute pressure data from the selected stations. A lack of data is related to, among other things, station maintenance, power failure for various reasons or erroneous data.

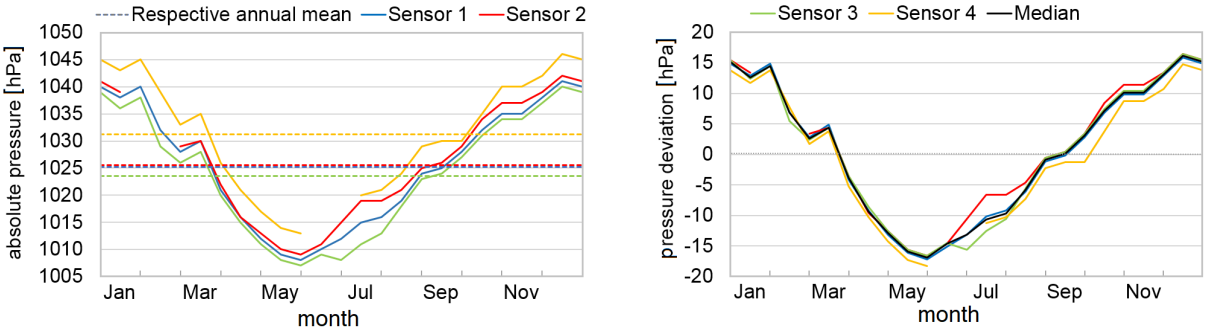

(a) Absolute pressure time-series.

(b) Mean-free time-series.

Figure 4.2: Schematic illustration for handling the annual dataset of a four-sensor array. Different pressure at the various sensors (a) can result from calibration or from different altitudes, since the arrays have an aperture of 1 km to 3 km (Evers and Haak, 2010). Here, temporarily missing data for sensors 2 and 4 have no significant consequence in terms of deriving the median (b) as time-series for a multi-sensor station.

The remaining datasets are up to 13 years long and, thus, sufficient for being analyzed with regard to dynamic features. Long-period phenomena, such as PWs, and short-period phenomena, such as GWs and tides, are well represented within this time interval. The time interval, however, is likely too short for identifying reliable trends; for instance, those associated with climate change. Since the analyses were based on the pressure deviation from the respective annual means, long-term trends were removed anyway. The remaining time-series clearly reveal characteristics of their geographic location. As an example, two datasets are shown, using the same scale, in Fig. 4.4 — those of the mid-latitude IS26 (Germany, Fig. 4.4(a)) and the tropical IS21 (Marquesas Islands, French Polynesia, Fig. 4.4(b)).

In the tropics, at IS21, the annual cycle is characterized by a comparatively small amplitude. The absence of large-scale pressure gradients has led to a dominant signature of small-scale phenomena, such as thunderstorms, or small-amplitude phenomena, such as solar tides. In the tropics, the semidiurnal tidal amplitude can amount to 1.3 hPa (Dai and Wang, 1999; Hoinka, 2007; Schindelegger and Ray, 2014). Even though this tidal amplitude is only around 0.1 % of the absolute air pressure, its contribution to the annual pressure fluctuation amplitude amounts to around 20 %.

At IS26, however, the annual amplitude (around 30 hPa) masks small-scale amplitudes, such as those of atmospheric tides. The negative deviations that predominantly occur in winter are larger than the positive deviations that occur throughout the year. In winter, temperature gradients between the equator and North Pole are at their greatest due to differing solar radiation and, thus, energy balance. Compensating processes (baroclinic instabilities) result in stronger westerlies and more intense (low-pressure) cyclones than in summer.

Figure 4.3: Daily-based availability of absolute pressure data at the selected IMS stations. White boxes indicate missing data.

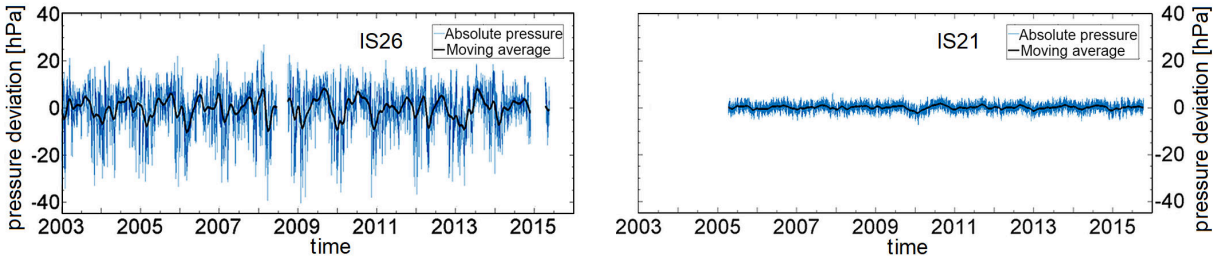

(a) IS26. (b) IS21.

Figure 4.4: Absolute pressure data recordings of IS26 (a) and IS21 (b), shown as deviations from the annual means. The moving average highlights the superordinate annual variation.

Compared to the around 11,000 surface-based stations of the Global Observing System (GOS) of the World Meteorological Organization (WMO), the majority of which also record atmospheric pressure (WMO, 2018a), the IMS infrasound network is relatively coarse. Nevertheless, given its accuracy and high temporal resolution, the almost continuous barometric recordings by the IMS infrasound network constitute a uniquely global set of data. Although the WMO prescribes that its newly implemented barometric sensors fulfill certain requirements, such as 0.1 hPa resolution and an output averaging time of 1 min (WMO, 2014), the reporting intervals actually vary between 1 min, 10 min, 1 h and 3 h in the GOS, depending on the station (WMO, 2018b). The Integrated Surface Database (Smith et al., 2011) provides hourly data from meteorological stations worldwide, including the GOS. These are standardized, in terms of quality control and data format. The higher temporal resolution of the IMS infrasound station data, the high accuracy and the multi-sensor array configurations are a valuable feature when studying atmospheric dynamics. As an example,

a similar barometric array with four sensors was used by Hauf et al. (1996) for deriving GWs from pressure fluctuations. Using the IMS arrays, such analyses can be performed on a global scale.

4.3 The MERRA-2 reanalysis data

The results of this study have been compared with the Modern-Era Retrospective analysis for Research and Applications, version 2 (MERRA-2). MERRA-2 is NASA's latest atmospheric reanalysis of the modern satellite era, provided by the Global Modeling and Assimilation Office (Gelaro et al., 2017). Data are available on a 0.625° x 0.5° grid, starting from 1980 (Bosilovich et al., 2016). Since ECMWF's ERA-interim and the HRES operational analysis fields only provide data at the main meteorological times (0, 6, 12, 18 UTC; Section 2.2), interpolation methods would be necessary for detailed studies of tides with periods shorter than 24 h (Ray and Ponte, 2003). MERRA-2 has the benefit of providing data at an interval of 3 h, either as instantaneous or as time-averaged fields (Bosilovich et al., 2016). For this study, the 3 h time-averaged surface pressure field was retrieved (Global Modeling and Assimilation Office, 2015). The data were interpolated for the locations of the 17 IMS stations defined in Section 4.2. Analogously to Fig. 4.4, the MERRA-2 time-series for IS26 and IS21 are shown in Fig. B.1 on page 111.

Various spectral analysis methods were adapted to both the IMS barometric data and the MERRA-2 data in order to analyze the tidal effects at various IMS infrasound stations, and to derive other features related to atmospheric dynamics from the pressure fluctuations (e.g., PWs).

4.4 Spectral analysis tools

The spectral methods used include, inter alia, wavelets and the PSD of the time-series. Computing the PSD of a time-series provides a first impression of the dataset. Marty et al. (2010) retrieved the PSD from intervals of 12 d for studying GWs and tidal effects in infrasound data. Here, time windows of six months were chosen. Consequently, single days of missing data did not significantly affect the analysis. Where considerable data gaps existed in the time-series (see Fig. 4.3), the PSD calculation was rejected for that particular year. An example of a PSD is given in Fig. 4.5(a), based on the pressure fluctuation at IS26 from 2003 to 2015. A combined PSD plot for all selected stations is provided in Section 4.5. In addition, the PSD was calculated using the Lomb–Scargle algorithm, which is capable of handling missing data without reducing the data basis (Lomb, 1976; Scargle, 1982); an example is given in Fig. 4.5(b). The mean and standard deviation of the PSD were calculated in sliding frequency windows with fixed widths ($\Delta f = 5 \cdot 10^{-7}\,\mathrm{Hz} \approx 0.043\,\mathrm{d}^{-1}$) in order to determine the 90 % and 99 % confidence levels. These were added to the Lomb–Scargle PSD spectrum for classifying the significance of the peaks. The Lomb–Scargle PSD of the MERRA-2 time-series is in good agreement with the PSD retrieved from IMS data.

Another useful and often-used tool in geophysical studies is the computation of a wavelet analysis (Daubechies, 1990). In this study, this was based on the Morlet wavelet function. Barometric time-series can be analyzed in the time–frequency space, enabling the determination of both the dominant frequencies and their temporal variation (Torrence and Compo, 1998). Figure 4.6 includes the wavelet power spectrum for IS26. Since the diurnal tide is not very prominent at IS26 (cf. Fig. 4.5), this is hidden by synoptic pressure fluctuations, rather than being represented by a distinct line. The semidiurnal tide is, however, recognizable as distinct line in both figures. The wavelet power spectrum does not provide detailed information on smaller period scales, or even seasonal variations, within the diurnal period range.

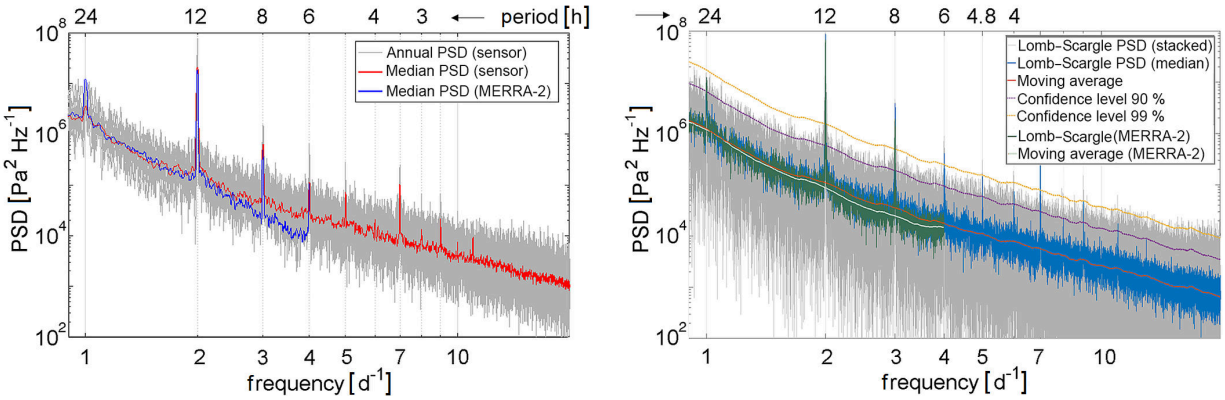

(a) PSD. (b) Lomb–Scargle PSD.

Figure 4.5: PSD plots of surface pressure variations at IS26. (a) The red curve depicts the median PSD for the entire period, from 2003 to 2015, as derived from the barometric sensor. Each of the gray PSD curves belongs to a single year within this period. Panel (b) shows the Lomb–Scargle PSD spectrum based on the entire time-series. In both panels, the solar tides appear as sharp peaks. The MERRA-2 reanalysis revealed a higher PSD for the diurnal tide.

4.5 Discussion of the results

In this section, the findings on several dynamic features of the barometric data considered are discussed. The focus is on the geographic and temporal variability of the solar atmospheric tides.

4.5.1 Geographic variability of dynamic features

To compare the tidal features at different stations, the median PSD curves were color-coded and sorted according to station latitude (Fig. 4.7). For the MERRA-2 data, this PSD spectrum is given in Fig. B.2 on page 112.

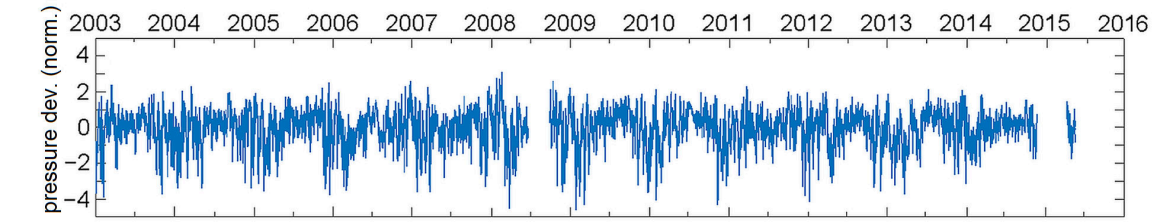

(a) Normalized pressure time-series.

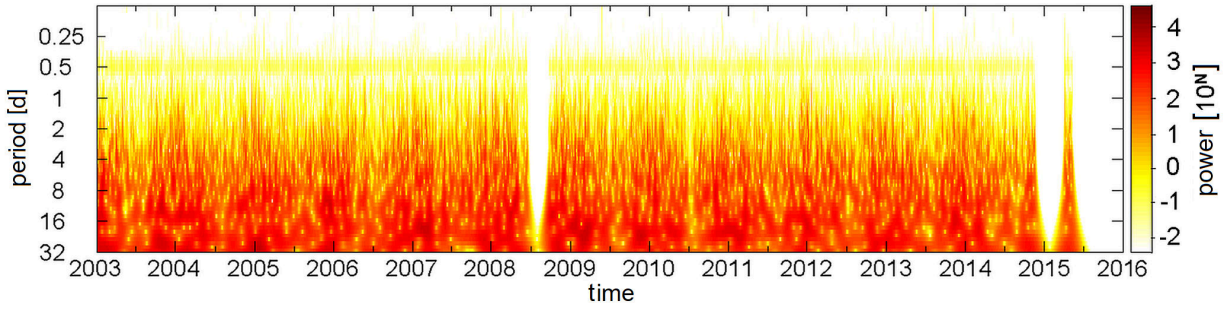

(b) Power spectrum.

Figure 4.6: Wavelet analysis for IS26, from 2003 to 2015. The time-series in panel (a) corresponds to Fig. 4.4(a), but is normalized by its standard deviation, which amounts to 8.78 hPa. The resulting power spectrum (b) is color-coded. The ordinate axis represents the Fourier period (in days).

Phenomena in the period scale exceeding 1 d

In general, the PSD increases with decreasing frequency. At periods exceeding 1 d, tropical stations can be clearly distinguished because the PSD values are significantly lower than at latitudes above ±30°. The difference is of the order of one magnitude. At middle and high latitudes, extratropical cyclones and PWs lead to larger pressure fluctuations compared to the tropics, where air pressure fluctuations are relatively small throughout the year. This is shown in Fig. 4.4(b). In Fig. 4.6, the wavelet spectrum provides extended information on PW scales (periods of up to 32 d). These are strongest in the winter months, when the temperature gradients between the equator and North Pole are at their greatest.

The solar tides

The geographic differences between the tidal effects on air pressure are worth discussing, in the context of previous studies on atmospheric tides derived from barometric data. In Fig. 4.7, tidal peaks clearly appear with up to 9 cpd. The most striking peak, in terms of a constantly high PSD, was the semidiurnal tide (12 h). Also, 3 cpd and 4 cpd — terdiurnal (8 h) and quarterdiurnal (6 h) tides, respectively — were recognized at the majority of stations. Generally speaking, several tidal modes were dominant throughout

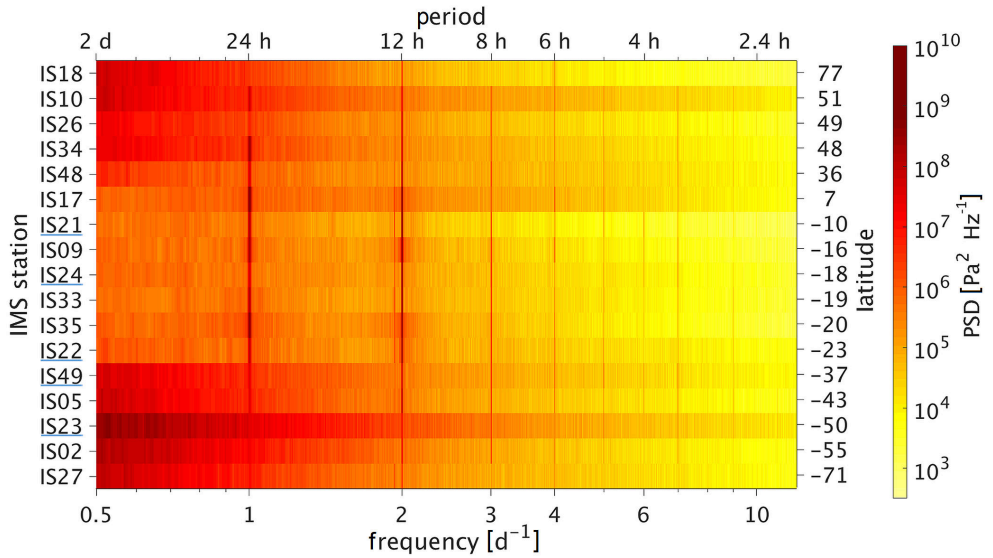

Figure 4.7: Median PSD of the selected datasets. The IMS infrasound stations are sorted from north (top) to south (bottom), with the latitudes indicated on the right-hand axis. Stations on (small) islands are underlined. The darker the color, the higher the PSD. The corresponding spectrum for MERRA-2 data can be found in Fig. B.2 on page 112.

both hemispheres, starting with a period of 24 h, which is known to be the solar diurnal tide.

According to the findings on global pressure oscillations by Haurwitz (1965), whose study was based on more than 200 irregularly distributed stations, the amplitude of the diurnal tide decreases with increasing latitude, following the latitudinal decrease in solar insolation. By using the IMS infrasound stations, and considering the picture provided in Fig. 4.7, a similar conclusion has been deduced. The PSD and, consequently, the amplitudes reach maxima at the low latitudes, and almost disappear at the high-latitude IS18 and IS27. The PSD, however, does not steadily decrease towards the polar regions. For example, IS34 and IS10 are characterized by relatively large PSD values, which can be explained by the continental location of the sensors. In summer, the rapid warming of the landmasses causes a stronger diurnal effect. Also, even in the tropics, the PSD values differ markedly, since the amplitude of the diurnal tide strongly depends on local surface conditions (Haurwitz, 1965). Over the oceans, this is weaker than over landmasses (Dai and Wang, 1999); for example, the PSD is comparatively weak at maritime stations like IS21, IS24 and IS22. The mid-latitude stations in the Southern Hemisphere are, in the main, located on islands or are otherwise close to an ocean; hence, the corresponding PSD values are generally weaker than in the Northern Hemisphere.

Dai and Wang (1999) also emphasized a strong diurnal tide over high terrain. This might have contributed to the respective prominent PSD signal at IS34 in Mongolia. Extracting the tidal components from the PSD spectrum shows that the diurnal oscillation is not the strongest tide. Haurwitz (1965) even claimed that the amplitude of the semidi-

urnal tide was "generally considerably larger than that of the diurnal oscillation" (p. 362). Regarding tropical stations, this agrees with Fig. 4.8, in which the means of the monthly amplitudes of the tidal components are given for each station. The amplitude means of the semidiurnal tide are much larger than the diurnal ones for most stations, particularly at the low-latitude stations; hence, the 12 h oscillation can often be easily recognized in barometric recordings at tropical stations (e.g., Oberheide et al., 2015), where large-scale pressure oscillations do not exist (see Fig. B.3 on p. 112). The pressure maxima occur at approximately 10:00 and 22:00 local solar time (Haurwitz, 1956; Dai and Wang, 1999; Marty et al., 2010) or, more precisely, "about 2.3 h before solar noon and solar midnight" (Whiteman and Bian, 1996, p. 530).

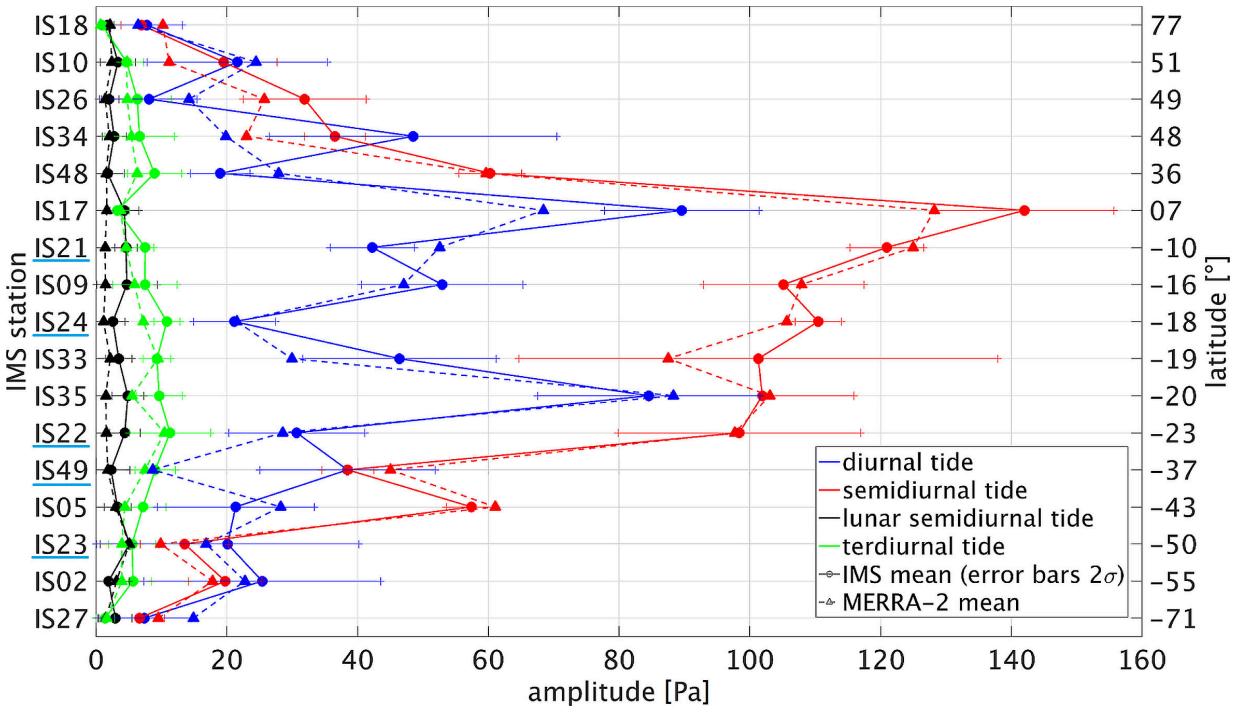

Figure 4.8: Comparison of the mean tidal amplitudes, as calculated from IMS sensor time-series and MERRA-2 reanalysis. The mean amplitudes of the solar tides are in good agreement. The lunar tides are enhanced at tropical IMS stations, but are barely represented by MERRA-2. Reproduced from Hupe et al. (2018), error bars added.

At high latitude stations, however, the diurnal tide amplitude is greater than the semidiurnal component. The semidiurnal tide is driven by, amongst other things, the absorption of solar radiation by water vapor (Whiteman and Bian, 1996). Both the concentration of water vapor and the insolation are highest in the tropics. Consequently, the maxima can be found at low latitudes, where the effect of the diurnal tide is exceeded; for instance, the amplitude mean found for IS17, which is located at 7°N, amounts to 1.4 hPa (diurnal tide – 0.9 hPa), compared to 0.1 hPa to 0.2 hPa at high latitudes.

The amplitude means of the terdiurnal tide are smaller by about one order of magnitude

at tropical stations. Amplitude maxima can be found in the tropics (IS22 – 13 Pa) and minima at high latitudes, where the amplitude is less than 2 Pa. Spectral analyses of the MERRA-2 time-series resulted in slightly lower estimates of the terdiurnal tide. These can be traced back to the 3 h sampling of the reanalysis data, which might be too sparse for exact estimates of the 8 h cycle.

The generally good agreement with the amplitude means derived from the MERRA-2 time-series underlines the capability of the IMS infrasound network to measure atmospheric dynamics, such as solar tides or GWs. Conversely, the findings herein imply that the solar tide representation in MERRA-2 is accurate.

The lunar tides

The most striking PSD peaks in Fig. 4.7 are clearly related to the solar day. In addition, the individual PSD curves of certain IMS stations revealed a secondary semidiurnal peak. This can also be recognized from Fig. 4.7 at a couple of equatorial stations, but not in the equivalent MERRA-2 analysis (Fig. B.2, p. 112). The period is 12 h and 25 min — exactly half a lunar day. At IS27, it is striking that the lunar tide appears to be even more prominent than the diurnal solar tide. Further significant peaks were generally found at tropical stations, such as IS17 and IS21. Figure 4.9 shows the Lomb–Scargle PSD spectra of IS27 and IS21, both showing a highly significant peak next to the main (solar) semidiurnal peak. This peak is not matched by MERRA-2. The monthly mean amplitude of the semidiurnal oscillation of the lunar tide was added to Fig. 4.8; this is very small in relation to the solar tides.

A study by Chapman and Westfold (1956) indicated that the global distribution of the lunar semidiurnal tide is similar to that of its solar counterpart; hence, the mean annual amplitude reaches a maximum in equatorial regions and decreases with increasing latitude (Haurwitz and Cowley, 1969; Schindelegger and Dobslaw, 2016). Combined with its generally small amplitude (Lindzen and Chapman, 1969), this explains why distinct signatures of the lunar semidiurnal tide (Fig. 4.7) are mainly concentrated at tropical stations in this study. In this context, the evidence of a tidal peak related to the lunar day at the Antarctic IS27 is even more surprising. The monthly amplitude mean found at IS27 is only 3 Pa, however. For the MERRA-2 data, a mean amplitude of 2 Pa was calculated, although the lunar tide does not seem well represented (see Figs. 4.9(a) and B.2). The significant PSD peak raises a question about the excitation mechanism of the tidal signal — the dynamic effect of the gravitational pull of the moon seems to be too low in the Antarctic region. Because IS27 is mounted on the Ekstroem Ice Shelf, the ocean tide may have affected the barometric recordings to a small, but considerable, extent by vertically lifting the sensor.

Vertical sensor lifting can be induced by the body tide, the ocean tide itself and ocean tide loading effects. Near IS27, these excitations amount to around 4 Pa (Schindelegger and Dobslaw, 2016). The open-ocean tide amounts to 0.5 m (Kohyama and Wallace, 2014). To a certain extent, the Ice Shelf moves with the ocean tide. This may enhance the barometric effect of the lunar tide, as the vertical movement translates into a barometric signal.

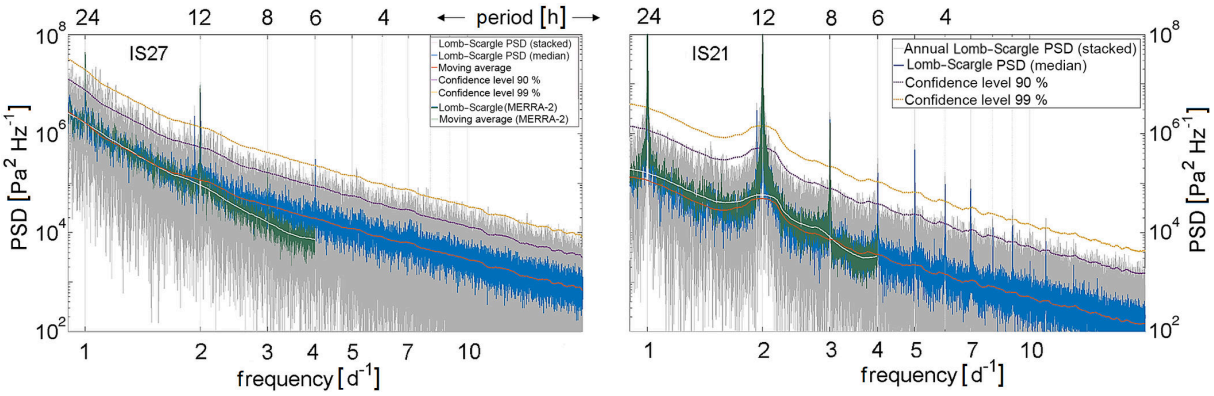

(a) IS27. (b) IS21.

Figure 4.9: Lomb–Scargle PSD curves for (a) IS27 (Antarctica) and (b) IS21 (Marquesas Islands). The peaks next to the predominant semidiurnal peak are related to the lunar day. These are not present in the MERRA-2 reanalysis.

4.5.2 Seasonal variability of the solar tides

Refocusing on the solar tides, the monthly PSD was computed to derive the seasonal variability of the diurnal, semidiurnal and terdiurnal tides. Figure 4.10(a) shows the monthly PSD for IS21 in the period range between 3 h and 5 d. Several tidal harmonics are marked by distinct horizontal lines. At first sight, the semidiurnal oscillation does not exhibit an annual variation. To specify the seasonal characteristics, the variances of the most dominant tides are given in Fig. 4.10(b). It appears that the PSD of the semidiurnal tide is not particularly uniform throughout a year, but rather mostly exhibits two maxima. These predominantly occur in the equinoctial months, which is in line with the studies of Hann (1918) and Haurwitz and Cowley (1973). The diurnal tide variance is generally smaller than the semidiurnal tide variance. The maxima seem to occur without a clear periodic cycle. The terdiurnal tide is maximized twice per year. In addition to its absolute annual maximum during winter, a secondary weaker maximum was detected during summer. Ray and Poulose (2005) previously reported this seasonal variation of the terdiurnal tide from barometric recordings in the USA; this can now be validated by the global IMS infrasound stations. The variation in the monthly mean amplitudes (not shown) of both MERRA-2 and IMS data is in line with this annual cycle.

In Fig. 4.11, the occurrence months of the absolute variance maxima between 2003 and 2015 are depicted (one maximum each year). Each month (represented by a rectangle) is highlighted in the color of the respective tidal harmonic, if the annual maximum of the variance was detected in this month in at least three years (i.e., approximately 25 % of the time). This enabled to detect seasonal patterns for each of the tides.

The annual maximum of the terdiurnal tide (green) is, on average, detected during the winter months. A second, smaller maximum is detected during the summer months, as validated at IS21 in Fig. 4.10 (Ray and Poulose, 2005). An exception was provided by the

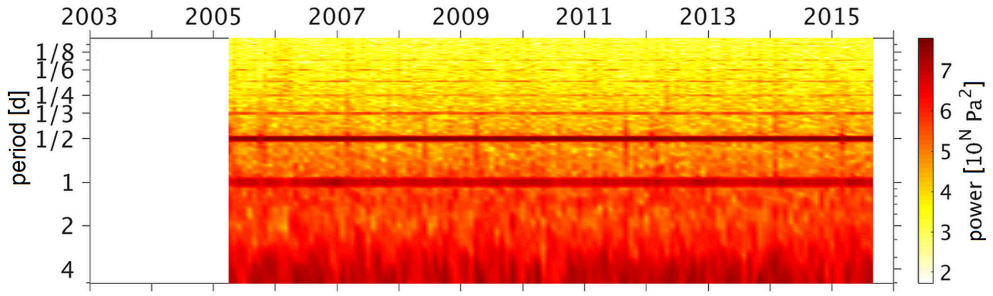

(a) PSD time-series.

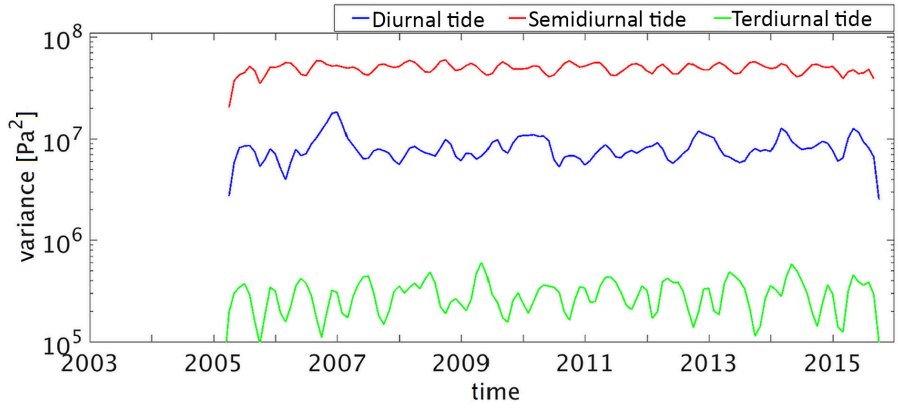

(b) Tidal variances.

Figure 4.10: Color-coded PSD spectrum (a) of the monthly air pressure fluctuations at IS21, as a function of time and Fourier period, and variances of the diurnal, semidiurnal and terdiurnal tide (b).

equatorial IS17 at which the terdiurnal tide power is relatively constant throughout the year. Besides a small maximum in December or January, the occurrence of another small maximum ranges between March and July, depending on the year considered.

The annual cycle of the semidiurnal tide (red) exhibits two maxima during the equinoxes, with only a small difference in the PSD (Hann, 1918; Haurwitz and Cowley, 1973). The absolute maximum predominantly occurs during the spring equinox. The semiannual cycle, showing maxima around the equinoxes, was also found in the ECMWF reanalysis, after interpolation of the 6 h fields (Van den Dool et al., 1997; Díaz-Argandoña et al., 2016). Exceptions include the high-latitude stations. At IS18, the maxima were detected in the northern winter, whereas at IS27, the maxima of the semidiurnal tide were distributed over several months. Because of the low tidal amplitude at high latitudes, variances in the tidal period ranges are certainly affected by noise.

As can also be recognized from Fig. 4.11, the annual variation of the diurnal tide (blue) does not show as clear a pattern as the aforementioned tidal components. The maxima would be expected during summer, when solar radiation leads to the increased heating of land masses (Haurwitz and Cowley, 1973; Dai and Wang, 1999). At mid-latitudes, a

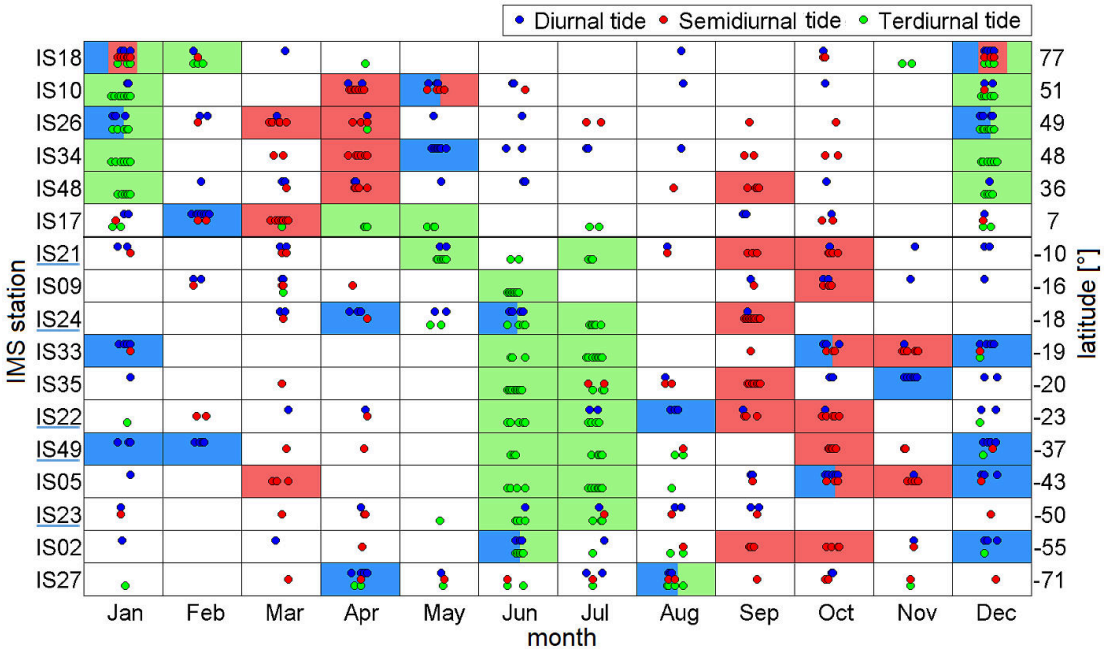

Figure 4.11: Detection times of the primary annual maxima of tide variances between 2003 and 2015. The thick black line depicts the transition from northern to southern latitudes. For each IMS infrasound station indicated on the left-hand axis, each dot marks the month in which the absolute maximum of each year, between 2003 and 2015, appeared. The offsets between the dots have no physical meaning. By highlighting accumulations of the annual maxima, seasonal patterns and differences between the Northern and the Southern Hemispheres become apparent.

semiannual cycle is known from observations (Hann, 1918), but the absolute maximum was primarily found during (early) summer. This is also a finding of the observations that agrees with the MERRA-2 time-series; however, the annual cycle of the diurnal tide strongly depends on the geographic location of the station. At maritime stations — for example, those on oceanic islands, such as IS21 (Marquesas Islands) or IS22 (New Caledonia) — the annual variation of the diurnal tide is small, resulting in a variable appearance of the annual maximum, or even no explicit maximum. Contrarily, at IS34 in Mongolia, the maxima of the diurnal tide are always in the summer season, when the Asian continent is dominated by warm air masses. During winter, when the high-pressure system and cold air mass prevails, the diurnal tide is less powerful. At other stations at mid and high latitudes, the low-amplitude diurnal tide is often hidden in the noise or masked by synoptic pressure gradients. In particular, this regards IS02, IS10, IS18, IS23, IS26 and IS27. Therefore, the seasonal variation found here is not as clear as expected from the theory of excitation by insolation (e.g., Dai and Wang, 1999). Instead of an annual cycle exhibiting one maximum in summer (Haurwitz and Cowley, 1973), maxima can partly be found in winter (Fig. 4.11), since the largest pressure gradients are present in those months.

4.6 Summary

Based on absolute surface pressure data from the global IMS infrasound network, the signatures of the atmospheric tides, derived using spectral analysis tools, were compared with the surface pressure reanalysis from MERRA-2. The capability of this network to capture the temporal and geographical variability of atmospheric dynamics has been demonstrated (**Question I** of Section 1.5). Besides the tidal pressure oscillations thermally induced by insolation, the sensors of the IMS infrasound network are also capable of representing the gravitationally-forced lunar tide.

The lunar semidiurnal tide was detected at almost all of the IMS stations, despite its small amplitude (Lindzen and Chapman, 1969). Its PSD peak is highly significant at all tropical stations. The distinctness of this signature at low latitudes is certainly also a result of the accurate sensitivity of the barometric sensors at the IMS infrasound stations. Following a review on atmospheric tides by Lindzen and Chapman (1969), the availability of hourly, and even shorter-term, barometric data has been proven to be of much benefit. This is underlined by the fact that the existence of the lunar tide could not be proven in the MERRA-2 time-series. In contrast, a significant semidiurnal lunar tide was even found at the Antarctic IMS station, although this might be spurious, potentially being an indirect sensor-lifting effect of the ocean tide (Schindelegger and Dobslaw, 2016).

The spectral analyses showed that quantitative measures of the diurnal, semidiurnal and terdiurnal tides — for instance, PSD and amplitude — are well represented by both IMS recordings and MERRA-2 data. Despite the different sampling intervals of 1 s (IMS) and 3 h (MERRA-2), only slight differences were found. These can be related to the spatial resolution of the reanalysis fields and local effects at the IMS stations. The global observation of the diurnal and semidiurnal solar tides presented in this chapter are in broad accordance with previous studies, which were based on observations and model analyses. The IMS infrasound network is smaller than previous networks (e.g., Haurwitz, 1965; Dai and Wang, 1999), but it is equipped with highly accurate barometric sensors that are uniformly distributed around the globe. In the future, GWs, which are in the period range of between 10 min and several hours, could be examined, given the accuracy and high temporal resolution of the barometric data from the IMS infrasound network; however, this depends on the amplitudes of the GW signatures, which could be superimposed by tidal harmonics.

Data assimilation in existing empirical models of both solar (e.g., Dai and Wang, 1999; Schindelegger and Ray, 2014) and lunar (e.g., Kohyama and Wallace, 2014; Schindelegger and Dobslaw, 2016) tides at ground level would be a valuable application of the IMS infrasound data. At present, the focus of such empirical models is often limited to the diurnal and semidiurnal tides. The accurate barometric IMS datasets also allow for analyzing the global characteristics of higher tidal harmonics. For this purpose, the set of selected IMS infrasound stations is extendable. So far, the 13 years' worth of data used in this study have also revealed valuable findings on the seasonal variation of the terdiurnal tide. Other tidal harmonics and their excitation sources could be studied, since up to 9 cpd clearly ap-

pear in the PSD analysis of the barometric IMS dataset. For example, the quarterdiurnal tide has been investigated in only a few studies. The one by Pramanik (1926) was based on only continental stations. By using the IMS infrasound network, maritime regions could also be represented, considering stations located on islands.

Studies of the terdiurnal tide, with a period of 8 h, have only been performed on a more regional scale so far, for example, in the USA (Ray and Poulose, 2005), or as a collection of data in the absence of a uniform network (Hann, 1918). Here, a semiannual cycle of the terdiurnal tide, with maxima in summer and winter, has been identified on a global scale. The excitation mechanism of the terdiurnal tide must be different or more diverse, compared to the diurnal and semidiurnal tide, respectively. Wave–wave interactions are considered to be at least a secondary source of atmospheric tides (e.g., Forbes and Wu, 2006; Moudden and Forbes, 2013).

5 | Assessing NWP model uncertainties using infrasound detections from microbaroms

Chapter 4 demonstrated the capability of the IMS infrasound network to characterize atmospheric waves on a global scale — the thermal tides. This chapter addresses **Question II**, using PMCC infrasound detections from the globally observed microbaroms to assess NWP models representing the middle atmosphere. Temperature profiles from the CORAL instrument, which was collocated to IS26 in 2016, allow an estimation of the effect of temperature variability on infrasound propagation and signal detection.

Significant portions of this chapter have already been published by Hupe et al. (2019), entitled 'Assessing middle atmosphere weather models using infrasound detections from microbaroms'. For the sake of consistency in this thesis, only minor text changes have been applied.

5.1 Overview

At the IDC in Vienna, the IMS infrasound data are routinely processed to detect coherent, low-frequency pressure waves (Marty, 2019). Among these are microbaroms, a quasi-continuous natural infrasound source generated by standing ocean surface waves (Donn and Naini, 1973). They are regularly and globally detected, covering a frequency range between 0.1 Hz and 0.5 Hz (see Section 1.2). In the context of the CTBT, they produce a high false-alarm rate in automatic detection lists of the IDC (e.g., Arrowsmith, 2018), and thus extend the time required to provide the reviewed event bulletins. Understanding the seasonal variations in microbarom sources and atmospheric propagation parameters allows a quicker identification and rejection of such detections.

The focus of this study was to better understand seasonal variations in the characteristics of the microbarom detections, such as the amplitude and direction of arrival, as recorded at IS26 in southern Germany (48.85°N, 13.71°E). The modeling was carried out with regard to the spatio-temporal variability of the source term and propagation conditions in the middle atmosphere. The spatiotemporal evolution of the sources was repre-

sented by the ocean wave interaction model that was developed by the French Research Institute for Exploitation of the Sea (IFREMER) for estimating seismic noise (Ardhuin et al., 2011). Prediction of the azimuthal distribution was adapted from Landès et al. (2014). Using middle atmosphere properties (i.e., vertical profiles of wind speed and temperature), derived from NWP model data of the ECMWF, Landès et al. (2014) explained the seasonal variation of microbarom signals.

In this study, the signal amplitude at the station was modeled by applying the attenuation relation proposed by Le Pichon et al. (2012). This accounts for the effects of the source frequency, propagation range and along-path effective sound speed as a measure of atmospheric propagation conditions. According to Chapter 3, microbaroms can potentially propagate through the atmosphere over large distances due to low absorption at 0.1 Hz to 0.5 Hz (Sutherland and Bass, 2004) and efficient atmospheric ducting between the ground and the stratopause (Drob et al., 2003; Landès et al., 2014). Ducting is dependent on the three-dimensional wind and temperature field, and the propagation direction (Chapter 3). The main characteristics of SSW events have been successfully derived from directional microbarom amplitude variations resulting from changes in stratospheric propagation conditions (e.g., Smets and Evers, 2014). As infrasonic waves propagate into the middle atmosphere, significant features of the vertical structure of temperature and wind are reflected in the signal detected on the ground (e.g., Kulichkov, 2010). Unresolved fluctuations in the temperature or wind profiles that form the waveguide may significantly affect the received signals.

Uncertainties in the considered ECMWF data products were quantified using recent high-latitude observations. A temperature bias in the ECMWF operational HRES analysis (L137) part of the IFS has been highlighted by comparing it to measured temperature profiles from middle atmosphere lidar systems (Ehard et al., 2017b; Hildebrand et al., 2017). For quantifying biases and deviations in middle atmosphere temperatures at mid-latitudes, and their potential effects on amplitude predictions at IS26, a portable lidar for measuring temperature profiles between 30 km and 90 km altitude was collocated to the station for seven months in 2016. The distribution of the effective sound speed profile was adjusted using measured differences between operational ECMWF HRES analyses and lidar profiles. This was used as input for calculating the attenuation of the source pressure. A range of uncertainty for the predicted amplitude at IS26 was inferred, showing that uncertainties in NWP models can strongly affect the predicted amplitudes.

5.2 Microbarom observations in Germany

For the eight-element infrasound array IS26, the PMCC algorithm (Cansi, 1995, see Chapter 2) was used for detecting coherent waves with frequencies of up to 5 Hz. Focusing on the frequency range of microbaroms (0.1–0.5 Hz), the detections follow a seasonal variation in azimuth (Fig. 5.1). During winter, strong predominant signals are detected from northwesterly directions; whereas during summer, signals are more scattered and less pronounced, originating from northerly or southeasterly directions. This is related to the

prevailing winds in the stratosphere forming the essential waveguide between the ground and stratopause altitudes. Here, the presence of the ground-to-stratosphere waveguide was estimated by the maximum effective sound speed ratio between 40 km and 60 km over IS26 (Eqs. 3.5 and 3.7 in Chapter 3).

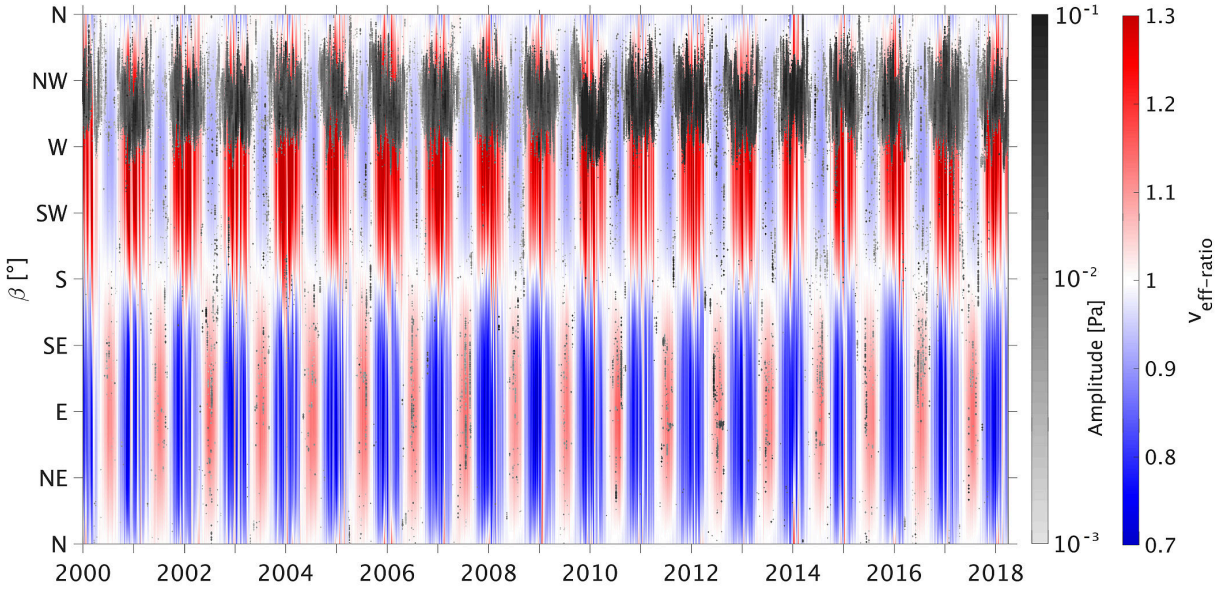

Figure 5.1: More than 10^6 infrasound detections from microbaroms (0.1–0.5 Hz) are shown in the back-azimuth vs time domain. Only events with family sizes of at least 40 pixels were considered. The amplitude is shown graduated in gray on a logarithmic scale. The colored background highlights the maximum $v_{eff-ratio}$ between 40 km and 60 km altitude, derived from ECMWF HRES fields, indicating favorable (red) and unfavorable (blue) propagation conditions. Reproduced from Hupe et al. (2019).

5.3 Identifying the sources of microbaroms detected in southern Germany

Microbarom source terms were modeled using the noise generation theory due to non-linear ocean wave interaction, as developed by Ardhuin and Herbers (2013). Input to that model were data from NASA's wave action model, WAVEWATCH-III, and ECMWF surface winds (Ardhuin et al., 2011). The output covers a global 0.5° x 0.5° grid, up to ±78° latitude, with a temporal resolution of 3 h.

The source region considered herein was the area between 20°N and 78°N, within a longitudinal range between 60°W and 80°E. As shown in Fig. 5.2, the source amplitudes are strongest in the North Atlantic Ocean, where the dominant frequency is between 0.2 Hz and 0.3 Hz. This corresponds to the mean back-azimuths of microbarom detections at

IS26, ranging from 240° to 360° (southwest to north). Along the coastlines, in shallower water and in spatially limited seas, the dominant frequencies are higher due to reduced wavelengths compared to the open ocean (Fig. 5.2(b)). Further analyses in this study referred to the dominant frequency range between 0.15 Hz and 0.35 Hz. In addition, filtering parameters were applied to the PMCC processing results in order to focus on detections with high significance (Table 5.1). These filters resulted in 6,893 remaining detections for the considered three-year period, from 2015 to 2017, of which more than 95 % originated from north-westerly directions. For these dominant directions, the maximum acoustic source pressure of the model, determined for each $\delta\beta \pm 1°$, is shown in Fig. 5.3(a).

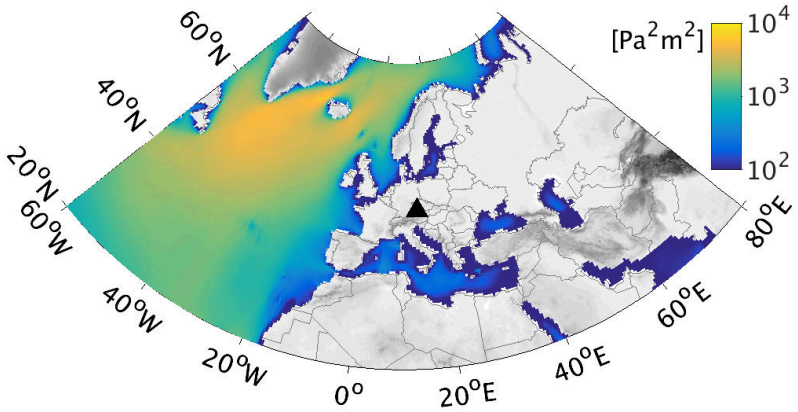

(a) Mean acoustic source pressure.

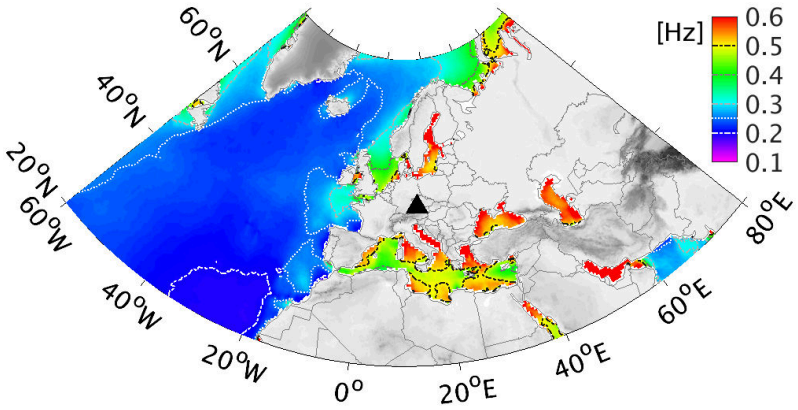

(b) Dominant frequencies.

Figure 5.2: The model of Ardhuin et al. (2011) provided spectral output of the source pressure. At each grid point, the maximum spectral source pressure was integrated over the period from 2015 to 2017, and normalized by the number of time steps (a). The same calculation was performed using the frequency assigned with the maximum source pressure, in order to retrieve the dominant frequency at each grid point (b). Reproduced from Hupe et al. (2019).

Table 5.1: Applied filtering parameters for studying microbaroms with high significance in PMCC detections. Reproduced from Hupe et al. (2019).

PMCC measures	**minimum**	**maximum**
Family size	40	-
Center frequency of the family [Hz]	0.15	0.35
Frequency of family members [Hz]	0.10	0.50
Fisher ratio	3	6
Fisher ratio x RMS amplitude [Pa]	0.01	-

Since the model of Ardhuin et al. (2011) was developed for estimating seismic noise, a scaling factor, S, needed to be applied to translate the source pressure into infrasound amplitudes. A generally applicable value of S was not elaborated by Ardhuin et al. (2011), however. In this study, the observed amplitude was compared to the modeled one on a relative scale, with a scaling factor of $S = 1/2{,}000$. Further developments to determine an exact value of S should account for the source directivity (Brekhovskikh et al., 1973) and the source's geometric characteristics — the fact that several grid points contribute to the detected signals, since standing ocean waves are a surface-like, rather than a point-like, independent source of infrasound (Smets and Evers, 2014).

A realistic, semi-empirical attenuation relation, considering stratospheric winds and geometric spreading, was evaluated by Le Pichon et al. (2012). This parameterized the factors controlling attenuation, with respect to different frequencies (f) and values of $v_{eff-ratio}$, representative of realistic atmospheric conditions. The following formula was proposed for calculating the attenuation coefficient at a distance, r (in km), from a reference distance to the source of 1 km:

$$A_p(f, r, v_{eff-ratio}) = \frac{1}{r}\, 10^{\frac{a(f)\, r}{20}} + \frac{r^{b(f, v_{eff-ratio})}}{1 + 10^{\frac{d-r}{s(f)}}} \tag{5.1}$$

The first term of Eq. 5.1 describes the near-field attenuation in the shadow zone, where a parameterizes the dissipation of direct waves. The second term accounts for far-field attenuation in the geometrical acoustic duct region, and is controlled by three parameters: b defines the geometrical spreading and attenuation of waves, and s is a scaling distance representing attenuation in the shadow zone, the width of which is given by d.

To model the amplitude, each grid point of the source model was assigned the azimuth (α) and distance (r) to IS26. For each α (equal to $\beta - 180°$), the daily mean value for $v_{eff-ratio}$ was obtained by averaging the ECMWF HRES analysis of temperature and horizontal winds at the receiver at 00 UTC and 12 UTC (Fig. 5.3(b)). In order to account for geometric acoustic ducting in the stratopause region, the maximum of $v_{eff-ratio}$ was determined as being between 40 km and 60 km. Using r and $v_{eff-ratio}$, the attenuation coefficient (A_p, Eq. 5.1) was calculated for each potential source grid point with $f = 0.2$ Hz, and tabulated values for a, b, s and d from Le Pichon et al. (2012). Parameter b

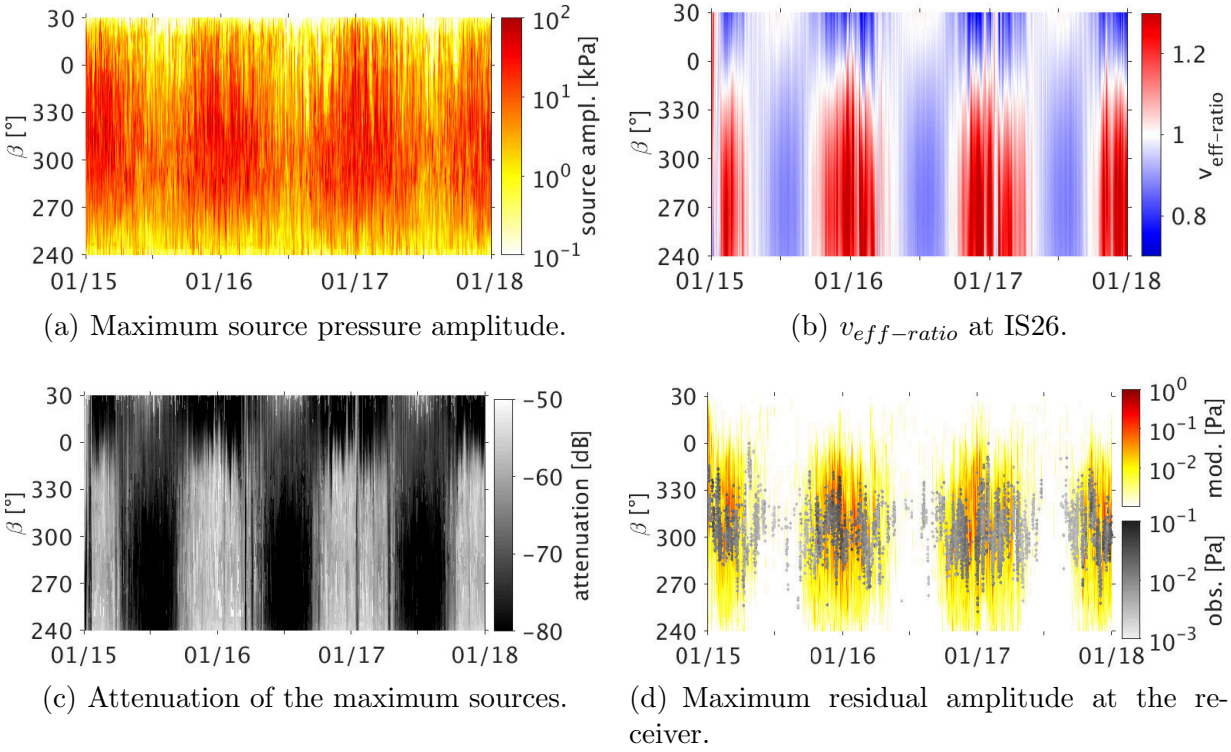

(a) Maximum source pressure amplitude.

(b) $v_{eff-ratio}$ at IS26.

(c) Attenuation of the maximum sources.

(d) Maximum residual amplitude at the receiver.

Figure 5.3: For the dominant back-azimuth range ($\beta = \alpha - 180°$) and f set to 0.2 Hz, the maximum acoustic source pressure for each β (a) and $v_{eff-ratio}$ (b) are shown. Attenuation was calculated using Eq. 5.1, shown here (in dB) for the grid point of the maximum source pressure (c). The predicted amplitude (d) at the receiver was calculated as the maximum of the attenuated source terms per $\delta\beta \pm 1°$. Figure C.1 on page 113 covers the entire back-azimuth range, and provides the distance of (a) that contributed to (c). Reproduced from Hupe et al. (2019).

was additionally interpolated with regard to $v_{eff-ratio}$. The attenuation of the maximum sources is shown in Fig. 5.3(c).
At all grid points, the source pressure was then multiplied by the attributed A_p and the scaling factor S to obtain the residual pressure. The expected amplitude at the receiver was estimated at the maximum of the residual pressure for each $\delta\beta \pm 1°$ (Fig. 5.3(d)). The PMCC detections are superimposed in Fig. 5.3(d). Obviously, the modeled amplitudes reflect both source strength and prevailing winds (Fig. 5.3(b)) in their seasonal variations throughout the year.

5.4 Uncertainties in infrasound attenuation modeling, estimated using lidar

Overall, Fig. 5.3 shows reasonable agreement between the PMCC detections and the predicted back-azimuths. The observed seasonal variations in amplitude are also consistent with the source and propagation models. In particular, large amplitudes and the increased number of detections during winter agree with the modeling, as well as the significantly reduced number of microbarom detections during summer. This indicates that infrasound detections originating from ocean swell in the North Atlantic are well understood, with respect to infrasound propagation in the atmosphere; however, it has recently been shown that temperature and wind profiles provided by the ECMWF differ from measurements in the middle atmosphere (e.g., Hildebrand et al., 2017). Since the ECMWF analysis fields are commonly used for determining the effective sound speed, it is important to assess how these differences would affect microbarom modeling. This can be essential during the equinoxes and summer, when $v_{eff-ratio}$ is close to, or even below, one (see also Fig. 3.4). The investigation of such uncertainties may lead to a better understanding of outliers in the detections and, thus, false alarms at the IDC.

The CORAL system, as introduced in Chapter 2, was collocated to IS26 between May and November 2016. More than 400 h of observations, over 83 nights, were used to quantify the bias in ECMWF temperatures between 30 km and 70 km altitude. All the nighttime mean profiles of CORAL, and the deviations of the corresponding ECMWF vertical profiles, are shown in Fig. 5.4. The overall mean shows a cold bias in the ECMWF analyses from 45 km upwards, amounting to 5 K at 50 km altitude (deviations of around 4.5 K within 2σ) and 12 K at 58 km altitude (6 K within 2σ). This is in accordance with observations made by Ehard et al. (2017b) and Hildebrand et al. (2017). Note that Rapp et al. (2018) already considered monthly mean observations from the same CORAL observations and found significant biases between the ECMWF analysis fields and both radio occultation and the CORAL measurements (Rapp et al., 2018, figs. 7 and 8).

The following approach estimated the effect of biases in NWP models on amplitude modeling. (i) Considering the model output times, t_{mod}, given at intervals of 3 h, for each time period, $t_{mod}\pm3$ h, the maximum observed amplitude in the direction β_{obs} was compared with the maximum predicted pressure at IS26 in the direction $\beta_{obs} \pm 5°$. Therefore, two predicted amplitude ranges were computed (note that, if no detection was found within a 6 h time window, the interpolation considered the direction of the detection that was nearest in time). (ii) One deterministic amplitude value was obtained for a $v_{eff-ratio}$ based on the ECMWF temperature and wind profiles at the receiver (cf. Section 5.2). Using this value, an amplitude range was calculated in order to reflect short-term variations in source strength. Upper and lower limits were determined as two-day sliding maxima and minima of the deterministic values, respectively. (iii) The $v_{eff-ratio}$ was randomly perturbed, given the range of the observed temperature deviations measured during the CORAL campaign in 2016. ECMWF wind profiles were combined with the perturbed temperature profiles incorporating the measured mean bias (up to 12 K) and deviations from the ECMWF

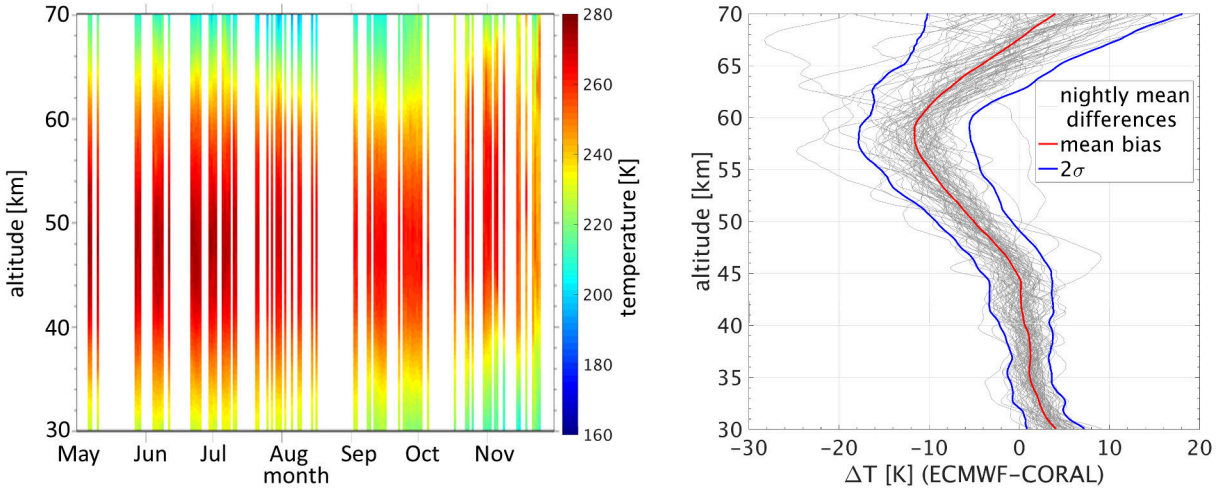

(a) Nightly mean temperature profiles. Reproduced from Blanc et al. (2019).

(b) Bias and deviations of the ECMWF. Reproduced from Hupe et al. (2019).

Figure 5.4: (a) Collocated to IS26, CORAL obtained temperature profiles of the middle atmosphere on every third night, on average. (b) Eighty-three nightly mean differences between ECMWF and CORAL (gray) resulted in a cold ECMWF mean bias (red) above 45 km. This increased up to 12 K at 58 km altitude, where deviations of 6 K are within the 2σ interval (blue). The nightly mean ECMWF temperature was calculated between 18 UTC and 06 UTC, corresponding to the approximate operation times of CORAL.

analysis fields (up to 6 K within 2σ). The range of uncertainty of the modeled amplitude was obtained by first excluding amplitude deviations outside the 2σ confidence interval, and then applying the two-day sliding maxima and minima, as per (ii).

According to Eq. 3.5, a temperature bias alters the speed of sound, c_T, but wind is another important term that contributes to the effective sound speed. Although no obvious mean bias was found by Hildebrand et al. (2017) or Rüfenacht et al. (2018) for the horizontal wind components in the ECMWF analysis fields, differences in the 2σ confidence interval amounted to $\pm 40\,\mathrm{m\,s^{-1}}$. The temperature bias and deviations found using the CORAL data qualitatively agree with the ones found using the Rayleigh–Mie–Raman (RMR) lidar at the Arctic Lidar Observatory for Middle Atmosphere Research (ALOMAR) in northern Norway in March and August 2016. Therefore, ECMWF wind differences derived from the same measurement campaign were applied to the simulations. Analogous to estimating amplitude uncertainties by temperature, as described in (iii), 100 calculations for perturbations of meridional and zonal ECMWF winds, incorporating observed 2σ deviations ($\pm 40\,\mathrm{m\,s^{-1}}$), were performed. The uncertainties of the temperature effect, and the combined effect of temperature and wind, are shown in Fig. 5.5.

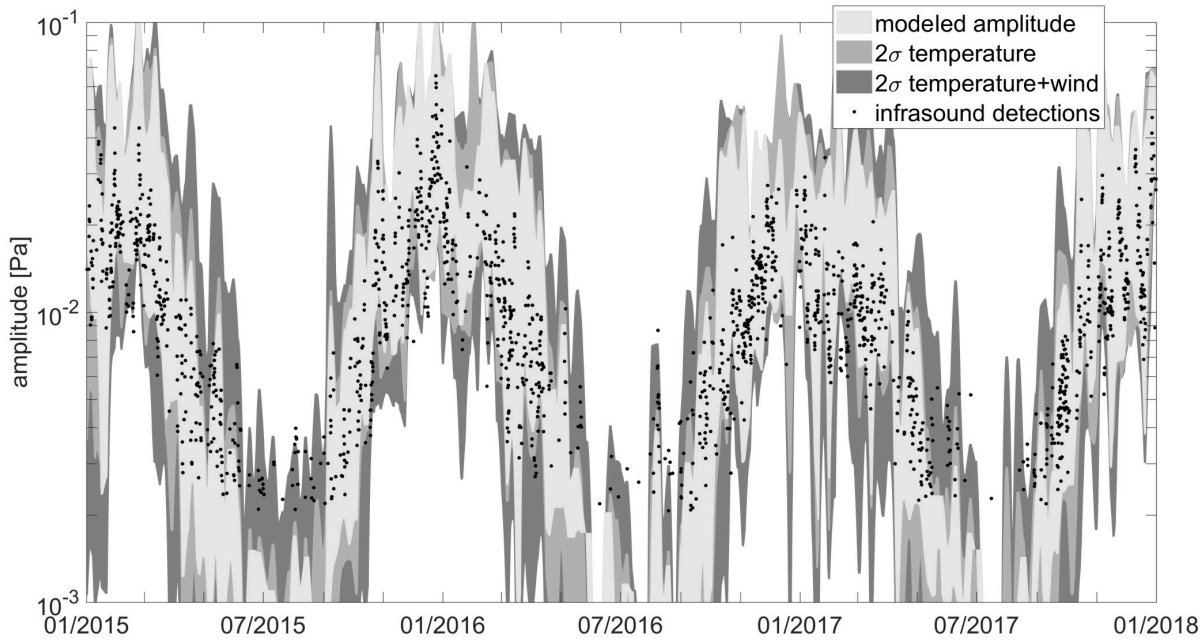

Figure 5.5: The modeled amplitude range, based upon ECMWF data, was determined from sliding two-day minimum/maximum deterministic values. This accounts for the fluctuation in source strength, which was also seen in the detections (black dots). Amplitude modeling uncertainties were estimated by ECMWF temperature and wind perturbations, based on CORAL measurements at IS26 and on RMR lidar data from the ALOMAR observatory in northern Norway (Hildebrand et al., 2017; Rüfenacht et al., 2018), respectively. Reproduced from Hupe et al. (2019).

5.5 Discussion of the results

The results are summarized in Table 5.2. Of the observed amplitudes, 76.8 % are in the range of the modeled amplitudes, based upon the ECMWF analyses of wind and temperature. This rate, however, varies with season, as does the number of detections at IS26. During summer (May to August), in only 12 % of all time windows, at least one signal is detected; 29.4 % of the maximum amplitudes can be predicted by solely using the ECMWF analysis fields. During winter (November to February), these rates are significantly higher (47 % and 81.4 %, respectively).

As seen in Fig. 5.5, warming the stratopause by the determined mean bias of up to 12 K, and incorporating 6 K of uncertainty, weakly impacts downwind propagation during winter for arrivals from the prevailing northwesterly directions. Nevertheless, amplitude predictions improve by 10.3 % to 87.1 %. When combining temperature perturbations with wind deviations of up to $40\,\mathrm{m\,s^{-1}}$, even 96.5 % of detections are predicted. The remaining discrepancies can be seen in the aftermath of the SSWs, which occurred in January 2015 (Manney et al., 2015) and 2017 (Xiong et al., 2018); however, these are well

resolved by the ECMWF analyses (Fig. 5.3(b)) and the predicted amplitudes, which match observations that were half of the seasonal mean value (16 mPa). In December 2016, large amplitudes were modeled, despite a markedly reduced number of detections (60 % and 56 % less compared to 2015 and 2017, respectively). The uncertainty is significantly increased, so that amplitudes can range from 1 mPa to 90 mPa, whereas the ECMWF analyses only cover amplitudes between 9 mPa and 40 mPa. The uncertainty indicates that propagation conditions might have changed, possibly because of a minor SSW.

Obviously, temperature and wind perturbations can markedly affect propagation conditions. As a result, uncertainties in the modeled amplitude increased during the equinox periods (Fig. 5.5), when the mean zonal wind circulation of the stratosphere weakens and reverses. The number of time windows that showed at least one detection are slightly lower (40.9 %) than during winter, and the amplitude prediction rates are slightly higher (+4 %). In summer, the low prediction rate, using the ECMWF analyses (29.4 %), was caused by amplitudes modeled below the noise threshold of the station (around 2.5 mPa; see Matoza et al., 2013). These were either not detected by the PMCC algorithm or were filtered out (Tab. 5.1); however, 12 % of the time windows still provided observations, exhibiting amplitudes near the threshold. These observations can only be predicted when accounting for wind and temperature deviations within the 2σ confidence interval. The prediction rate was significantly improved, to 87.2 % (temperature only – 40.9 %). This implies that the atmospheric conditions had temporarily changed, weakening attenuation at the receiver, especially in 2015 (Fig. 5.5).

Overall, modeling the amplitudes, while considering uncertainties resulting from middle atmosphere wind and temperature models, significantly improves the ability to explain microbarom amplitudes. The improvement amounts to 8.7 % and 19.9 % when accounting for the uncertainty effects of temperature, and combined wind and temperature, respectively. Considering the large propagation ranges for North Atlantic sources (more than 3,000 km; see Fig. C.1 on p. 113), thermospheric returns are unlikely (Sutherland and Bass, 2004), as opposed to arrivals from North Sea sources involving shorter propagation paths. Thus, part of the unresolved variability observed in the amplitude of the microbaroms from the North Atlantic can provide useful integrated information about dynamical properties in the stratospheric waveguide. Occasionally, at shorter ranges, microbaroms likely originate

Table 5.2: Amplitude modeling scores (percentages per season); in brackets – number of 3 h time windows with at least one detection.

range of...	**all** (2,661)	**winter** (1,253)	**summer** (320)	**equinoxes** (1,088)
amplitude	76.8 %	81.4 %	29.4 %	85.5 %
2σ temperature	85.5 %	91.7 %	40.9 %	91.4 %
2σ temp.+wind	96.7 %	96.5 %	87.2 %	99.6 %
percentage of all	100 %	47.1 %	12.0 %	40.9 %

from the Mediterranean ($\beta = 165°$) — for example, in summer 2017 — despite unfavorable propagation conditions in the stratospheric waveguide. The remaining discrepancies might be caused by errors in the tabulated parameters a, b, d and s, used in Eq. 5.1. These are mean values, determined from synthetic simulations (Le Pichon et al., 2012), and possibly do not fully describe all atmospheric states. In this study, ECMWF wind and temperature profiles were taken at the receiver, instead of the entire propagation path (e.g., Landès et al., 2014). Since, for the first time, a lidar was located at an IMS infrasound array, this allowed direct comparison of the NWP products (temperature data) with the lidar profiles. Although propagation modeling might be improved by considering the atmospheric conditions over the entire path, the approach used here has already provided results that are consistent with the observations (Fig. 5.3). Further studies should explore how far this assumption is valid in the studied region, dependent on the time of year. Moreover, collocating a lidar to IS26 that is capable of measuring wind profiles would be beneficial in estimating the impacts of local uncertainties in ECMWF wind profiles on amplitude modeling; however, given the agreement of temperature biases found in the lidar data, using deviations from comparable wind observations at the ALOMAR observatory is the best available approximation to date.

Further investigations are also needed to more rigorously determine the scaling factor, S, of the microbarom source term, in order to pursue quantitative comparisons between observations and modeling results. Additional improvements would include integrating the microbarom source term along each great circle path, assuming independent radiating monopole sources (Waxler and Gilbert, 2006), rather than considering the maximum source contribution.

Despite comparable predicted amplitudes in different directions (Fig. 5.3(d)), PMCC detections do not completely cover the expected range of back-azimuths. The detections are rather concentrated on specific directions. Besides the fact that atmospheric specifications are not considered over the entire propagation path, the reduced spreading of the back-azimuths could be explained by the intrinsic limitations of the PMCC algorithm. The PMCC solely detects the most prominent coherent sources in a given time and frequency window (Cansi, 1995). In future applications, alternative array processing techniques, such as the multiple signal classification algorithm (Schmidt, 1986), could overcome this limitation by providing detections from different directions at the same time.

5.6 Summary

The combined use of the operational ECMWF HRES analyses and the IFREMER ocean wave interaction model, together with a semi-empirical attenuation relation, allowed the modeling of directional microbarom amplitude variations, resulting from changes in stratospheric propagation conditions at IS26. With this approach, the seasonal variation in microbarom amplitudes is well explained. In addition, accounting for the known uncertainties in such models, regarding middle atmosphere winds and temperature, improves the predictions, especially during summer (**Question II** of Section 1.5). In this context, using

the atmospheric conditions at the receiver led to good agreement between modeling results and observations. Installing lidars along the paths between infrasound stations and potential sources would not be practicable, in terms of infrastructure requirements and cost effectiveness, due to the multitude of conceivable propagation pathways. Therefore, it can be anticipated that measuring wind and temperature profiles at IMS infrasound stations will be suitable for improving the understanding of microbarom observations. Such efforts are essential in the context of the CTBT because microbaroms complicate verifications by producing high false-alarm rates in routine data processing at the IDC. Better understanding the accuracy of NWP models, and how this applies to infrasound propagation in the middle atmosphere, will help to reduce the high false-alarm rates. The results imply that adding a systematic middle atmosphere temperature offset to the commonly used ECMWF temperature profiles through lidar measurements could improve predictions of the IMS infrasound network detection capability (Appendix A) on shorter time scales by up to 10 %; however, further studies are needed, including from more than one station. For more continuous operation, autonomous lidars, such as CORAL, or other technologies, such as wind radiometers, would be highly appropriate, along with the development of lidar prototypes that are also capable of wind measurements. Capitalizing on such scientific and technical advances should reinforce the potential benefit of the routine and global use of natural infrasound detections for civil and scientific applications.

6 | MAWs — A global view

The global analysis of MAW detections addresses **Question III** and ultimately allows conclusions to be drawn on the hypothesis concerning the link between MAW and GW occurrence.

6.1 Overview

As already introduced in Section 2.1.1, the infrasound bulletins provide the majority of detections in the frequency domain 0.1 Hz to 0.5 Hz (around 60 %; see Ceranna et al., 2019), including microbaroms, meteorites, volcanoes and explosions (Campus and Christie, 2010). The wide source regions of microbaroms — the open oceans in both the Northern and Southern Hemispheres (Landès et al., 2014) — contrast with the spatially limited regions of MAW origins. Therefore, it is not surprising that the frequency domain below 0.1 Hz contributes to only around 10 % of the detections (Ceranna et al., 2019).

In order to focus on the significant detections related to MAWs, the filters defined in Table 6.1 were applied to the detection lists. These filters account for the signal characteristics of MAWs reported in previous studies, which have typically been observed with periods of between 10 s and 100 s (e.g., Larson et al., 1971; Thomas et al., 1974; Greene and Howard, 1975). The upper frequency limit of PMCC family members was chosen differently here (0.07 Hz, or around 14 s) to ensure their discrimination from the microbarom detections (see Table 5.1 in Chapter 5). Dominant periods of MAW events have been reported as covering 20 s to 80 s, with an average of 50 s (Larson et al., 1971), or, more narrowly, 20 s to 40 s (Bedard, 1978). Therefore, in addition, the lower and upper limits of the center frequencies were set to 0.02 Hz (50 s) and 0.05 Hz (20 s), respectively. Note that auroral activity at similar frequencies (Wilson et al., 2010) is generally not represented in the detections because of the standard configuration of the PMCC method (Chapter 2). Auroral signatures are recognized by apparent phase velocities greater than $500\,\mathrm{m\,s^{-1}}$ (due to their origin at high altitudes), whereas PMCC allows for apparent phase velocities between $300\,\mathrm{m\,s^{-1}}$ and $500\,\mathrm{m\,s^{-1}}$.

Figure 6.1 provides an overview of the number of filtered detections per month at all of the IMS infrasound stations from January 2003 to July 2017. The mean back-azimuths for each month are color-coded. The number of detected events naturally varied between seasons (Chapter 3), but also between stations (e.g., IS50 and IS52), which is related to the proximity of the source region. Even at stations that are close to potential source regions,

Table 6.1: Applied filtering parameters for studying MAWs with high significance in PMCC detections.

PMCC measures	minimum	maximum
Family size	10	-
Center frequency of the family [Hz]	0.02	0.05
Frequency of family members [Hz]	0.01	0.07
Fisher ratio F	3	-

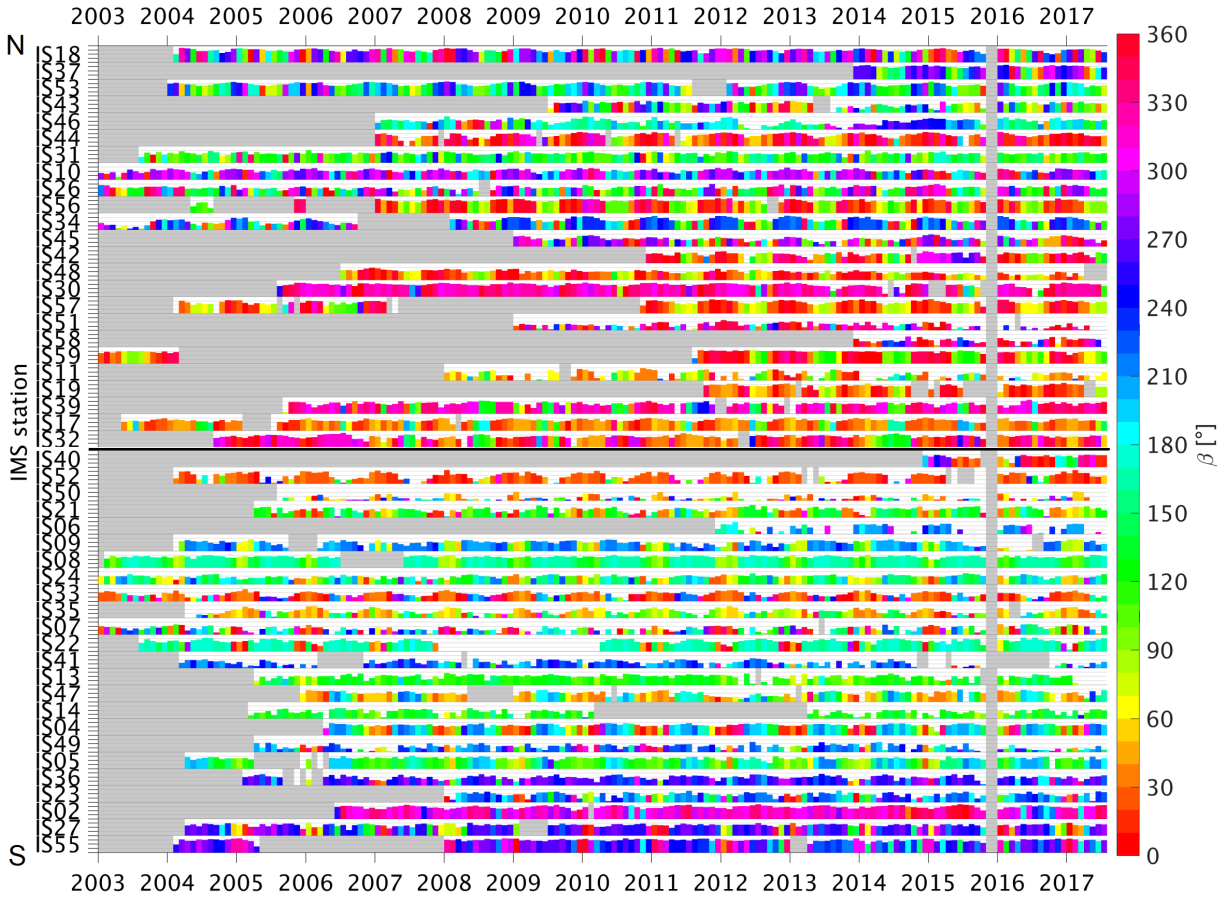

Figure 6.1: The monthly number of PMCC MAW detections is shown for all IMS station datasets available from the German NDC. The stations are sorted from north (top) to south; the horizontal black line reflects the equator. The logarithmic scale indicates from 10^0 to 10^4 detections at each station. Colors code the monthly mean back-azimuths; gray boxes indicate missing data or the lack of PMCC results at the time of writing, when the data from end-2015 were subject to reprocessing.

such as IS09 (Brazil) and IS41 (Paraguay), the detections differed by about an order of magnitude. Such differences are related to the array configurations, the number of sensors or environmental noise conditions.

Concerning the monthly mean back-azimuths, a semi-annual pattern was identified at most of the sites. Note that a semi-annual pattern was also found for the microbaroms, showing mean back-azimuths well correlated with the predominant stratospheric wind directions, "the primary factor controlling the signal detectability" (Ceranna et al., 2019, p. 476). Here, for MAW detections (Fig. 6.1), westerly (purples) and easterly (greenish) back-azimuths were not as pronounced as for the microbarom detections. It seems rather that the northerly components in the back-azimuths (reddish) were pronounced at tropical and subtropical latitudes in the Northern Hemisphere (i.e., between IS32 near the Equator and IS42 on the Azores). Similarly, both southerly (cyan) and northerly components were found at low latitudes in the Southern Hemisphere. At middle and high latitudes, however, the monthly mean back-azimuths seem to be associated with the stratospheric circulation. These observations posed two questions:

1. Are the source regions of regularly detected MAWs solely located at middle and/or high latitudes?
2. Are MAW detections almost independent of the stratospheric circulation, and thus not limited to propagation in the ground-to-stratosphere waveguide?

These issues are addressed in the course of this chapter, with the aim of answering the following decisive questions concerning the source mechanism, which has not been completely understood in former studies, as reviewed in Section 1.4.

3. Is the excitation mechanism of MAWs subject to seasonal variability?
4. Is the occurrence of MAWs linked to GW activity?

6.2 Determination of MAW source regions

When evaluating all detections at a single station, it became clear that the azimuthal distribution was complex, to the extent that different sources can affect the monthly distribution. This had already been observed at IS53 (Alaska) and IS55 (Antarctica) by Wilson et al. (2010). Based on the dataset shown in Fig. 6.1, a monthly climatology was built for each station. The average annual and azimuthal distributions of detected MAWs for IS02 (Tierra del Fuego, Argentina) and IS10 (Manitoba, Canada) are shown in Fig. 6.2. These stations are situated close to already known source regions of MAWs in the southern Andes and the northern Rocky Mountains, respectively. As a first-order visual approximation, the dominant back-azimuths (northwest at IS02 and west at IS10) consequently fit well with the MAW localizations retrieved from the seven-station network that was used by Greene and Howard (1975).

In more detail, three features are striking in Fig. 6.2. First, the number of monthly detections in southern Argentina was much higher than in Canada; second, the dominant

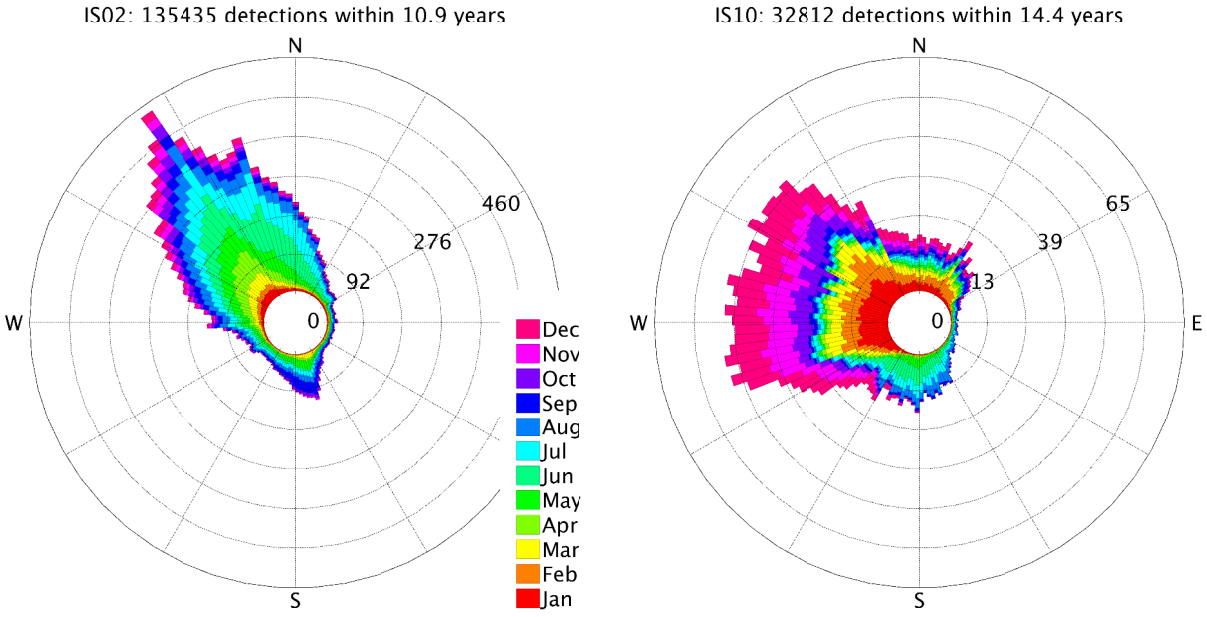

(a) IS02 in Argentina.

(b) IS10 in Canada.

Figure 6.2: The polar plots show the azimuthal distribution of detections attributed with center frequencies between 0.02 Hz and 0.05 Hz. The total number of detections in this MAW frequency domain, and the data availability (in years), are indicated at the top. Each bin covers 3° in back-azimuth. The radius (note the different scales) linearly represents the average number of detections per back-azimuth bin and year. The color code depicts the monthly distribution, providing a first indication of the prevailing directions per season.

direction of arrivals was more pronounced or prominent at IS02; third, at both stations, a seasonal variation was evident in both the number of detections and β. The seasonal variation was opposed in the dominant back-azimuth bins, which means that most arrivals were detected during winter. At IS10, a secondary peak appeared in the southerly direction during spring and early summer (greenish in Fig. 6.2(b)); however, the maximum monthly number of detections per azimuth bin (five in June) was lower than in the dominant directions during winter (12 in January). Multiple, but seasonally varying peaks, were also found at a number of other stations, including IS09, IS47 and IS59 (cf. Figs. D.1 to D.3, pp. 116–124 for all considered stations).

Consequently, it was not appropriate to consider only the primary or mean back-azimuths to localize the sources using the cross-bearing method (Section 2.1.3). Instead, up to three peaks were retrieved from the monthly histograms of the back-azimuth distributions to account for different sources potentially being detected at a station. For evaluating the peaks, their prominence was an important measure. This was the difference between the peak and the point where the histogram increased to a higher peak; if no higher peak remained, the histogram minimum, or a closer edge value, became the refer-

ence level. Thus, prominence can be considered to be a relative peak height. Overall, the peaks had to fulfill the following conditions:

- The peak was higher than the monthly mean, and there was at least one detection per month.
- The peak had to be 35° distant from other peaks.
- The minimum peak prominence (from the background detections) was 0.5.
- The minimum peak width at half prominence was 15°.

Based on these input conditions, the peaks were calculated using the built-in MATLAB algorithm 'findpeaks'; an example with indications of the applied conditions is given in Fig. D.4 (p. 128). Figure 6.3 shows the results for IS02 and IS10 in January, April, July and December. The dominant direction at IS02, which was northwesterly (315°), did not shift throughout the year, and the peak was very prominent. The seasonal variability was recognizable by the number of detections, being highest in austral winter and lowest in summer. A secondary peak that appeared in October (170°) was likely associated with the Antarctic Peninsula, because IS27, located eastward, exhibited a prominent peak at around 270° (see Fig. D.6 on p. 133, and also Figs. D.5 to D.7 on pp. 129–137 for the other

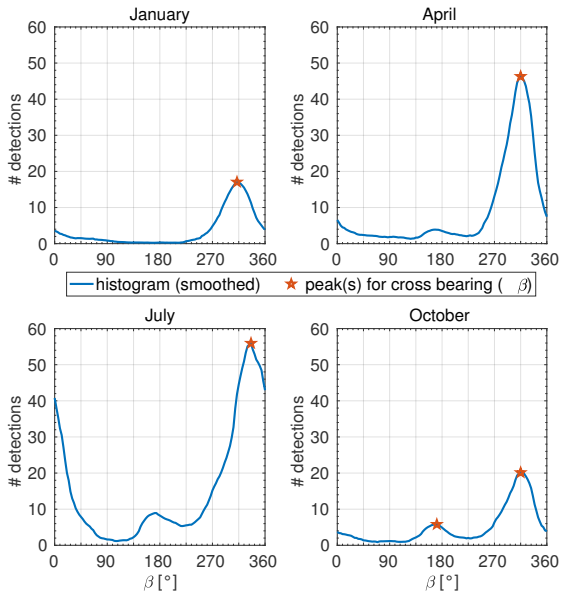

(a) IS02 in Argentina.

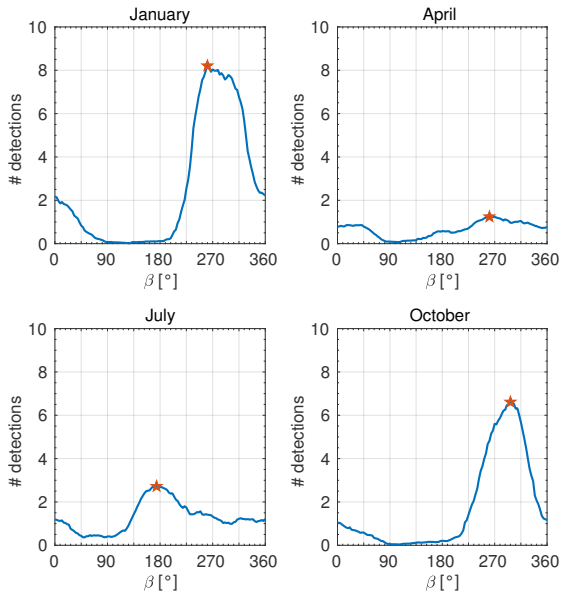

(b) IS10 in Canada.

Figure 6.3: The azimuthal distribution of detections in the MAW frequency domain is shown for four months of the year. The histogram curves show the number of detections per 3° bin. A moving average, with the window length of 10 bins (i.e., ±15°), has been applied. Note the differing ordinates for the stations. The back-azimuths of the evaluated peaks served as input for the cross-bearing method.

stations). For IS10, Fig. 6.3(b) shows that detections from the northwest were maximized in the winter months, whereas detections from the south were only dominant during summer.

Using the determined back-azimuths from all stations on a monthly basis, the cross-bearing algorithm, as introduced in Section 2.1.3, was applied in order to calculate the source regions of dominant signals. Only results from three intersection points were accepted in order to ensure that only the most accurate localizations were considered. Since multiple station combinations can cause the same detection source region to be represented several times, the absolute number of cross-bearing hits is not representative of the number of actual detections from such a region. It is rather an issue of how many stations detected that source, which depends on several factors, such as station coverage and detection capability. The sum of cross-bearing hits was calculated per 3° x 3°.

Figure 6.4 shows a stacked view of global MAW hotspot regions through one year, normalized by the maximum number, which can be found over the Tibetan Plateau. In addition to the Rocky Mountains and southern Andes hotspots, which had already been identified by Greene and Howard (1975), the East Siberian Mountains (in the very northeast in Fig. 6.4) are highlighted as well. These hotspots are all associated with mountain ranges at middle to high latitudes. An exception is the hotspot region over the US, east of the Rocky Mountains. Examining the seasonal variability of the hotspot regions may clarify their origin.

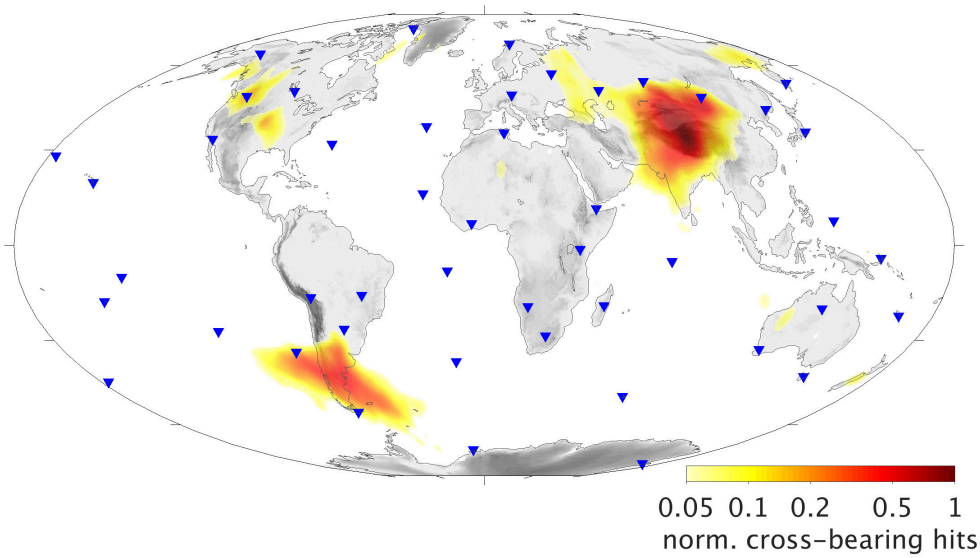

Figure 6.4: This global view of MAW hotspots resulted from monthly cross-bearing localizations stacked over one year (see Fig. D.8 on p. 141 for the raw localizations). The reference for normalization is the global maximum of cross-bearing hits per 3° x 3°. The number of cross-bearing hits per hotspot (logarithmic scale) depends on the number of detecting stations. Gray background colors indicate topography, ranging from light ($z < 250$ m) to dark ($z > 7{,}500$ m) gray. Blue triangles depict the IMS infrasound stations (labels given in Fig. 1.2).

6.3 The monthly variation of MAW source regions

The monthly cross-bearing results (Fig. 6.5) show that the identified source regions are subject to seasonal variability. The dominant hotspots are evaluated.

Tibetan Plateau

The detected source region of the most pronounced hotspot covers a wide area; it is centered over the Tibetan Plateau, but actually extends from the Himalayas in the south (highest peak – 8,848 m) to the Tian Shan (7,439 m) and Altai Mountains (4,506 m) in the north, and from the Pamir Mountains in the west (7,649 m) to the Qilian Shan in the east (5,826 m), all surrounding additional mountain ranges. In fact, conceivable sources exist over the entire region. Since the IMS stations surround the area, but are not located in, an exact separation of sources by cross-bearing is not promising on a monthly basis.

It appears, however, that the core of the hotspot area is associated with the Tibetan Plateau in January and February. In March and April, it extends farther to the north, and the Tian Shan and Altai mountain ranges become more emphasized. In May, fewer and fuzzier cross-bearing hits are calculated, whereas the western part — the Pamir Mountains — is emphasized. At this point, the maximum number of cross-bearing hits is only around 10 % of those in winter. After the hotspot disappears in summer, it returns over the Tian Shan Mountains in October, and again expands to the Himalayas in December.

Overall, MAWs originating from this hotspot were extensively detected at the IMS infrasound stations during winter. Two stations — IS31 (northwest; $\beta = 125°$) and IS32 (southwest; $\beta = 45°$) — detected MAWs during both summer and winter, from the same direction.

The Rocky Mountains and Pacific Coast Ranges

From October to January, a hotspot around, and north of, IS56 can be seen, covering the US Coast Range in Washington (highest mountain – 4,392 m) and parts of the Canadian Rockies (3,954 m). The cross-bearing also emphasizes the Alaska Range (6,200 m) and the Aleutian Islands (1,900 m) in October. All of these mountain ranges are part of the Pacific Ring of Fire; hence, many volcano peaks are characteristic of this hotspot. The closest IMS stations — IS53 ($\beta = 128°$), IS56 ($\beta = 325°$) and IS57 ($\beta = 9°$) — provide a clear indication of this hotspot region up to March (Fig. D.3, p. 126). From April to July, the number of detections from the southeast (IS53) and north-northwest (IS56, IS57) was significantly reduced, by up to 95 %, compared to January (Fig. D.7, p. 139).
The reason for the hotspot disappearance in February and March is that the number of detections from farther stations reduced during these months. Consequently, fewer cross-bearing hits resulted, especially when the back-azimuths yielded two, instead of three, intersection points; such a case is shown for this source region in Fig. 2.3(b) (orange lines).

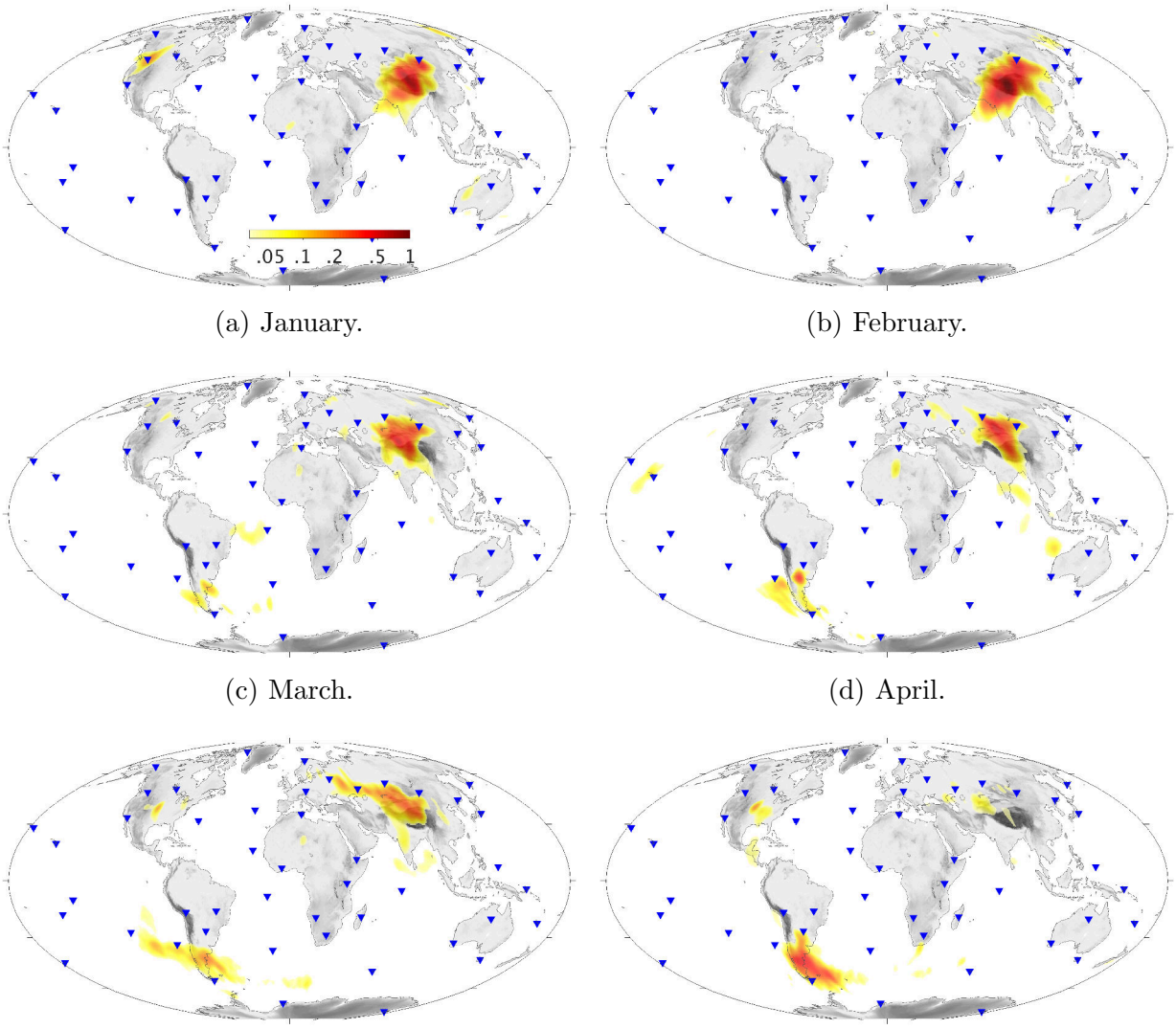

(a) January. (b) February.

(c) March. (d) April.

(e) May. (f) June.

Figure 6.5: Monthly variation of global MAW hotspots, resulting from cross-bearing, for January to June (a – f) and July to December (g – l). The number of localizations per 3° x 3° is normalized by the maximum of all the months. The maximum can be found over the Tibetan Plateau in February.

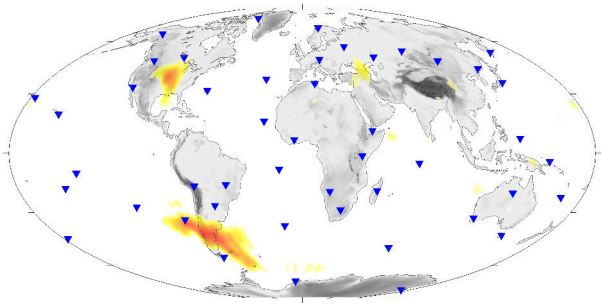

(g) July.

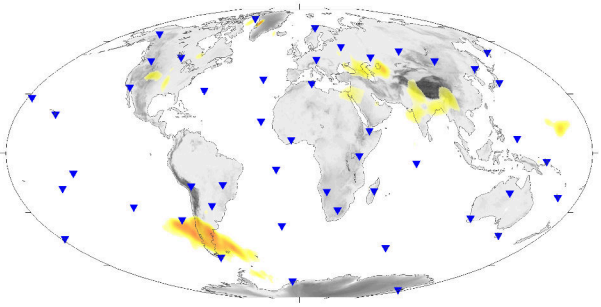

(h) August.

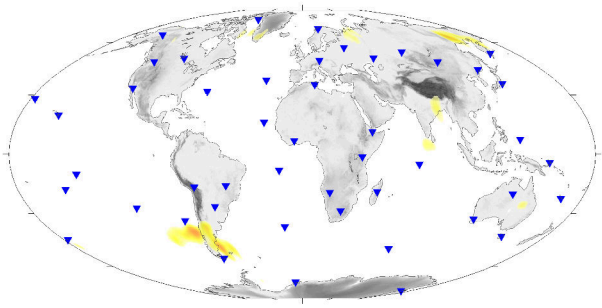

(i) September.

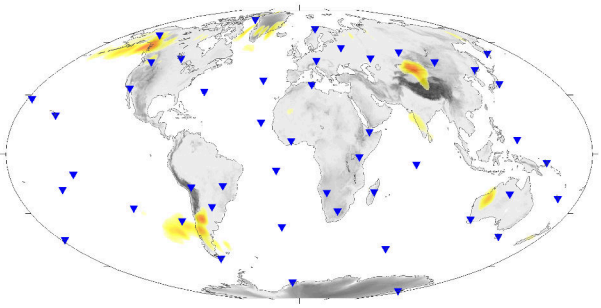

(j) October.

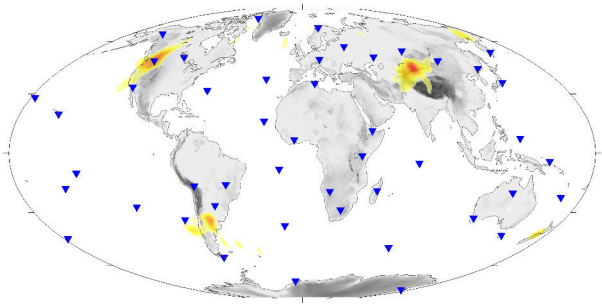

(k) November.

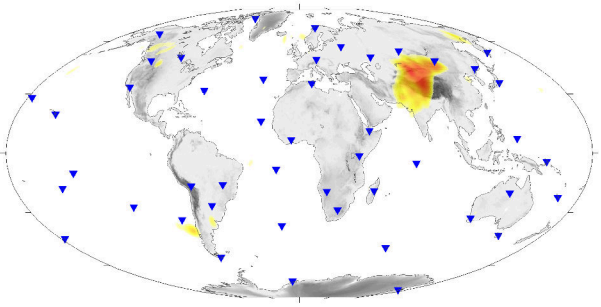

(l) December.

Figure 6.5: Monthly cross-bearing results (cont.).

Overall, MAWs originating from the Canadian Rockies and the Pacific Coast Ranges were frequently detected at IMS infrasound stations during winter, and sporadically (i.e., fewer stations and fewer detections) during summer. This is in line with previous observations from Larson et al. (1971) and Thomas et al. (1974), using local infrasound arrays, and from Greene and Howard (1975), who used a microbarometer network comparable to today's IMS in North America, in terms of station sites.

Southern Andes

The hotspot of the southern Andes, which had already been identified as a MAW source region by Greene and Howard (1975), was detected during most of the year, as Fig. 6.5 indicates. The latitudinal extent ranged from 30°S — the region with the highest mountains of the Andes (summit: Mount Aconcagua; 41.67°S, 70.00°W, 6,961 m elevation) — to the southern tip of the continent (55°S), where the mountains (mostly volcanoes) reach elevations of 1,500 m to 2,500 m. This broad latitudinal range (around 2,700 km) of conceivable sources is likely the reason for the longitudinal range of cross-bearing hits. If the IMS stations detect different sources within that region (e.g., the closest to each station), relying on the respective back-azimuths will fail to exactly match any of the actually detected sources by triangulation. The considered uncertainty of ±5° might also have introduced additional deviations to the west and east. More details about this hotspot are discussed in Section 6.4.
Nevertheless, the cross-bearings of MAW observations by Greene and Howard (1975) reflect the same latitudinal range as the hotspot region derived herein. Their event-based source localizations emphasized the lees of the highest mountains at the northern edge of the hotspot; however, this emphasis could have been favored by technical issues, as their southern-most array was operated in the same area.

Overall, the southern Andes are an obvious source region of MAWs in the Southern Hemisphere. A seasonal cycle in the number of detections is evident, with a maximum in winter. The IMS infrasound station at the southern tip of the continent (IS02), however, experiences a relatively large number of detections in summer (maximum 17 detections per month) from almost the same direction as in winter (56 detections).

East Siberian Mountains

Cross-bearing hits are enhanced over the very eastern part of Siberia (peaks up to 2,000 m) from September to March. Among the contributing stations are IS44, IS45, IS58 and IS59. The maximum number of detections per month varies between two (IS45, October), four (IS58, October), 20 (IS59, January) and 45 (IS44, January). This source region is less prominent than the aforementioned ones, but it conforms to the annual cycle.

Central USA

This source region was not anticipated because it is not directly associated with the Rocky Mountains, at first sight, and it appears as a hotspot only during summer (May to August).

IS10 ($\beta = 174°$), IS53 ($\beta = 96°$), IS56 ($\beta = 120°$) and IS57 ($\beta = 60°$) detected the hotspot (see histograms for July in Fig. 6.3(b), and Fig. D.7 on p. 139). Bedard (1978) actually identified a MAW source region in the lee of the Rocky Mountains over Colorado that could roughly match the source region identified herein, but the emphasis of this hotspot is more to the east, and the seasonality is contradictory to the observations of Bedard (1978). Therefore, it is more likely that this identified source region is unrelated to orography and should rather be associated with the occurrence of severe storms in the central USA. Bowman and Bedard (1971) reviewed several infrasound observations made in the USA during the 1960s and 1970s. Coherent signal periods of 5 s to 62 s and amplitudes of 0.02 Pa to 1 Pa were observed when severe storm cells coincided with tornadoes or hail. Following Goerke and Woodward (1966), the back-azimuths of the signals reflected the paths of moving storm cells. The noise generation mechanisms were assessed in a case study by Georges (1973) who found infrasound originating from severe storms in the form of pulsed signals over distinct time intervals of around 20 min. He hypothesized that these could have been induced by the strong upwinds of rapidly growing convective cells. During the study, however, only a quasi-stationary strong storm, accompanied by tornadoes and hail, produced clear coherent signals at the microbarometers, whereas other moving convective systems did not. Therefore, he concluded that the most intense storms featured infrasound. Consequently, Noble and Bedard (2006) reported on efforts to establish a local infrasound network for tornado detection and warning.

Overall, the hotspot identified during summer was caused by the frequent occurrence of severe storms in an area of the USA that is often referred to as 'tornado alley' in the media (e.g., Powers, 2018). Low-frequency infrasound observations originating from such sources, and exhibiting similar properties as MAWs, were found between May and August (Bowman and Bedard, 1971). This agrees with Fig. 6.5.

Further results from cross-bearing

Figure 6.5, and Fig. D.8 (p. 141), show further regions where cross-bearing hits have accumulated. Among these are Greenland and the Caucasian region in the Northern Hemisphere, and northwestern Australia and New Zealand in the Southern Hemisphere.

Greenland: Parts of Greenland are highlighted between August and October, although the main MAW activity would be expected during winter. An issue already identified in Chapter 4 is that only a few IMS infrasound stations are operated at high latitudes; for example, array IS37 (Norway) is the closest to IS18 in Greenland, at a distance of more than 2,500 km. The azimuthal distribution of detections has provided an indication of several peaks at IS18, including a few to the south and southeast (Fig. D.1(k), p. 118), where the mountains are a maximum of 3,694 m high. IS37 ($\beta = 290°$) and IS26 ($\beta = 325°$) also detected MAW signals that potentially originated from Greenland; however, back-azimuths from more distant stations are ambiguous because of the topographic complexity in the Northern Hemisphere. Supplementing IMS data with European experimental arrays (e.g., Pilger et al., 2018) may be useful for assessing this potential hotspot in the future.

Caucasus: The issues mentioned for Greenland are also applicable to the Caucasian region, where the highest elevation is 5,642 m. The region is weakly highlighted from June to August. The back-azimuths of IS19 ($\beta = 0°$), IS26 ($\beta = 111°$) and IS48 ($\beta = 69°$) contributed to cross-bearing intersections over the Caucasian region (e.g., July); the corresponding average number of detections was low (maximum five at IS19). Additional cross-bearing hits leading to this potential source region (and also further north; e.g., May) were secondary cross-bearing hits from stations that, in the first order, detected the Tibetan Plateau hotspot. For this reason, the Caucasus seems overrated using the chosen method. Single events would need to be analyzed to study the characteristics of this source region in detail (which is beyond the scope of this study).

Northwestern Australia: The emphasized appearances in January and October are the result of spurious intersections due to the wide range used for cross-bearing (10,000 km). The closest stations (e.g., IS04, IS05 and IS07) did not detect any MAW sources in northwestern Australia.

New Zealand: Figure D.8 (p. 141) shows an accumulation of cross-bearing hits over the South Island of New Zealand (highest peak – 3,724 m). Obviously, the horizontal extent does not include the northern island. The contributing arrays were IS05 ($\beta = 105°$), IS22 ($\beta = 165°$) and IS36 ($\beta = 265°$). More details are given in Section 6.4.

As a first conclusion towards the first question of this chapter (p. 63), dominant MAW sources were preferentially found at mid-latitudes (i.e., 30°–60°) in both hemispheres. This could be indicative of a relation to the jet-streams, either with regard to propagation effects or in terms of excitation conditions, as proposed by Larson et al. (1971). At high latitudes, the coarse station network complicates the reliable identification of source regions using the cross-bearing method. MAW signals were detected from manifold mountain ranges in the Northern Hemisphere, however. Another pronounced source region turned out to be related to severe storms in the central USA, and not to the orography.
On a global scale, the Tibetan Plateau in Asia and the Andes in South America are the most dominant source regions. The cross-bearing method did not necessarily reflect the actual occurrence or frequency of the source mechanisms since the number of detecting stations could be related to the propagation conditions, as was determined for the microbaroms in Chapter 5. Therefore, the dominant Andes hotspot, and the less pronounced one in New Zealand, are analyzed in more detail in the following section. The focus was to validate and understand the seasonality of MAW detections (second and third questions), supported by using ray-tracing.

6.4 Validation of the propagation conditions for two Southern Hemisphere hotspots

So far, MAW source regions have shown a seasonal cycle because stations have detected MAWs most often in winter; the majority of hotspot regions have also produced MAW signals at fewer stations in summer, as seen, for instance, at IS02 at the southern tip of South America.

6.4.1 Southern Andes

The surprising feature of this hotspot was the number of cross-bearing hits west and east of the anticipated source region, although the azimuthal distributions of the detections showed relatively distinct peaks at IS02 (Fig. 6.3(a)) and other surrounding stations (e.g., IS08, IS09 and IS13; Fig. D.5, p. 130). Therefore, either the arrays were more sensitive to the closest sources or the source mechanism acts on a broad latitudinal scale. The peak widths actually amounted to at least 45° at half peak prominence (see Section 6.2), which would allow for bearings covering the entire source region on the continent.

Figure 6.6 shows the time-series of β and the RMS amplitude at IS02. Here, the seasonal cycle is evident; the majority of MAW signals were detected in winter, from both the Andes (north) and the Antarctic Peninsula (south). Accordingly, the amplitudes were largest in austral winter and smallest in summer, differing by half an order of magnitude. The lower amplitude limit — the station's noise threshold — did not significantly vary with season. A seasonal variation in phase velocities was not found, as the detections covered the entire range between $300\,\mathrm{m\,s^{-1}}$ and $500\,\mathrm{m\,s^{-1}}$ independently of the season (Fig. D.9, p. 142). This implies that both stratospheric and thermospheric returns were detected, supported by the fact that such ranges of back-azimuth, RMS amplitude and phase velocity were also detected during single events. For instance, the 24 h event shown in Fig. D.10 (p. 143) included 486 PMCC detections within a β range of 300° and 360°; this β range was even covered within 1 h of time. The observed β range might represent mountains from the nearby west-northwest to the far north of IS02. The mean direction during the event was 330° ($\sigma = \pm 16.4°$), the RMS amplitude averaged at 16 mPa ($\sigma = \pm 8.8$ mPa) and the mean phase velocity was $394\,\mathrm{m\,s^{-1}}$ ($\sigma = \pm 55\,\mathrm{m\,s^{-1}}$).

To validate the propagation conditions, the 2D-FD ray-tracer that was introduced in Section 2.4 was used. Propagation modeling was carried out for all months over 10 years (2007–2016), based on along-path vertical temperature and wind profiles. According to the example in Section 3.3, the monthly averaged HRES operational ECMWF analysis fields were supplemented by MSISE-00 and HWM07 data. Here, the source was assumed to be in the southern part of the Andes hotspot region (49°S, 73°W) at an elevation of 3,200 m; the rays were started at angles of between 1° (upward) and 179° (downward). The modeled source frequency was 0.05 Hz, that is, the upper center frequency threshold. Note that, according to Chapter 3, lower frequencies would be subject to even smaller atmospheric absorption rates.

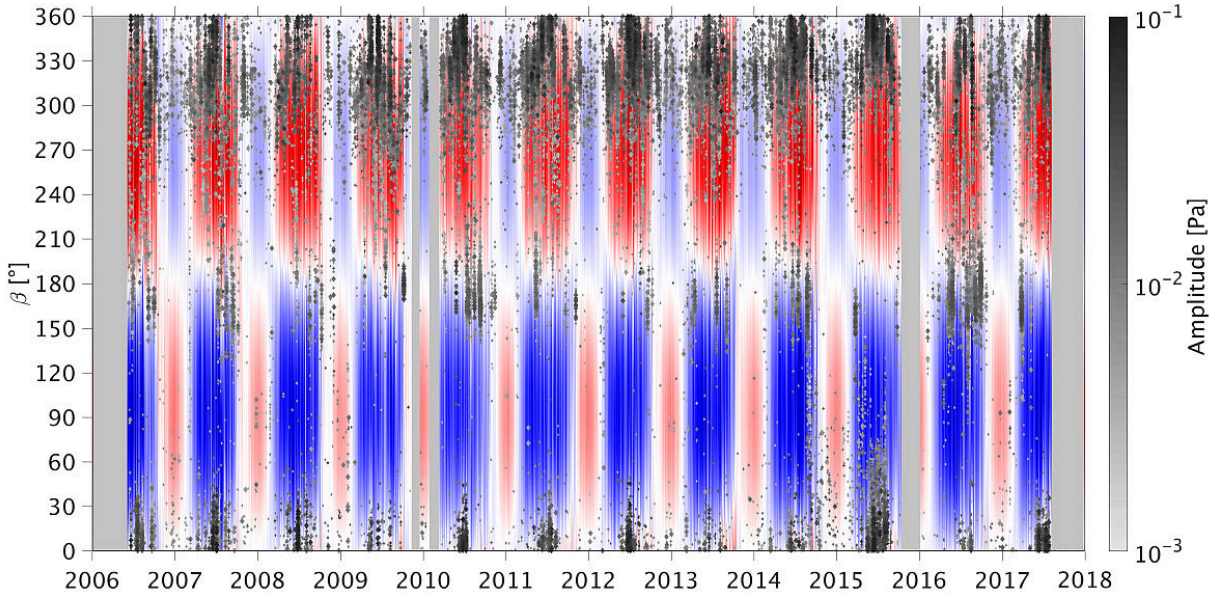

(a) MAW detections at IS02.

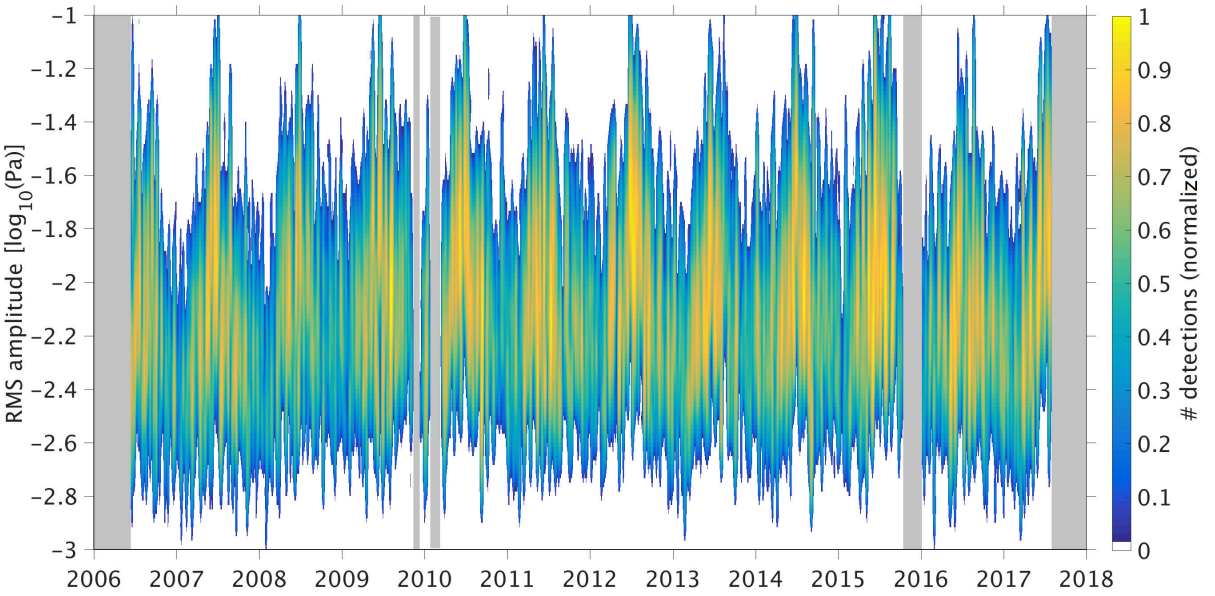

(b) Variation in the number of detections with RMS amplitude.

Figure 6.6: Temporal variation of the MAW detections with back-azimuth (a) and RMS amplitude (b) at IS02. In (a), the maximum $v_{veff-ratio}$ between 40 km and 60 km is color-coded (equivalent to Fig. 5.1). Detections from the south (150°–210°) originate from the Antarctic Peninsula, while other accumulations of detections can be related to the Andes. Here, the number of detections in (b) was evaluated per 7 d and 0.05 $\log_{10}$(Pa), normalized by the maximum value. The gray columns indicate a lack of data availability.

Monthly mean ray-tracing statistics for the 10 years are given for selected stations in Table 6.2, including IS02 (749 km to the south-southeast), IS08 (3,663 km to the north), IS09 (4,352 km to the north-northeast), IS14 (1,806 km to the northwest), IS21 (7,500 km to the east) and IS27 (4,043 km to the southeast). All of these showed monthly distribution peaks reflecting the Andes hotspot. The statistics only include the parameters for those rays that best connect the source and the receiver. More precisely, the 'best ray' is determined as the one that directly passes the location of the receiver or that is closest to it (vertical). It features the shortest possible path (travel time) and yields, for instance, the accumulated atmospheric absorption (A_a) and the apparent phase velocity (v_{app}). Stratospheric (I_s) and thermospheric (I_t) returns were treated separately. Simulations were statistically neglected if the calculated best rays were elevated by more than 10 km at the receiver.

Table 6.2: The ray-tracing results for selected stations that have detected the Andes as a MAW source region are based on monthly mean atmospheric conditions for the period 2007 to 2016. The numbers (0–10) reflect the amount of simulation runs (one per year and month) for which a best-ray solution (<10 km above the receiver) was calculated between the source (49°S, 73°W) and the respective IMS station. Consequently, the numbers indicate the detection likelihood, with regard to both stratospheric (I_s) and thermospheric (I_t) propagation paths. In addition, the mean and the standard deviation of atmospheric absorption (A_a) and phase velocity (v_{app}) are given for these simulation runs.

	IS02		IS08		IS09		IS14		IS21		IS27	
	I_s	I_t	I_s	I_t	I_s	I_t	I_s	I_t	I_s	I_t	I_s	I_t
January	0	10	0	10	0	9	10	8	10	8	0	9
February	0	10	3	10	0	10	6	8	6	8	0	8
March	3	10	6	9	1	10	4	9	4	9	6	9
April	8	10	6	10	10	7	0	10	0	10	9	7
May	9	10	8	9	10	9	0	10	0	10	9	9
June	10	9	5	9	9	8	0	10	0	10	9	5
July	10	10	7	6	6	9	0	10	0	10	9	4
August	9	10	5	6	8	9	0	10	0	10	9	6
September	7	10	9	9	8	9	0	10	0	10	9	7
October	2	10	9	7	8	10	5	6	5	6	5	9
November	0	10	7	8	0	10	10	8	10	8	1	9
December	0	10	4	10	0	10	10	7	10	7	0	9
$\overline{A_a}$ [dB]	0.1	3.8	0.7	15.0	0.6	22.7	0.4	5.7	1.3	19.4	0.4	17.3
$\sigma(A_a)$ [dB]	0.1	1.6	0.4	19.0	0.3	21.6	0.3	7.2	0.9	16.7	0.3	15.4
$\overline{v_{app}}$ [m s^{-1}]	339	382	325	380	348	388	326	393	329	368	340	379
$\sigma(v_{app})$ [m s^{-1}]	7	17	4	48	12	41	11	44	18	54	9	34

Ground-to-stratosphere solutions were found for the stations located south (IS02), southeast (IS27) and north (IS08 and IS09) of the source region between March and October. During summer (November to February), stratospheric ducting was highly unlikely for these stations. These simulations are in line with the seasonal variation of the hotspot (Section 6.3); however, IS14 and IS21 also detected MAWs from the direction of the Andes in April and July, when stratospheric conditions were unfavorable for westward propagation. Therefore, propagation in the ground-to-thermosphere waveguide had to be considered. This was successfully modeled for the majority of the stations for most of the year, despite long propagation ranges of up to 7,500 km (IS21). Thermospheric propagation explained the detections at IS13, IS14, IS21 and IS24, upstream of the stratospheric jet during winter, and accordingly at IS02 and IS09 in the summer. Ray-tracing examples for IS02 are given in Fig. D.12 (p. 146). Moreover, the high phase velocities of more than $400\,\mathrm{m\,s^{-1}}$ that were regularly detected support the conclusion that propagation of MAWs is generally not limited to stratospheric ducts (see Section 3.2). The long-range detectability of MAWs due to thermospheric propagation and low attenuation at MAW frequencies is essential in order to assess the seasonal variation of the source mechanism.

6.4.2 New Zealand

MAWs originating from the South Island of New Zealand (44°S, 170°E) were detected by three or four stations all year round. Monthly maps that present the cross-bearing results specifically for New Zealand are given in Fig. D.11 (p. 144). The azimuthal distributions continuously show prominent detection peaks at IS22 (2,460 km to the north-northeast; $\beta = 165°$) and IS36 (1,080 km to the east; $\beta = 265°$). The highest peak values were found at IS22 in July (59), as opposed to only three detections in December. The number of detections was generally lower at IS36 (13 at the highest peak in May), but the seasonal cycle was comparable (two detections at the lowest peak in January). The increased detection numbers between April and September agree with the ray-tracing results for IS36, as provided in Table 6.3. Here, the source was set to 3,000 m altitude. Wave propagation within the ground-to-stratosphere waveguide was only modeled between April and September. A very strong effective sound speed inversion at the stratopause resulted in reduced transmission of waves to the upper atmosphere, and thus fewer ray-tracing solutions for the thermospheric returns. A ray-tracing example for propagation between the source and IS36 is shown in Fig. D.13 (p. 147).

The ground-to-thermosphere waveguide is essential for explaining the detections at IS22, compared to the ray-tracing statistics. Arrivals due to stratospheric ducting were modeled during summer and, sporadically, in spring. This is contradictory to the number of detections, which significantly increased during winter, with five times more detections than at IS36. The propagation path to IS22 is mainly northward. The small westward component of the propagation path favors stratospheric ducting during summer. As learned from Chapter 5, small-scale fluctuations in temperature and wind can significantly affect propagation conditions, especially when $v_{eff-ratio}$ is close to one. It is noted that adding the mean bias identified in ECMWF HRES temperature fields to monthly mean profiles

Table 6.3: Ray-tracing statistics for stations detecting a MAW source over New Zealand. The numbers (0–10) reflect the amount of simulation runs (one per year and month) for which a best-ray solution (<10 km above the receiver) was calculated between the source (44°S, 170°W) and the respective IMS station. Consequently, the numbers indicate the detection likelihood, with regard to both stratospheric (I_s) and thermospheric (I_t) propagation paths. In addition, the mean and the standard deviation of atmospheric absorption (A_a) and phase velocity (v_{app}) are given for these simulation runs.

	IS05		IS07		IS22		IS36	
	I_s	I_t	I_s	I_t	I_s	I_t	I_s	I_t
January	10	7	10	8	8	9	0	10
February	10	10	10	7	6	10	0	10
March	0	10	0	10	0	10	3	10
April	0	10	0	10	0	10	10	6
May	0	10	0	10	0	10	10	6
June	0	10	0	10	0	10	10	4
July	0	10	0	9	0	9	10	4
August	0	10	0	10	0	10	8	4
September	3	9	0	10	2	9	5	10
October	9	8	4	10	3	10	0	10
November	10	9	3	9	9	10	0	10
December	9	10	10	9	10	9	0	10
$\overline{A_a}$ in dB	0.2	5.1	0.7	23.9	0.7	7.6	0.1	6.4
$\sigma(A_a)$ in dB	0.1	5.9	0.4	21.4	0.2	12.9	0.1	8.3
$\overline{v_{app}}$ in m s^{-1}	334	381	339	372	327	359	350	395
$\sigma(v_{app})$	11	43	10	43	4	44	18	51

did not qualitatively change the ray-tracing results for IS22 (hence, this is not shown here). Single detections could certainly be the result of small-scale fluctuations, but these cannot explain the high number of detections at IS22 during winter. Therefore, the seasonal cycle of detections must rely particularly on the ground-to-thermosphere waveguide.
Figure D.14 (p. 148) shows corresponding ray-tracing examples, which prove that atmospheric absorption is weak enough to allow long-distance propagation and detection. Note that the thermospheric return heights were modeled to be lowest during winter (<110 km). The absorption rates of these returns are only around 1 dB, whereas returns from altitudes above 110 km experience absorption of 9 dB, on average. This explains the exceptionally high amount of signals detected during the absence of a stratospheric waveguide.

Overall, Table 6.3 indicates that thermospheric absorption is higher than for stratospheric wave propagation to IS36, however. The detected amplitudes at IS22 must, conse-

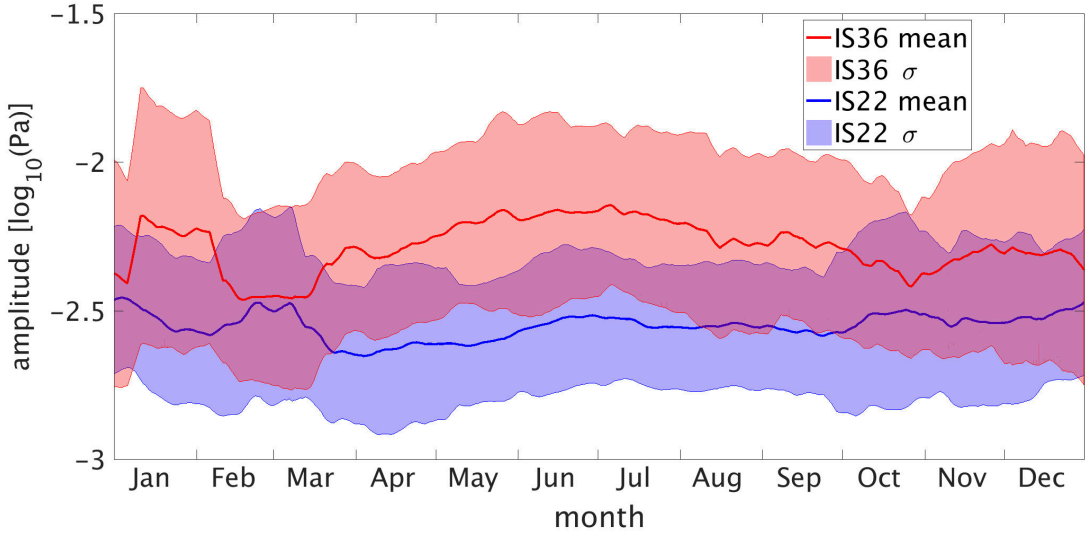

Figure 6.7: Amplitudes of detections from the New Zealand MAW hotspot are compared at IS22 ($145° < \beta < 185°$) and IS36 ($245° < \beta < 285°$). The graphs show the sliding mean and standard deviation of detected amplitudes within time windows of ±15 d. Note that the sensors differ in distance from New Zealand's South Island by around 1,300 km.

quently, be lower than at IS36. This is validated by comparing the average amplitudes at both stations throughout the year (Fig. 6.7). The IS22 mean amplitudes are relatively constant, which supports the theory that thermospheric propagation is generally relevant. The slight increase in amplitudes in summer goes along with the modeled stratospheric returns (weaker attenuation). Amplitudes detected at IS36 tend to be higher during winter, favored due to stratospheric eastward propagation; however, the second increase in amplitudes in summer is again surprising in this context, since thermospheric returns were favored. Figure D.13(a) on page 147 shows a ray-tracing result in which tropospheric ducting was modeled for one fifth of the range between source and receiver. As discussed in Chapter 3, this is rather unlikely when relying on monthly mean atmospheric conditions. Nevertheless, it coincides with quasi-negligible attenuation, and the flat elevation angle launching the ray to the thermosphere leads to downward refraction at relatively low return heights. This combination eventually results in low absorption rates. Ray-tracing provided single solutions of combined tropospheric and thermospheric ducting during December, January and February ($\overline{A_a} < 1$ dB). Bearing in mind that monthly mean atmospheric conditions were considered here, it is likely that the high summertime amplitudes in Fig. 6.7 were caused by single events of combined tropospheric and thermospheric ducts.

MAW signals originating from New Zealand were also detected at IS05 almost all year round (1,860 km to the west; $\beta = 105°$), but most detections were observed between September and May (up to 20, see Fig. D.5(b) on p. 129). During summer, only three detections (July) were superimposed by azimuthal distribution peaks from other directions (e.g., Antarctica). The ray-tracing results agreed with this, as a ground-to-stratosphere

waveguide for westward propagation was favored during summer, and only thermospheric returns were to be expected during winter. The atmospheric absorption for thermospheric ducting was lowest during winter.

At IS07 (4,250 km to the northwest; $\beta = 137°$), the number of detections at low frequencies was generally less, by about one order of magnitude (Matoza et al., 2013), because low-amplitude signals are often hidden in the noise spectrum. Given the propagation range and, thus, accumulated attenuation, peaks with only two detections were found in January (stratospheric returns) and from June to August (thermospheric returns).

The main results of the detailed analyses of the Southern Hemisphere hotspots, and conclusions with regard to questions 2 and 3 (see page 63), are:

- Detections from MAW hotspot regions were observed all year round, and were generally not limited to the presence of ground-to-stratosphere waveguides.
- The ground-to-thermosphere waveguide is essential at MAW frequencies; low absorption rates allowed long-range propagation and detections at more than 7,000 km from the sources.
- The presence of ground-to-stratosphere waveguides resulted in increased amplitudes at the receivers, leading to enhanced detection capability due to better discrimination from noise.
- MAW sources are enhanced during winter, as the number of observations is higher — taking propagation conditions into account — compared to summer.
- The source amplitudes of the Southern Hemisphere hotspots are likely not subject to seasonal variation; the seasonal variability of the detected amplitudes is primarily caused by atmospheric absorption in the different waveguides.

For the two latter conclusions, however, the source mechanism is certainly relevant (question 3). According to Section 1.4, it is obvious that source generation is somehow linked to tropospheric winds. Therefore, the wind conditions at these hotspots during MAW events are examined in the following.

6.5 Meteorological tropospheric source conditions

In the MAW hotspot regions found in the Southern Hemisphere, strong tropospheric winds prevail for most of the time. Monthly mean wind fields neither significantly differ throughout the year, nor are these appropriate for determining the source generation conditions of MAWs, which were shown to be regularly, but not continuously, detected. Therefore, the three-hourly reanalysis dataset of MERRA-2 (introduced in Section 4.3) was used to provide a high-resolution analysis of the wind conditions during MAW events. The focus here is on the detections at IS02 and IS36 because these are closest to the respective source regions, which implies that the propagation effects will be less significant. At more distant

stations, the detected amplitudes are generally lower, near the detection threshold, due to these experiencing enhanced atmospheric attenuation.

The travel times of signals originating from the southern Andes (49°S, 73°W) and New Zealand (44°S, 170°E) are shorter than the MERRA-2 time interval; for IS02, the average time for stratospheric propagation is around 36 min (at $r = 749$ km and $v_{eff} = 339\,\mathrm{m\,s^{-1}}$), and for IS36, this is around 51 min (at $r = 1{,}080$ km and $v_{eff} = 350\,\mathrm{m\,s^{-1}}$). All MAW detections were assigned the MERRA-2 time step available before the signal was recorded. (Note that taking the following, or nearest, MERRA-2 time step did not substantially change the results that are presented below.) The assumed coordinates were already used as source locations for ray-tracing in Section 6.4. Wind speed and direction at four MERRA-2 model levels, representing the 985 hPa (around 60 m above the ground – the model bottom level), 700 hPa (around 3 km), 500 hPa (around 5.5 km) and 300 hPa (around 9.4 km) levels, were obtained for the comparison with detected MAW parameters.

6.5.1 Winds during detections at IS02 from the southern Andes

Figure 6.8(a) shows that the predominant wind speed ranges from $15\,\mathrm{m\,s^{-1}}$ to $35\,\mathrm{m\,s^{-1}}$ at both 700 hPa and 500 hPa. Maxima appear at wind directions of 270°±30°, which is perpendicular to the Andes ridge. Near the ground (see Fig. D.15(a) on p. 149), the range of direction is narrower, and slightly shifted to the northwest (290°±20°). Figure 6.8(b) shows that the number of detections from westerly to northerly directions maximizes during high wind-speed conditions (20–38 $\mathrm{m\,s^{-1}}$) at the considered source location. The corresponding back-azimuth is between 320° and 330°, which actually covers the considered source location and, for example, the high mountain peak of Monte Fitz Roy (3,405 m). MAWs originating from the Antarctic Peninsula ($\beta = 170°$) are preferentially detected when the wind over the southern Andes is slower than $15\,\mathrm{m\,s^{-1}}$.

Figure 6.9 only considers those detections that originate from the southern Andes (i.e., $270° < \beta < 45°$). The distributions of the assigned wind speeds vs wind directions (Fig. 6.9(a) and Fig. D.16(a) on p. 150) do not show a significant difference from the climatological wind conditions (Fig. 6.8(a)) at all altitudes. So, it appears that the distribution maxima are a product of coincidence resulting from the mean conditions.

The mean wind conditions at all altitudes do not significantly vary by season; for instance, the annual mean wind speed at the 700 hPa level is $19.5\,\mathrm{m\,s^{-1}}$ ($\sigma = \pm 9.2\,\mathrm{m\,s^{-1}}$), and the monthly means differ only by a maximum of $2\,\mathrm{m\,s^{-1}}$. Therefore, it can be concluded that the preconditions for MAW source generation are consistent throughout the year if these are decisively related to tropospheric winds. The RMS amplitudes (Fig. 6.9(b)) increase with wind speeds at 700 hPa and around 60 m above the ground (Fig. D.16(b), p. 150), which also applies to the 850 hPa level (not shown). The slopes representing the most frequently detected amplitude per wind speed interval (yellow) incline with increasing altitude (500 hPa and 300 hPa); hence, the correlation between wind speed and MAW amplitude is strongest in the altitude range of the orographic obstacle.

However, the seasonal variation in MAW amplitudes detected at IS02 cannot be explained by the variation in cross-mountain winds. Figure 6.10 shows that the detected

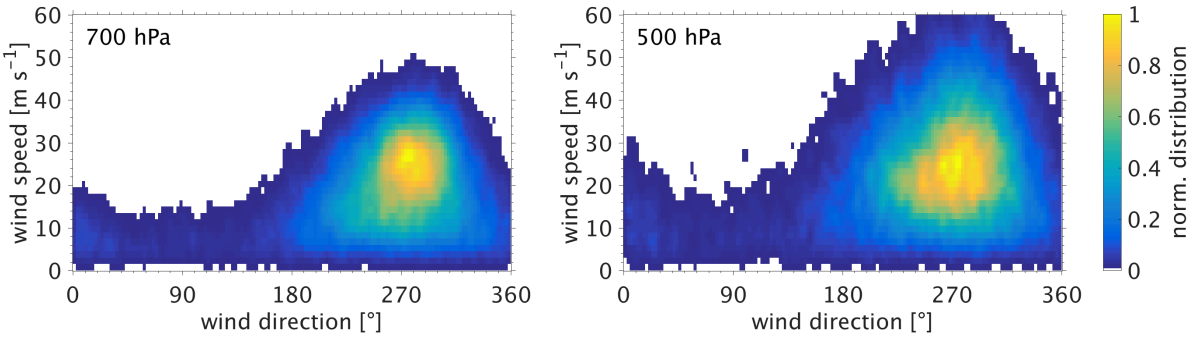

(a) Climatological distribution of MERRA-2 wind speeds vs wind directions (2004–2017).

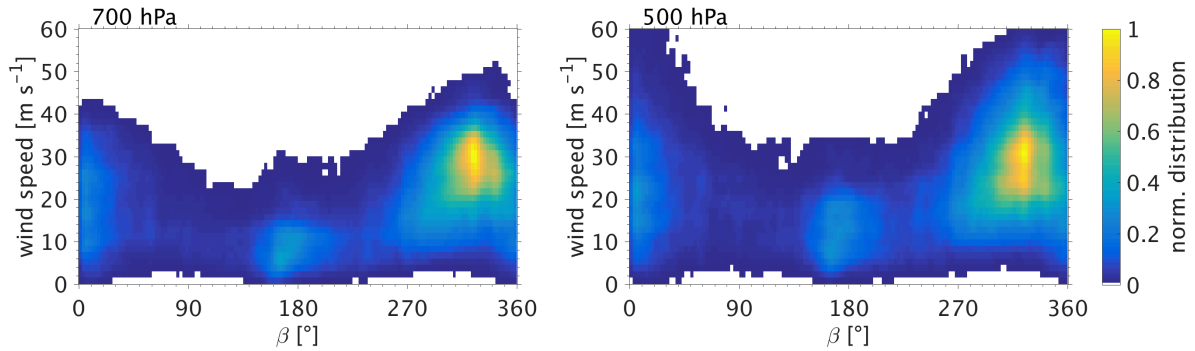

(b) Distribution of wind speeds (Andes) vs all back-azimuths of MAW detections at IS02.

Figure 6.8: Evaluation of MERRA-2 tropospheric winds at 700 hPa (left-hand column) and 500 hPa (right-hand column) at a source in the southern Andes (49°S, 73°W). The grid intervals are 2.5° (β and wind direction) and 1.5 m s^{-1} (wind speed). The distributions are normalized by the respective maximum values.

RMS amplitudes maximize during winter (around 21 mPa in June, $\sigma = \pm 15$ mPa) and are lowest in summer (7 mPa in February, $\sigma = \pm 5$ mPa). The mean event-related wind speed is generally higher (up to 5 m s^{-1}), compared to the climatological value, but this difference is consistent throughout the year. The maximum event-related wind speed nearly equals the climatological value during winter and is lower (around 5 m s^{-1}) during summer. This varying difference qualitatively corresponds with the annual variation in amplitude. However, the climatological mean and maximum cross-mountain winds are not enhanced during any particular season. Moreover, the occurrence frequency of strong cross-mountain winds exceeding 15 m s^{-1} (see Fig. D.17 on p. 151) is reduced during winter (around −20 %), which is contradictory to the seasonal variation in the number of MAW detections originating from the southern Andes (Section 6.4).

For New Zealand (see Section D.5, p. 152), the distribution of wind speeds vs MAW back-azimuths detected at IS36 peaks at higher wind speeds (>15 m s^{-1}) than the climatological wind distribution (<15 m s^{-1}). This is a possible explanation for fewer detections from this hotspot (around 10^4), compared to the southern Andes and IS02 (around 10^5).

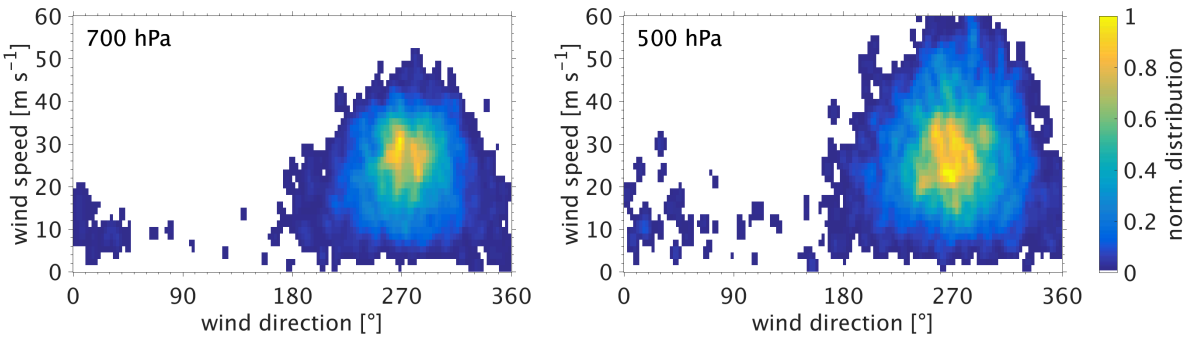

(a) Distribution of wind speeds vs wind directions during selected MAW events.

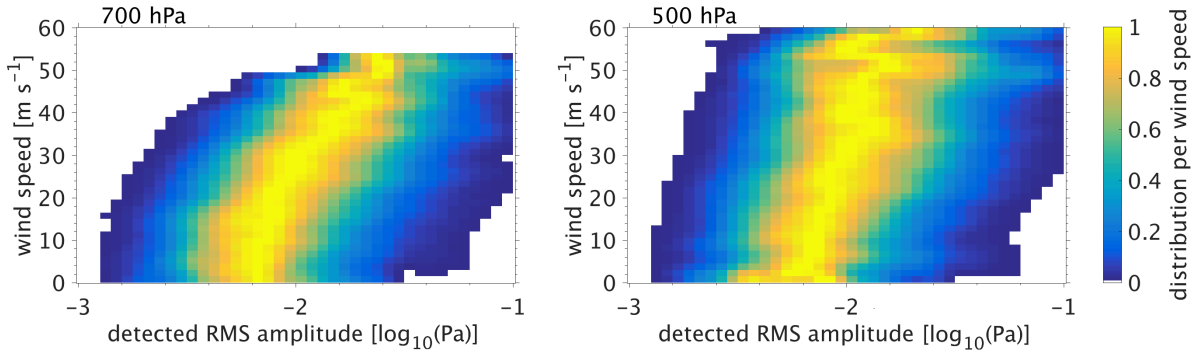

(b) Distribution of wind speeds vs MAW amplitudes.

Figure 6.9: Similar to Fig. 6.8, but only considering detected MAWs with back-azimuths between 270° and 45°, which correspond to the southern Andes; 102,847 detections remained. The grid interval for the RMS amplitude is 0.05 $\log_{10}$(Pa). The distribution in (b) is normalized per wind speed interval, showing a correlation between amplitude and wind speed. Note that, for the upper and lower wind intervals, fewer detections might infer uncertainties in the wind-normalized distributions.

The correlation between wind speeds at the source and MAW amplitudes detected at IS36 is qualitatively comparable to that for IS02. Accordingly, neither the seasonal variation in amplitude (see Fig. D.22, p. 156) nor the occurrence frequency of detected MAW events can be explained by the variation in cross-mountain winds (see Fig. D.23, p. 157).

As a consequence, enhanced cross-mountain winds alone cannot be the sole reason for MAW occurrence. On the other hand, the positive correlation between cross-mountain wind and RMS amplitude indicates at least some role of the winds in the process chain leading to MAW occurrence. With regard to orographic GW occurrence, which is analyzed in Section 6.6, static stability is considered to be a possible quantity for the excitation of MAWs.

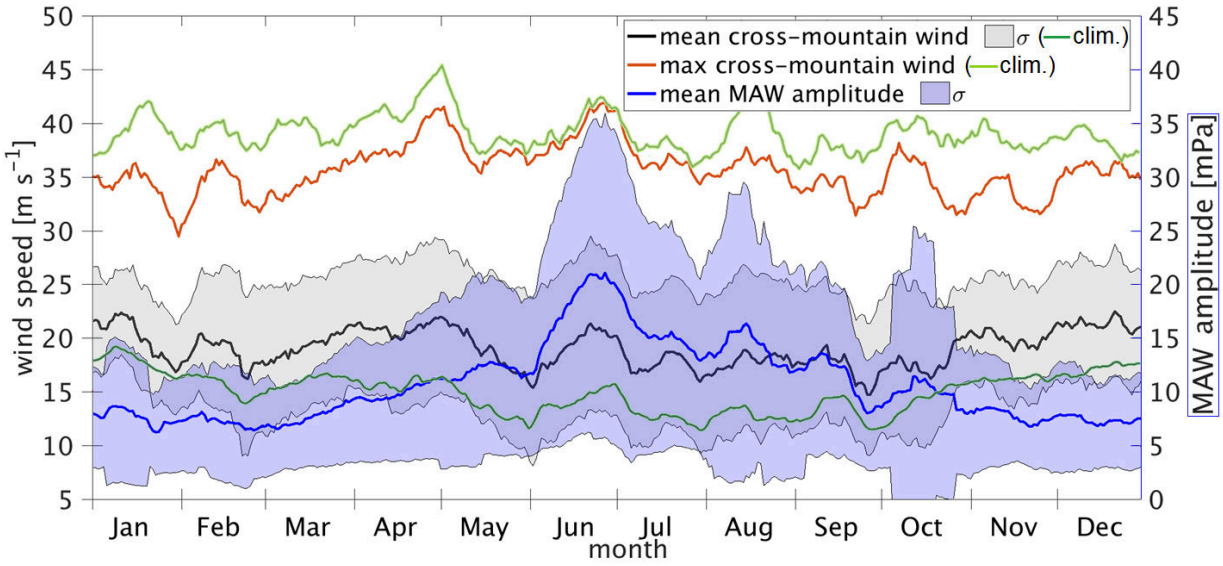

Figure 6.10: Annual variation in the amplitudes of MAWs (IS02) and cross-mountain winds (directional wind components between 225° and 315°) at 700 hPa (southern Andes). For each day of the year, the event-related mean (black) and maximum (orange) MERRA-2 cross-mountain winds were calculated for MAWs originating from the Andes. The green curves depict the respective climatological daily mean and maximum values from 2004 to 2017. A moving-average filter was applied to the results, using a span of 15 d.

6.5.2 Static stability during detections at IS02 from the southern Andes

A common measure for quantifying atmospheric static stability is the Brunt-Väisälä frequency, N_B. Here, this is calculated using MERRA-2 temperature data (T), according to the following formula (e.g., Andrews, 2010):

$$N_B^2 = \frac{g}{T}\left(\frac{\mathrm{d}T}{\mathrm{d}z} + \frac{g}{c_p}\right) = \frac{g}{T}\left(\frac{\mathrm{d}T}{\mathrm{d}z} + \frac{9.8\,\mathrm{K}}{1000\,\mathrm{m}}\right) \quad , \tag{6.1}$$

where g is the acceleration due to the Earth's gravity ($g = 9.81\,\mathrm{m\,s^{-2}}$) and c_p denotes the heat capacity under constant pressure ($c_p = 1{,}005\,\mathrm{J\,kg^{-1}\,K^{-1}}$). If $N_B^2 > 0$, a real solution for N_B exists; this is when the atmosphere is stably stratified. Figure 6.11 shows the annual distribution of N_B^2 near the ground (approximately 120 m) and at 850 hPa. Above the latter level, the distribution is relatively uniform throughout the year, so that $\overline{N_B^2} = 2 \cdot 10^{-4}\,\mathrm{s^{-2}}$.

Near the surface, an annual cycle in N_B^2 can be identified. Statically unstable conditions typically occur during summer, due to the heating of the surface that leads to a more negative temperature gradient ($\mathrm{d}T\,\mathrm{d}z^{-1} < -9.8 \cdot 10^{-3}\,\mathrm{K\,m^{-1}}$). During winter, the atmosphere is generally stably stratified, allowing greater values of N_B^2. This annual cycle diminishes with altitude; at the 850 hPa level (1.1 km), the mean value is almost constant throughout the year ($N_B^2 \approx 2 \cdot 10^{-4}\,\mathrm{s^{-2}}$). Figure 6.11 indicates that MAWs were mainly

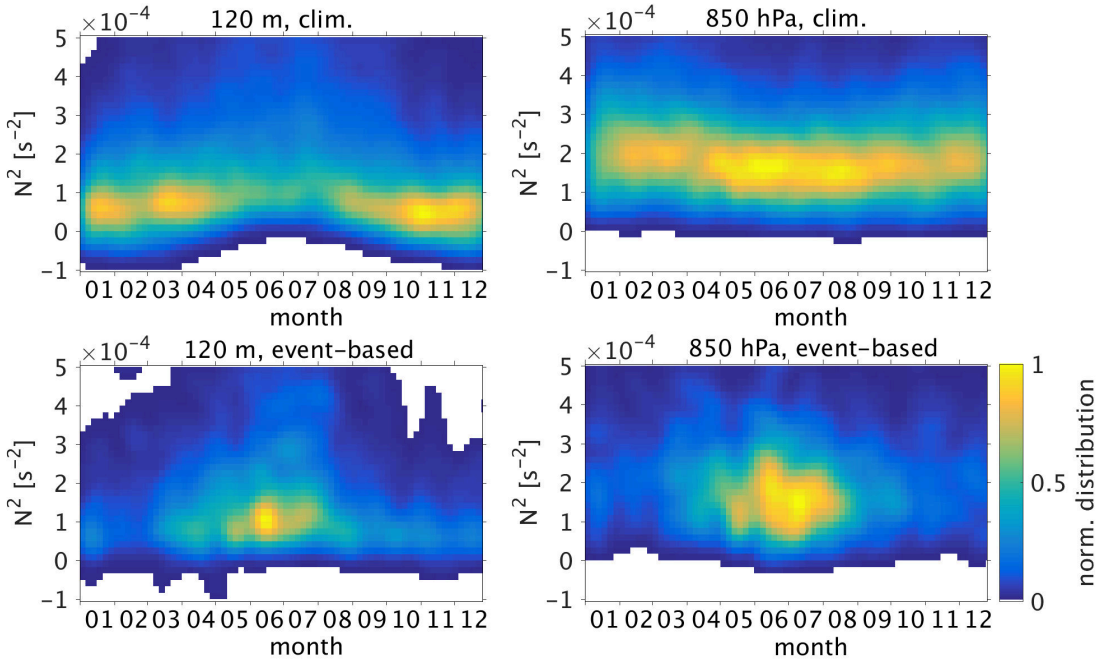

Figure 6.11: Climatological (top) and event-based (bottom) evaluation of the squared Brunt–Väisälä frequency (Andes/IS02). N_B^2 was calculated between the first and second model levels (approximately 120 m altitude, left-hand column) and at 850 hPa (right-hand column). Each distribution was normalized by its respective maximum value.

detected during stable conditions at both altitude levels; beyond that, however, the event-based distributions mainly reflect the annual variation in the number of detections and the occurrence frequency of N_B^2. A correlation between MAW occurrence and larger values of N_B^2, for instance, is not evident. Moreover, a correlation between the MAW amplitude and N_B^2 has not been found (not shown).

Based on the analysis of tropospheric winds and static stability, the conclusions regarding question 3 (see page 63) are:

- MAWs originating from the southern Andes and New Zealand hotspots are most frequently detected during synoptic conditions that result in flows perpendicular to the mountain ranges, mainly when strong wind speeds (20–40 m s^{-1}) occur at altitudes below the 500 hPa level. The mean wind conditions over the southern Andes are more favorable than those over New Zealand, thus explaining the differing number of detections by around one order of magnitude.
- The detected MAW amplitudes correlate with the magnitude of the winds in the vertical range of the orographic obstacle and, to some extent, above that.
- The (cross-)mountain winds alone cannot be the sole reason for the seasonal variation in MAW occurrence. Since the MAW sources are assumed to be enhanced during

winter (Section 6.4), the source generation mechanism requires an additional process or quantity.

- MAW occurrence (or detection) appears to require stable stratification of the boundary layer, but this does also not fully explain the seasonal variation in MAWs.

The question which additional physical processes could be involved in the source generation mechanism is discussed in Section 6.7. Given the correlation between MAW amplitude and wind speed (Figs. 6.9(b)), as well as stable stratification presumably required, the preconditions for MAW excitation are similar to those for orographic GW excitation (Chapter 1).

6.6 On the link between MAW and GW source regions

Both the southern Andes and New Zealand are well-known source regions of orographic GWs that propagate into the stratosphere and mesosphere (McLandress et al., 2000; Fritts and Alexander, 2003; Alexander and Teitelbaum, 2011; De la Torre et al., 2012; Kaifler et al., 2015; Hoffmann et al., 2016). A comparison of the global MAW source regions with recently published maps of GW occurrence in the stratosphere (e.g., those from Alexander et al., 2008a; Hoffmann et al., 2013) indicates the coincidence of both phenomena. This was studied in more detail so as to assess the question of whether the source mechanism of MAWs could be linked to that of orographic GWs.

6.6.1 Datasets used for comparison

The IMS infrasound network was used to study atmospheric wave phenomena on a global scale. Solar tides (Hupe et al., 2018, see Chapter 4) and GWs (Marty et al., 2010) were analyzed, as determined from absolute pressure data from the IMS infrasound network. Efforts were made to automatically detect GWs in differential pressure data by adapting the PMCC algorithm to lower frequencies (Blanc et al., 2019; Marlton et al., 2018, 2019). An overview of such GW detections at all of the IMS stations is given in Fig. 6.12 for 2009 to 2017. Obviously, the main azimuthal directions follow a clearer pattern, with respect to the latitude, than those observed for MAWs (Fig. 6.1). The detections were mainly attributed with back-azimuths that follow the tropospheric wind directions; hence, the prevailing signatures originated from coherent waves, which were embedded in the mean flow. These might also originate from coherent noise. As demonstrated in Chapter 4, the annual pressure amplitude is larger at mid-latitudes (e.g., around 30 hPa at IS26) than at tropical latitudes (of the order of 5 hPa). Consequently, winds, and thus noise due to winds, are also enhanced at middle and high latitudes. In general, the detected signals in the range of GWs are constrained to periods up to 3 h, as mentioned in Section 2.1.2; however, the current PMCC GW configuration has a bias towards periods of around 1 h. The apertures of the infrasound arrays presumably limit the detectability in terms of wavelength. GWs induced by deep convection at low latitudes are characterized by short horizontal

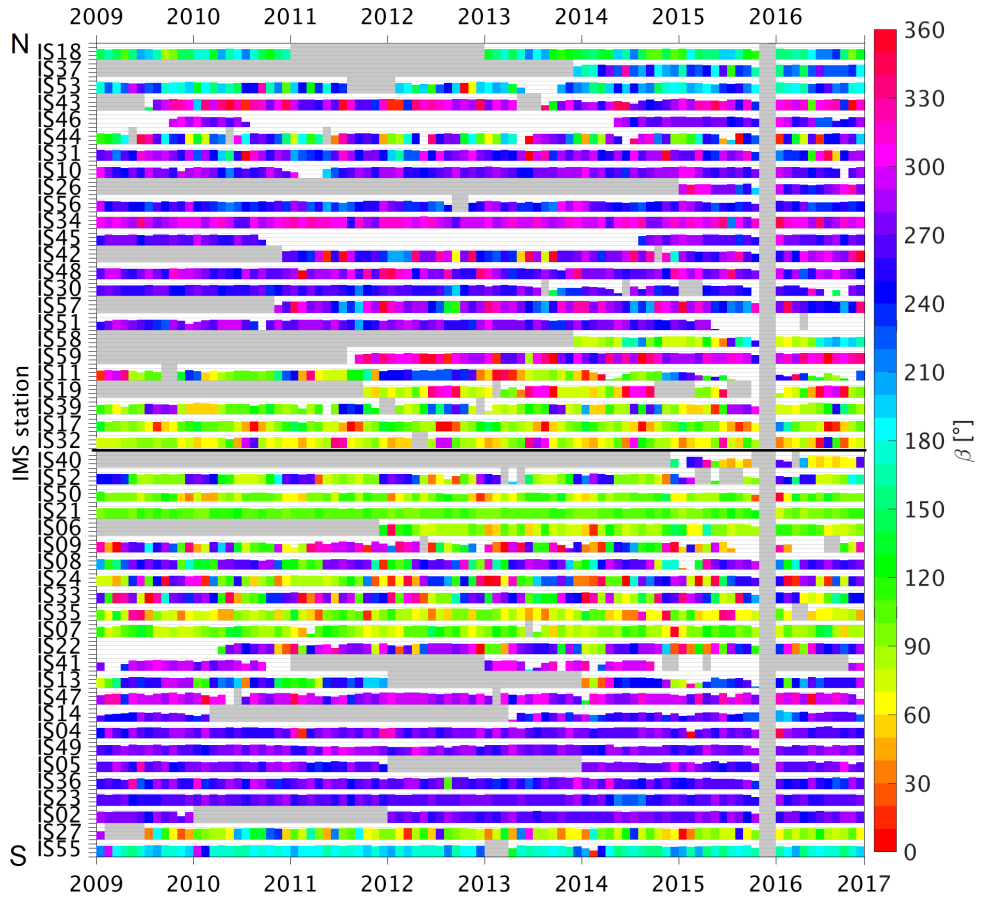

Figure 6.12: The monthly number of PMCC GW detections between 2009 and 2017 is shown for all IMS station datasets available at the German NDC. The stations are sorted from north (top) to south. The logarithmic scale ranges from 10^0 to 10^4 detections at each station; 10^3 detections were not exceeded. The color codes the monthly mean back-azimuth; gray boxes indicate missing data or a lack of PMCC results.

wavelengths (Ern et al., 2011) and various phase velocities (Fritts and Alexander, 2003). Detections at tropical stations, where the noise level is lower, best represent portions of GWs related to deep convection, as has been shown for IS17 (Blanc et al., 2018; Marlton et al., 2019).
Orographic GWs are observed in the lees of mountains (e.g., De la Torre et al., 2012; Hoffmann et al., 2016). Their characteristic horizontal phase velocities are generally around zero (Fritts and Alexander, 2003; Alexander et al., 2010). Consequently, the GWs detected at infrasound stations, if at all orographically induced, originate from nearby sources upstream of the receivers. At this point, it should be clear that a cross-bearing approach for GWs is obsolete.

For the aforementioned reasons, the MAW source regions identified in Sections 6.2 and 6.3 were compared with global GW activity that was derived from satellite observa-

tions. First GW observations using satellites were reported by Fetzer and Gille (1994). Eckermann and Preusse (1999) first analyzed orographic GWs in temperature variances from satellite data, including GW activity over the southern Andes. An overview of follow-up studies was given by Preusse et al. (2008). Recent global analyses of GW parameters have provided comprehensive climatologies on stratospheric GW parameters, such as absolute GW momentum fluxes (GWMF) and GW potential energy (GWPE) (Alexander et al., 2008a,b; Hoffmann et al., 2013, 2014, 2017). Orographic GWs are parameterized in ECMWF datasets. Comparisons with radio occultation data on a global scale, supported by lidar observations in Europe, led to the conclusion that GWs were better resolved in the ECMWF HRES operational analysis than in ERA-interim data (Rapp et al., 2018). Jewtoukoff et al. (2015) found good spatial and temporal agreement between stratospheric balloon observations and ECMWF HRES analyses at high southern latitudes, although the model underestimated GWMF. A comprehensive campaign — DEEPWAVE — was dedicated to GW observations over New Zealand, incorporating airborne and ground-based measurements (Fritts et al., 2016, 2018; Bramberger et al., 2017), such as lidar (Kaifler et al., 2015; Ehard et al., 2017a).

GRACILE: GW parameter climatologies from satellite data

Ern et al. (2017) produced the global GW climatology based on atmospheric infrared limb emissions observed by satellite (GRACILE). GRACILE provides zonal averages and global maps of GW parameters in the middle atmosphere, and is derived from the High-Resolution Dynamics Limb Sounder (HIRDLS) and the Sounding of the Atmosphere using Broadband Emission Radiometry (SABER) instruments on-board different satellites (Ern et al., 2018). The HIRDLS dataset is limited to three years of observations (March 2005 to February 2008), whereas GRACILE's SABER dataset is based on 13 years (February 2002 to January 2015). The GRACILE data include GW parameters, such as temperature variances, GWPE and GWMF.

For the comparison with global MAW hotspots, global maps of GWMF, based on SABER, were used, since the period under consideration roughly matched that of the IMS dataset (2003–2017). GRACILE provides the global data as monthly means per vertical bin of 10 km and per horizontal bin of 30° longitude times 20° latitude. The horizontally overlapping bins are centered on a 10° x 5° grid, and at vertical intervals of 10 km between the middle stratosphere and the mesopause (30–90 km). The latitudinal range permanently extends from 50°S to 50°N. In addition, latitudes up to 80° north and south are alternately covered, depending on the SABER viewing mode (Ern et al., 2018).

Figure 6.13 shows GWMF at two altitude levels for January. Increased values are found in the subtropics, due to deep convection during summer, and at middle to high latitudes during winter. The latter feature multiple GW sources, including jet-stream instabilities, fronts and orography (e.g., Ern et al., 2011). The decrease in GWMF with altitude is related to GW dissipation; this effect is weaker at low latitudes (Ern et al., 2018).

MAW hotspots were compared with GWMF at the lowest available level (i.e., 30 km). Instead of the absolute GWMF, its deviation from the zonal mean was considered; thus,

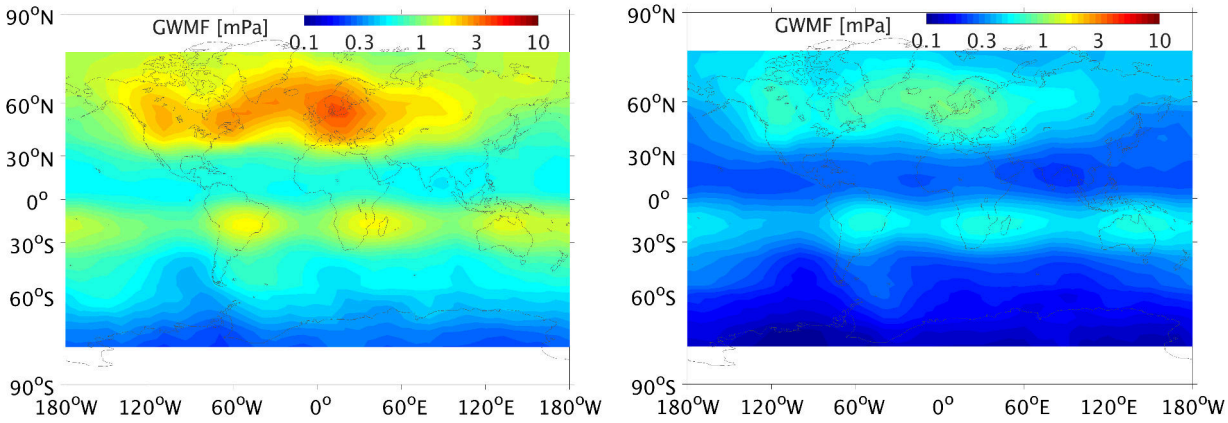

(a) $z = 30\,\mathrm{km}$ (b) $z = 40\,\mathrm{km}$

Figure 6.13: Absolute GWMF (January) based on SABER, reproduced from the GRACILE dataset provided by Ern et al. (2017).

positive deviations indicate enhanced GW activity, presumably originating from the troposphere.

Lightning data for identifying GW hotspots related to deep convection

Although Fritts and Alexander (2003) noted that the theory of GW excitation by convection is relatively complex, given the wide range of intrinsic frequencies and phase speeds observed, convection is well accepted as a GW source at low latitudes. To distinguish GW source regions related to deep convection and represented by GRACILE, a high-resolution monthly climatology (HRMC) of lightning activity was taken into consideration herein. Cecil (2015) provided gridded monthly flash rates, composed of data from two satellite-based detectors — the Optical Transient Detector (OTD) and the Lightning Imaging Sensor (LIS). The HRMC is given on a $0.5^\circ \times 0.5^\circ$ grid as the mean flash rate per square kilometer and day in the middle of a month (Cecil et al., 2014). The HRMC database is based on 5 years for the OTD and more than 10 years for the LIS. The LIS was limited to low latitudes up to 38°; however, a combination of both instruments allows global coverage.

Here, monthly flash rates lower than $2\,\mathrm{km}^{-2}$ were excluded for reasons of significance and clarity.

6.6.2 Comparison and discussion of MAW and GW source regions

GWMF and lightning activity are color-coded in Fig. 6.14. Monthly MAW hotspots are depicted as black contour lines, which reflect all of the source regions of Fig. 6.5. Comparisons are supported by the wind field of ECMWF operational HRES analyses at the

500 hPa level, calculated as monthly means for the period 2007 to 2016. As an indication of strong winds at the 500 hPa level, the green contour line represents mean wind speeds of $20\,\mathrm{m\,s^{-1}}$.

Low latitudes

McLandress et al. (2000) already found a strong correlation between stratospheric GW variances and deep convection at subtropical latitudes. Here, it can be anticipated that enhanced lightning activity would generally match enhanced GWMF in the tropics and subtropics. The extent of those regions is related to deep convection in the Intertropical Convergence Zone. The hotspot allegedly found in the **central USA** between May and August coincides with enhanced flash rates and GWMF, which are related to deep convection; hence, the association of the detected infrasonic signals with severe storms (Section 6.3) has been confirmed.

Southern Hemisphere

In their comprehensive review of GWs in the middle atmosphere, Fritts and Alexander (2003) stated that GW variances peak at middle to high latitudes in winter. This finding was based on different observation techniques, such as radiosondes and satellites. McLandress et al. (2000) found a strong correlation between GW variances and topography at mid-latitudes, particularly over the **southern Andes**. Their observations are in line with the dataset of Ern et al. (2017), according to which the Andes hotspot features the global GWMF maximum. GWMF is strongly enhanced from April until October, and agrees with the determined MAW source regions. In addition, GWMF is slightly enhanced in March and November, which principally also corresponds to the pattern exhibited by the identified MAW source regions.
During November and December, convective activity, indicated by enhanced flash rates, extends to around 40°S, partly matching the determined MAW source regions. Satellite observations evaluated by Hoffmann et al. (2013, figs. 6 to 10) show that slightly enhanced GW activity at the southern tip of the continent during summer is likely related to convection; however, reports of severe storms, including tornadoes, in southern Argentina or Chile are unknown. Moreover, the dominant back-azimuth of detections at IS02 ($\beta = 315°$) is not shifted to the north (i.e., towards the maximum flash rates), but rather agrees with the dominant back-azimuths of the other months. Therefore, it can be assumed that the majority of detections in the MAW frequency range actually originated from MAW sources. Fewer detections at fewer surrounding stations (Section 6.3) might have caused more imprecise cross-bearing results, compared to winter.

In Fig. 6.14, MAW activity over **New Zealand** is only pronounced in November, but MAWs were observed all year, as discussed in Section 6.4. Hoffmann et al. (2016) clearly identified New Zealand as one of the strongest hotspots of orographic GWs in the Southern Hemisphere. They determined orographic GW hotspots by evaluating upstream and downstream variances in temperature perturbations at about 40 km altitude in 10-year

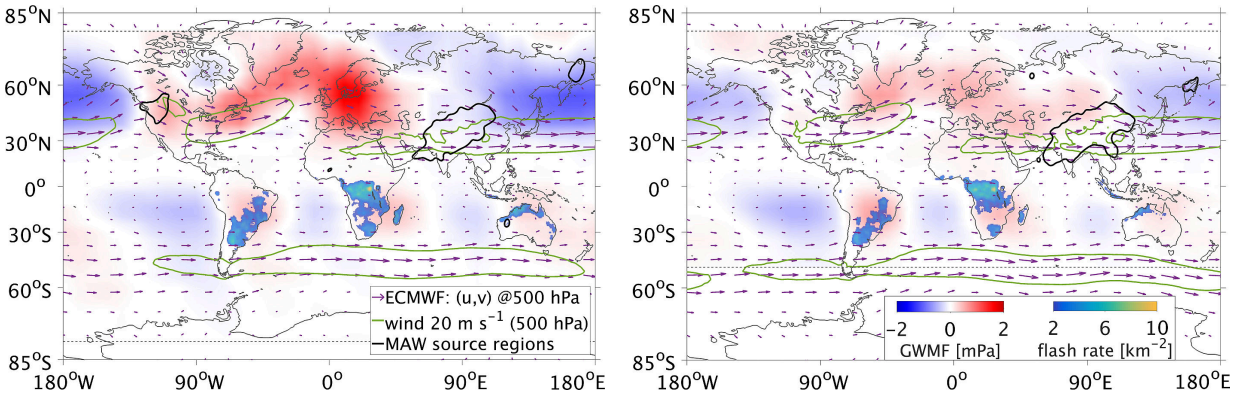

(a) January. (b) February.

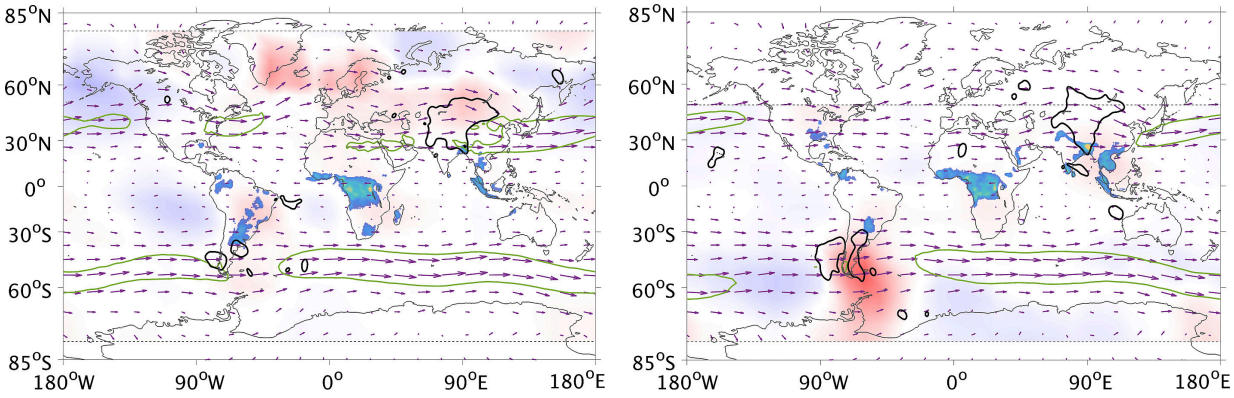

(c) March. (d) April.

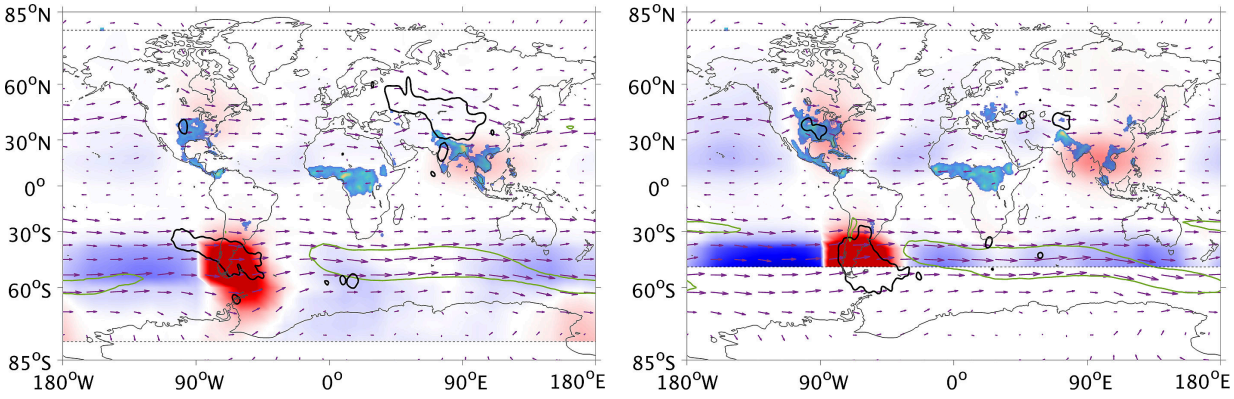

(e) May. (f) June.

Figure 6.14: Comparison of GWMF from GRACILE/SABER (Ern et al., 2017) with MAW hotspots as identified in Fig. 6.5 (MAW contours represent the threshold of 0.05 normalized cross-bearing hits). Supporting information comprises lightning activity (Cecil, 2015) and ECMWF wind fields from the IFS (ECMWF, 2014). GWMF data are shown as deviations from the zonal mean GWMF. Dashed lines denote the latitudinal coverage of GRACILE data, which depends on the alternating viewing mode of SABER.

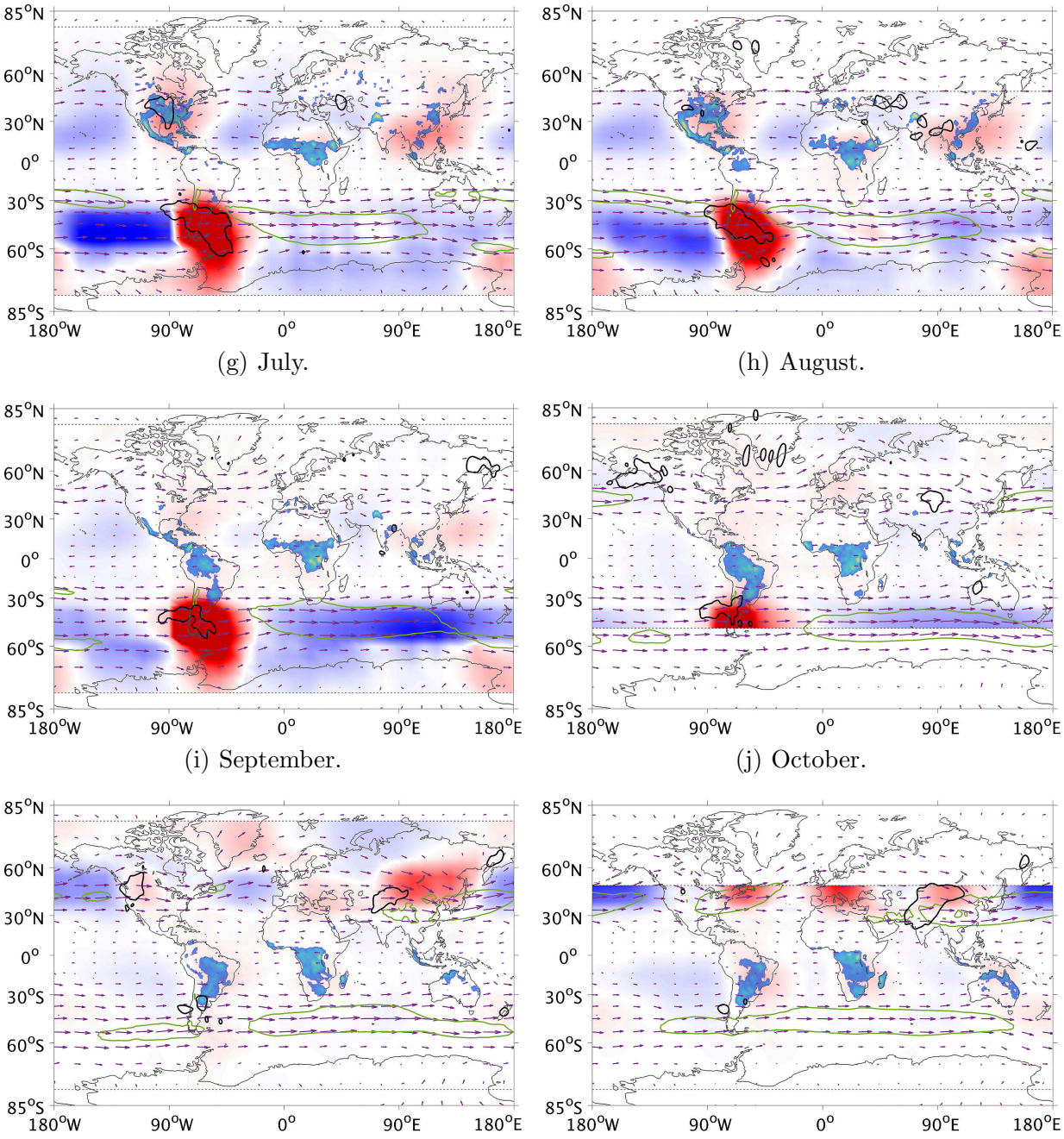

(g) July. (h) August.

(i) September. (j) October.

(k) November. (l) December.

Figure 6.14: (cont.) The best GRACILE (SABER) coverage is provided in alternating months (left-hand panels).

high-resolution satellite observations. GRACILE data do not highlight New Zealand by strongly enhanced GWMF, however, either in absolute GWMF data or in zonal perturbations of GWMF.
One reason for this is the coarse resolution of the horizontal bins used in the GRACILE climatology (30° x 20°). Another reason is the peculiarity of the atmospheric conditions over New Zealand. Kruse et al. (2016), referring to GW measurements and model simulations during the DEEPWAVE campaign, pointed out a climatological feature termed the 'valve layer', which controls the vertical propagation of GWMF into the middle stratosphere during winter. This layer is characterized by a wind speed minimum at altitudes of between 15 km and 25 km above an upper-troposphere wind maximum (Kruse et al., 2016). The weakening wind speed causes the vertical wavelength of a GW to become smaller, resulting in a steepening wave. If the initial GW amplitude is large, the GW is ultimately forced to break, depositing the transported momentum. The valve layer especially affects large-amplitude GWs induced by strong tropospheric forcing, whereas small-amplitude GWs (with weak GWMF) can propagate through this layer without breaking, causing large amplitudes in the mesosphere (e.g., Kaifler et al., 2015; Bramberger et al., 2017).

Figure 6.15 shows examples of monthly mean zonal wind speed profiles over the southern Andes (blue) and New Zealand (orange) in January (dashed line) and July (solid line). Over both regions, a critical level (where $\overline{u} = 0\,\mathrm{m\,s^{-1}}$) exists at around 22 km during January, filtering upward-propagating orographic GWs in the lower stratosphere (e.g., Kaifler et al., 2015). A difference between the vertical propagation conditions is evident in

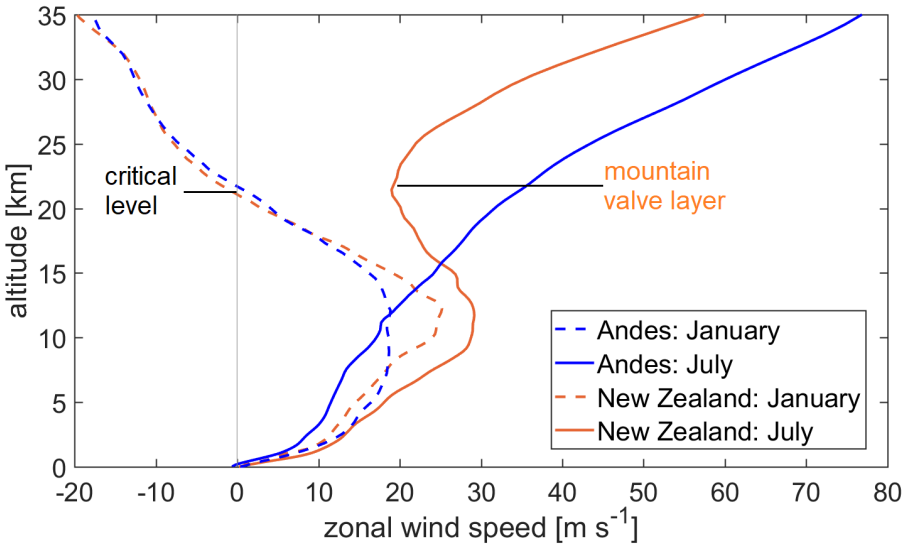

Figure 6.15: Monthly mean zonal wind speed profiles over the Andes (49°S, 73°W) and New Zealand (44°S, 170°E) in January and July 2016. Data were calculated from the ECMWF HRES analyses at the grid points equal to those previously considered to be MAW source regions. Over New Zealand, the valve layer can be recognized by a wind minimum between 15 km and 25 km during July.

July. While the vertical wind-speed gradient over the southern Andes is entirely positive in the considered altitude range, the zonal wind speed over New Zealand exhibits a maximum at 12 km ($\overline{u} = 28\,\mathrm{m\,s^{-1}}$), reflecting the jet-stream near the tropopause, and minimizes below 25 km ($\overline{u} = 18\,\mathrm{m\,s^{-1}}$).

The valve layer between 15 km and 25 km explains the GW activity over New Zealand during winter being unresolved in the GWMF data in GRACILE, the lowest level of which is at 30 km. During summer, the critical level filters any upward-propagating orographic GWs. This does not exclude that orographic GWs can be induced in the troposphere; for instance, orographic GW events have been sporadically observed during recent measurements using CORAL in the lee of the southern Andes in late summer (Kaifler and Kaifler, 2018; Kaifler, 2018b).

At high latitudes, two regions of enhanced GWMF can be found over the Antarctic Peninsula and the Transantarctic Mountains in the east (74°S, 162°E). Both are strong source regions of orographic GWs in the Southern Hemisphere (Hoffmann et al., 2013, 2016; Jewtoukoff et al., 2015). MAW signals that can be related to the Antarctic Peninsula were detected at IS02 ($\beta = 170°$) and IS27 ($\beta = 250°$) during spring and autumn. MAWs originating from the direction of the Transantarctic Mountains were detected at IS05 ($\beta = 200°$) and IS36 ($\beta = 180°$) during winter. As mentioned in Section 6.4, the relatively coarse distribution of IMS arrays at high latitudes prevents the obtaining of enough cross-bearing results to highlight these hotspots.

Northern Hemisphere

The MAW hotspot of the northern **Rocky Mountains** agrees with enhanced GWMF in January and November. In October, the main MAW activity is located further north, despite the reduced wind speeds and neutral GWMF. Hoffmann et al. (2017) noted that stratospheric GW observations over the Rocky Mountains were rare because low stratospheric wind speeds prevent GWs from propagating upward in this region. This agrees with the example of monthly mean zonal wind speeds during January and July 2016, shown in Fig. D.24 on page 158.
Obviously, positive GWMF perturbations that are detached from lightning activity cover large scales of middle and high latitudes during winter. This agrees with previous global observations that have determined GW hotspots in Scandinavia (e.g., Rapp et al., 2018), Greenland (Leutbecher and Volkert, 2000; Limpasuvan et al., 2007) and the UK (Hoffmann et al., 2013, 2017). Lidar measurements have proved that the Scandinavian Mountains are a potential source of orographic GWs (Ehard et al., 2016; Wagner et al., 2017). It was stated in Section 6.2 that pairs of IMS infrasound stations detect MAWs that can be associated with those regions. However, the station coverage, the multitude of possible sources and the dominance of the hotspot over central Asia complicate determinations of other hotspots in the Northern Hemisphere using the described cross-bearing approach.

The most prominent hotspot of MAW detections over the **Tibetan Plateau** coincides with GWMF that is rather enhanced over the Altai Mountains, north of the Tibetan Plateau, than over the Himalayas. Strong winds occur all year round over the entire region;

the indicated threshold of 20 m s^{-1} at the 500 hPa level is exceeded over the Himalayas between November and March, when the MAW hotspot is most pronounced. Contrarily, the strongest GWMF perturbations are found over Europe (Scandinavia), especially in January. For an explanation of the only slightly enhanced GWMF over central Asia, refer to Zeng et al. (2017), who evaluated satellite data from the lower stratosphere (15–30 km) during 2007 to 2015. They explicitly focused on the Tibetan Plateau and found orographic GWs during winter and spring. In agreement with Alexander et al. (2008b), who found enhanced GWPE up to the tropopause, upward-propagating GWs were generally filtered at levels of low wind speed below 30 km altitude.
Herein, a source region is considered at the western border of China, west of the Tibetan Plateau, where zonal winds cross a range of the Pamir Mountains that are up to 7,649 m high. Figure 6.16 shows a strong tropospheric wind-speed maximum of around 30 m s^{-1} between altitudes of 8 km and 10 km during both January and July 2016. The minimum wind speed in the valve layer amounts to 13 m s^{-1}. The critical level is at around 15 km during summer. Consequently, the excited GWs do not reach altitudes that are represented by the GRACILE dataset. Similarly to New Zealand, this MAW hotspot appears to be linked to orographic GW occurrence, limited to the troposphere.

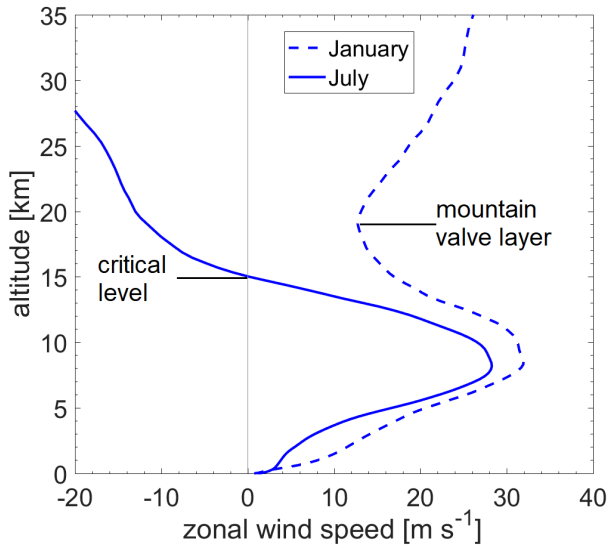

Figure 6.16: Monthly mean zonal wind speed profiles over the Pamir Mountains (38°N, 75°E) in the west of the Tibetan Plateau during January and July 2016. At the chosen location within the large potential source region, the zonal wind best approximates the cross-mountain wind. Data were calculated from the ECMWF HRES analyses. The valve layer (January) and the critical level (July) are clearly recognizable.

The MAW hotspot over the **East Siberian Mountains** is the only one at which GWMF is generally reduced. Despite the issues of high-latitude detections, as mentioned above, the number of cross-bearing hits here is significant during winter. Hoffmann et al. (2017) actually identified the East Siberian Mountains as a potential source of orographic

GWs. Critical levels exist during both January (around 13 km) and July (around 20 km); a weak westward flow ($\overline{u} = -6\,\mathrm{m\,s^{-1}}$) prevails in the winter troposphere (Fig. D.25, p. 158).

6.6.3 Annual variation of zonal mean MAW and GW activity

Estimations of zonal MAW and GW activity are given in Fig. 6.17. MAW activity is based upon the number of cross-bearing hits per 3° x 3°, as described in Section 6.2. Monthly mean differences from the annual zonal mean per 3° of latitude are shown, normalized by the overall maximum, resulting in fluctuations around zero. Consequently, positive (negative) values indicate enhanced (reduced) MAW activity compared to the zonal mean, and the global maximum is reflected by one. Zonal mean GW activity was calculated accordingly, using GWMF of the GRACILE dataset at 30 km (Fig. 6.17(b)).

The annual variation shows good qualitative agreement between MAWs and GWs. A reason for the qualitative differences in the Northern Hemisphere and at high latitudes, in general, is the distribution of the IMS infrasound stations relative to potential orographic MAW and GW source regions. Tropical activity is naturally not represented in the MAW data, but both MAW and GW activity exhibit similar patterns at mid-latitudes, especially in the Southern Hemisphere. In the Northern Hemisphere, MAW activity is strongest from December to May, and GW activity peaks at slightly higher latitudes during November to March. Both MAW and GW activity are reduced during summer.

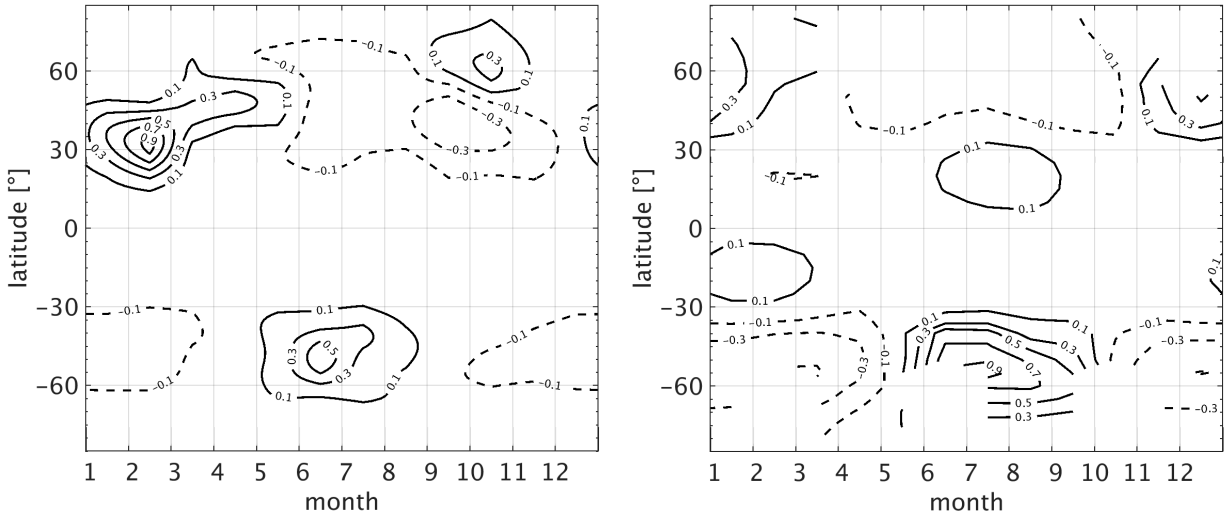

(a) MAWs. (b) GWMF at 30 km altitude.

Figure 6.17: Comparison of the annual variability of zonal mean MAW hotspots and zonal mean stratospheric GWMF. Variability is reflected as deviation from the zonal mean, normalized by its absolute maximum. (a) MAW source regions, as deduced from the cross-bearing hits shown in Fig. 6.5. (b) Stratospheric GWMF at 30 km altitude, as deduced from GRACILE's global map data (e.g., Fig. 6.13(a)).

According to the GRACILE data, the strongest GW activity is reflected by the southern Andes. GRACILE does not account for the potential source of orographic GWs over the Tibetan Plateau due to the valve layer present in the lower stratosphere (Fig. 6.16). The Tibetan Plateau is the most prominent MAW hotspot in the Northern Hemisphere instead, which explains the quantitative differences in Fig. 6.17, concerning the overall maximum. These differences, however, pose the question of whether the source generation of MAWs is primarily related to tropospheric cross-mountain winds — these are stronger over the Tibetan Plateau (Fig. 6.16) than over the Andes (Fig. 6.15) — or whether it is directly related to the excitation, or breaking, of orographic GWs (question 4 of this chapter, see page 63).

6.7 Discussion of the possible MAW source generation mechanism

For the Andes and New Zealand, it is presumed that tropospheric winds certainly play a role in the MAW generation process, but the cross-mountain winds alone are not sufficient for explaining the seasonal variation in MAW occurrence (Section 6.5.1). For the dominant hotspot in the Northern Hemisphere, the same result can be anticipated when accounting for the enhanced number of detections during winter, as opposed to the strong tropospheric winds during both summer and winter (Fig. 6.16).

Stable stratification has been considered to be another possible precondition for MAW generation, being in common with the excitation of orographic GWs. It is likely that MAWs are preferentially detected during stable conditions, but a correlation between enhanced stability and MAW occurrence, or amplitude, is not evident (Section 6.5.2). Stable stratification implies less turbulent noise at the ground, which causes an enhanced detection capability of a sensor during winter. Nevertheless, global MAW source regions match well-known orographic GW hotspots in the Southern Hemisphere. In addition, the presence of the valve layer indicates that MAW hotspots identified in the Northern Hemisphere could also agree with orographic GW occurrence.

A possible link between MAWs and orographic GW occurrence can either solely be caused by the meteorological preconditions or by a common excitation mechanism. Assuming that the source amplitude of MAWs is primarily correlated to cross-mountain wind, the preconditions in the southern Andes and New Zealand are consistent all year round; however, the winter-time amplitudes, as detected at IS02 (Fig. 6.10) and IS36 (Fig. 6.7), are larger than in summer. On the other hand, amplitudes detected at IS22 are slightly enhanced during summer. **What causes the seasonal variation in the detected amplitudes of MAWs?**

According to the ray-tracing results (Section 6.4), ground-to-stratosphere ducting can be expected between April and September for IS02 and IS36, resulting in less attenuation, whereas thermospheric returns are, on average, stronger attenuated (by around 6 dB). These ray-tracing results correspond to the detected amplitudes at both stations. Sim-

ilarly, this applies to IS22 in the opposed season; hence, stratospheric winds explain at least a great portion of the variation in detected amplitudes. A smaller portion might be associated with the maximum cross-mountain wind speeds found during MAW events in summer (Fig. 6.10).

Which process is elementary in the excitation of MAWs, leading to the increased occurrence frequency during winter?

A meteorological criterion could be the occurrence or strength of wind gusts. Chunchuzov (1994) suggested that strong gusts in non-stationary flows around mountains would produce superimposing acoustical impulses, becoming (coherent) infrasound signals. He assumed that non-stationary flows were "caused by advection of turbulent large-scale inhomogeneities" (Chunchuzov, 1994, p. 2196). Analyzing this in the future would require the use of local wind and turbulence measurements, rather than three-hourly reanalysis data of MERRA-2. With regard to the matching orographic GW hotspots, a direct link between MAW excitation and GW occurrence seems worth to be considered. The following theories are conceivable:

(1) The MAW source generation mechanism is related to the tropospheric excitation and occurrence of orographic GWs, independent of whether these propagate into the upper stratosphere or are filtered below it.

(2) Breaking GWs, either in the lower stratosphere valve layers or in the mesosphere, produce infrasonic waves.

Both imply that orographic GWs induce MAWs. In a general infrasound context, Damiens et al. (2018) modeled the impact of tropospheric winds, orographic GWs and low-altitude critical levels on the acoustic wave field in mountainous regions. However, a direct link between the excitation of MAWs and that of GWs seems — apart from the meteorological requirements — rather unlikely, due to the different wave scales. High-resolution modeling by Lund et al. (2018) has provided strong evidence that GWs breaking over the Andes, as a result of instabilities in the mesosphere, produce infrasonic waves that propagate upstream and downstream. Similarly, GW breaking at lower altitude ranges, such as the valve layer that is characteristic over mountainous regions in winter, could play a role in MAW excitation over New Zealand or the Tibetan Plateau. In this case, a correlation between MAW and orographic GW amplitude, and thus wind speed, would be reasonable. However, due to the predominant altitude range of breaking GWs differing at the hotspots, a bias in apparent phase velocity would be expected in infrasound detections at the ground. Indeed, the actual detections of both IS02 and IS36 cover the entire range from $300\,\mathrm{m\,s^{-1}}$ to $500\,\mathrm{m\,s^{-1}}$, even during particular events. Although Thomas et al. (1974) rejected breaking lee waves as a potential source of MAW signals using power spectra of the recorded signals, the high-resolution simulations by Lund et al. (2018) clearly indicate the production of infrasound when orographic GWs break.

In conclusion, with regard to question 4 of this chapter (see page 63), a link between MAW and orographic GW activity, either in the physical requirements for their occurrence or in the excitation itself, is not ultimately clarified. Some relation in the meteorological requirements — e.g., cross-mountain winds — is likely. Further analyses should focus on local wind and turbulence measurements, and enhanced numerical simulations including

different atmospheric conditions, such as those over New Zealand, will allow the further assessment of such theories mentioned above.

6.8 Summary

Herein, the IMS infrasound network was used to identify global MAW source regions, using a cross-bearing method, and to better understand their occurrence and propagation. For this purpose, monthly mean detections, from observations of up to 15 years, were evaluated, rather than single events. The Tibetan Plateau in central Asia and the South Island of New Zealand were well identified as global MAW source regions at mid-latitudes, in addition to the already known one in the southern Andes and the northwest of North America. At high latitudes — in particular, in the Northern Hemisphere — the relatively coarse station network complicated the robust identification of source regions using the elaborated cross-bearing method. The two well-identified hotspots in the Southern Hemisphere were focused on, as these are characterized by clear topographic features, compared to the multitude of mountain ranges in central Asia.

About **Question III** of Section 1.5, it was found that MAWs originating from the hotspot regions were generally observed all year round. The presence of the ground-to-stratosphere waveguide resulted in increased amplitudes at the receivers. Moreover, many detections were explained by the ground-to-thermosphere waveguide, which is a difference to microbarom detections (Chapter 5). The substantially low absorption rates at low frequencies enabled long-range propagation and occasional detections, with amplitudes around the detection thresholds, at distances of more than 7,000 km from the sources.

The event-based wind analysis showed a clear correlation between MAW amplitude and the magnitude of cross-mountain wind speed over the southern Andes and New Zealand; hence, in source regions where winds are variable throughout the year, the detected MAW amplitudes should be subject to seasonal variation. MAW detections originating from the Andes and New Zealand exhibited a seasonal variation in amplitude, although the cross-mountain wind conditions are consistent throughout the year. In this case, the seasonal variability of the detected amplitudes was therefore primarily associated with attenuation in the different waveguides.

The prominent MAW hotspots in the Southern Hemisphere matched those of well-known source regions of orographic GWs observed in the stratosphere. At dominant MAW hotspots where no enhanced stratospheric GW activity was found during winter, the valve layer is present in the lower stratosphere. This layer causes GWs to break before they encounter the middle stratosphere.

Cross-mountain winds appeared to be a necessary condition for inducing MAWs, but winds are not sufficient to explain the MAW occurrence frequency, being enhanced during winter. Since stable stratification also appeared to be not sufficient in this context, further possible processes were briefly discussed. These included turbulent tropospheric flows and a link between MAWs and orographic GWs breaking in different layers of the atmosphere. These processes need to be further investigated in a future study.

7 | Overall summary and conclusions

The IMS infrasound recordings have provided an opportunity to study a poorly investigated type of coherent waves in the atmosphere — the so-called MAWs — that were first observed in the 1960s. Reports on observations of MAWs have been very limited and mainly date back to the 1970s. Possible source generation mechanisms have been proposed, based on measurements from regional sets of microbarometers for up to two years; however, it was remarked that the generation mechanism was difficult to clarify since infrasound detections from MAWs were subject to atmospheric variability. Since then, the exact source mechanism has remained unresolved; isotropic turbulence caused by non-stationary flows in mountainous terrain was considered to be the most likely.

The objective was to identify the global source regions and characteristic features of infrasonic MAWs, using the entire IMS infrasound network. It was hypothesized that MAWs and orographic GWs share common physical conditions required for their occurrence. A direct link between both types of waves could make the infrasound network a unique ground-based technology for monitoring orographic GW sources on a global scale. Three questions (I–III) were raised in Section 1.5 as a guide through this thesis. These are referred to in the following summary of infrasound observations, in the context of wave activity in the atmosphere.

Question I: Does the station coverage of the IMS infrasound network allow the study of atmospheric wave phenomena on a global scale?

Barometric recordings at the IMS infrasound stations exhibit a broad spectrum of dynamic wave activity in the atmosphere. The spectrum ranges from PW scales with periods of greater than one day, to atmospheric tides at fractions of the solar day, to infrasonic waves at periods of seconds, such as microbaroms. Geographical and seasonal characteristics of thermally-induced atmospheric tides were derived from absolute pressure data and compared with the reanalysis provided by MERRA-2. The IMS data allowed a very accurate characterization of the tides with periods of 24 h, 12 h and 8 h. Remote sites (e.g., islands and polar regions) exhibited special features in terms of amplitude or noise conditions. The high precision of the sensors also enabled the identification of the gravitationally-induced half-day lunar tide, which modifies air pressure at lower amplitudes than solar tides. The availability of hourly, and even shorter-term, barometric data proved to be a great benefit. Other harmonics of the solar tides could be assessed in detail in the future since the PSD analyses highlighted up to 9 cpd. A comprehensive analysis of the globally present atmospheric tides led to the conclusion that the global coverage offered by the IMS infrasound network, and its data precision, generally enable global studies on

atmospheric dynamics; the main advantage of atmospheric tides is, however, their distinct spectral appearance, in contrast to PWs and GWs.

Question II: Do NWP models appropriately reflect middle atmosphere variability in order to allow the explanation of infrasound detections by propagation modeling?

The PMCC method was applied to the available IMS infrasound data sets to derive the properties of waves, including microbaroms and MAWs, from differential pressure data. An essential factor influencing the detection capability of the infrasound network, and thus the PMCC method, is the variability in atmospheric dynamics. The stratospheric jet-stream mainly controls the relevance of middle and upper atmospheric waveguides for infrasound propagation. Its semi-annual reversal causes the seasonal mean azimuthal variation in microbarom detections (0.1–0.5 Hz), but explaining short-scale fluctuations requires accurate knowledge of temperature and winds in the middle atmosphere. Collocated lidar measurements of temperature profiles, and infrasound at IS26, allowed the quantification of biases and deviations in the ECMWF operational HRES analysis. Using a wave interaction source model, and a realistic attenuation parameterization, enabled the modeling of microbarom amplitudes at IS26. Incorporating perturbations of temperature and wind, based on the determined biases and deviations, explained up to 97 % of the microbarom detections, especially during summer. Moreover, the results implied that adding a systematic middle atmosphere temperature offset to the commonly used ECMWF temperature profiles, as identified by lidar measurements, could improve predictions of the IMS infrasound network detection capability on shorter time scales by up to 10 %.

Question III: Will a global analysis of MAW detections, using the IMS infrasound network, improve the understanding of MAW occurrence, compared to the findings on MAWs from the 1970s?

Monthly MAW source regions were globally identified, using the elaborated cross-bearing approach. The dominant ones, all at mid-latitudes, are the Tibetan Plateau in central Asia, New Zealand's South Island and the southern Andes, the latter of which had already been determined in the 1970s. In contrast to microbaroms, it turned out that MAW detections do not merely follow the stratospheric wind directions and, at some stations, MAWs were observed all year round. Investigating the two well-identified hotspots in the Southern Hemisphere helped to better understand the complex effects of excitation and propagation conditions on the detected wave parameters. The correlation between tropospheric wind conditions and MAW amplitudes indicated that strong cross-mountain winds (e.g., wind speeds $>15\,\mathrm{m\,s^{-1}}$ at 700 hPa) are a necessary condition for MAW occurrence, and MAW amplitudes increase with wind speed. The acoustic waveguides primarily determine the detected amplitude where the wind conditions do not significantly change throughout the year. Despite resulting in smaller amplitudes, the ground-to-thermosphere waveguide enables the explanation of detections far away from the source, up to 7,000 km. However, neither the propagation conditions nor the tropospheric winds alone were a sufficient reason for enhanced MAW occurrence during winter. The stratification of the troposphere — in particular, the atmospheric boundary layer — is more stable during winter,

being the only apparent analogy between static stability and MAW occurrence.
The global MAW source regions identified using the IMS infrasound network were compared with the GRACILE climatology of stratospheric GW parameters. In the Southern Hemisphere, the mid-latitude MAW hotspots showed good agreement with well-known source regions of orographic GW activity. The results concerning the Northern Hemisphere were not as clear as for the Southern Hemisphere. The majority of such ambiguous cases was well explained by considering the zonal wind profiles, which exhibited critical levels or valve layers that cause upward-propagating orographic GWs to break in the lower stratosphere, instead of breaking in the mesosphere.

Overall, mid-latitude MAW source regions were successfully determined using the IMS infrasound recordings. Analyzing the complexity of atmospheric propagation and source conditions led to the conclusion that tropospheric winds play a significant role in MAW excitation. This meteorological precondition is in common with the excitation of orographic GWs. However, this study revealed that another quantity or process must be involved in the excitation of MAWs to explain their seasonal occurrence. Given the matching source regions, it was discussed that orographic GWs could directly induce MAWs when breaking in different atmospheric layers, as a result of instabilities. Turbulent flows around mountains have also been considered to produce the MAW signals. Consequently, further studies are needed to clarify the exact source mechanism of MAWs, and the question whether the ground-based infrasound observations of MAWs can be used as an indirect method for monitoring orographic GW sources depends on the outcome of such studies.

8 | Outlook

As a next step, the CORAL system in Argentina offers the opportunity to compare collocated infrasound and lidar measurements again, at one of the globally most active hotspots of MAWs and GWs. During austral winter 2018, Kaifler (2018b) identified several large-amplitude orographic GW events in temperature profiles. The simultaneous detections of MAWs would consolidate the theory of a link between MAWs and orographic GWs. If a link in the excitation of MAWs and orographic GWs can be validated, observing MAWs using the IMS infrasound network would be a unique ground-based opportunity to estimate orographic GW source activity globally, in near-real time.

Moreover, the current CORAL campaign in Argentina provides a valuable opportunity for continuing on Chapter 5, using more than one station. The method and results of modeling the microbarom amplitudes could contribute to the understanding and reduction of false alarms during routine data processing at the IDC, concerning the CTBT. In the future, improved analyses could be achieved by equipping additional infrasound stations with lidars, or equivalent upgrades that can measure the profiles of horizontal winds.

For future analyses addressing the generation mechanism of MAWs and a possible link between MAWs and orographic GWs, the non-dimensional mountain height could be a suitable correlation measure. The non-dimensional mountain height relates the static stability, the cross-mountain wind component and the mountain height, allowing to distinguish non-linear (around the mountains) and linear (over the mountains) flows (e.g., Bramberger et al., 2017). Moreover, the MAW source generation theory based on non-stationary flows causing isotropic turbulence due to instabilities could be associated with the Reynolds number (Chunchuzov, 1994). Local wind measurements, instead of reanalysis data, need to be used when correlating MAW occurrence with wind gusts.

Detailed analyses of MAW detections and GW occurrence in the Northern Hemisphere could be achieved, for instance, by incorporating data from experimental infrasound arrays in Europe (e.g., Pilger et al., 2018) and the USA (De Groot-Hedlin and Hedlin, 2015), the latter also being capable of detecting GWs because of its large apertures. In this context, future work should focus on enhancing the cross-bearing method; for example, by adding weighting functions. These should not only reflect the detection parameters such as the number or family sizes (Landès et al., 2012), but also should ideally account for the detection capability of the network during the considered period (see Appendix A). For this purpose, the attenuation relation used in Chapter 5 could be useful.

Appendices

A | The detection capability of the IMS infrasound network

Given the low-pass filtering character of the atmosphere (Chapter 3), the number of infrasound stations of the IMS (60) is sufficient in order to detect atmospheric explosions with a minimum yield of 1 kt TNT-equivalent worldwide at any time (Marty, 2019). The detection capability of the IMS infrasound network can be defined as the time-dependent "ability to detect and locate atmospheric explosions" (Green and Bowers, 2010, p. 1). Two measures allow an estimation of the detection capability:

- the minimum yield required to detect a signal; and
- the smallest detectable source amplitude.

A better performance of the network results in lower values of these measures; for instance, a smallest detectable amplitude of 0.1 Pa makes a lower detection threshold than 0.5 Pa and, thus, a better detection capability. The lowest thresholds are achieved when requiring a distinct event to be detected at only one station (hereafter, a 'one-station coverage'). Two- and three-station coverages have also been referred to (e.g., Le Pichon et al., 2019); these go along with higher detection thresholds. Yield and amplitude measures have in common the following factors controlling the network performance: in addition to signal attenuation during propagation, as described in Section 3.2, the *SNR* is essential for evaluating whether a source can be detected at a station or not (Le Pichon et al., 2009; Green and Bowers, 2010). The *SNR* depends on local noise conditions at the receiver, mainly wind and the signal frequency content. The IMS infrasound stations are installed in remote places in different environments (e.g., forests, islands, polar regions), and noise conditions are, thus, highly variable throughout the network (Bowman et al., 2005; Matoza et al., 2013). Since turbulent mixing increases noise at the surface, the *SNR* varies with daytime (Le Pichon et al., 2009; Pilger et al., 2015; Mialle et al., 2019).

Several studies have addressed the detection capability of the IMS infrasound network, each attempting to enhance modeling towards more accurate conditions, be it the representation of atmospheric conditions and uncertainties, the use of background noise models, or yield estimates (Le Pichon et al., 2009, 2012, 2019; Green and Bowers, 2010).
The probabilistic approach of Green and Bowers (2010), incorporating noise and propagation uncertainties, resulted in detection thresholds of 90 % probability, and showed seasonal variation. Green and Bowers (2010) focused on a relatively wide frequency band (0.04–6.6 Hz), finding out that incorporating winds from the HWM93 model (Hedin et al., 1996)

decreased the detection thresholds in their simulations. In agreement with Le Pichon et al. (2009), who used a deterministic approach and considered a more detailed description of the stratospheric winds (ECMWF operational HRES analyses), the detection capability was found to be best during the solstices; however, the location performance was reduced at the same time, due to the directional nature of the propagation conditions. Nevertheless, two-station coverage within the IMS infrasound network allowed for the conclusion that its design goal to detect explosions of 1 kt TNT-equivalent was fulfilled at any time of the year, in a frequency range of 0.2 Hz to 2 Hz (Le Pichon et al., 2009). This was an important milestone, after Stevens et al. (2002) estimated the detection capability with partially slightly higher TNT-equivalents, using a probabilistic approach that preceded that of Green and Bowers (2010). In order to predict a signal's amplitude at any location, these studies made use of empirical attenuation relations that allowed scaling of the yield estimations into pressure amplitudes. These relations were based upon historical events of chemical and nuclear explosions (e.g., Whitaker, 1995; Whitaker et al., 2003), whilst stratospheric circulation was considered using a correction factor (Whitaker, 1995).

Improvement using a more realistic parameterization of atmospheric attenuation

An improvement was introduced by Le Pichon et al. (2012), who evaluated a more realistic, semi-empirical relation for stratospheric winds and atmospheric attenuation (Eq. 5.1, p. 53). The advanced attenuation relation was empirically determined from more than 9,000 frequency-dependent parabolic equation method simulations, and led to an understanding that the detection capability of the IMS infrasound network was better than previously analyzed (Le Pichon et al., 2012). Based on that study, a global distribution of the minimum attenuation of a signal detected at one-station coverage is shown in Fig. A.1. The depiction of minimum attenuation is nearly proportional to the minimum amplitude required to be detected: Weak attenuation means that low-amplitude signals can be detected in the same order as strongly attenuated signals of higher-amplitude sources at the receiver; however, station noise conditions were not considered during that study.

The attenuation relation of Le Pichon et al. (2012) highlighted that atmospheric attenuation that increased with frequency resulted in decreased network performance. Figure A.1 illustrates this effect, especially with increasing distance from the stations. Areas with the lowest minimum attenuation can generally be found in the stratospheric upwind directions of stations. The seasonal variability of the network performance, which is mainly caused by the middle atmosphere circulation, is shown in Fig. A.2. Note that a two-station coverage is required in Fig. A.2, which results in greater minimum amplitudes (stronger attenuation) than in Fig. A.1. During the reversal of the stratospheric circulation the thresholds are highest (Figs. A.2(b) and A.2(d)) due to an unstable waveguide.

Le Pichon et al. (2019) recently extended the previous study by adding random wind perturbations of $10\,\mathrm{m\,s^{-1}}$ to the ECMWF profiles, and included station noise, in order to calculate the detection capability. The result for one-station coverage was that the detection thresholds of the IMS infrasound network were highest during the equinoxes,

coinciding with the largest annual uncertainties due to wind. This finding was especially significant at frequencies of 0.8 Hz and higher, amounting to an order of magnitude in the amplitude thresholds (Le Pichon et al., 2019). The lowest values, and thus the highest detection capability at low uncertainty, outside of SSW events, was provided during the solstices. The lower the frequency, the lower the detection threshold and its uncertainty.

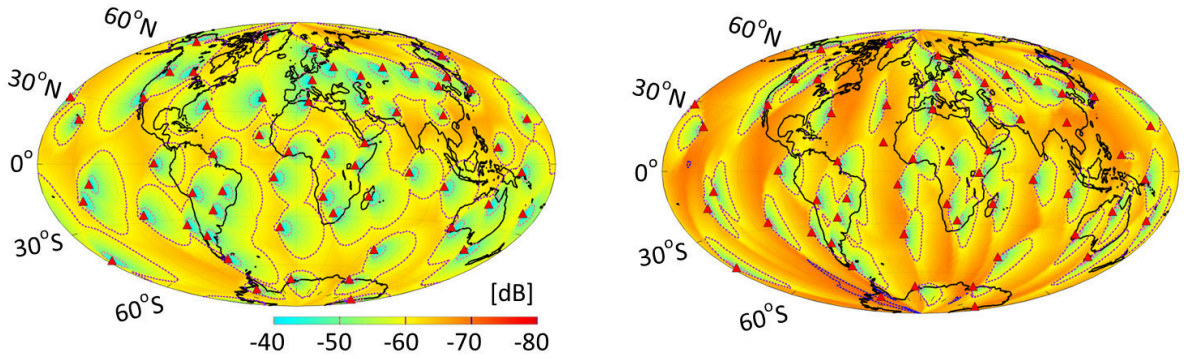

(a) 0.2 Hz. (b) 1.6 Hz.

Figure A.1: The geographical distribution of the full IMS infrasound network performance is shown for two frequencies, as calculated for 1 January 2010. The minimum signal attenuation (in dB) for one-station coverage was calculated using the ECMWF operational HRES analysis. These figures were adapted from Le Pichon et al. (2012).

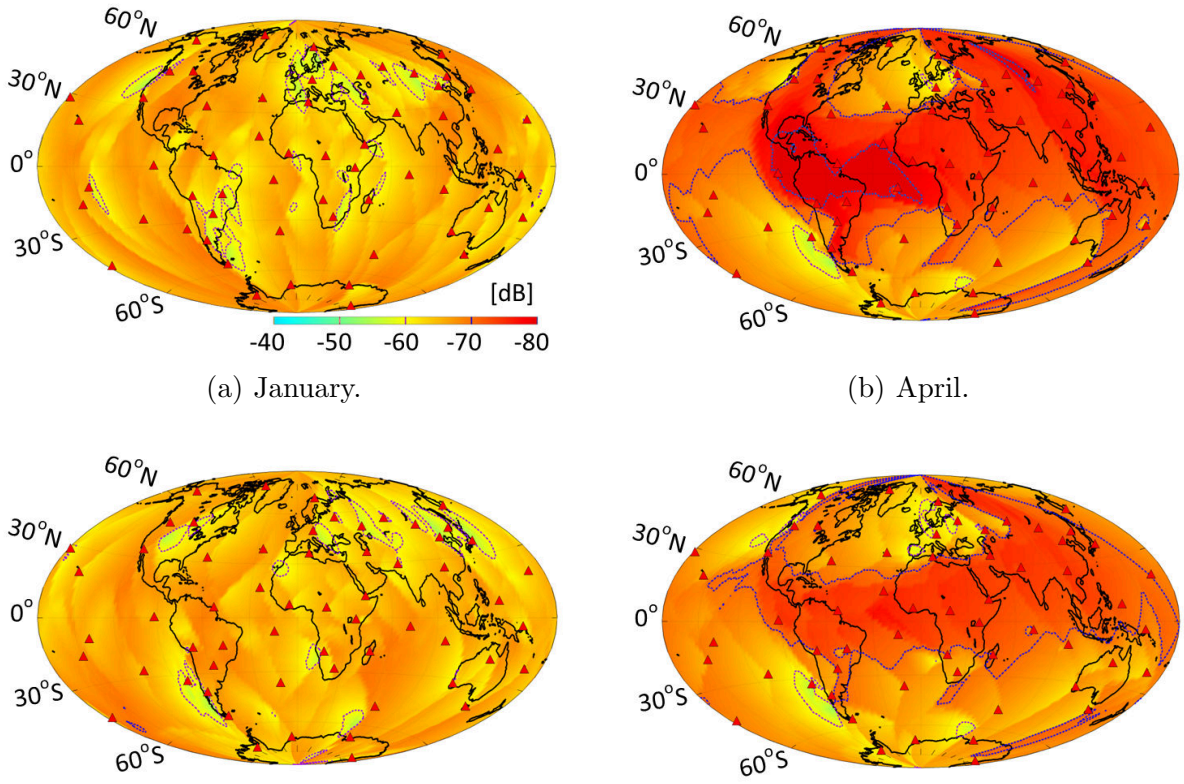

(a) January.

(b) April.

(c) July.

(d) October.

Figure A.2: The seasonal variability of the network performance is shown for 0.8 Hz. ECMWF HRES winds were used to calculate the smallest signal attenuation on 1 January, April, July and October 2010 with two-station coverage. These figures were adapted from Le Pichon et al. (2012).

B | Absolute pressure data from IMS infrasound stations

Additional figures corresponding to Chapter 4 are provided in this part.

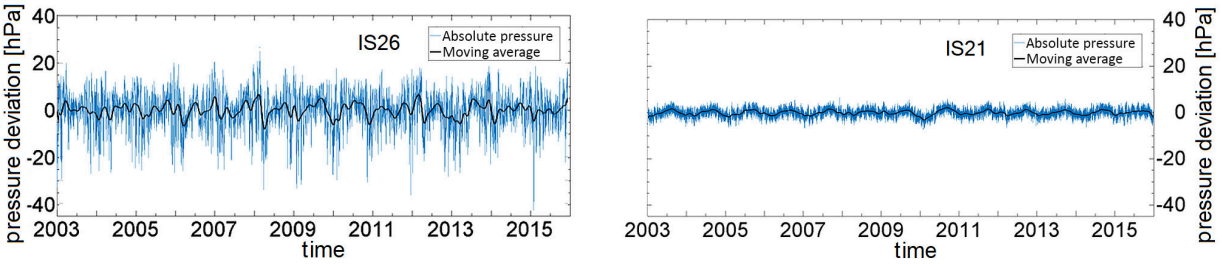

(a) IS26. (b) IS21.

Figure B.1: Absolute surface pressure data of MERRA-2 at IS26 (a) and IS21 (b), as deviations from the annual means. The moving average highlights the superordinate annual variation. See also Fig. 4.4.

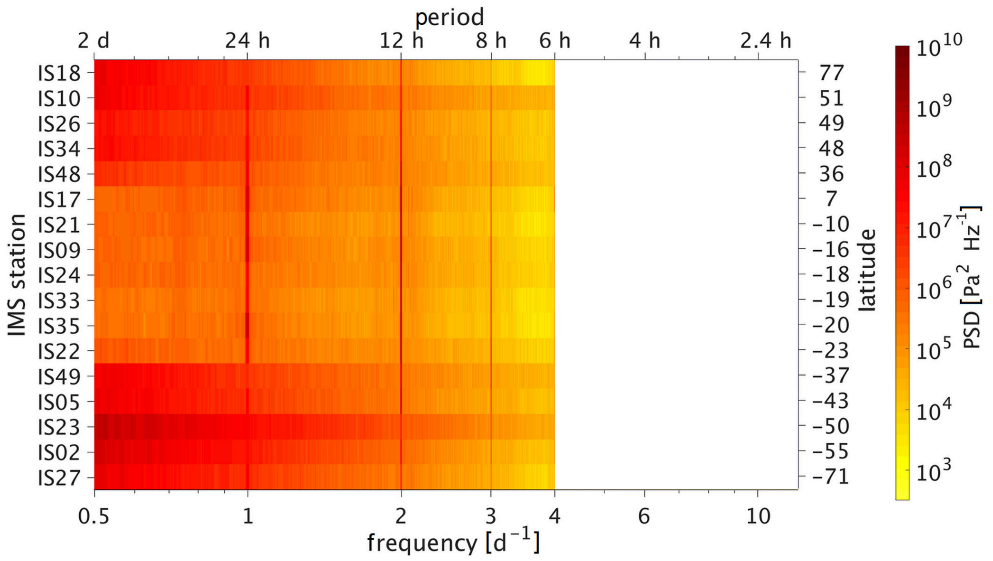

Figure B.2: Median PSD spectrum of the MERRA-2 time-series (analogous to Fig. 4.7). The period range was limited to 6 h due to the sampling interval of the MERRA-2 data (3 h). The color bar is slightly different from that in Fig. 4.7. The most significant difference is that the lunar semidiurnal tide is not represented in the MERRA-2 data.

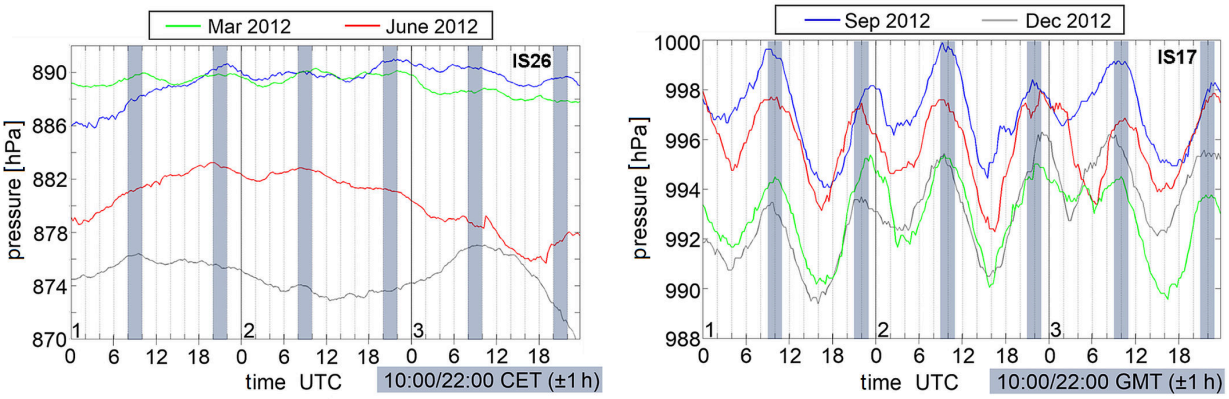

(a) IS26.

(b) IS17.

Figure B.3: Absolute pressure on three days in different seasons at (a) IS26 (UTC+01) and (b) IS17 (UTC+00). The semidiurnal tide can clearly be detected visually at the tropical IS17, whereas, at IS26, synoptic pressure variations mask the reduced tidal effect in the mid-latitudes. The gray columns indicate the expected times of the pressure maxima of the semidiurnal tides (e.g., Haurwitz, 1956). Note that these barometric recordings are shown for 2012 and are not necessarily representative of any of the four seasons.

C | Microbarom amplitude modeling

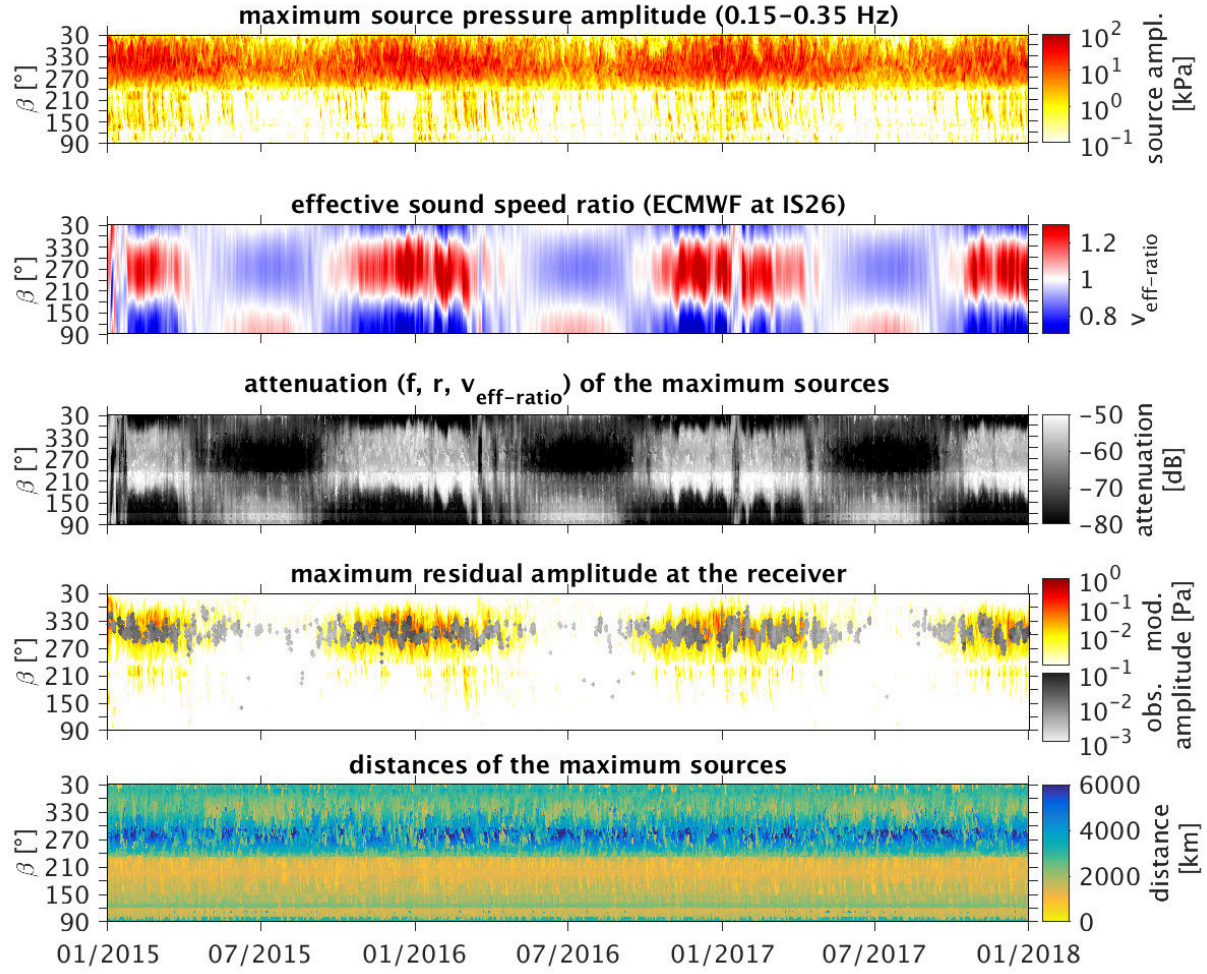

Figure C.1: Similar to Fig. 5.3, but for the entire back-azimuth range, and also including the distance of the maximum sources (bottom). Between 30° and 90°, no potential microbarom sources exist in the geographic area of interest. Reproduced from Hupe et al. (2019).

D | MAWs

Additional figures corresponding to Chapter 6 are provided in this part.

D.1 Annual and azimuthal distribution of PMCC detections

Based upon Fig. 6.2, the azimuthal distributions of detections between 0.02 Hz and 0.05 Hz at almost all IMS infrasound stations are shown in this section. The recently certified stations IS03, IS20 and IS60 are not included because they had only a short period of data coverage.

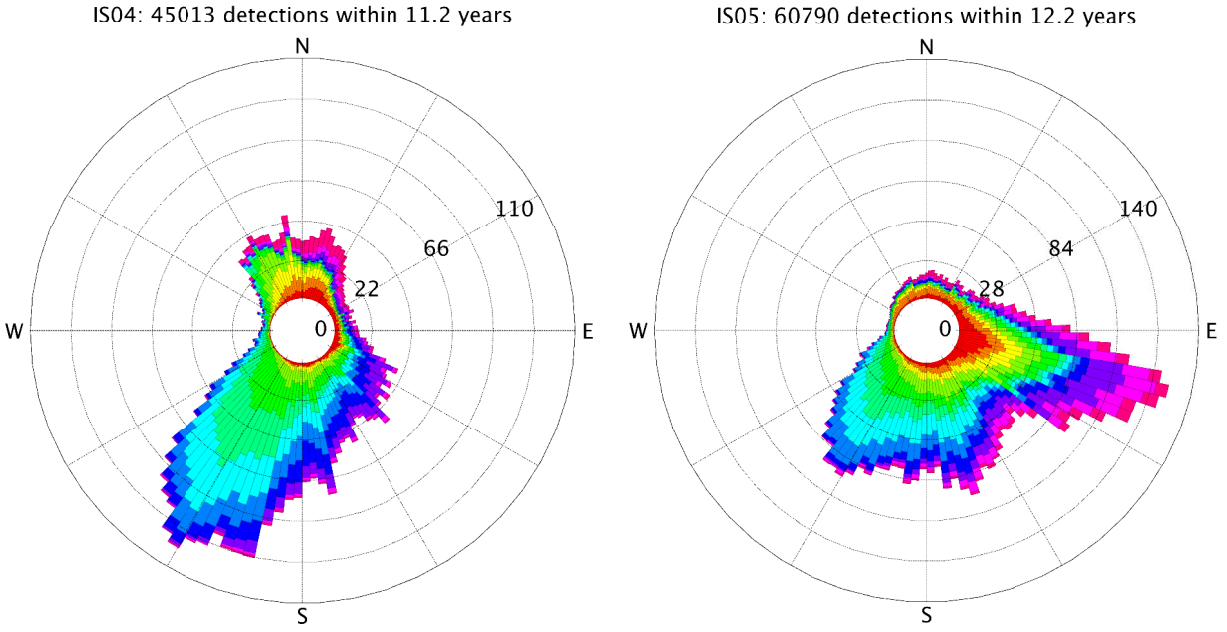

(a) IS04.

(b) IS05.

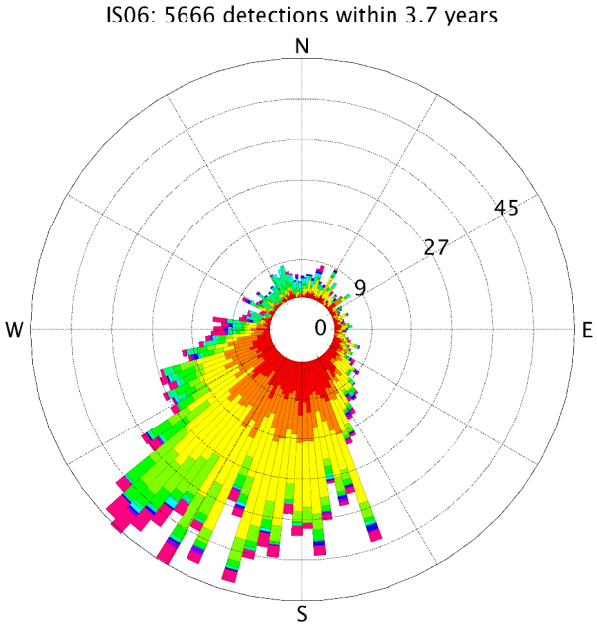

(c) IS06.

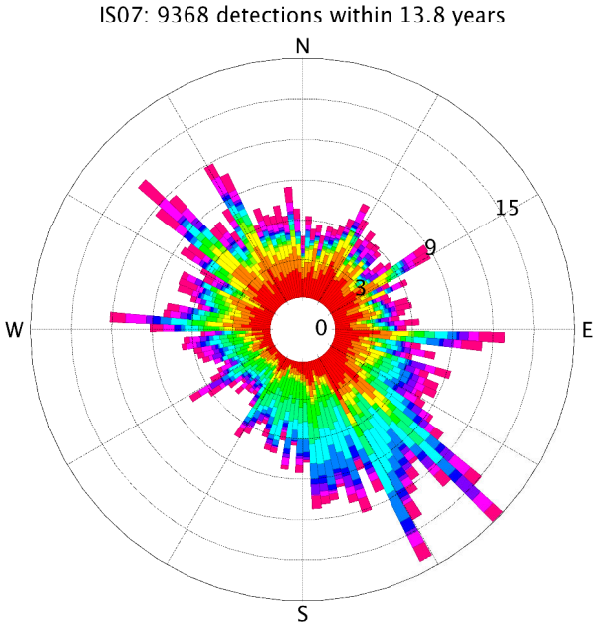

(d) IS07.

Figure D.1: The polar plots show the azimuthal distribution of detections attributed with center frequencies of between 0.02 Hz and 0.05 Hz. The radius linearly represents the average number of detections per year. The total number and the data availability are indicated at the top. Each bin covers 3° in back-azimuth, whereas the color (same as in Fig. 6.2) depicts the monthly distribution, from January (inside, red) to December (outside, rose).

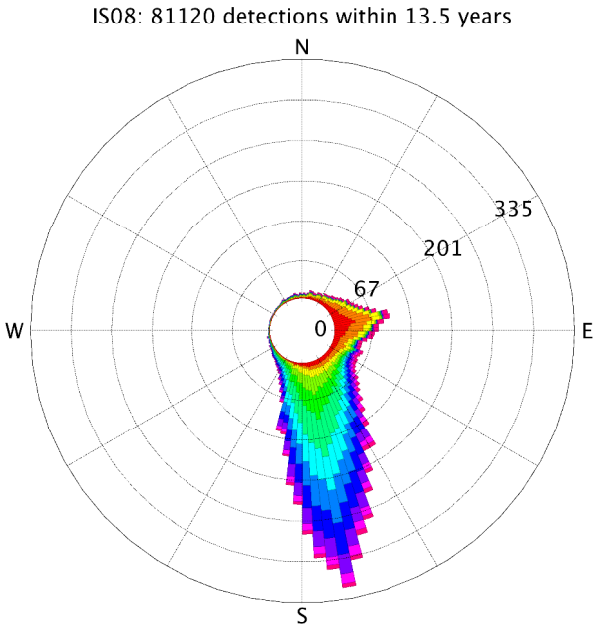

(e) IS08.

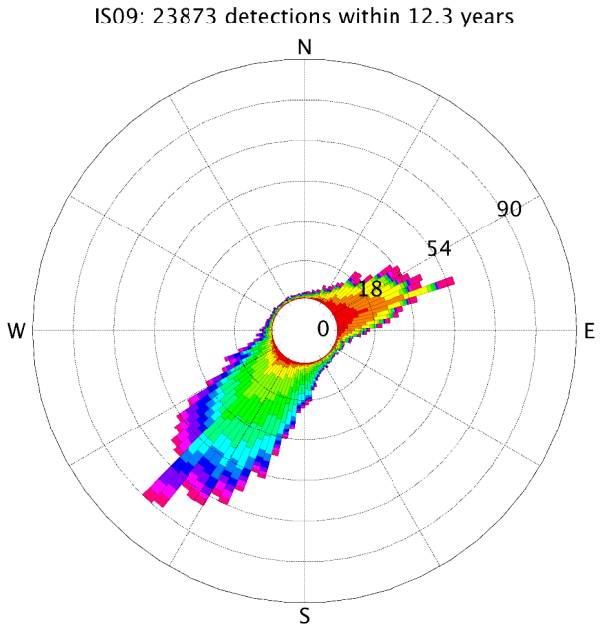

(f) IS09.

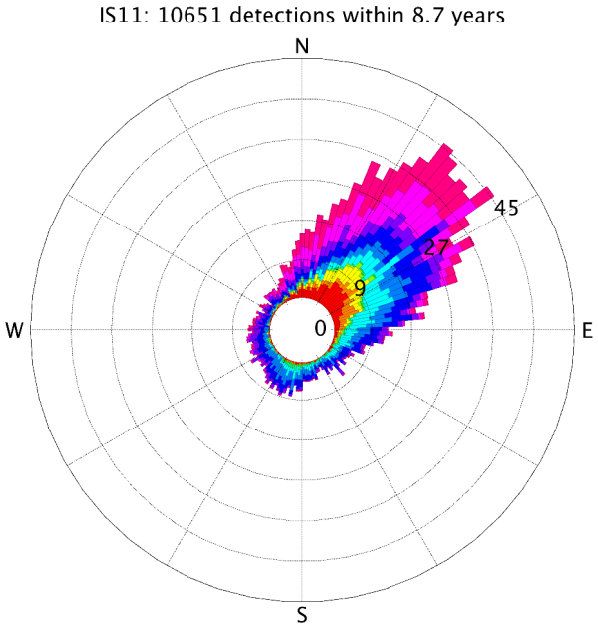

(g) IS11.

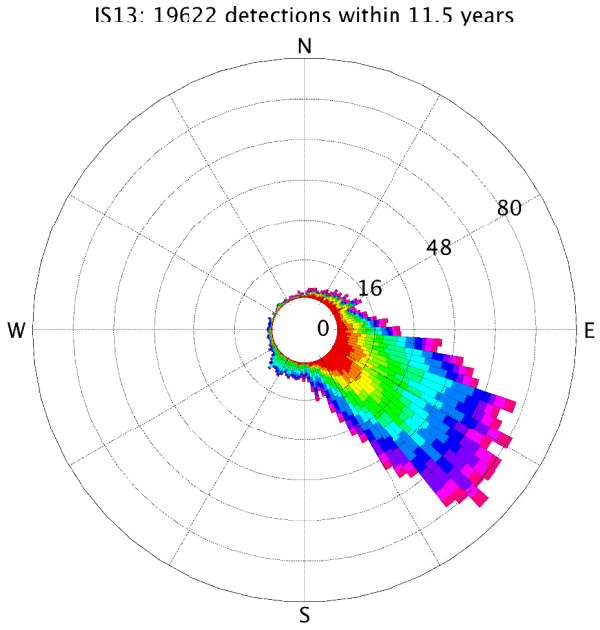

(h) IS13.

Figure D.1: (cont.)

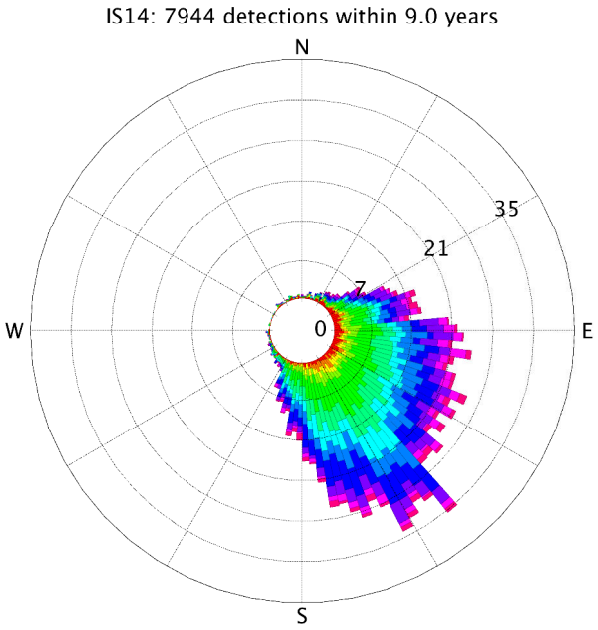

(i) IS14.

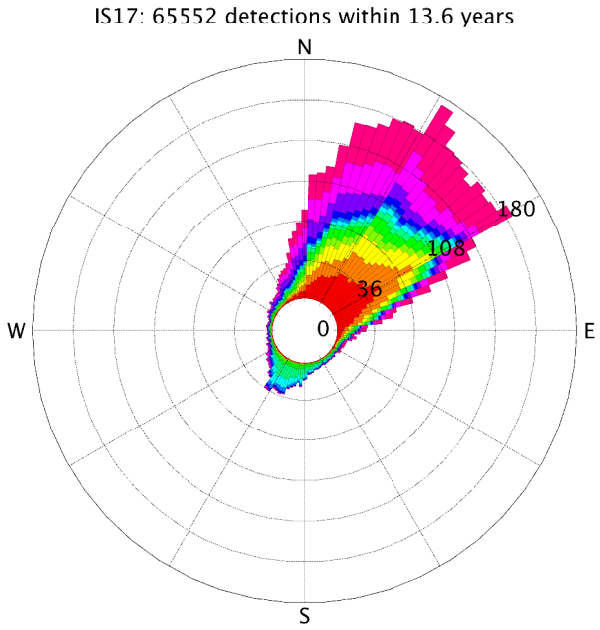

(j) IS17.

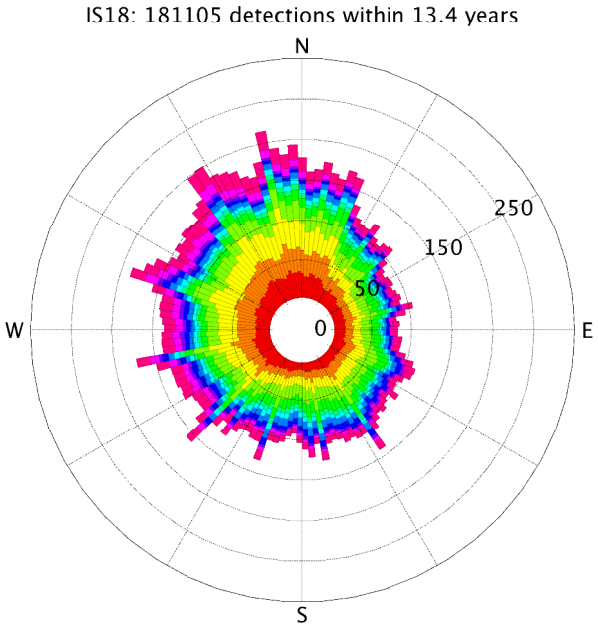

(k) IS18.

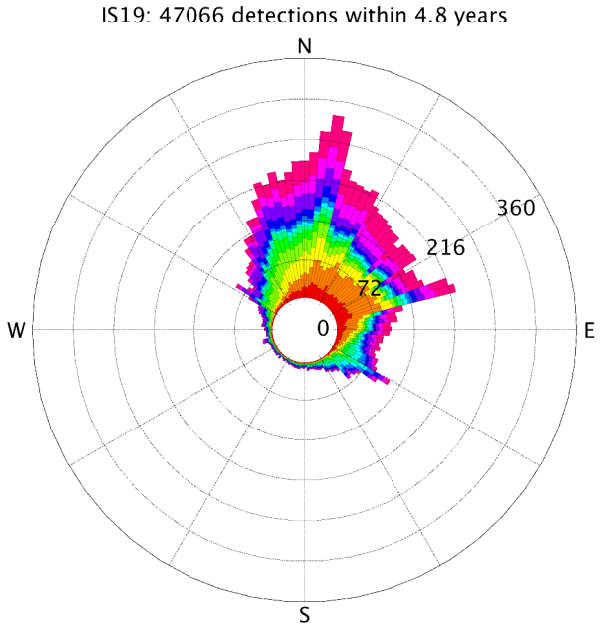

(l) IS19.

Figure D.1: (cont.)

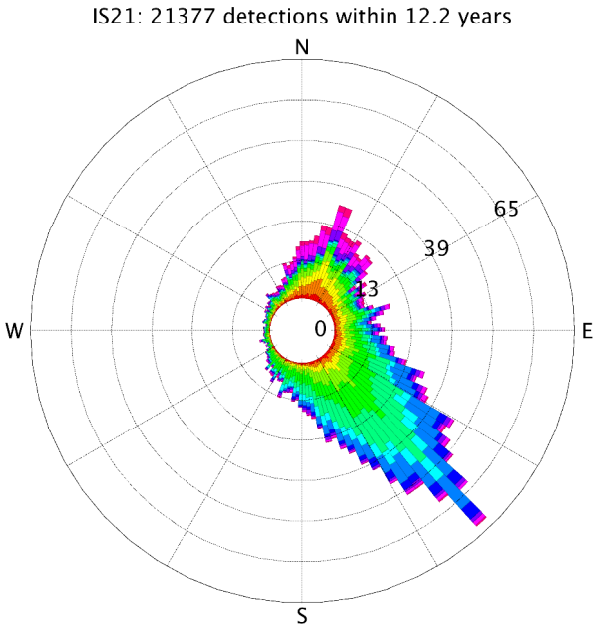

(m) IS21.

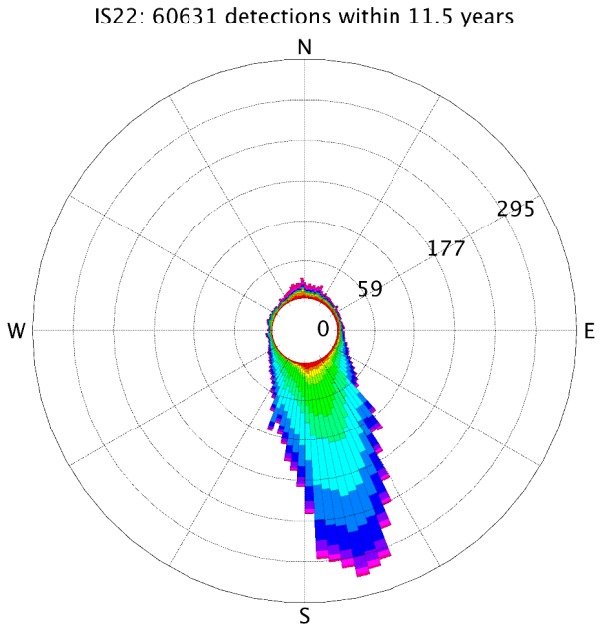

(n) IS22.

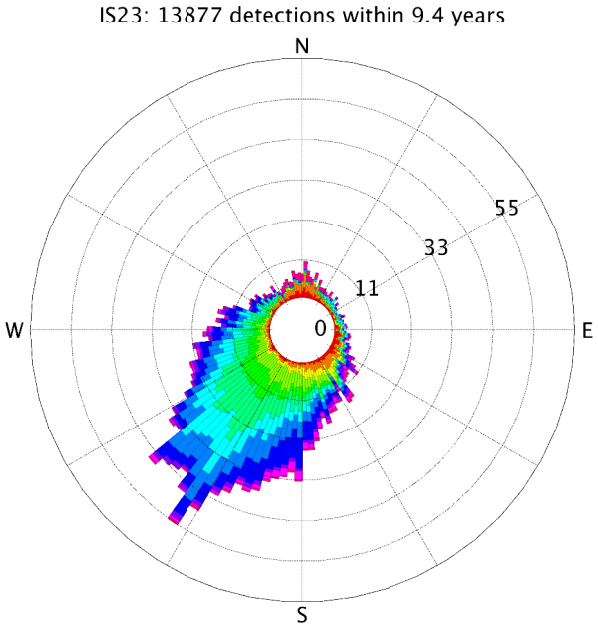

(o) IS23.

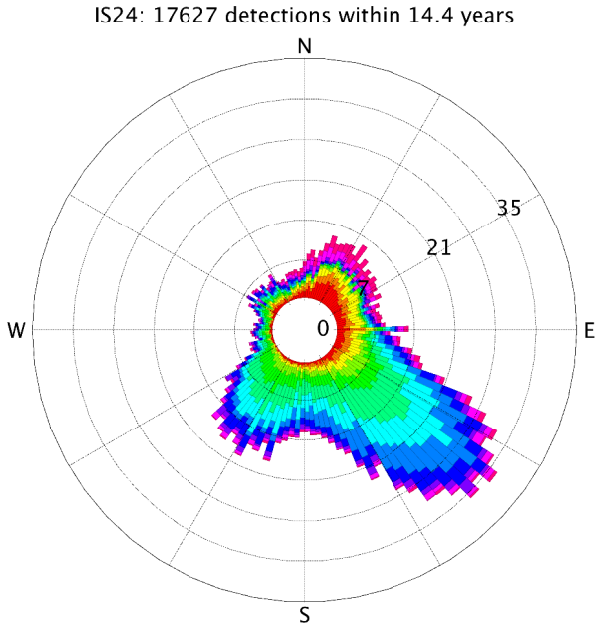

(p) IS24.

Figure D.1: (cont.)

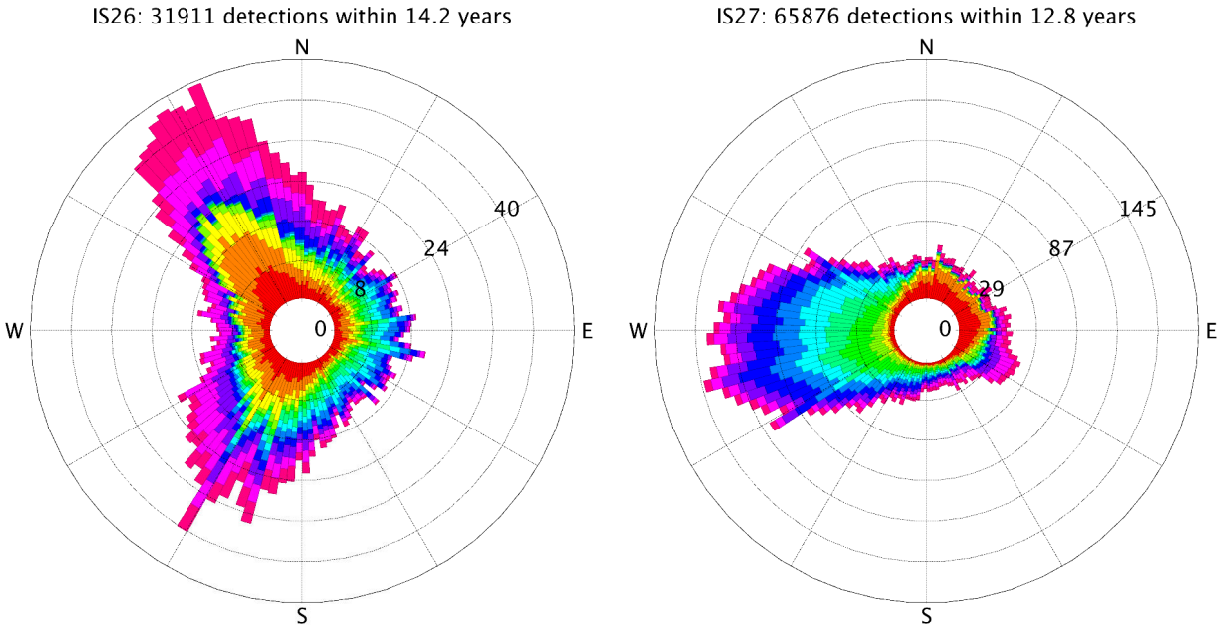

(a) IS26.

(b) IS27.

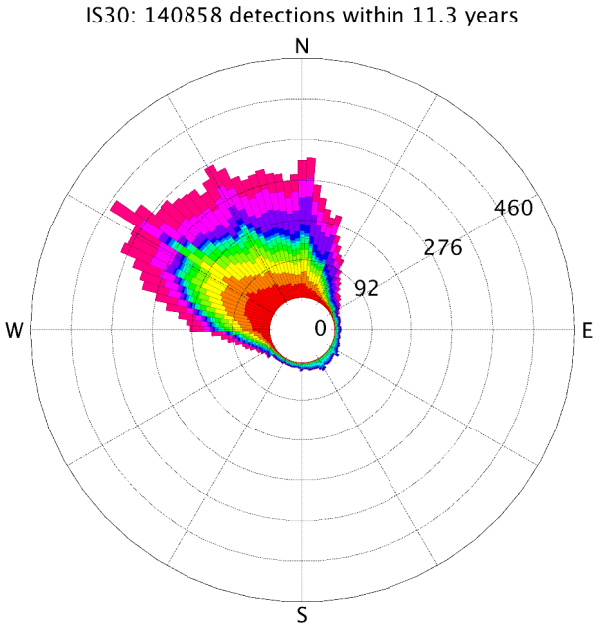

(c) IS30.

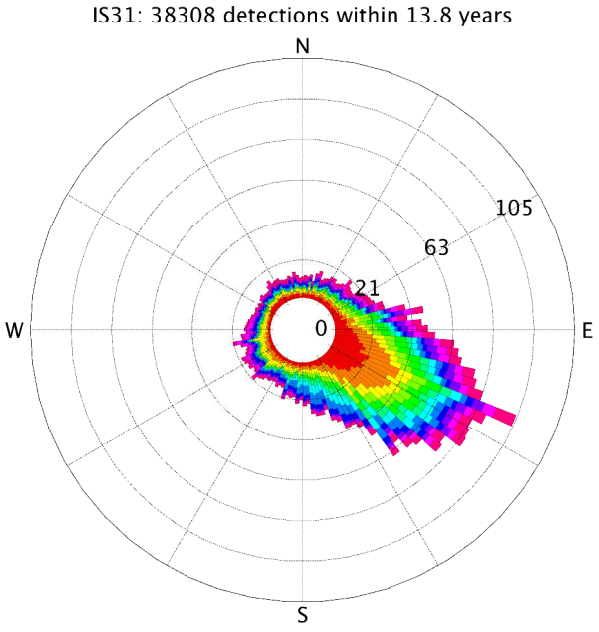

(d) IS31.

Figure D.2: As Fig. D.1, but for IS26 up to IS44.

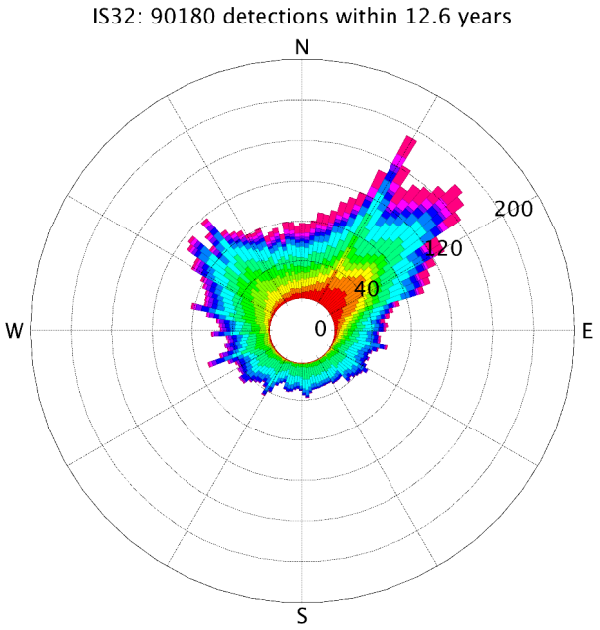

(e) IS32.

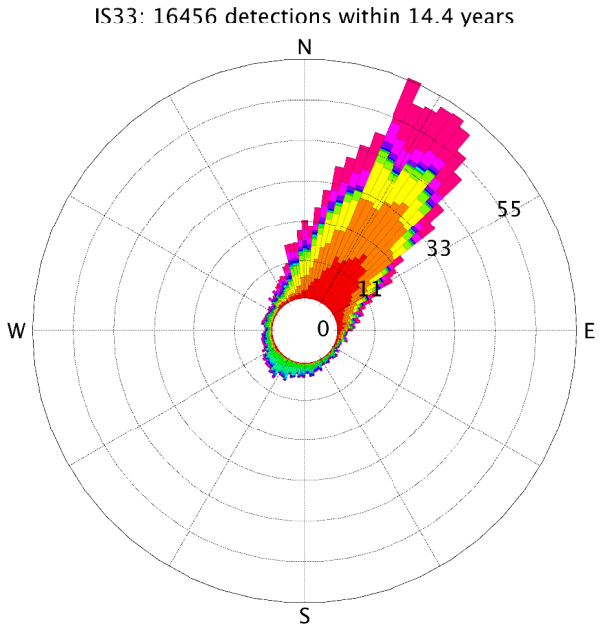

(f) IS33.

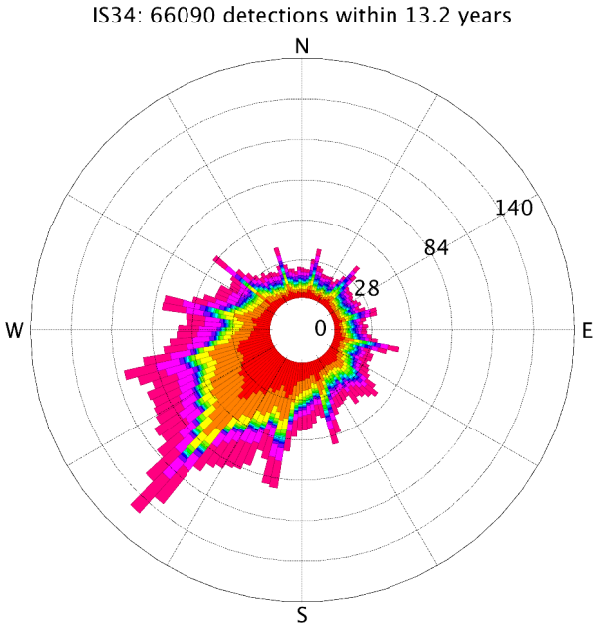

(g) IS34.

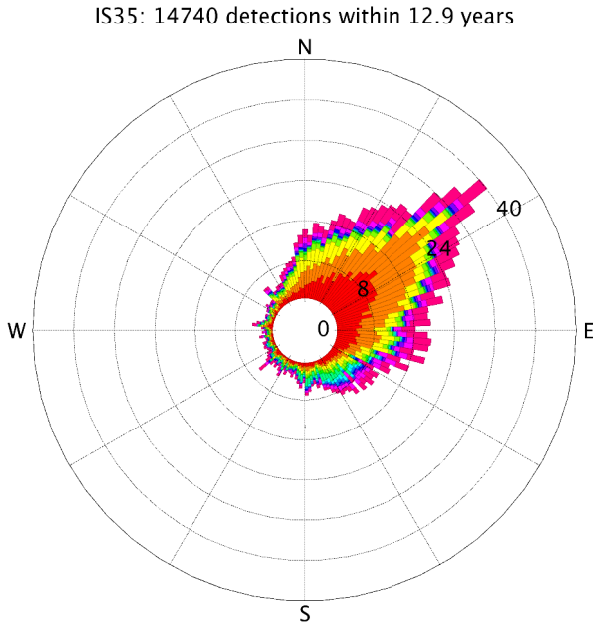

(h) IS35.

Figure D.2: (cont.)

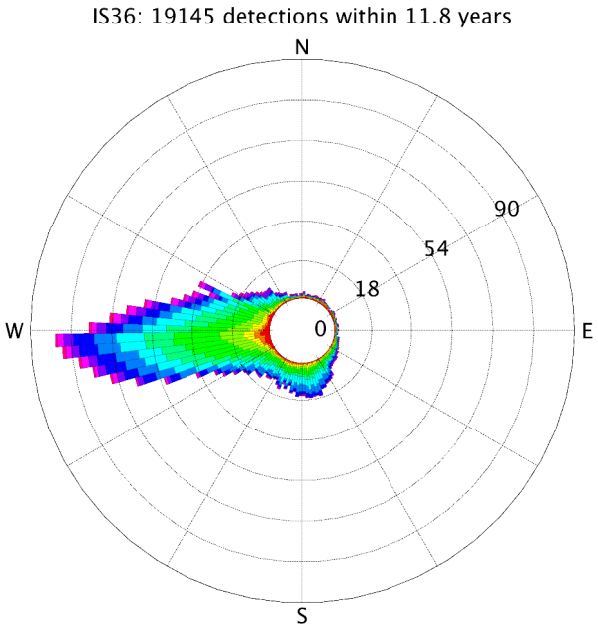

(i) IS36.

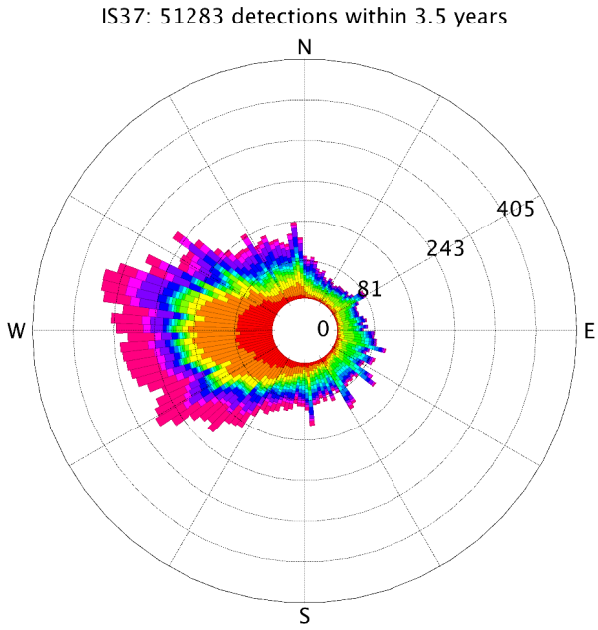

(j) IS37.

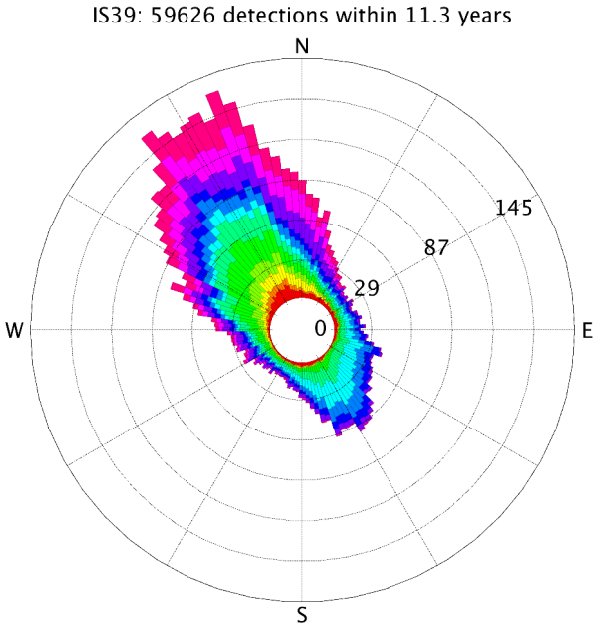

(k) IS39.

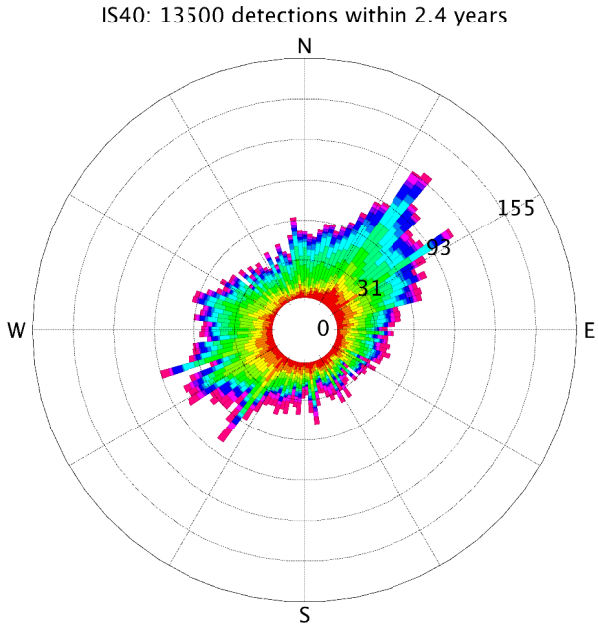

(l) IS40.

Figure D.2: (cont.)

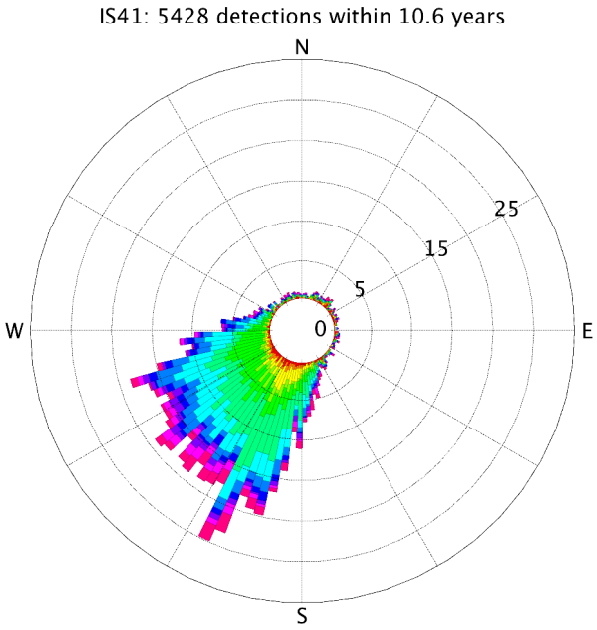

(m) IS41.

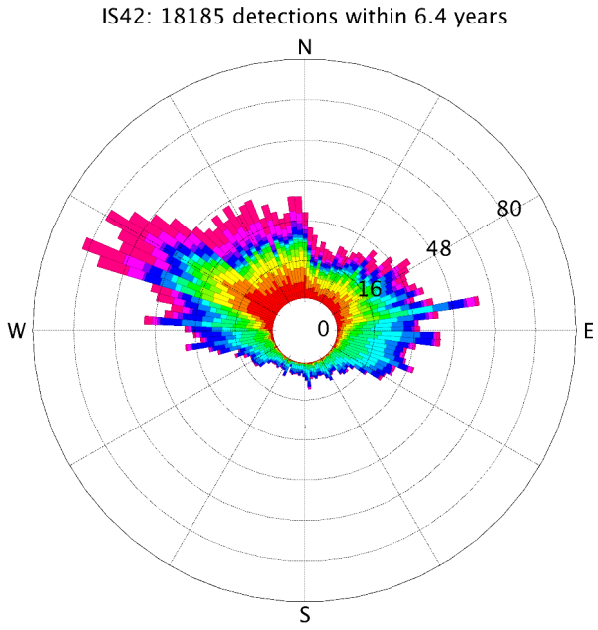

(n) IS42.

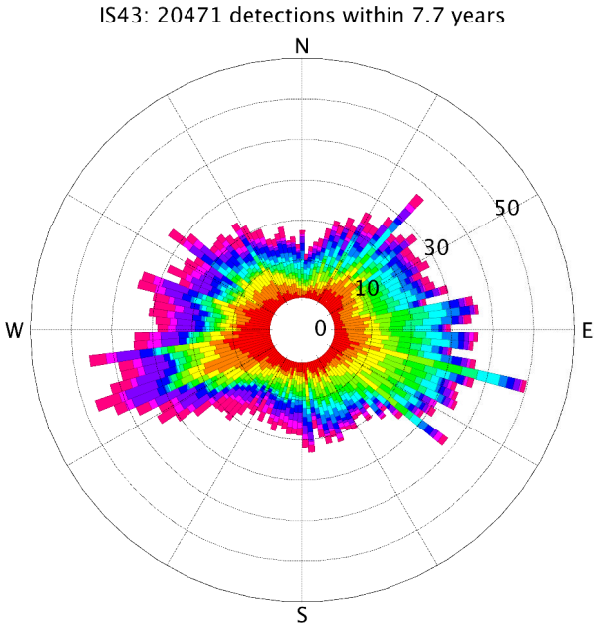

(o) IS43.

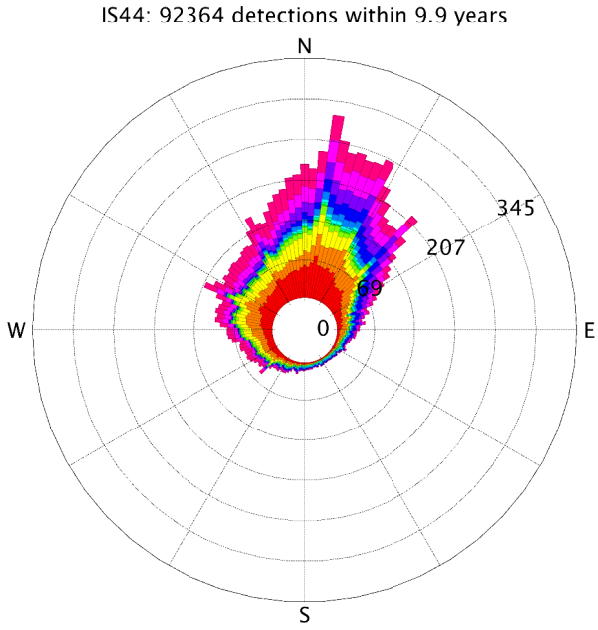

(p) IS44.

Figure D.2: (cont.)

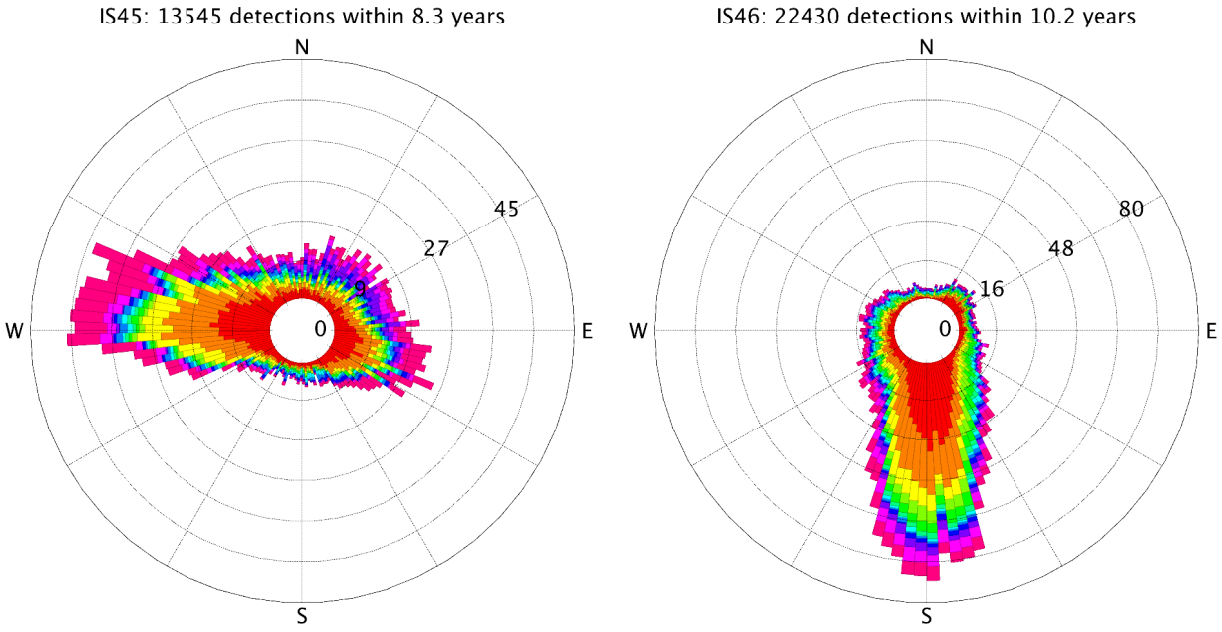

(a) IS45.

(b) IS46.

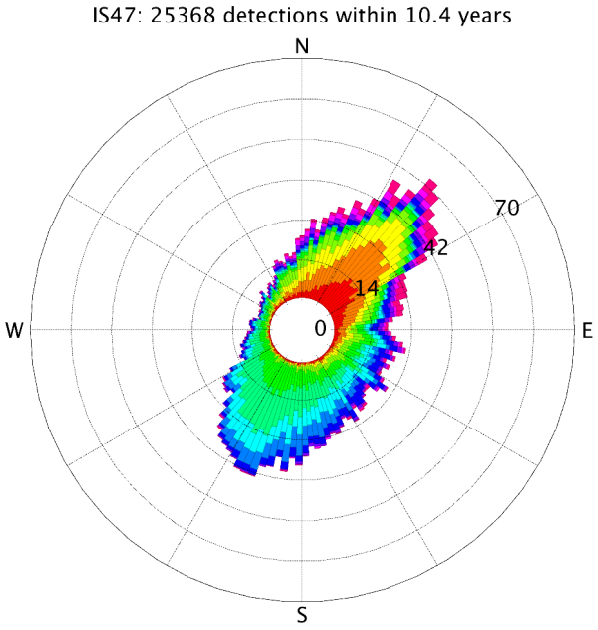

(c) IS47.

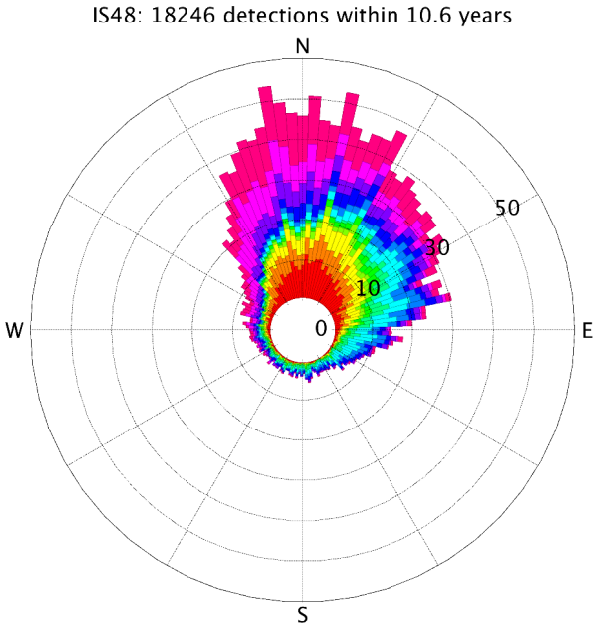

(d) IS48.

Figure D.3: As Fig. D.1, but for IS45 up to IS59.

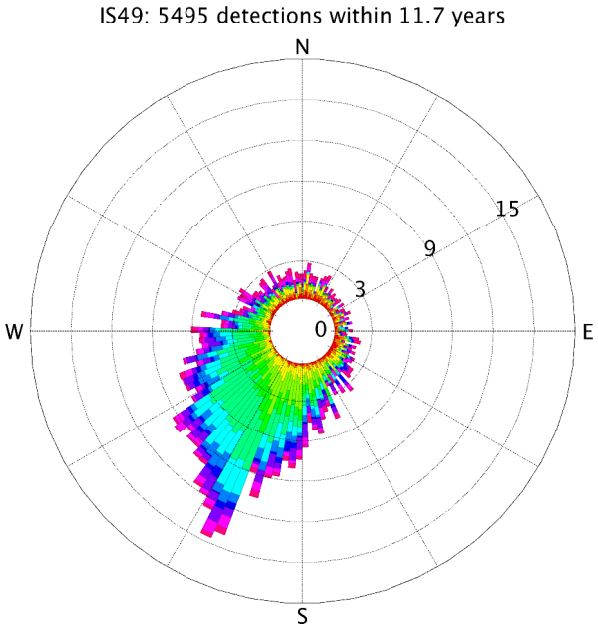

(e) IS49.

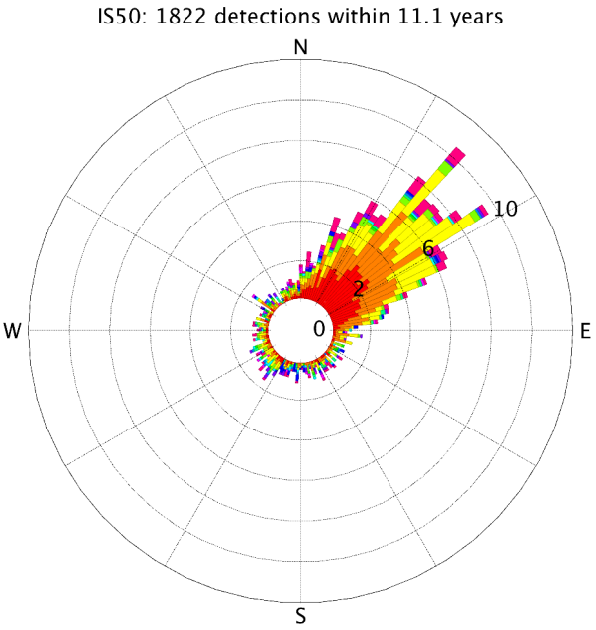

(f) IS50.

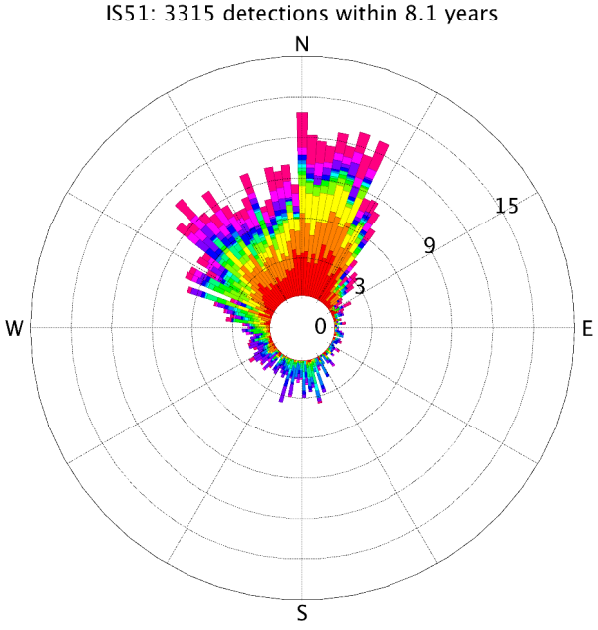

(g) IS51.

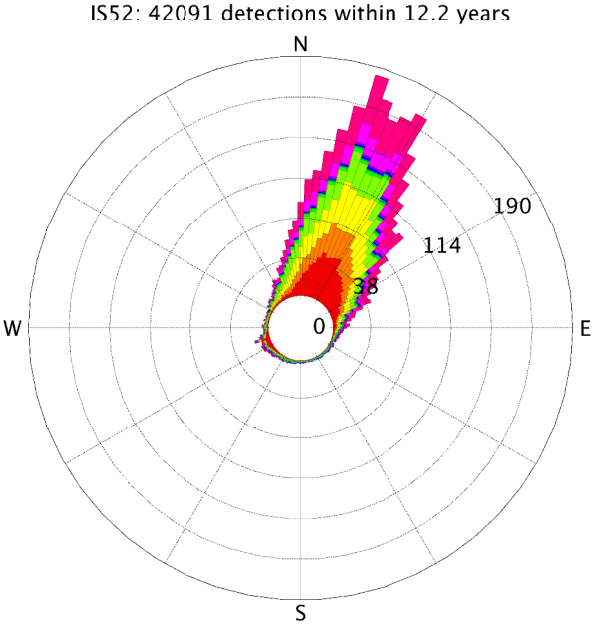

(h) IS52.

Figure D.3: (cont.)

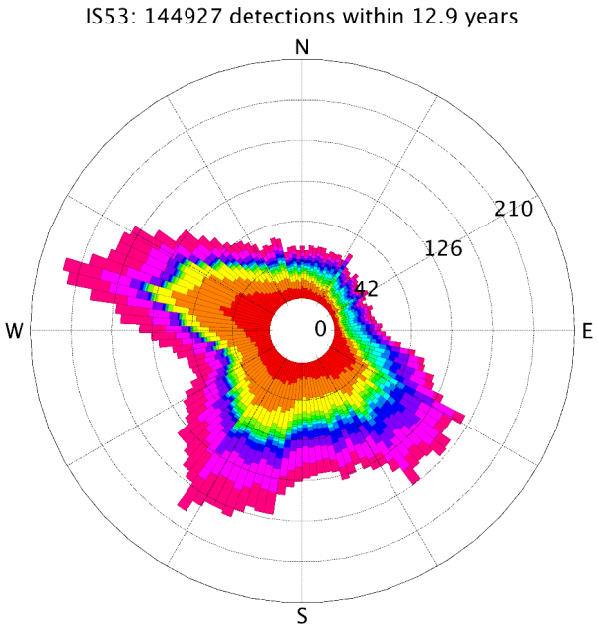

(i) IS53.

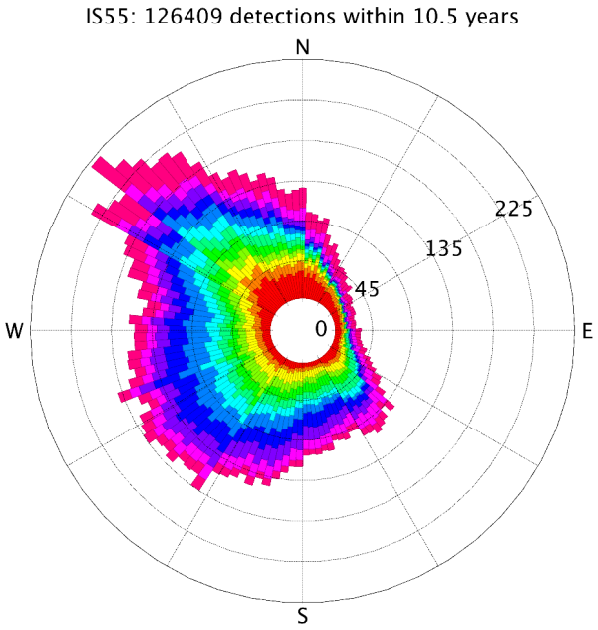

(j) IS55.

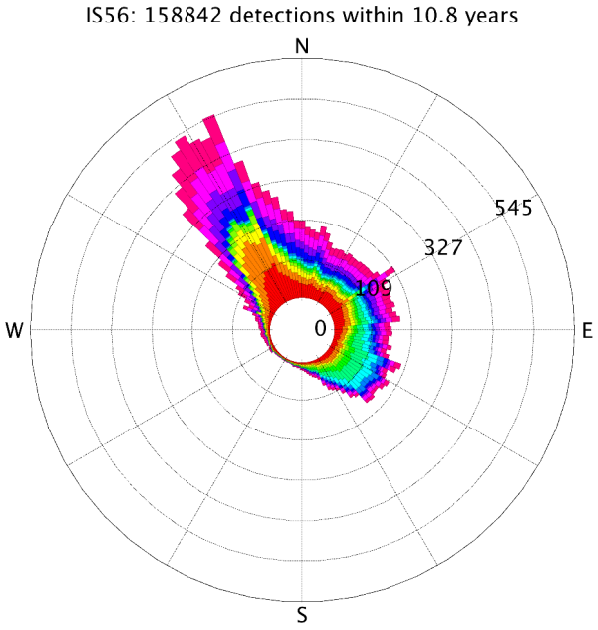

(k) IS56.

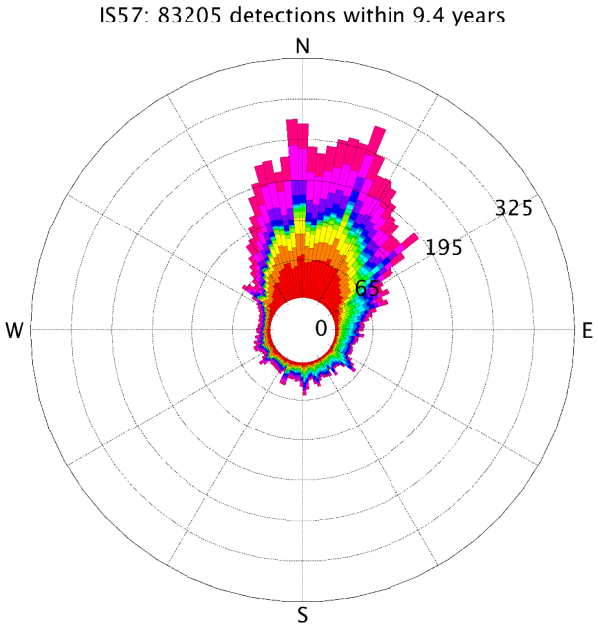

(l) IS57.

Figure D.3: (cont.)

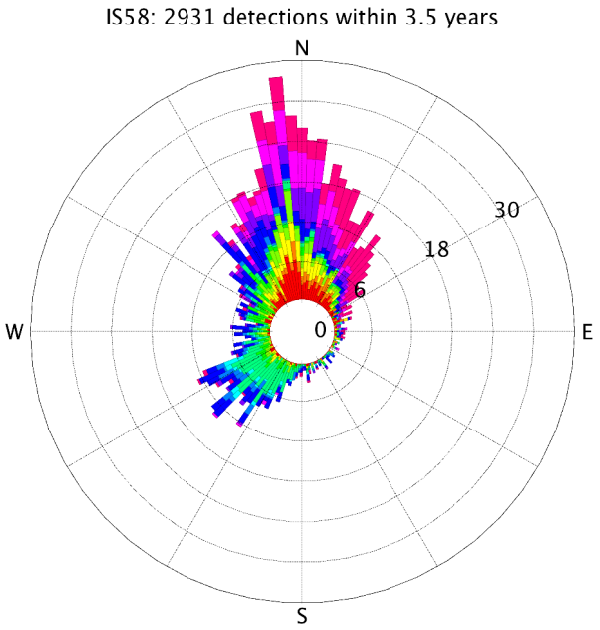

(m) IS58.

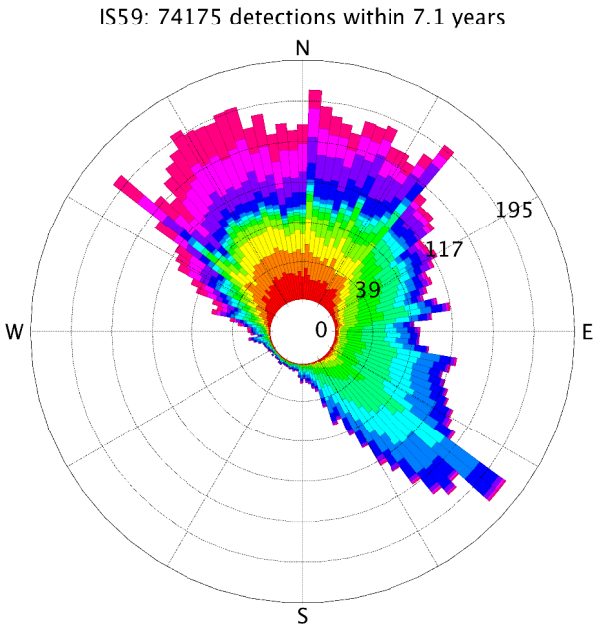

(n) IS59.

Figure D.3: (cont.)

D.2 Histograms of MAW detections at all IMS stations

Based on Fig. 6.3, the azimuthal distributions of detections at almost all IMS infrasound stations are shown for the four seasons in this section. The recently certified stations IS03, IS20 and IS60 are not included because they had only a short period of data coverage.

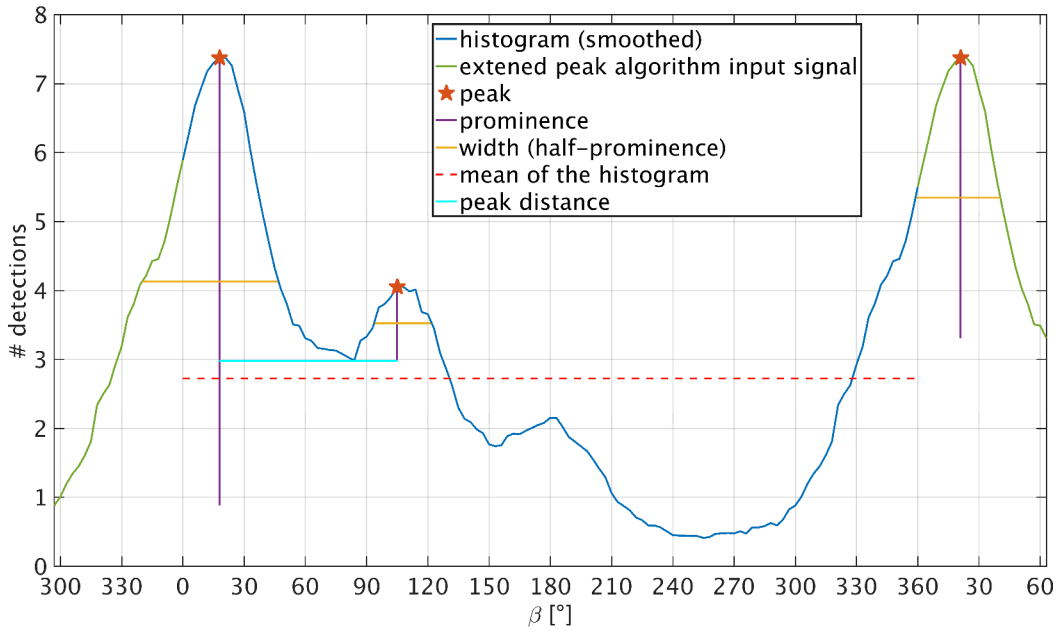

Figure D.4: Given the input parameters defined in Section 6.2, the MATLAB algorithm 'findpeaks' was used to evaluate the histogram peaks of azimuthal distribution. This figure highlights the parameters relevant to the peak selection of dominant back-azimuths for cross-bearing. The input for the algorithm was actually extended to correctly represent peaks and their parameters in northerly directions. Therefore, resulting duplicate peaks are easily identified and only considered once.

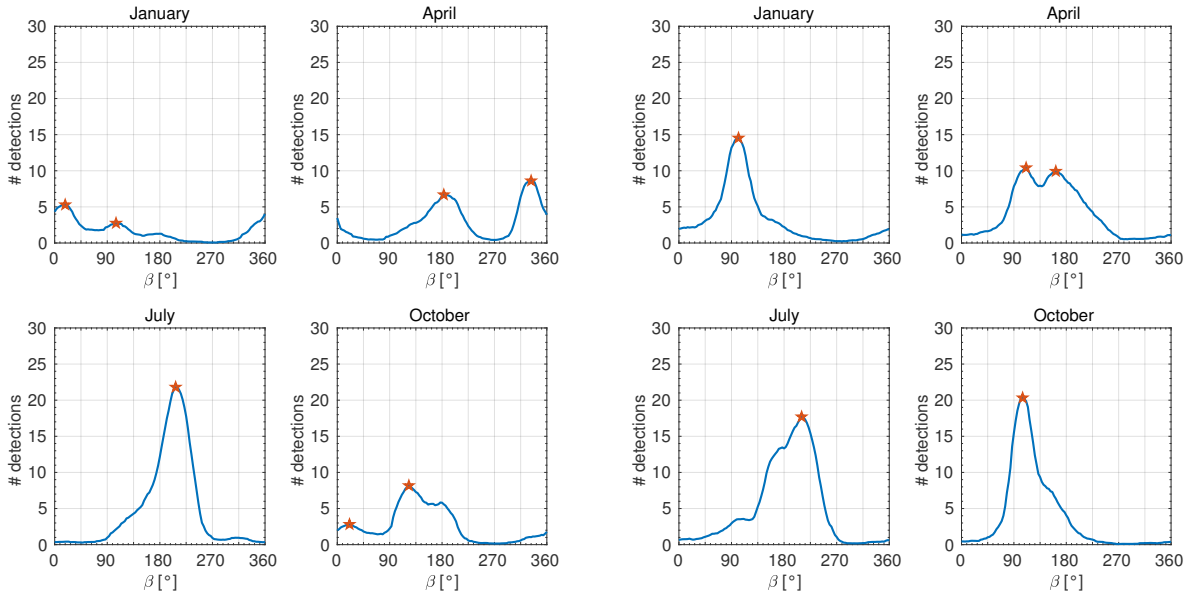

(a) IS04.

(b) IS05.

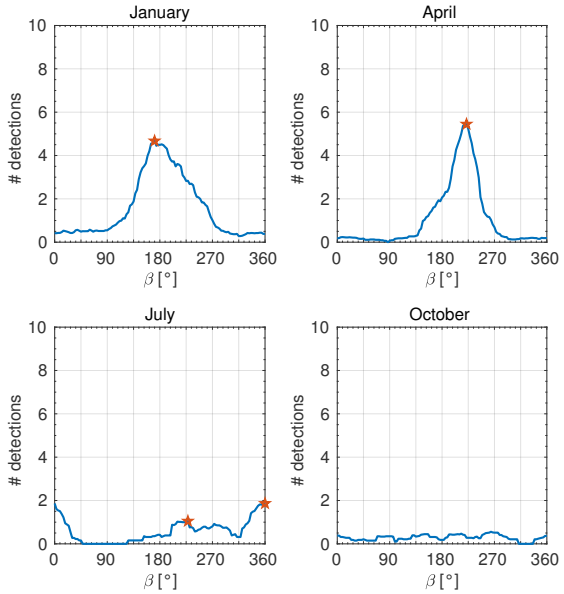

(c) IS06.

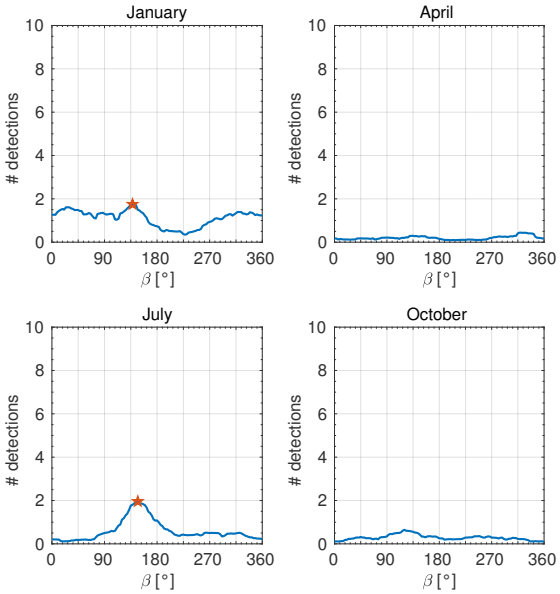

(d) IS07.

Figure D.5: As in Fig. 6.3, the azimuthal distribution of detections in the MAW frequency domain is shown for four months of the year. Histogram curves show the number of detections per 3° bin. A moving-average filter, with a span of 10 bins (i.e., 30°), was applied. Note the differing ordinates between the stations. Back-azimuths of the evaluated peaks (marked by a star) served as input for the cross-bearing method.

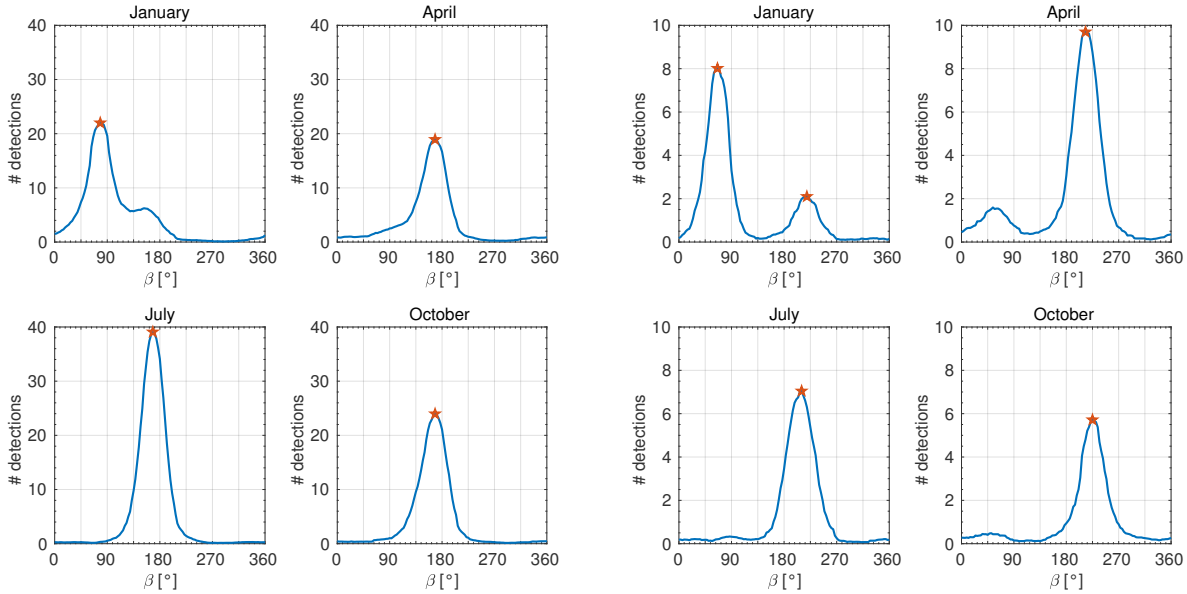

(d) IS08.

(e) IS09.

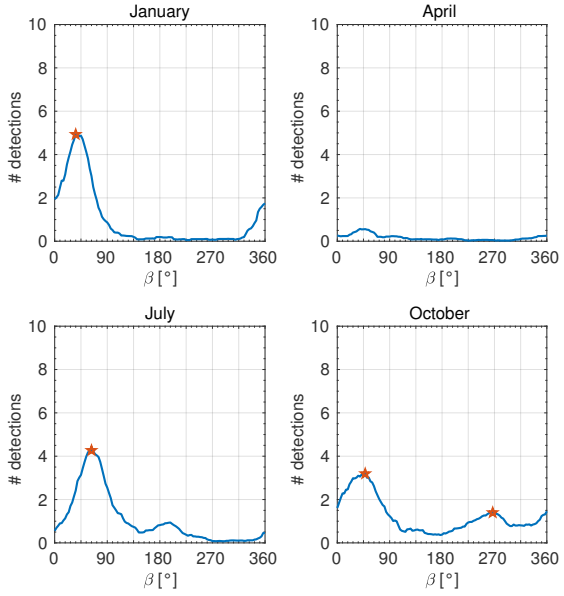

(f) IS11.

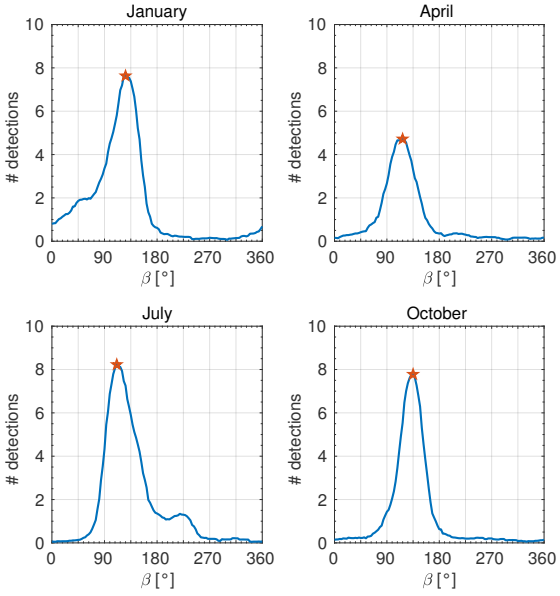

(g) IS13.

Figure D.5: (cont.)

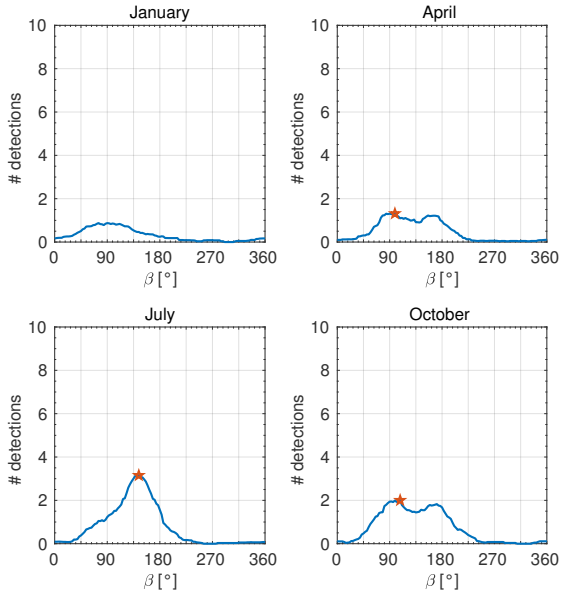

(i) IS14.

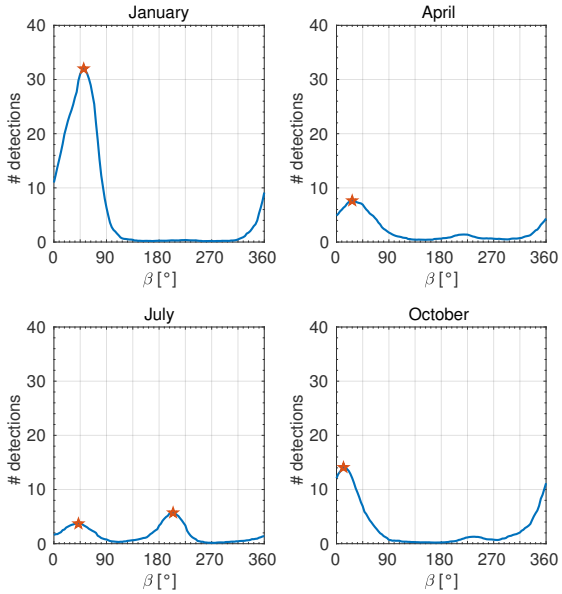

(j) IS17.

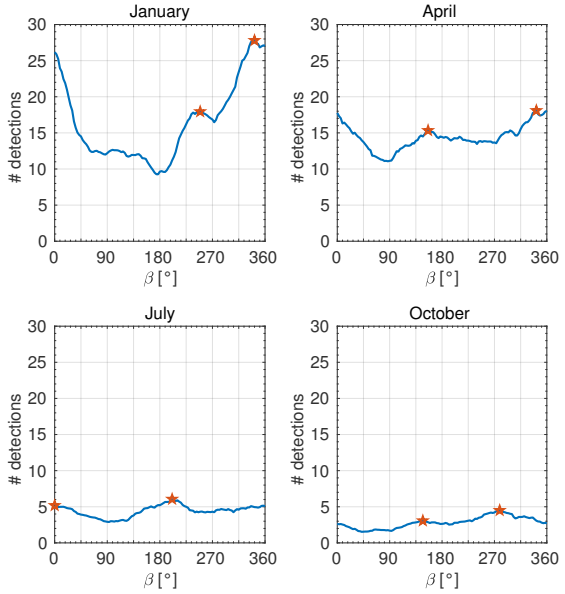

(k) IS18.

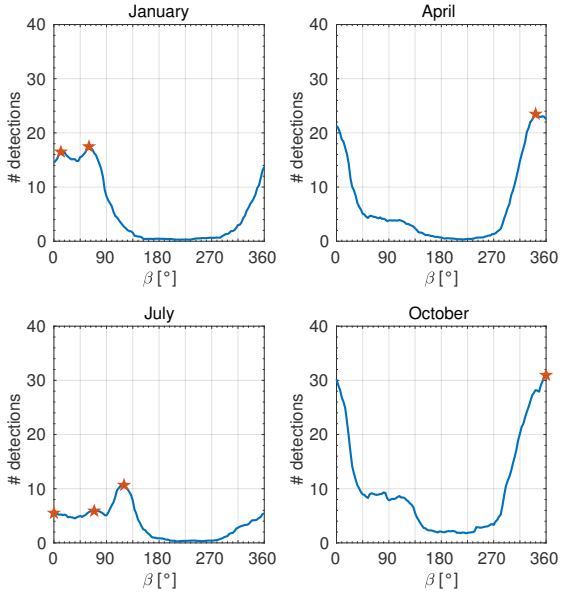

(l) IS19.

Figure D.5: (cont.)

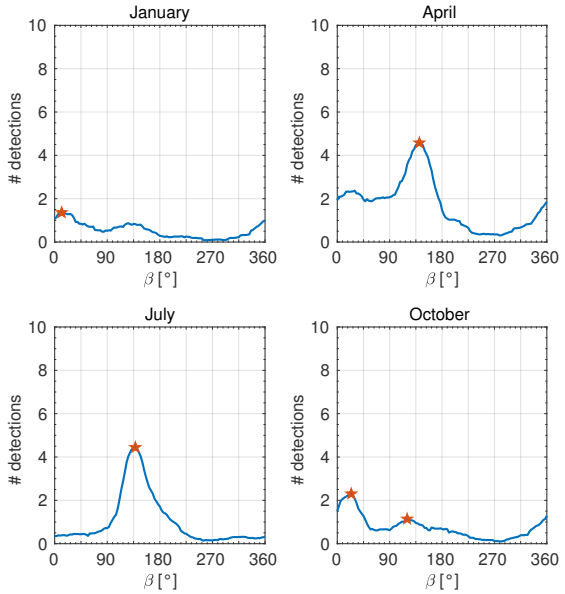

(m) IS21.

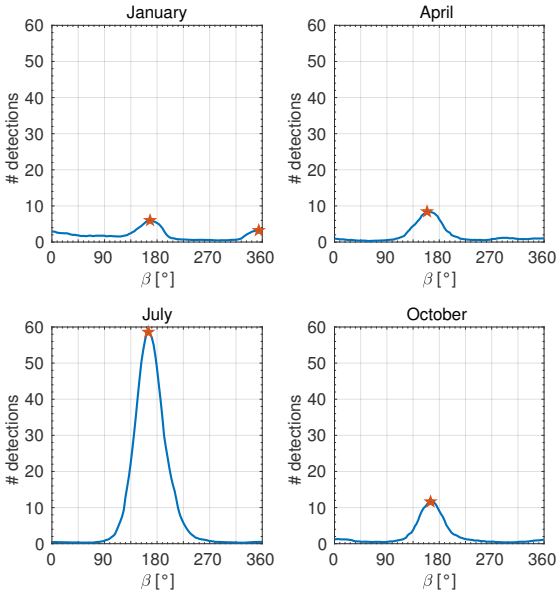

(n) IS22.

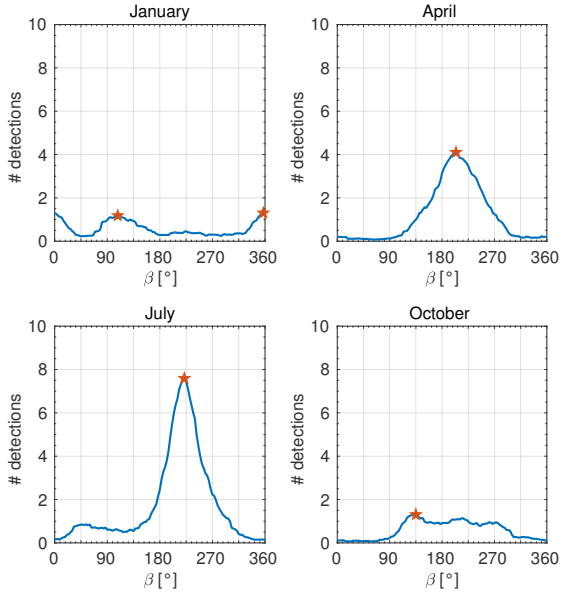

(o) IS23.

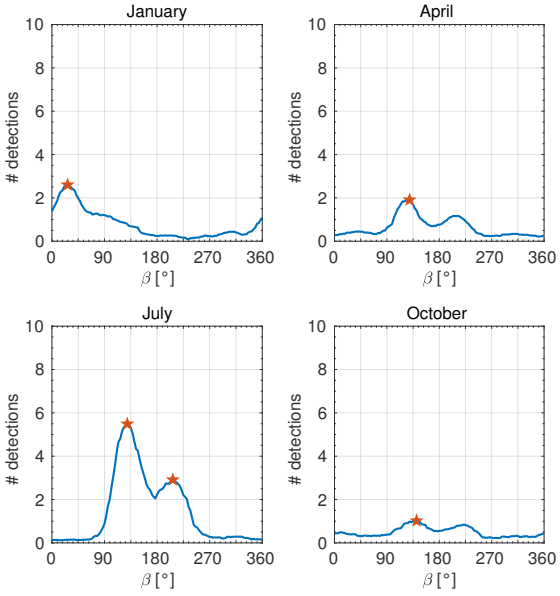

(p) IS24.

Figure D.5: (cont.)

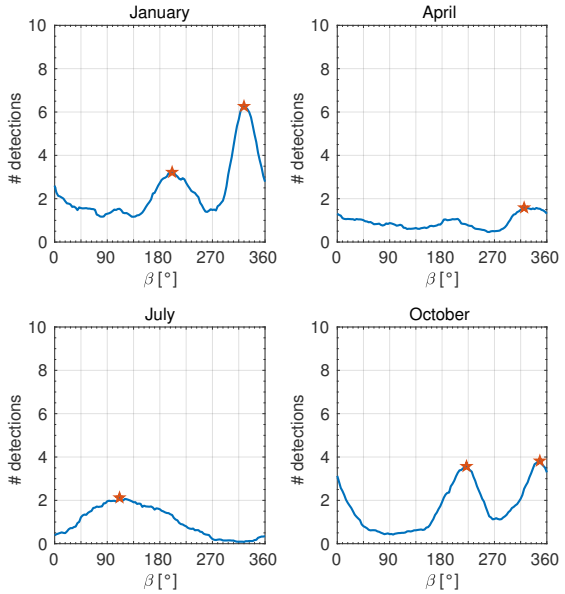

(a) IS26.

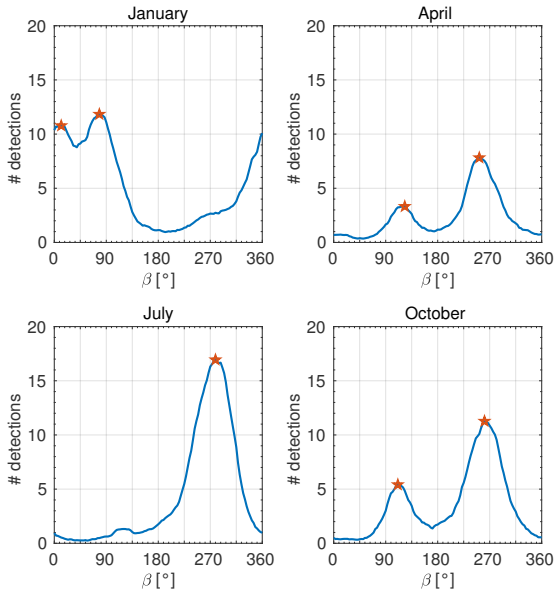

(b) IS27.

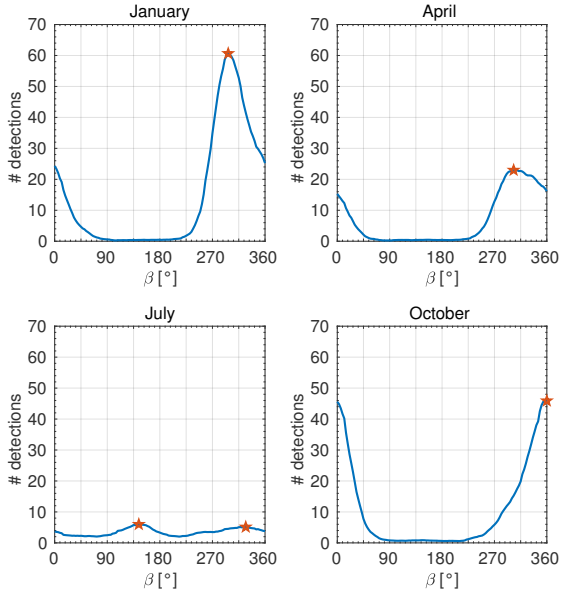

(c) IS30.

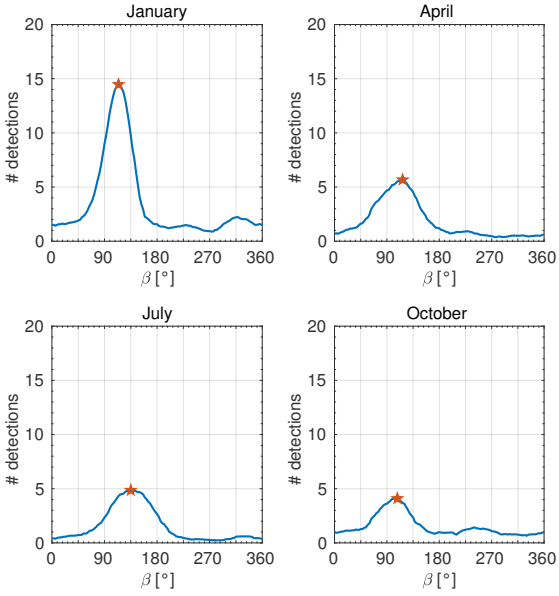

(d) IS31.

Figure D.6: As Fig. D.5, but for IS26 up to IS44.

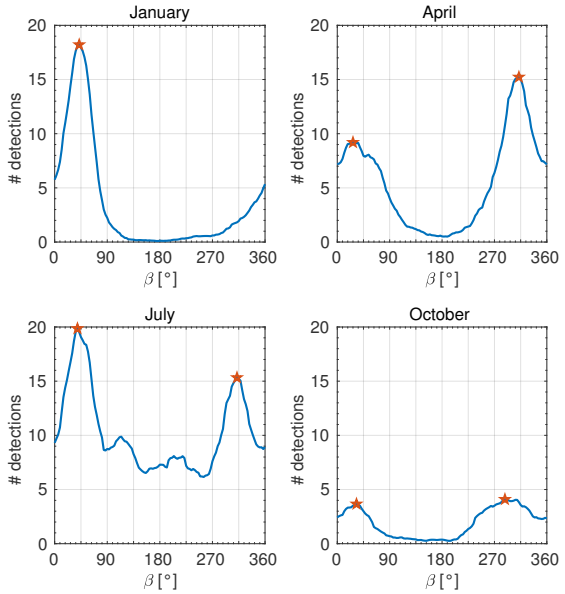

(d) IS32.

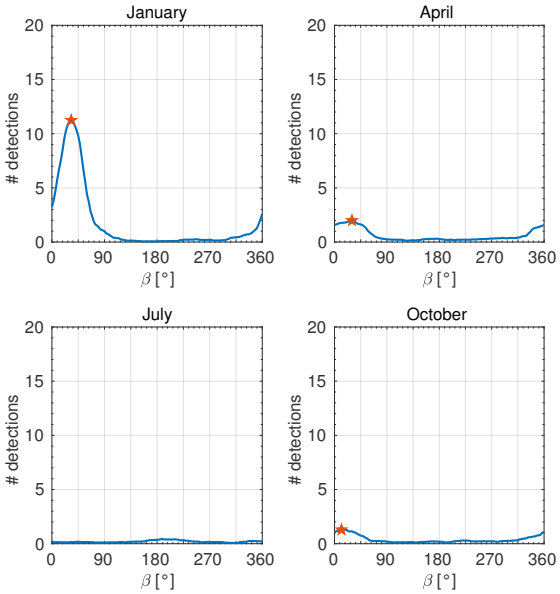

(e) IS33.

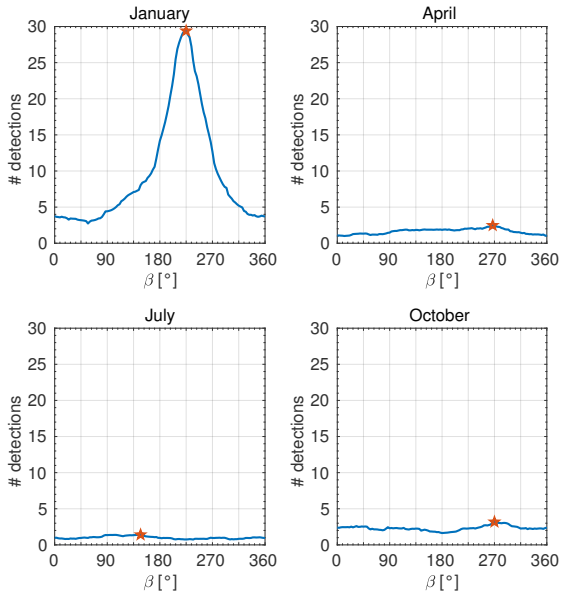

(f) IS34.

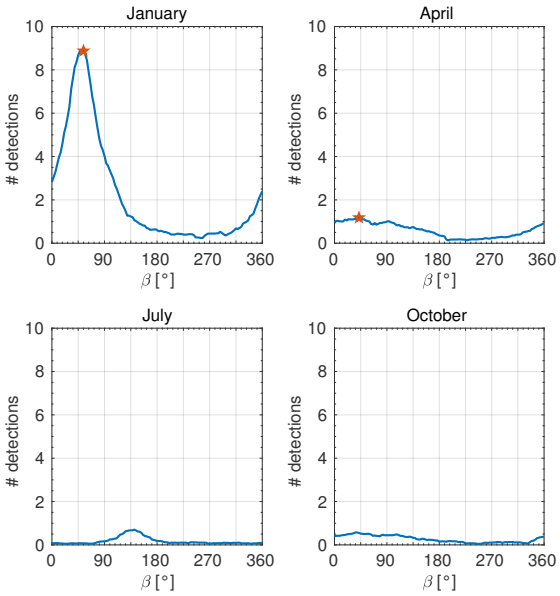

(g) IS35.

Figure D.6: (cont.)

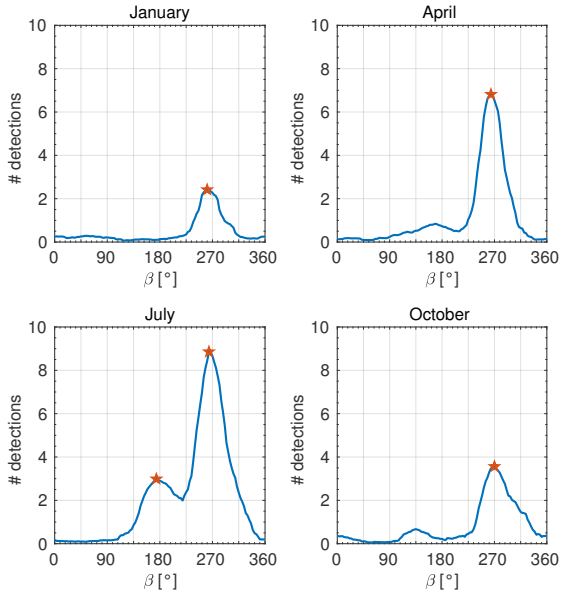

(i) IS36.

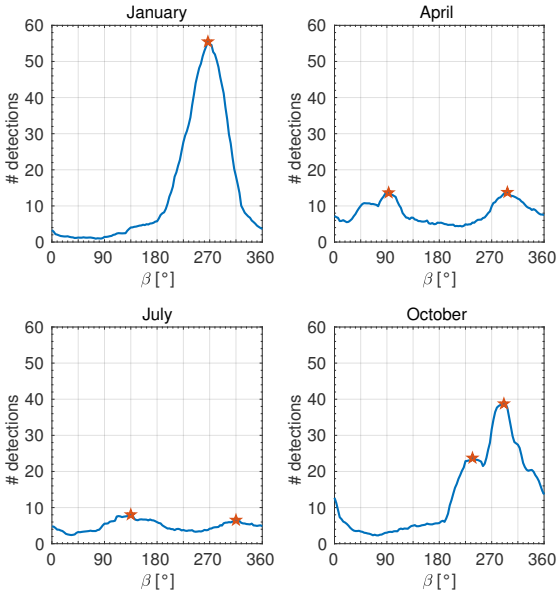

(j) IS37.

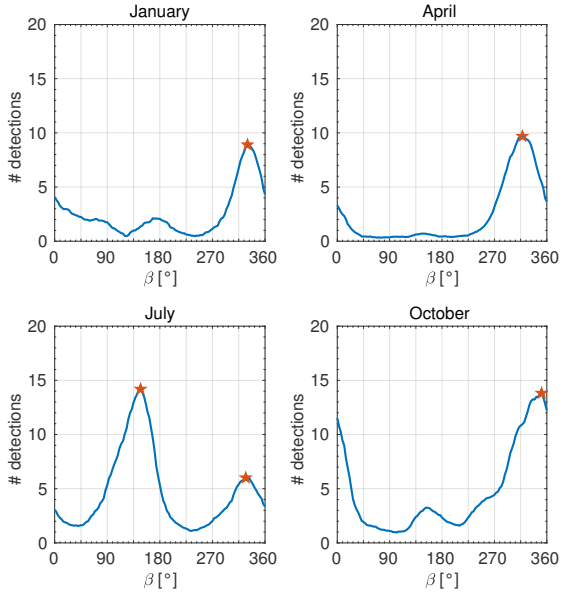

(k) IS39.

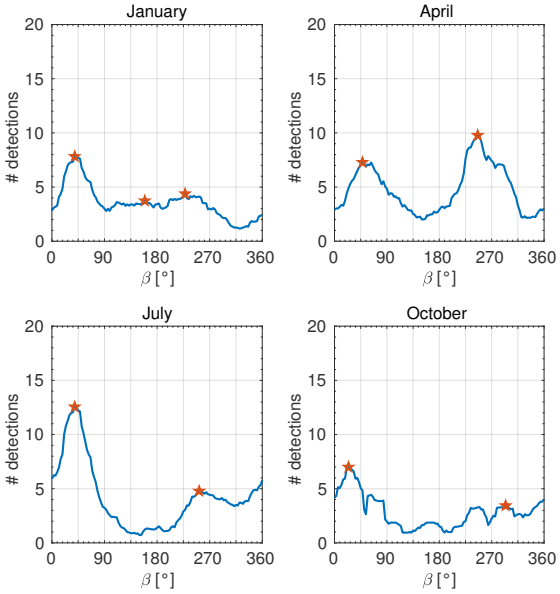

(l) IS40.

Figure D.6: (cont.)

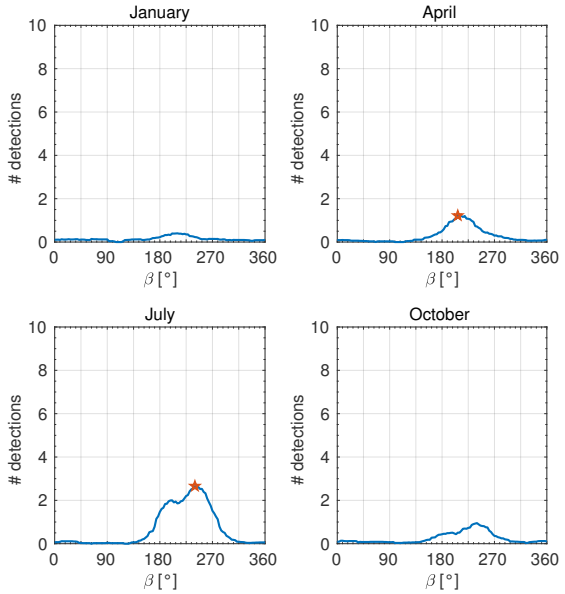

(m) IS41.

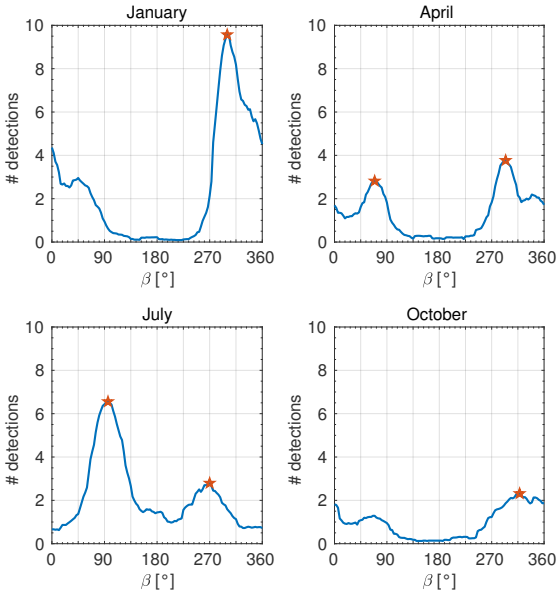

(n) IS42.

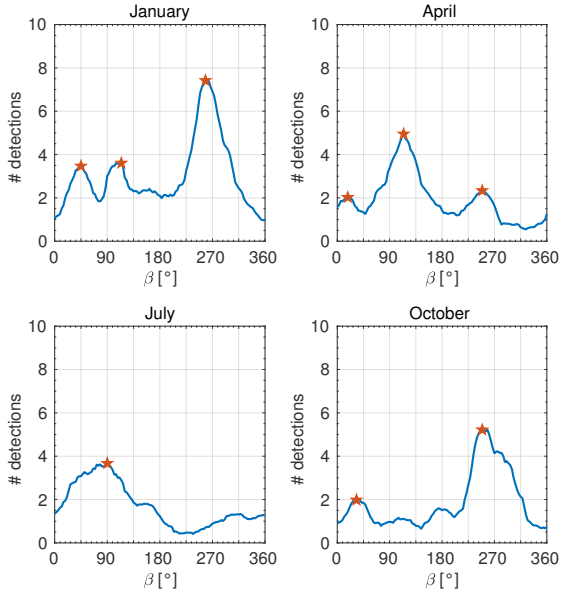

(o) IS43.

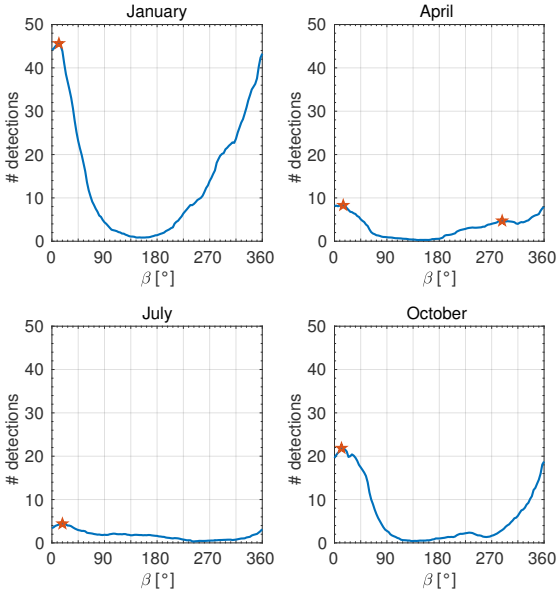

(p) IS44.

Figure D.6: (cont.)

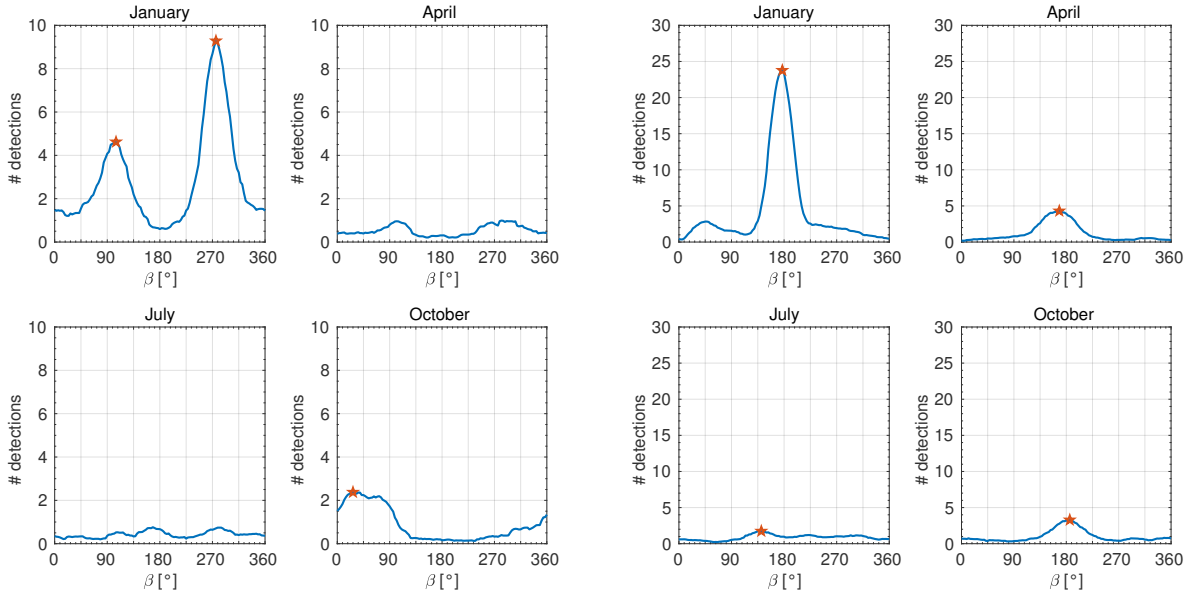

(a) IS45.

(b) IS46.

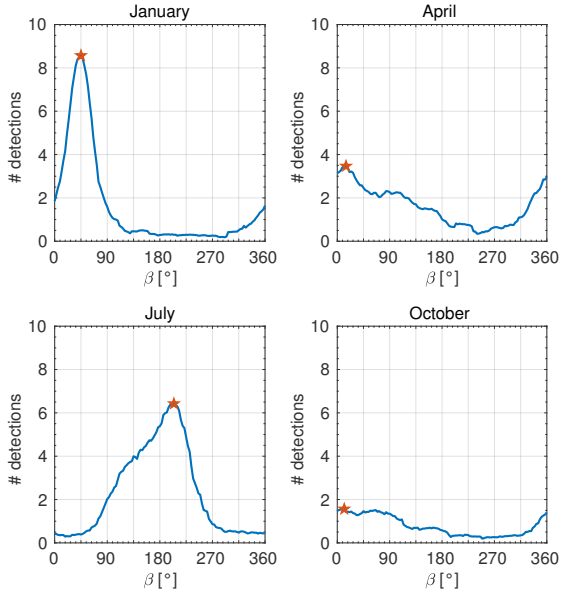

(c) IS47.

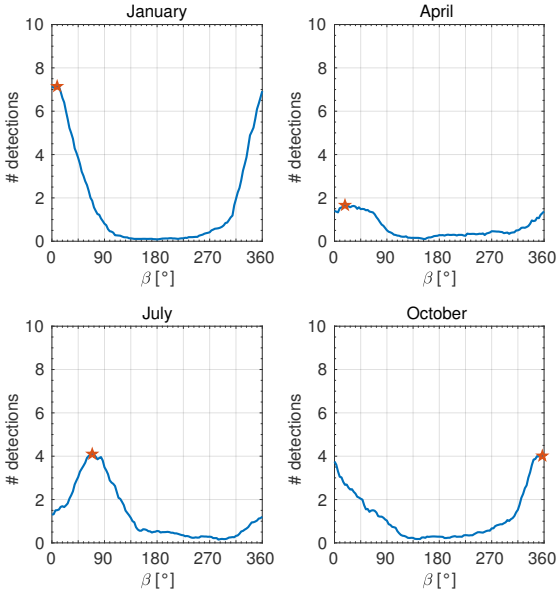

(d) IS48.

Figure D.7: As Fig. D.5, but for IS45 up to IS59.

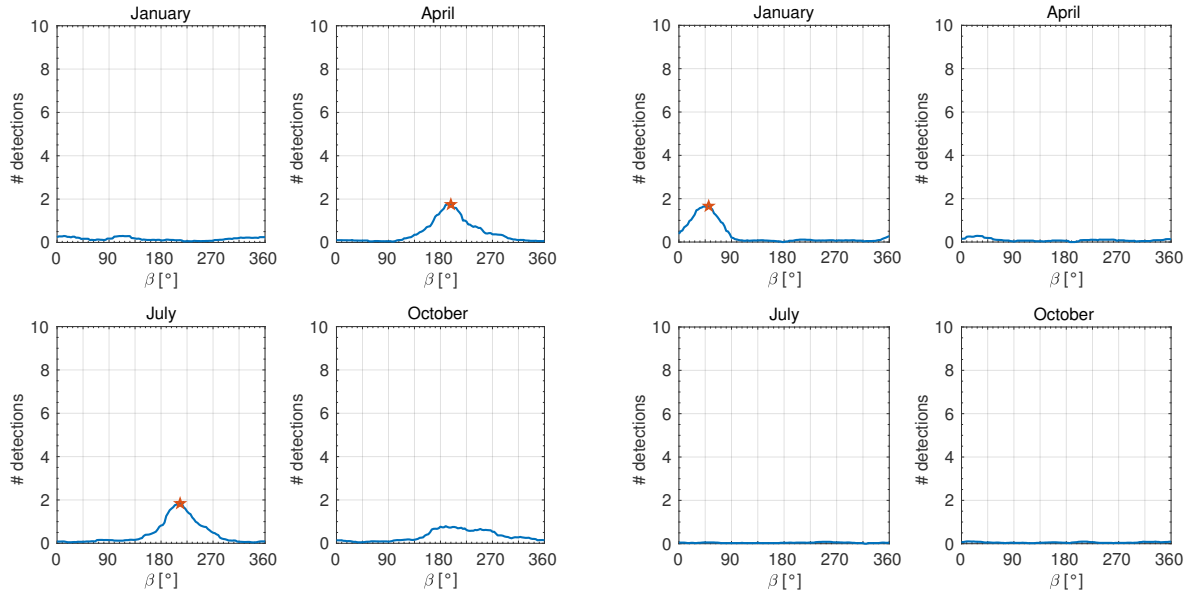

(d) IS49.

(e) IS50.

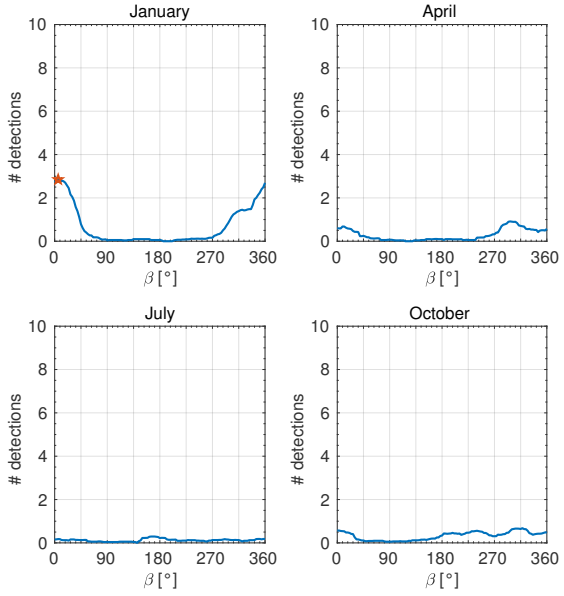

(f) IS51.

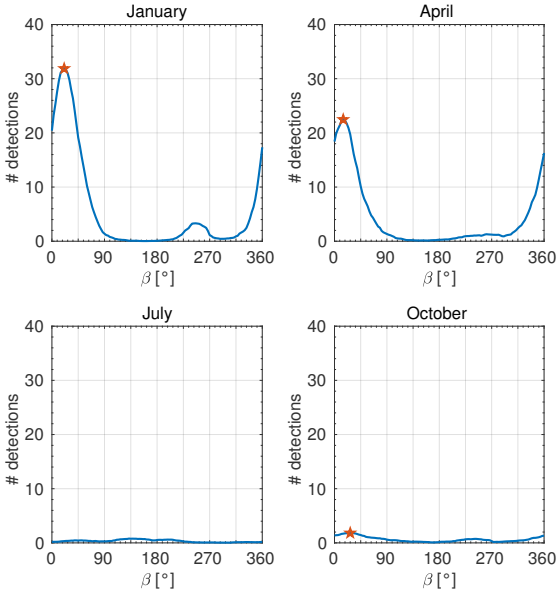

(g) IS52.

Figure D.7: (cont.)

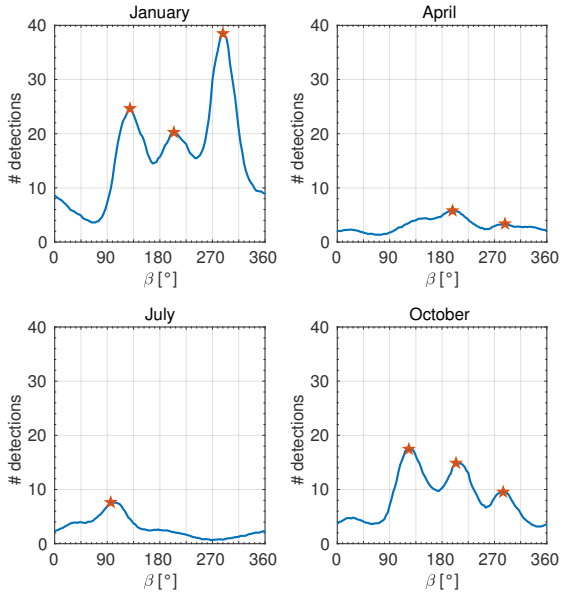

(i) IS53.

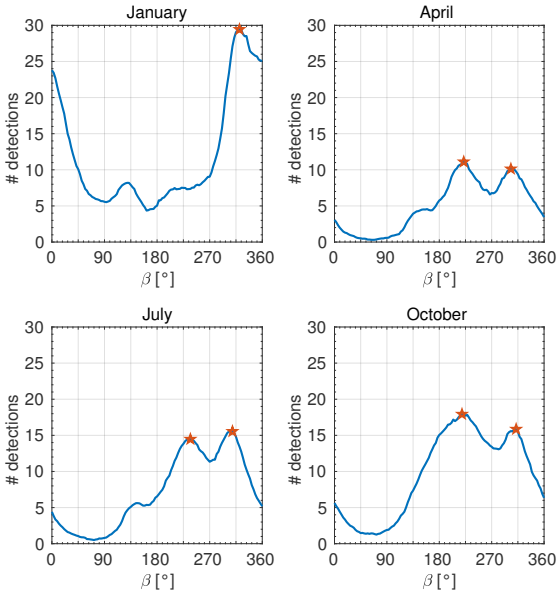

(j) IS55.

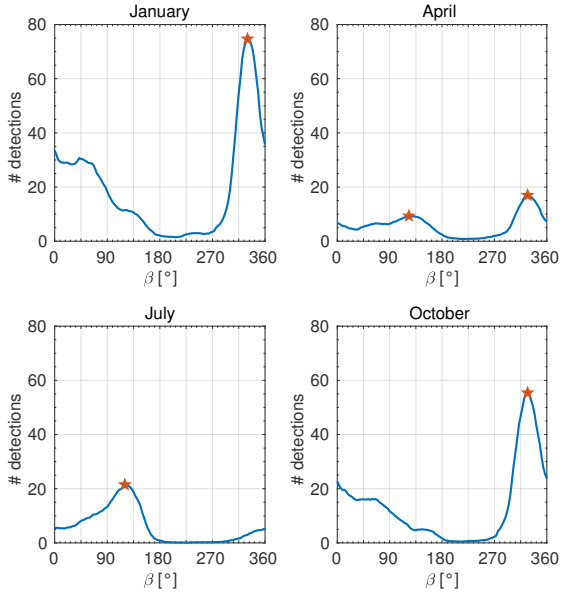

(k) IS56.

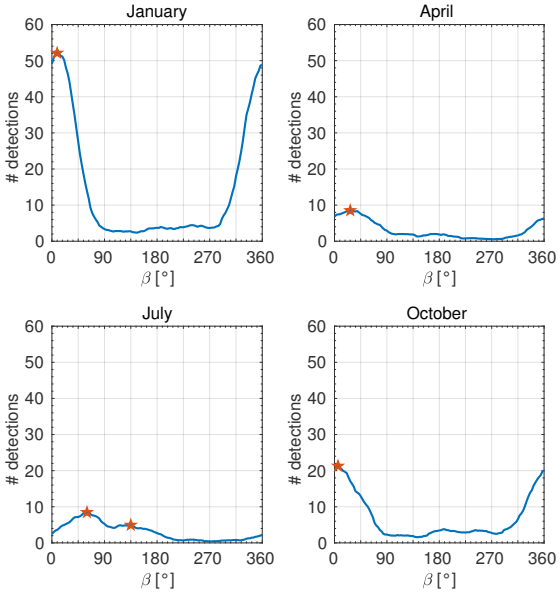

(l) IS57.

Figure D.7: (cont.)

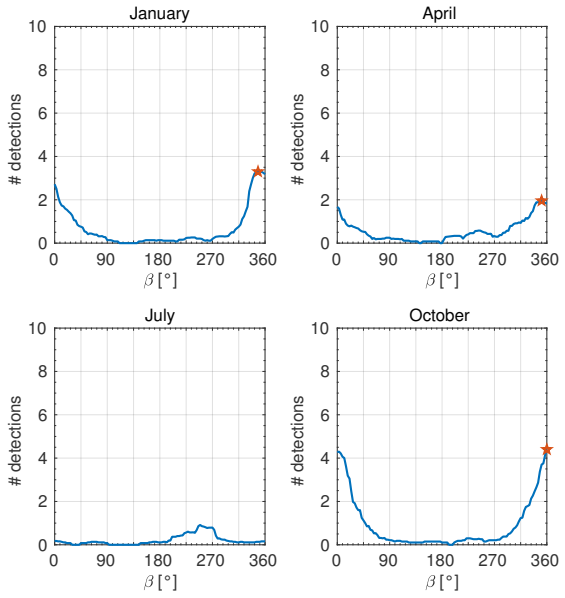

(m) IS58.

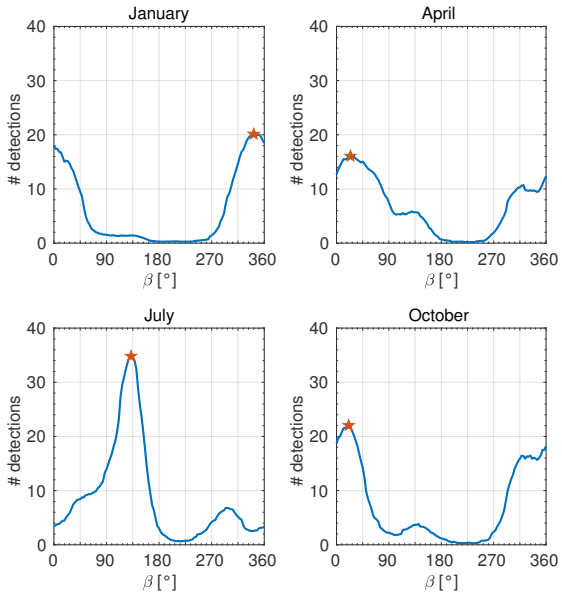

(n) IS59.

Figure D.7: (cont.)

D.3 MAW hotspots

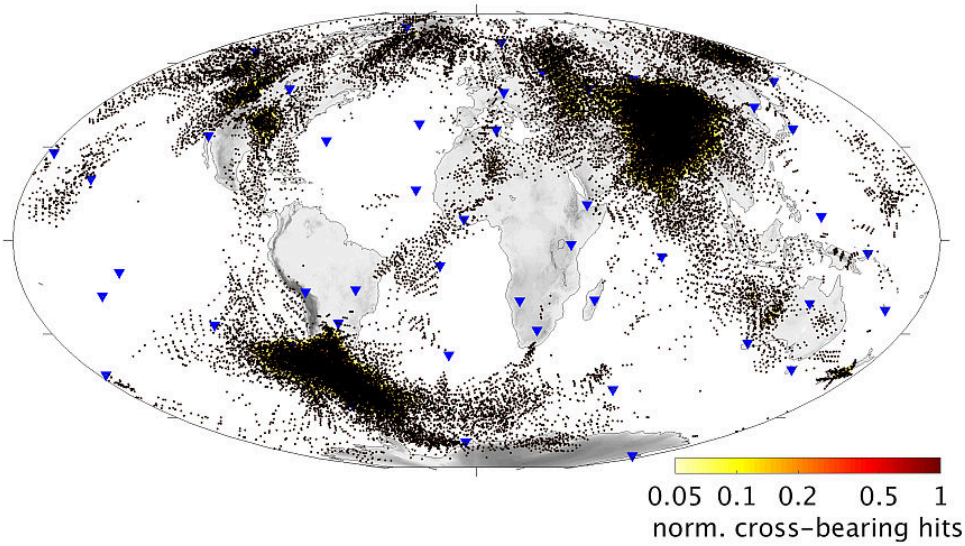

Figure D.8: As Fig. 6.4, but showing the resulting locations from the cross-bearing method superimposed.

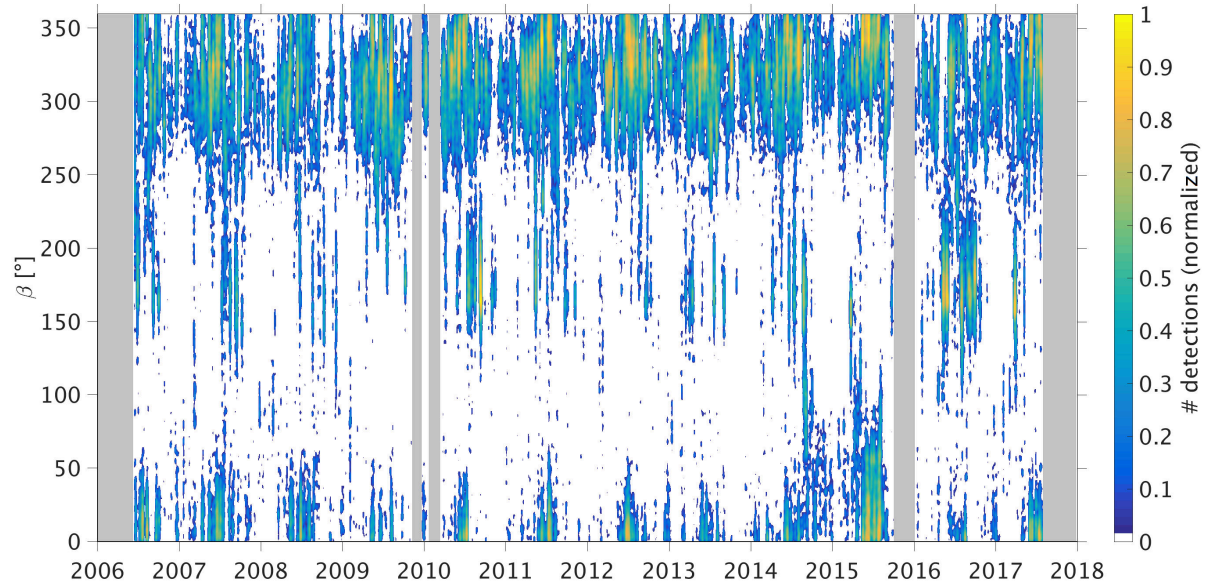

(a) Back-azimuth.

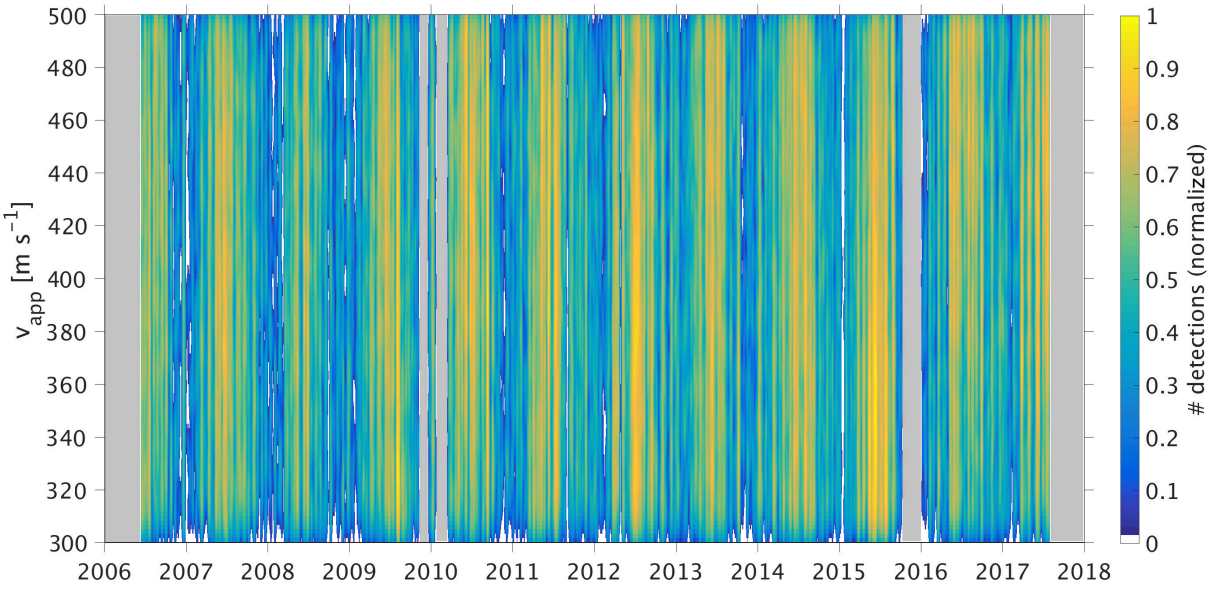

(b) Apparent phase velocity.

Figure D.9: Same as Fig. 6.6(b), but showing the back-azimuth and the apparent phase velocity of detections at IS02 (evaluated per 7 d and 3° or 10 m s^{-1}, respectively).

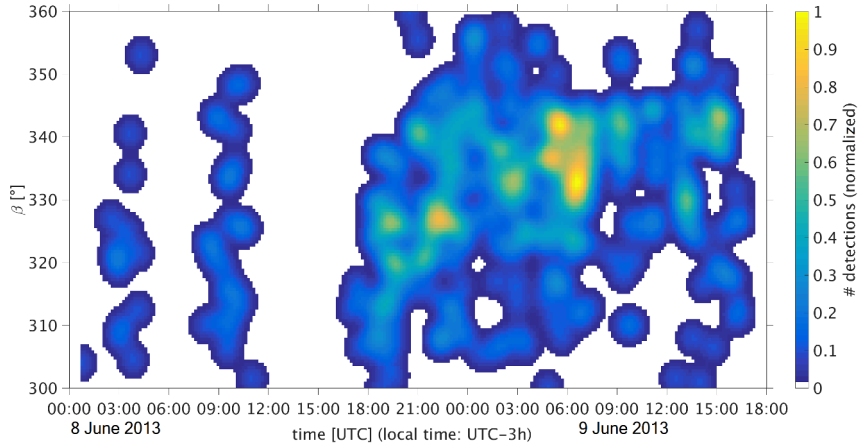

(a) Back-azimuth β.

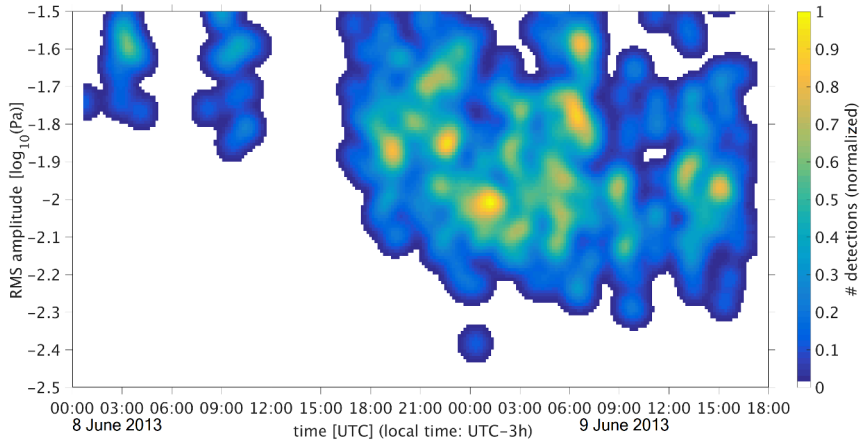

(b) RMS amplitude.

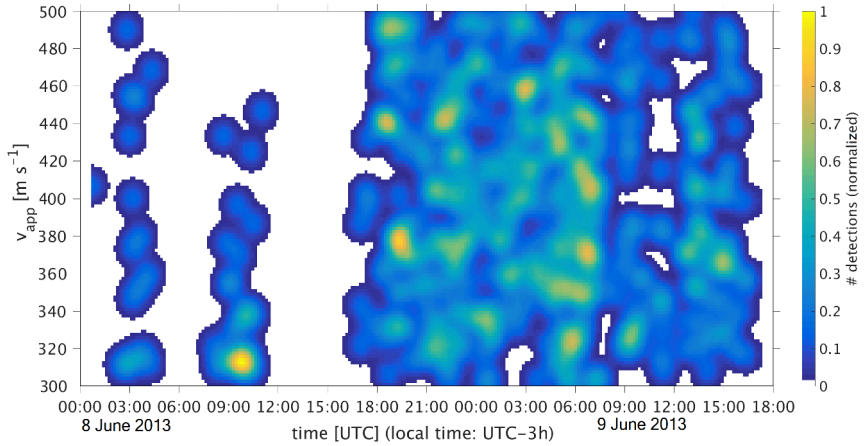

(c) Phase velocity.

Figure D.10: Detected parameters of a MAW event with a duration of around 24 h (IS02).

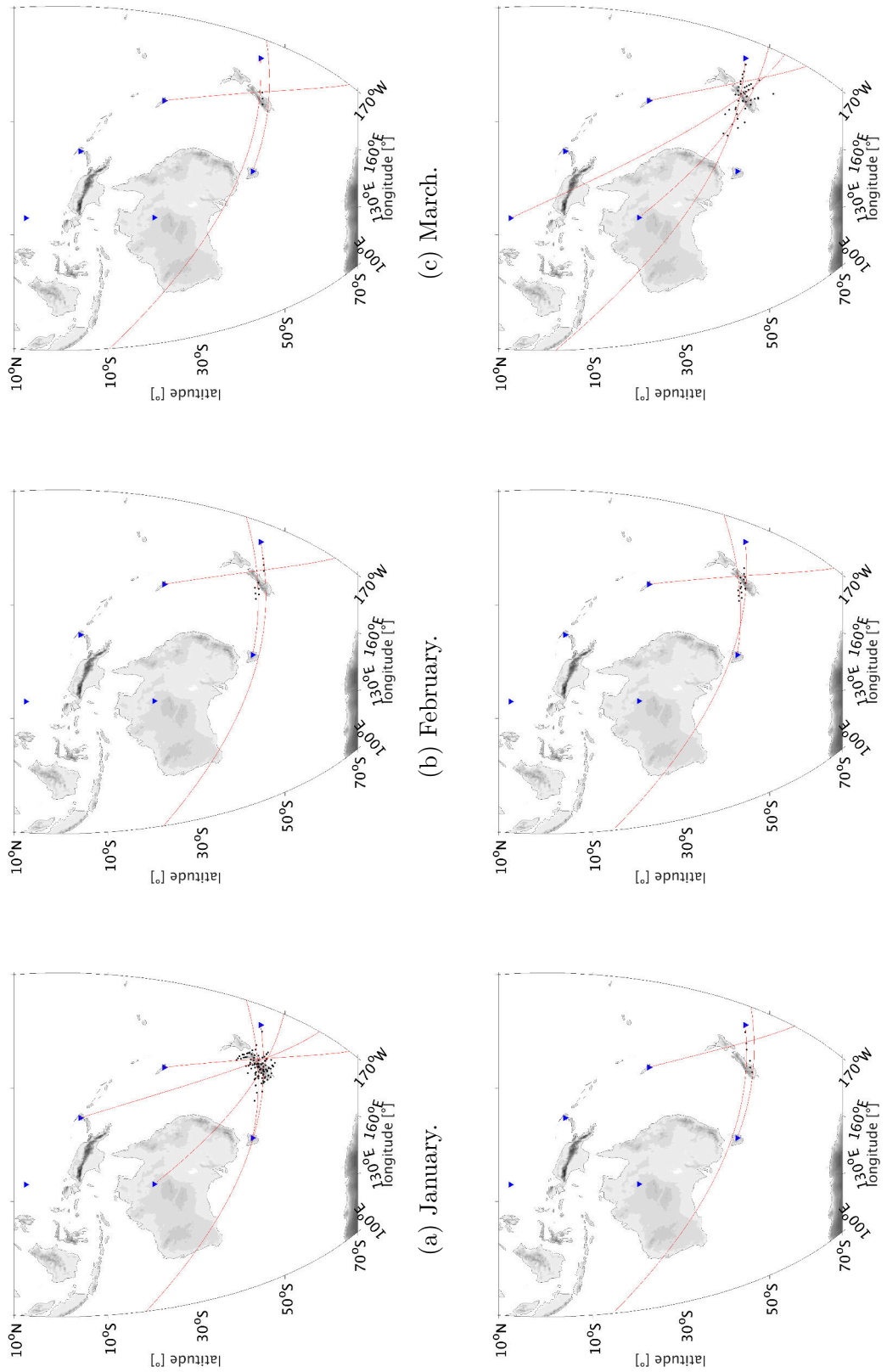

(a) January. (b) February. (c) March.

(d) April. (e) May. (f) June.

Figure D.11: Monthly cross-bearing results are shown for New Zealand, considering IMS stations where the dominant back-azimuth (red line along the great circle) coincides with the hotspot in at least one of the months.

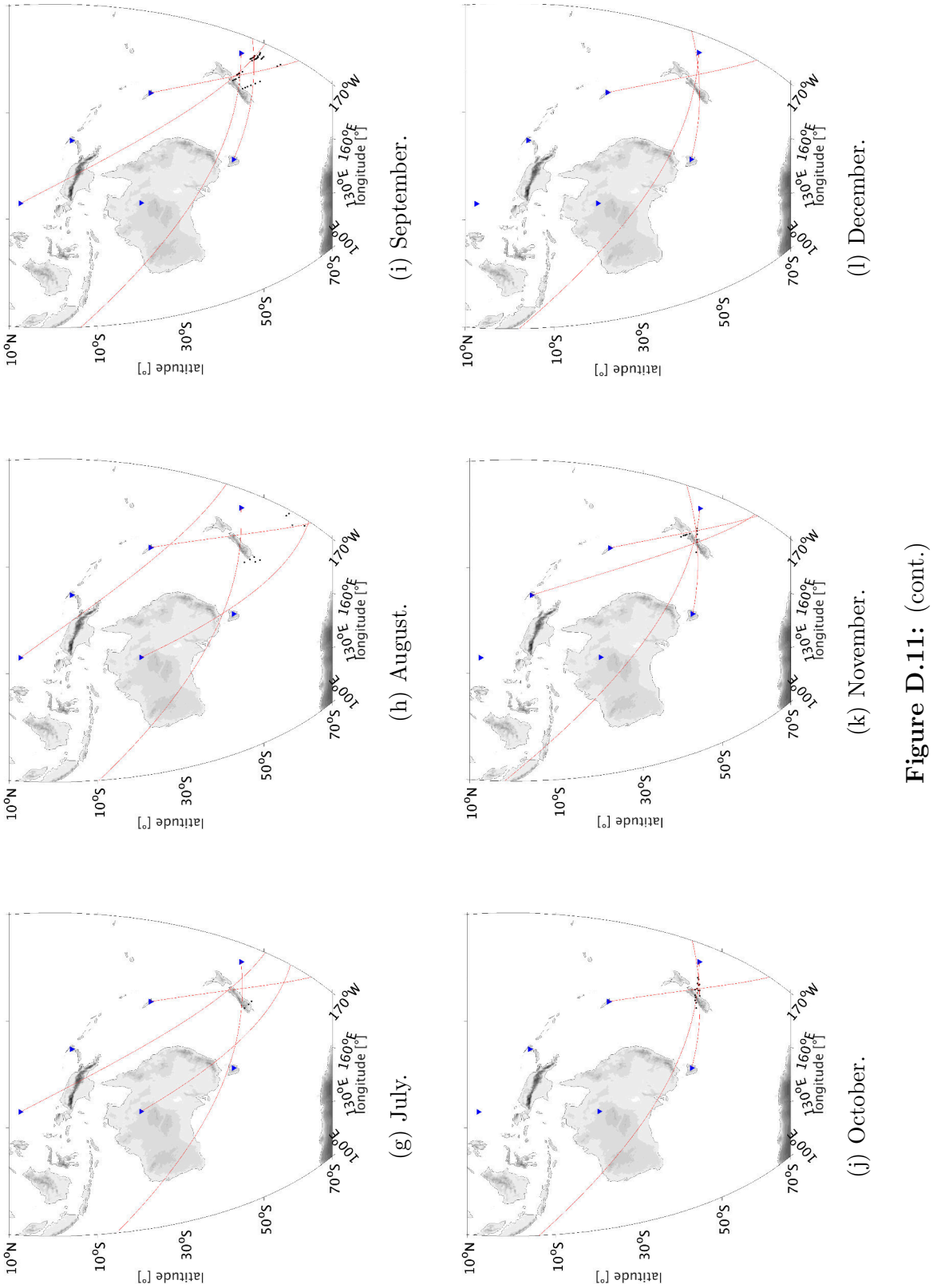

(g) July. (h) August. (i) September.

(j) October. (k) November. (l) December.

Figure D.11: (cont.)

D.4 Ray-tracing examples for the southern Andes and New Zealand

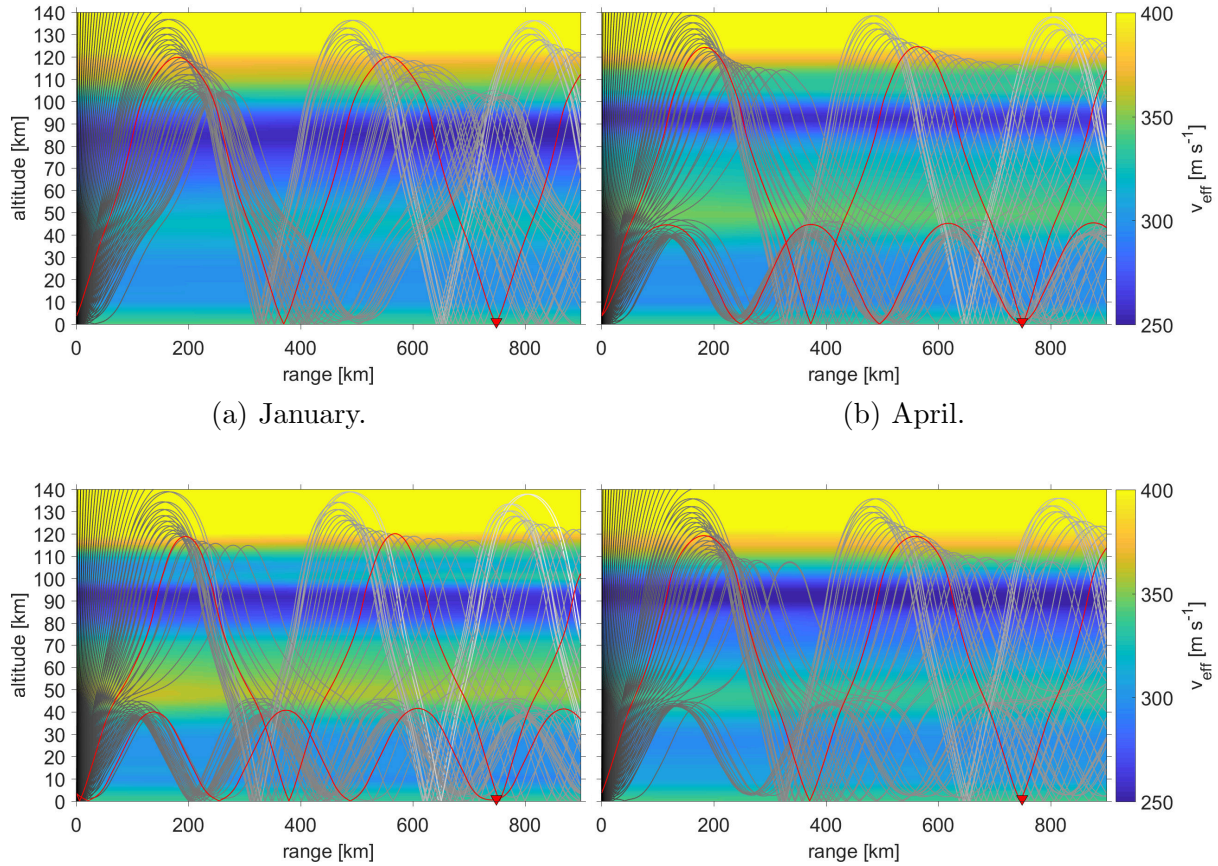

(a) January. (b) April.

(c) July. (d) October.

Figure D.12: Ray-tracing paths are shown for January, April, July and October 2016. The source (southern Andes) at 0 km on the left is elevated by 3,200 m. The receiver (red triangle) is IS02 near Ushuaia (Argentina) at a distance of 749 km from the chosen source (49°S, 73°W). The 'best rays' are depicted in red.

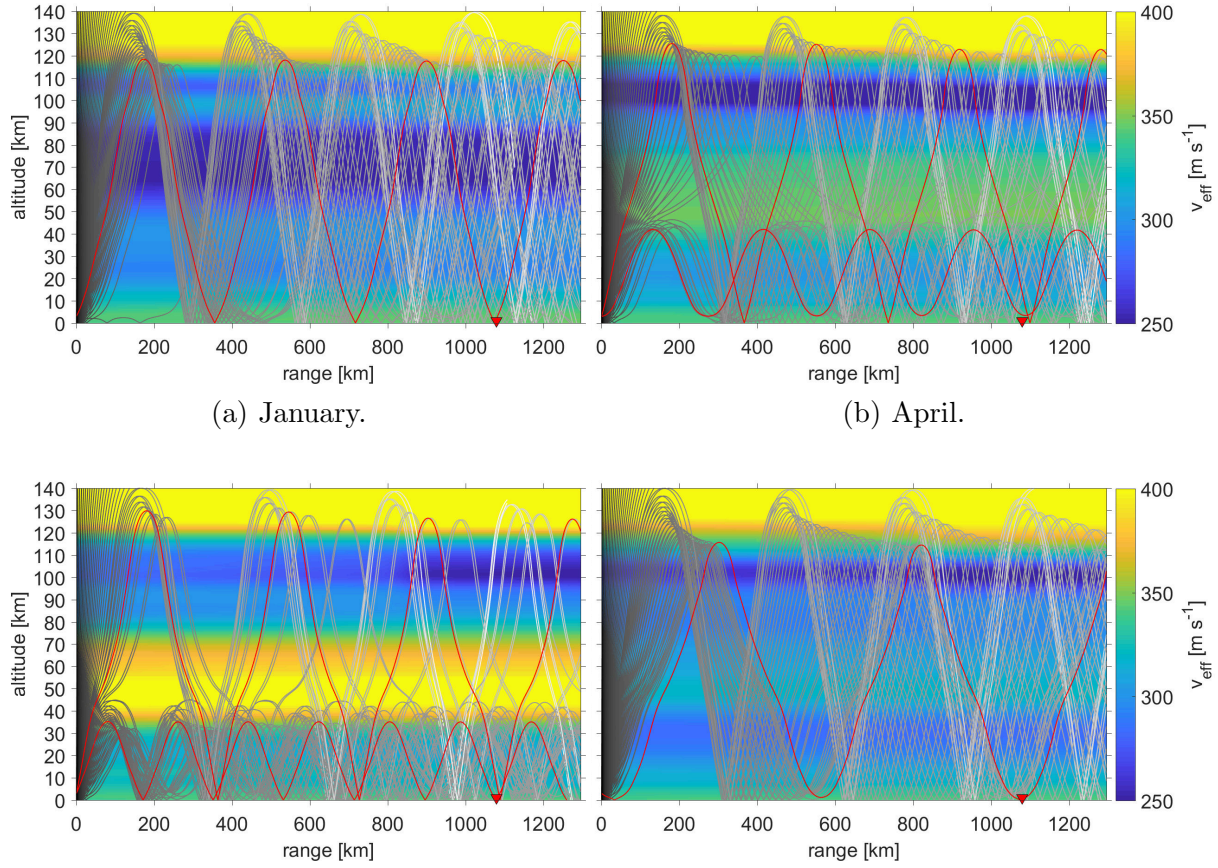

(a) January. (b) April.

(c) July. (d) October.

Figure D.13: Ray-tracing paths are shown for January, April, July and October 2016. The source (South Island, New Zealand) at 0 km on the left is elevated by 3,000 m. The receiver (red triangle) is IS36, east of New Zealand, at a distance of 1,080 km from the chosen source location (44°S, 170°E). The 'best rays' are depicted in red.

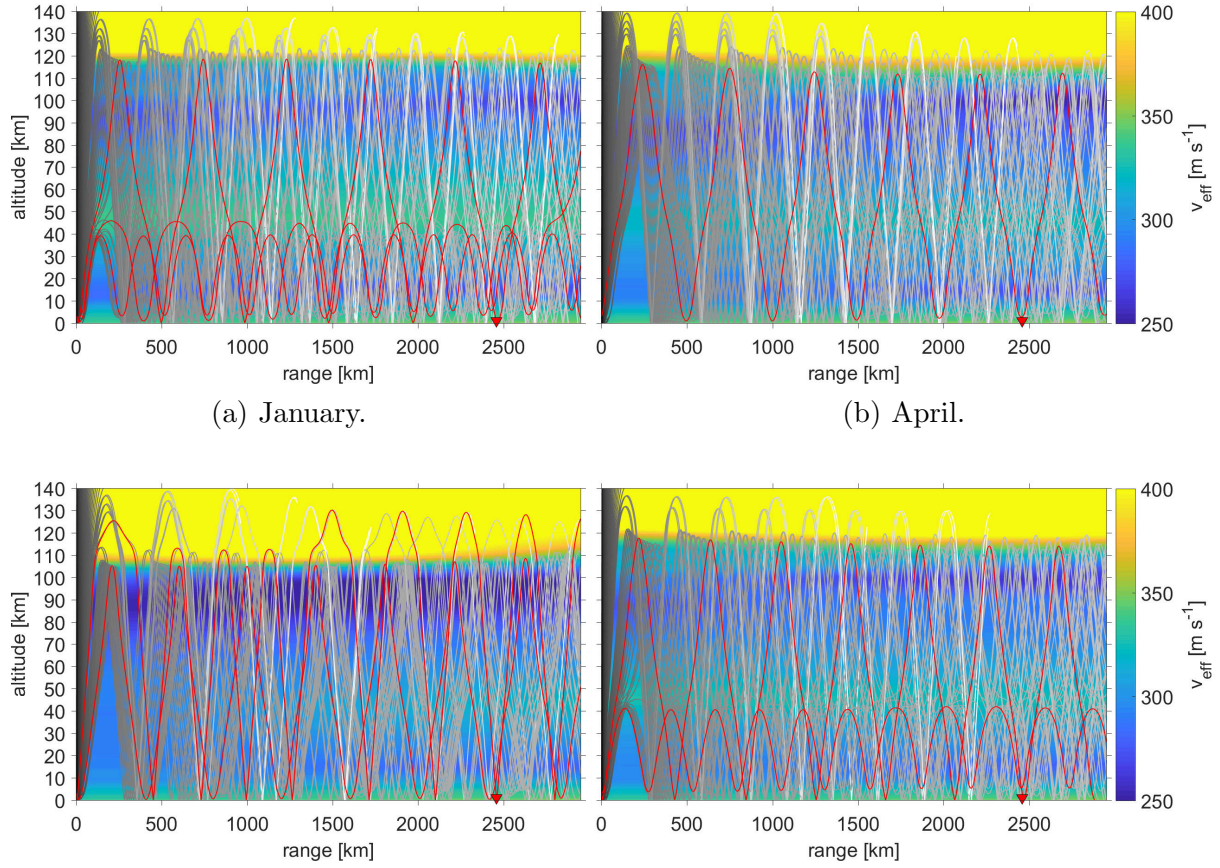

(a) January. (b) April.

(c) July. (d) October.

Figure D.14: Ray-tracing paths are shown for January, April, July and October 2016. The source (South Island, New Zealand) at 0 km on the left is elevated by 3,000 m. The receiver (red triangle) is IS22 (New Caledonia), north-northwest of New Zealand, at a distance of 2,460 km from the chosen source location (44°S, 170°E).

D.5 Tropospheric wind conditions over the southern Andes and New Zealand

Andes — IS02

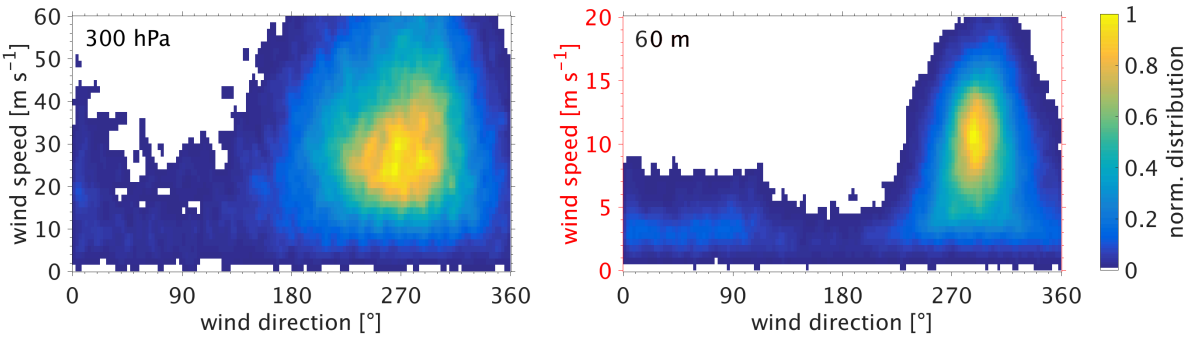

(a) Climatological distribution of MERRA-2 wind speeds vs wind directions (2004–2017).

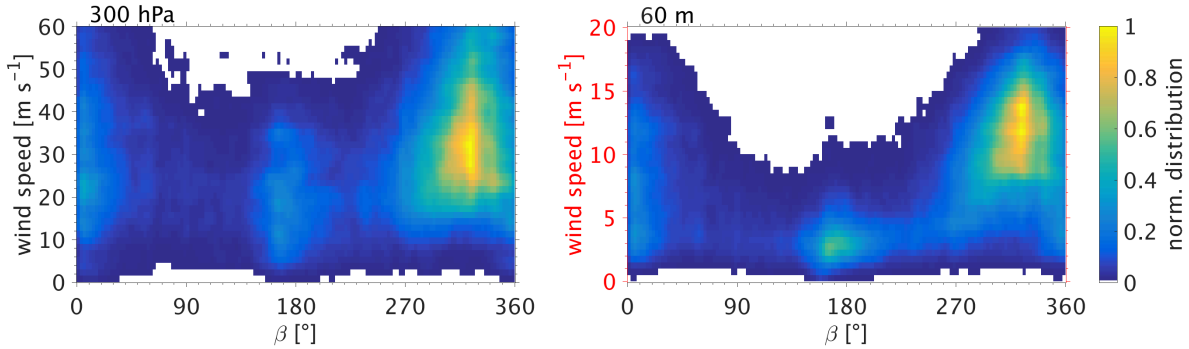

(b) Distribution of wind speeds (Andes) vs MAW back-azimuths during MAW detections.

Figure D.15: Andes/IS02; similar to Fig. 6.8, but for MERRA-2 winds at 300 hPa (left-hand column) and 60 m above the ground (right-hand column, different scale). The grid interval for wind in the right-hand column is 0.5 m s^{-1} (wind speed).

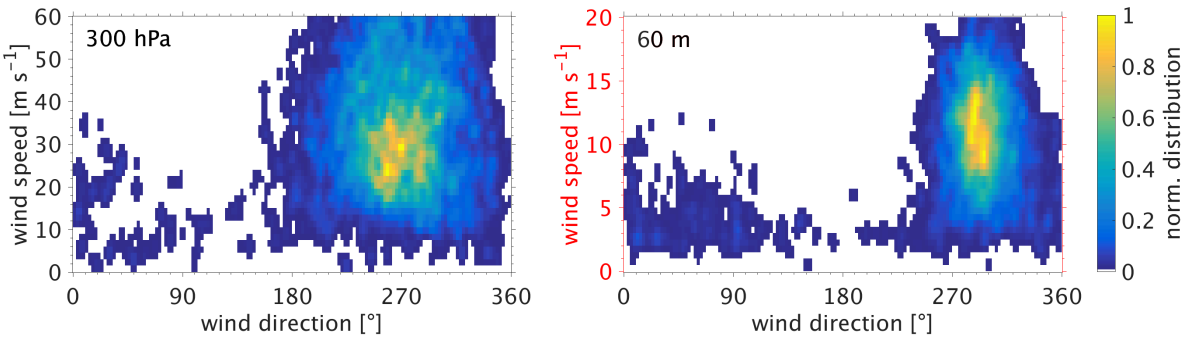

(a) Distribution of wind speeds vs wind directions during selected MAW events.

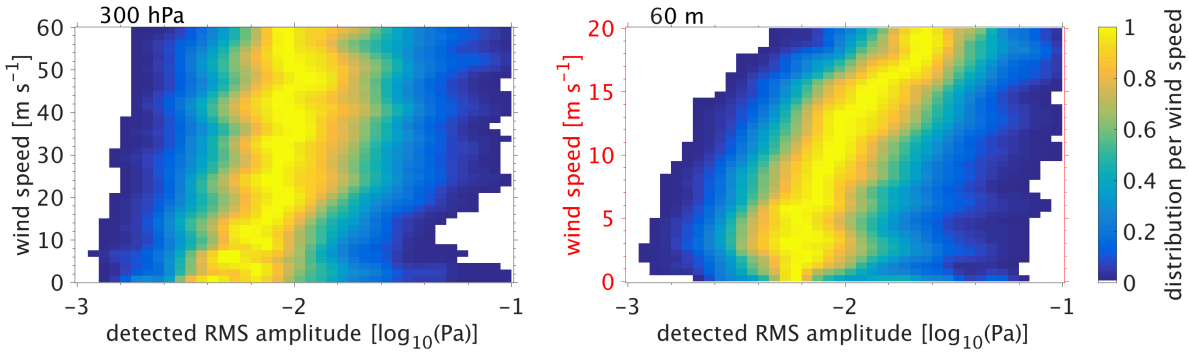

(b) Distribution of wind speeds vs MAW amplitudes.

Figure D.16: Andes/IS02; similar to Fig. 6.9, but for MERRA-2 winds at 300 hPa (left-hand column) and 60 m above the ground (right-hand column, different scale). The grid interval for the wind speeds in the right-hand column is 0.5 m s^{-1} (wind speed).

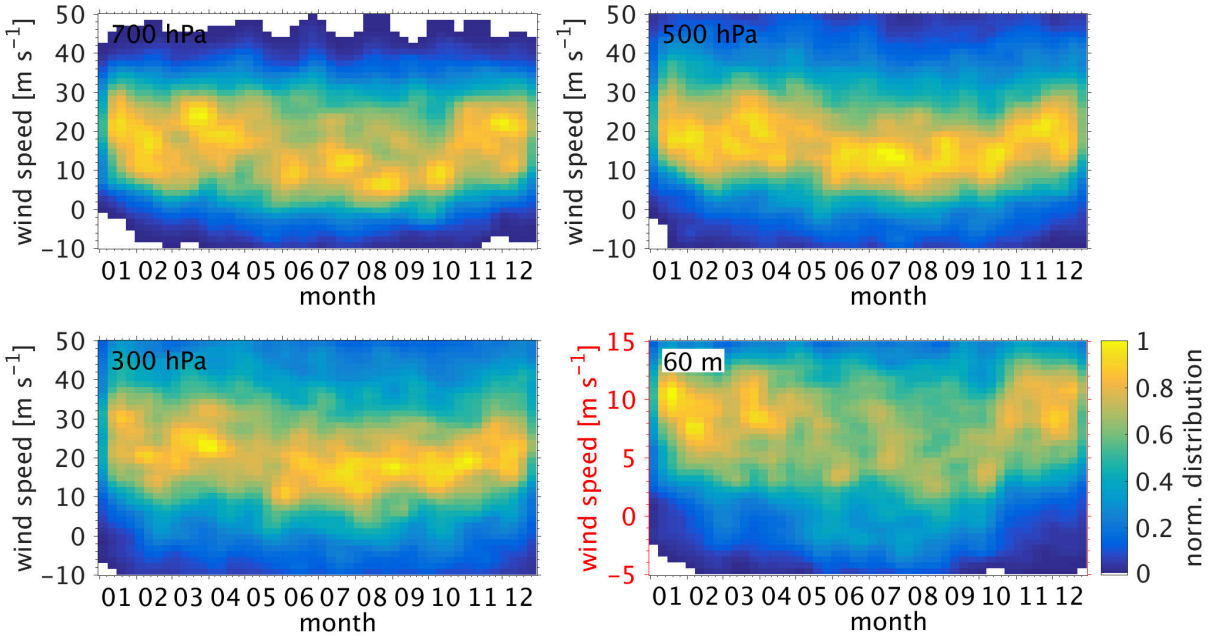

Figure D.17: Annual variation in cross-mountain wind speeds over the southern Andes. The occurrence frequency (normalized) of the directional cross-mountain wind speeds (270°) is provided as a stacked view for 2004 to 2017 (the intervals are 7.5 d and 3 m s^{-1}). For winds exceeding 15 m s^{-1}, the occurrence frequency is reduced during winter, which generally is contradictory to the number of detections.

New Zealand — IS36

Over the Southern Alps in New Zealand (44°S, 170°E) the mean wind speeds are lower than those over the southern Andes (700 hPa: $\|\overline{\boldsymbol{v}}_h\| = 13.6\,\mathrm{m\,s^{-1}}$, $\sigma = \pm 8.2\,\mathrm{m\,s^{-1}}$). A seasonal variation in wind speeds is again not evident. The predominant wind direction is around 270° at the evaluated pressure levels (Figs. D.18 and D.20). Northwesterly winds prevail near the ground (at around 60 m).
Interestingly, the distribution of wind speeds vs detected back-azimuths peaks at higher wind speeds (>15 $\mathrm{m\,s^{-1}}$) than the climatological wind distribution (<15 $\mathrm{m\,s^{-1}}$). This is a possible explanation for fewer detections from this hotspot (around 10^4), compared to IS02 and the southern Andes (around 10^5). The narrow back-azimuth range of the maximum ($\beta = 265° \pm 20°$) matches the estimated source location, and was used to filter the detections for Fig. D.19.

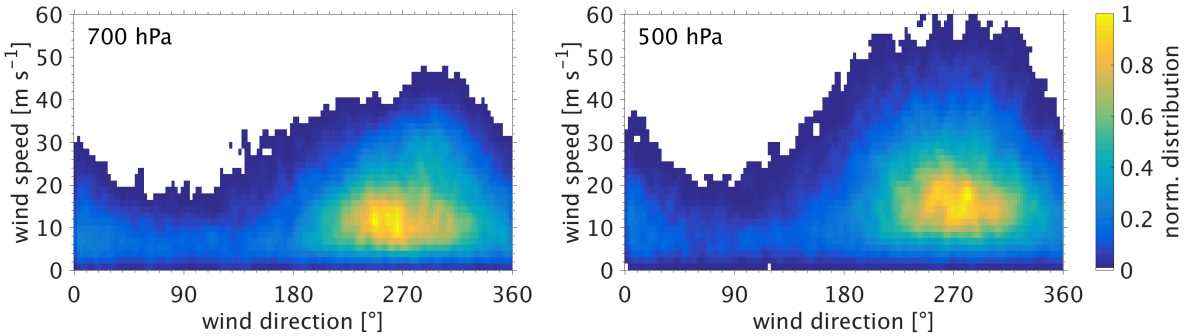

(a) Climatological distribution of MERRA-2 wind speeds vs wind directions (2004–2017).

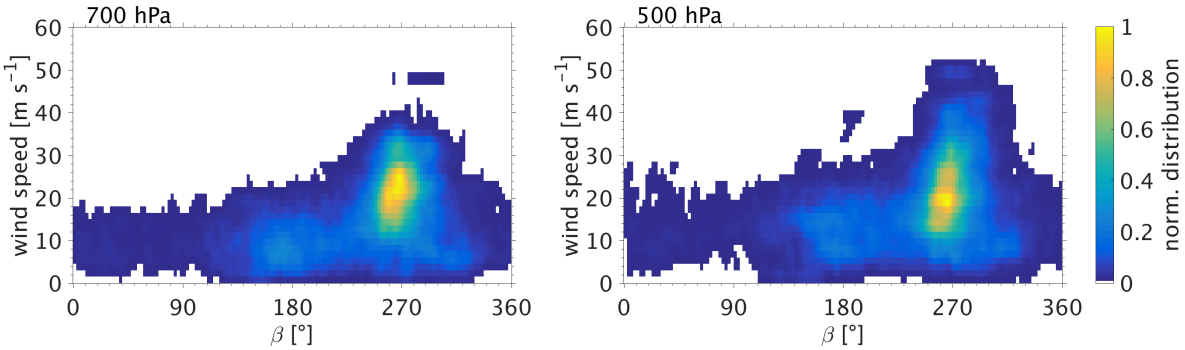

(b) Distribution of wind speeds vs MAW back-azimuths during MAW detections at IS36.

Figure D.18: Evaluation of MERRA-2 tropospheric winds at 700 hPa (left-hand column) and 500 hPa (right-hand column) at a source on the South Island of New Zealand (44°S, 170°E). The grid intervals are 2.5° (for β and wind direction) and 1.5 $\mathrm{m\,s^{-1}}$ (for wind speed). The distributions are normalized by the respective maximum values.

The analysis of wind speeds and wind directions during detections from the west does not simply reflect the climatological wind conditions over New Zealand. Since the island

and the Southern Alps feature a southwest-northeast orientation, the detections coincide with strong winds (maxima between 20 m s^{-1} and 30 m s^{-1}) from the northwest, and thus perpendicular to the island, rather than with the prevailing westerly winds. At 60 m above the ground, event-associated wind directions do reflect the climatological wind directions, but the shift to higher wind speeds is evident (cf. Figs. D.20(a) and D.21(a)). Some MAW events were obviously detected when southeasterly wind directions occurred at 700 hPa and 60 m above the ground. Such a flow is also perpendicular to the mountain range, but opposite in direction.

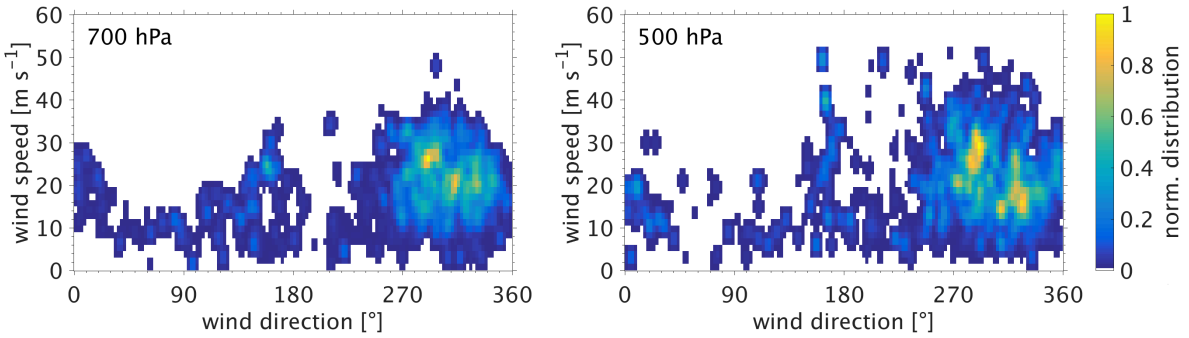

(a) Distribution of wind speeds vs wind directions during selected MAW events.

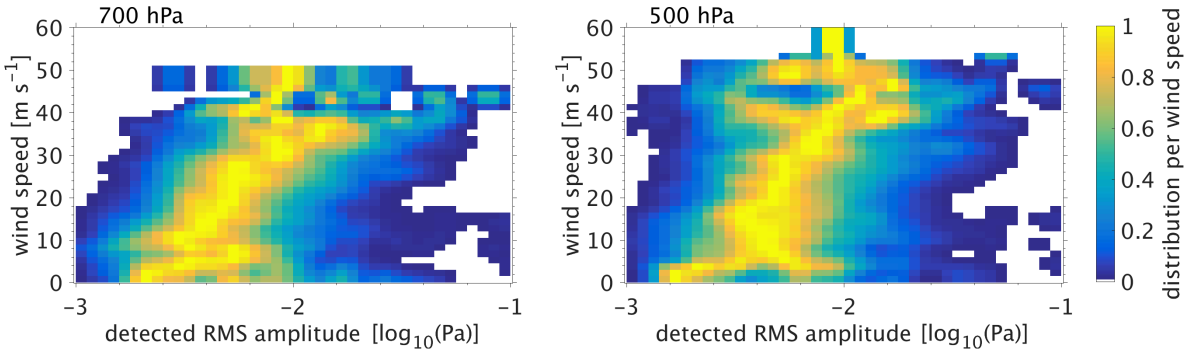

(b) Distribution of wind speeds vs MAW amplitudes.

Figure D.19: Similar to Fig. D.18, but only considering detected MAWs with back-azimuths between 245° and 285°; 13,032 detections remained. The grid interval for the RMS amplitude is 0.05 log$_{10}$(Pa). The distribution in (b) is normalized per wind speed interval, showing a correlation between amplitude and wind speed.

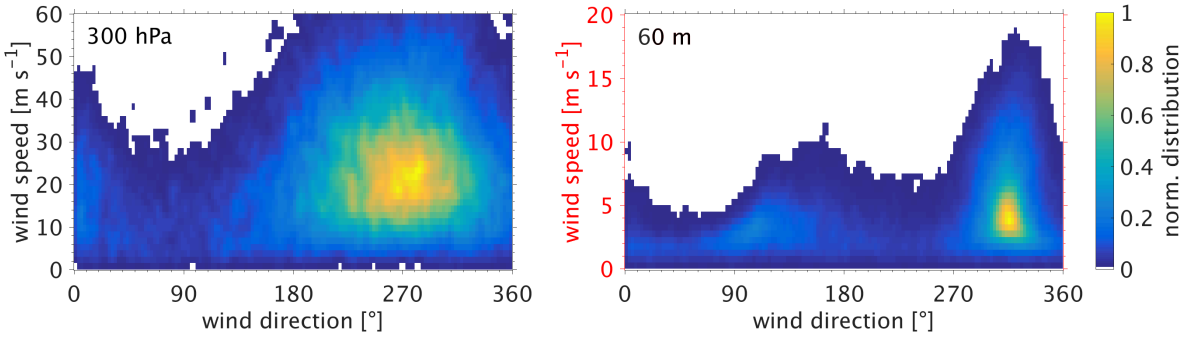

(a) Climatological distribution of MERRA-2 wind speeds vs wind directions (2004–2017).

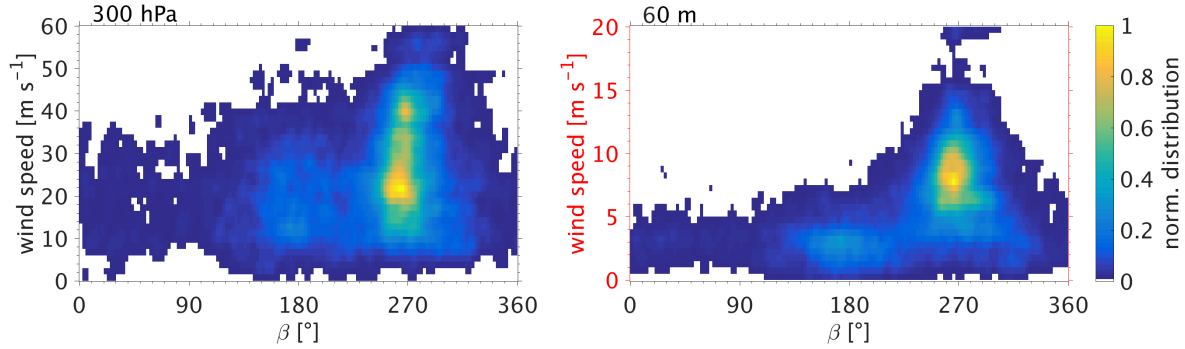

(b) Distribution of wind speeds vs MAW back-azimuths during MAW detections.

Figure D.20: New Zealand/IS36; similar to Fig. D.18, but for MERRA-2 winds at 300 hPa (left-hand column) and 60 m above the ground (right-hand column, different scale). The grid interval for wind in the right-hand column is 0.5 m s^{-1} (wind speed).

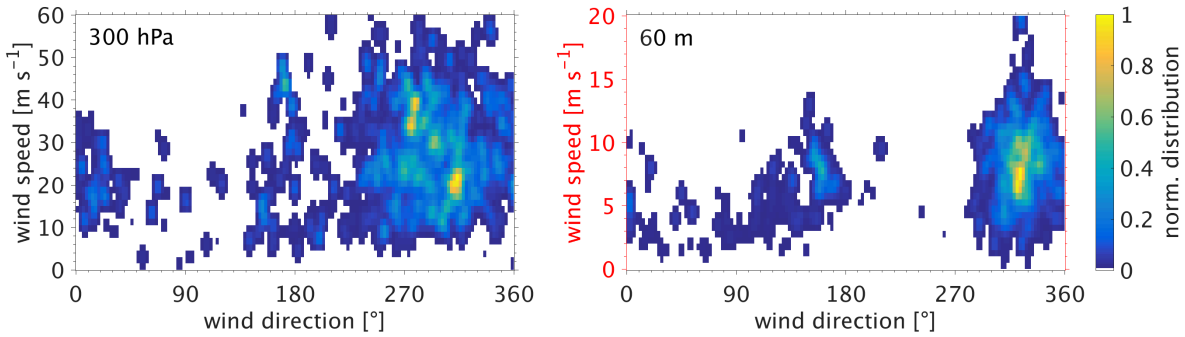

(a) Distribution of wind speeds vs wind directions during selected MAW events.

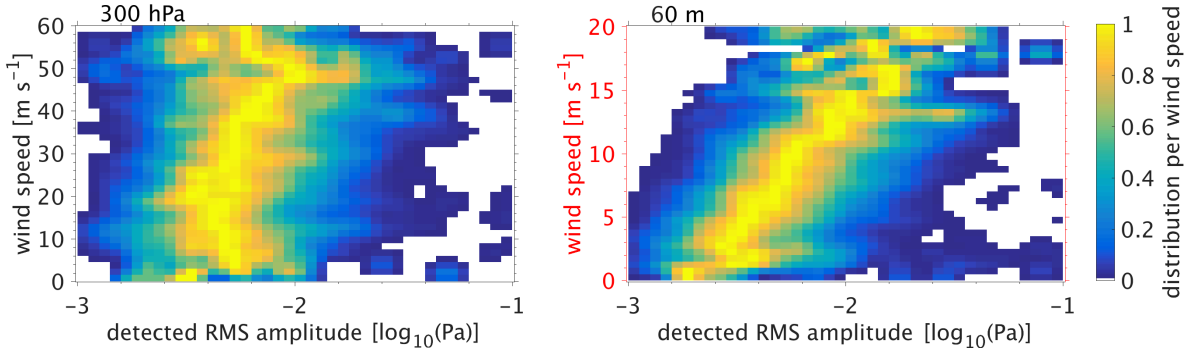

(b) Distribution of wind speeds vs MAW amplitudes.

Figure D.21: New Zealand/IS36; similar to Fig. D.19, but for the MERRA-2 winds at 300 hPa (left-hand column) and 60 m above the ground (right-hand column, different scale). The grid interval for the wind speeds in the right-hand column is 0.5 m s^{-1} (wind speed).

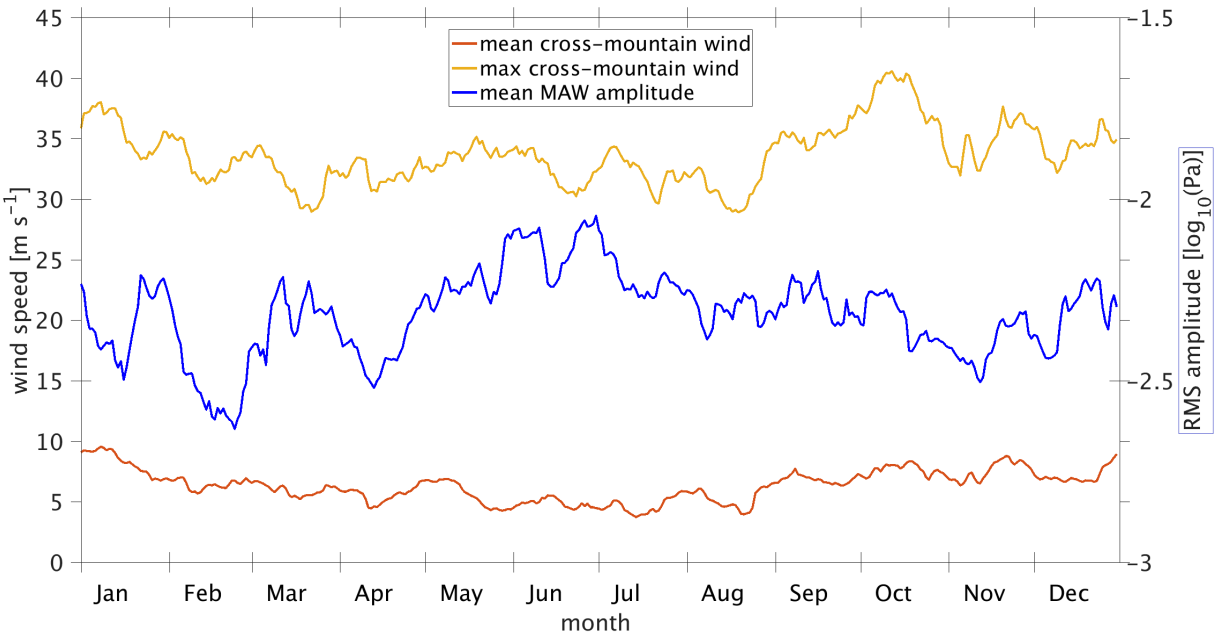

Figure D.22: Annual variation in amplitudes of MAWs (IS36) and cross-mountain winds at 700 hPa (New Zealand). For each day of the year, the mean and maximum MERRA-2 cross-mountain winds (wind components at 270°–360°) were calculated between 2004 and 2017. A moving-average filter was applied to the results, using a span of 15 d.

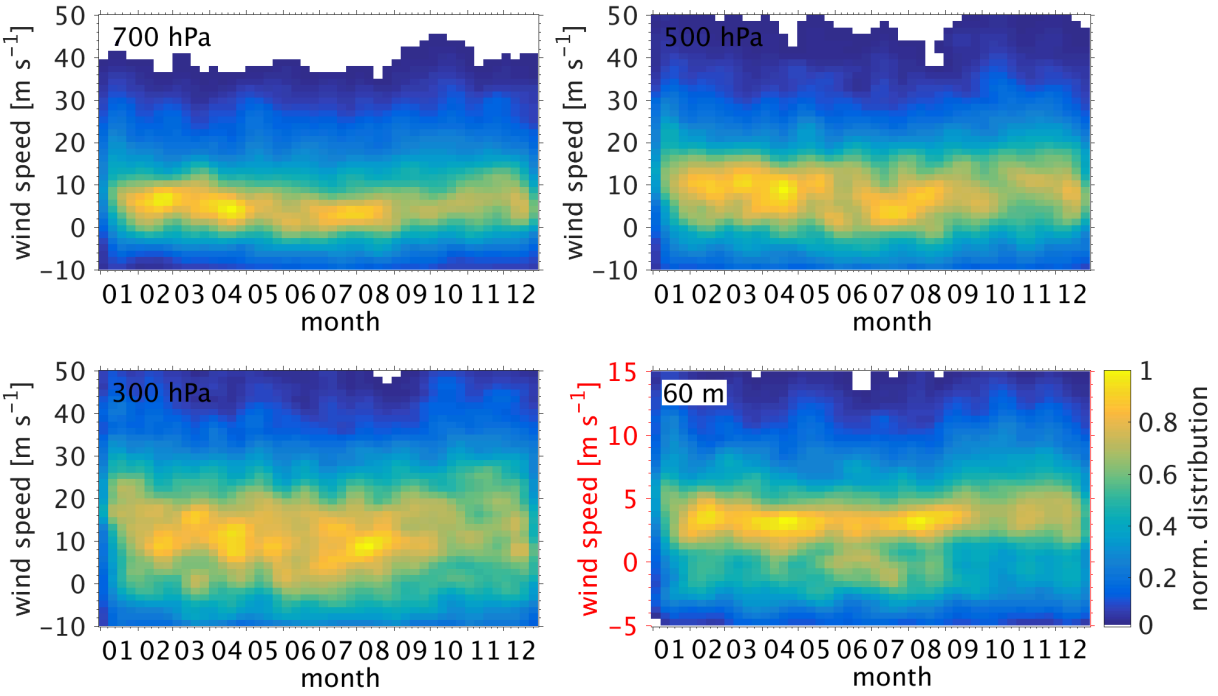

Figure D.23: Annual variation in cross-mountain wind speeds over New Zealand's South Island. The occurrence frequency (normalized) of directional cross-mountain wind speeds (315°) is provided as a stacked view for 2004 to 2017 (intervals are 7.5 d and 3 m s^{-1}). The distribution of the predominant wind speeds is consistent throughout the year, whereas an increased number of MAW detections from this hotspot (e.g., at IS22 and IS36) was found during winter (see Section 6.4).

D.6 Monthly mean zonal wind profiles

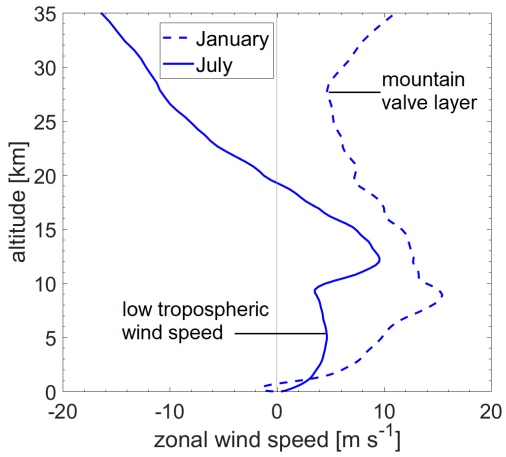

Figure D.24: Monthly mean zonal wind speed profiles over the northern Rocky Mountains (52°N, 119°W) during January and June 2016. Data were calculated from the ECMWF HRES analyses. During winter (January), a stratospheric wind minimum might cause attenuation of GWs propagating upward. During summer, the wind conditions in the lower troposphere are not favorable for orographic GW excitation (weak winds).

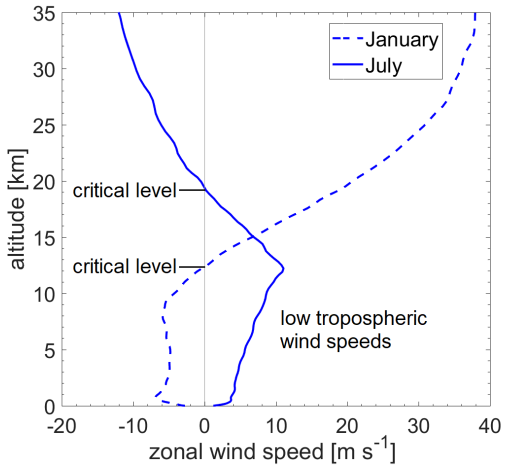

Figure D.25: As Fig. D.24, but for the East Siberian Mountains (60°N, 156°E).

List of Figures

List of Tables

Abbreviations & Symbols

Abbreviations

2D-FD	2-Dimensional Finite Differences
ALOMAR	Arctic Lidar Observatory for Middle Atmosphere Research (Norway)
ARISE	Atmospheric dynamics Research InfraStructure in Europe
BGR	*Bundesanstalt für Geowissenschaften und Rohstoffe* – German Federal Institute for Geosciences and Natural Resources
CEA	*Commissariat à l'énergie atomique et aux énergies alternatives* – French Alternative Energies and Atomic Energy Commission
CORAL	Compact Rayleigh Autonomous Lidar
cpd	cycles per day
CTBT	Comprehensive Nuclear-Test-Ban Treaty
CTBTO	Organization of the CTBT
DEEPWAVE	Deep Propagating Gravity Wave Experiment
DLR	*Deutsches Zentrum für Luft- und Raumfahrt* – German Aerospace Center
ECMWF	European Center for Medium-Range Weather Forecasts
GOS	Global Observing System
GRACILE	Gravity Wave Climatology Based on Atmospheric Infrared Limb Emissions Observed by Satellite
GW(s)	Gravity Wave(s)
GWMF	Gravity Wave Momentum Flux
GWPE	Gravity Wave Potential Energy
HIRDLS	High Resolution Dynamics Limb Sounder
HRES	High Resolution
HRMC	High Resolution Monthly Climatology
HWM	Horizontal Wind Model
IDC	International Data Center

IFREMER	*Institut Français de Recherche pour l'Exploitation de la Mer* – French Research Institute for Exploitation of the Sea
IFS	Integrated Forecasting System
IMS	International Monitoring System
IS*00*	(IS + two-digit number) Code for IMS infrasound stations, numbered from 01 to 60; e.g., IS26: IMS code for infrasound station no. 26, operated by BGR (Germany) in the Bavarian Forest near the town Freyung
LIDAR	Light Detection and Ranging
LIS	Lightning Imaging Sensor onboard the Tropical Rainfall Measuring Mission Satellite
MAW(s)	Mountain-Associated infrasonic Wave(s)
MERRA-2	Modern-Era Retrospective Analysis for Research and Applications, Version 2
MSISE	Mass Spectrometer and Incoherent Scatter Enhanced, a model from NRL
NASA	National Aeronautics and Space Administration
NDC	National Data Center
NRL	Naval Research Laboratory
NWP	Numerical Weather Prediction
OTD	Optical Transient Detector onboard Orbview-1
PMCC	Progressive Multi-Channel Correlation
PrepCom	Preparatory Commission of the CTBTO
PSD	Power Spectral Density
PW(s)	Planetary Wave(s)
RMR lidar	Rayleigh-Mie-Raman lidar
RMS	Root-Mean-Square
SABER	Sounding of the Atmosphere using Broadband Emission Radiometry
SNR	Signal-to-Noise Ratio
SSW	Sudden Stratospheric Warming
WMO	World Meteorological Organization

Symbols

α	(azimuthal) propagation direction, respective to 0° (North) clockwise
β	back-azimuth ($\beta = \alpha + 180°$)
$\hat{\boldsymbol{n}}$	unit vector normal to the wavefront; in the x-y-domain only, this is $\hat{\boldsymbol{n}}_\alpha$

κ	adiabatic exponent
ρ	density
σ	standard deviation
$\boldsymbol{v}_h$	horizontal wind vector
A_a	attenuation due to atmospheric absorption
A_p	attenuation coefficient for atmospheric infrasound propagation
A_s	attenuation due to geometric spreading
c	speed of sound (general notation)
c_p	heat capacity at constant pressure
c_T	adiabatic speed of sound
c_v	heat capacity at constant volume
F	Fisher ratio
f	frequency
I_s	stratospheric returns (ray-tracing)
I_t	thermospheric returns (ray-tracing)
K	bulk modulus
N_A	acoustic cut-off frequency
N_B	Brunt–Väisälä frequency
N_{array}	number of array elements
p	pressure
p_a	acoustic pressure
r	distance
R_s	specific gas constant
S	scaling factor for microbarom modeling
T	temperature
u	zonal wind component
v	meridional wind component
v_{app}	apparent phase velocity
$v_{eff-ratio}$	effective sound speed ratio between altitude z and the surface
v_{eff}	effective sound speed
w_α	along-path wind speed
z	altitude

Bibliography

Alcoverro, B. and A. Le Pichon (2005) Design and optimization of a noise reduction system for infrasonic measurements using elements with low acoustic impedance. *J. Acoust. Soc. Am.*, **117**(4), 1717–1727, doi:10.1121/1.1804966.

Alexander, M. J., J. Gille, C. Cavanaugh, M. Coffey, C. Craig, T. Eden, G. Francis, C. Halvorson, J. Hannigan, R. Khosravi, D. Kinnison, H. Lee, S. Massie, B. Nardi, J. Barnett, C. Hepplewhite, A. Lambert, and V. Dean (2008a) Global estimates of gravity wave momentum flux from High Resolution Dynamics Limb Sounder observations. *J. Geophys. Res.*, **113**(D15), D15S18, doi:10.1029/2007JD008807.

Alexander, M. J. and H. Teitelbaum (2011) Three-dimensional properties of Andes mountain waves observed by satellite: A case study. *J. Geophys. Res.*, **116**, D23110, doi:10.1029/2011JD016151.

Alexander, P., D. Luna, P. Llamedo, and A. de la Torre (2010) A gravity waves study close to the Andes mountains in Patagonia and Antarctica with GPS radio occultation observations. *Ann. Geophys.*, **28**(2), 587–595, doi:10.5194/angeo-28-587-2010.

Alexander, S. P., T. Tsuda, and Y. Kawatani (2008b) COSMIC GPS Observations of Northern Hemisphere winter stratospheric gravity waves and comparisons with an atmospheric general circulation model. *Geophys. Res. Lett.*, **35**, L10808, doi:10.1029/2008GL033174.

Andrews, D. G. (2010) *An introduction to Atmospheric Physics*. Cambridge University Press, New York, USA, second edition. ISBN 978-0-511-72966-9. 248 pp.

Ardhuin, F. and T. H. C. Herbers (2013) Noise generation in the solid Earth, oceans and atmosphere, from nonlinear interacting surface gravity waves in finite depth. *J. Fluid Mech.*, **716**, 316–348, doi:10.1017/jfm.2012.548.

Ardhuin, F., E. Stutzmann, M. Schimmel, and A. Mangeney (2011) Ocean wave sources of seismic noise. *J. Geophys. Res.*, **116**, C09004, doi:10.1029/2011JC006952.

ARISE (2018) ARISE data portal. Website. URL: `https://arise-portal.eu`, last accessed: 16 December 2018.

Arrowsmith, S. J. (2018) False alarms and the IMS infrasound network: understanding the factors influencing the creation of false events. *Geophys. J. Int.*, **215**(2), 1322–1337, doi:10.1093/gji/ggy350.

Assink, J. D., R. Waxler, and D. Drob (2012) On the sensitivity of infrasonic traveltimes in the equatorial region to the atmospheric tides. *J. Geophys. Res.*, **117**, D01110, doi:10.1029/2011JD016107.

Assink, J. D., A. Le Pichon, E. Blanc, M. Kallel, and L. Khemiri (2014a) Evaluation of wind and temperature profiles from ECMWF analysis on two hemispheres using volcanic infrasound. *J. Geophys. Res.*, **119**, 8659–8683, doi:10.1002/2014JD021632.

Assink, J. D., R. Waxler, P. Smets, and L. G. Evers (2014b) Bidirectional infrasound ducts associated with sudden stratospheric warming events. *J. Geophys. Res.*, **119**, 1140–1153, doi:10.1002/2013JD021062.

Baldwin, M. P. and T. J. Dunkerton (2001) Stratospheric Harbingers of Anomalous Weather Regimes. *Science*, **294**(5542), 581–584, doi:10.1126/science.1063315.

Baumgarten, G. (2010) Doppler Rayleigh/Mie/Raman lidar for wind and temperature measurements in the middle atmosphere up to 80 km. *Atmos. Meas. Tech.*, **3**(6), 1509–1518, doi:10.5194/amt-3-1509-2010.

Baumgarten, K., M. Gerding, and F.-J. Lübken (2017) Seasonal variation of gravity wave parameters using different filter methods with daylight lidar measurements at midlatitudes. *J. Geophys. Res.*, **122**(5), 2683–2695, doi:10.1002/2016JD025916.

Bedard, A. J. (1978) Infrasound Originating Near Mountainous Regions in Colorado. *J. Appl. Meteorol.*, **17**(7), 1014–1022, doi:10.1175/1520-0450(1978)017<1014:IONMRI>2.0.CO;2.

Berrisford, P., D. P. Dee, P. Poli, R. Brugge, M. Fielding, M. Fuentes, P. W. Kållberg, S. Kobayashi, S. Uppala, and A. Simmons (2011) The ERA-Interim archive Version 2.0. Report 1, ECMWF, Reading, United Kingdom. URL: `https://www.ecmwf.int/en/elibrary/8174-era-interim-archive-version-20`, 27 pp.

Blanc, E., L. Ceranna, A. Hauchecorne, A. Charlton-Perez, E. Marchetti, L. G. Evers, T. Kvaerna, J. Lastovicka, L. Eliasson, N. B. Crosby, P. Blanc-Benon, A. Le Pichon, N. Brachet, C. Pilger, P. Keckhut, J. D. Assink, P. S. M. Smets, C. F. Lee, J. Kero, T. Sindelarova, N. Kämpfer, R. Rüfenacht, T. Farges, C. Millet, S. P. Näsholm, S. J. Gibbons, P. J. Espy, R. E. Hibbins, P. Heinrich, M. Ripepe, S. Khaykin, N. Mze, and J. Chum (2018) Toward an Improved Representation of Middle Atmospheric Dynamics Thanks to the ARISE Project. *Surv. Geophys.*, **39**(2), 171–225, doi:10.1007/s10712-017-9444-0.

Blanc, E., K. Pol, A. Le Pichon, A. Hauchecorne, P. Keckhut, G. Baumgarten, J. Hildebrand, J. Höffner, G. Stober, R. E. Hibbins, P. J. Espy, M. Rapp, B. Kaifler, L. Ceranna, P. Hupe, J. Hagen, R. Rüfenacht, N. Kämpfer, and P. Smets (2019) Middle Atmosphere Variability and Model Uncertainties as Investigated in the Framework of the ARISE Project. *In* Le Pichon, A., E. Blanc, and A. Hauchecorne (eds.): *Infrasound Monitoring for Atmospheric Studies — Challenges in Middle-atmosphere Dynamics and Societal Benefits*, pp. 845–888. Springer, Dordrecht, the Netherlands. ISBN 978-3-319-75138-2, doi:10.1007/978-3-319-75140-5_28.

Blanc, E., A. Le Pichon, L. Ceranna, T. Farges, J. Marty, and P. Herry (2010) Global Scale Monitoring of Acoustic and Gravity Waves for the Study of the Atmospheric Dynamics. *In* Le Pichon, A., E. Blanc, and A. Hauchecorne (eds.): *Infrasound Monitoring for Atmospheric Studies*, pp. 647–664. Springer, Dordrecht, the Netherlands. ISBN 978-1-4020-9508-5, doi:10.1007/978-1-4020-9508-5_21.

Bosilovich, M. G., R. Lucchesi, and M. Suarez (2016) MERRA-2: File Specification. Office Note No. 9 (V1.1), Global Modeling and Assimilation Office, Greenbelt, MD, USA. URL: `https://gmao.gsfc.nasa.gov/pubs/docs/Bosilovich785.pdf`, last access: 18 August 2018. 73 pp.

Bowman, H. S. and A. J. Bedard (1971) Observations of Infrasound and Subsonic Disturbances Related to Severe Weather. *Geophys. J. R. Astron. Soc.*, **26**(1–4), 215–242, doi:10.1111/j.1365-246x.1971.tb03396.x.

Bowman, J. R., G. E. Baker, and M. Bahavar (2005) Ambient infrasound noise. *Geophys. Res. Lett.*, **32**, L09803, doi:10.1029/2005GL022486.

Brachet, N., D. Brown, R. Le Bras, Y. Cansi, P. Mialle, and J. Coyne (2010) Monitoring the Earth's Atmosphere with the Global IMS Infrasound Network. *In* Le Pichon, A., E. Blanc, and A. Hauchecorne (eds.): *Infrasound Monitoring for Atmospheric Studies*, pp. 77–118. Springer, Dordrecht, the Netherlands. ISBN 978-1-4020-9508-5, doi:10.1007/978-1-4020-9508-5_3.

Bramberger, M., A. Dörnbrack, K. Bossert, B. Ehard, D. C. Fritts, B. Kaifler, C. Mallaun, A. Orr, P.-D. Pautet, M. Rapp, M. J. Taylor, S. Vosper, B. P. Williams, and B. Witschas (2017) Does Strong Tropospheric Forcing Cause Large-Amplitude Mesospheric Gravity Waves? A DEEP-WAVE Case Study. *J. Geophys. Res.*, **122**(21), 11422–11443, doi:10.1002/2017JD027371.

Brekhovskikh, L. M., V. V. Goncharov, V. M. Kurtepov, and K. A. Naugolnykh (1973) The radiation of infrasound into the atmosphere by surface waves in the ocean. *J. Fluid Mech.*, **9**, 899–907.

Butler, A. H., J. P. Sjoberg, D. J. Seidel, and K. H. Rosenlof (2017) A sudden stratospheric warming compendium. *Earth Syst. Sci. Data*, **9**(1), 63–76, doi:10.5194/essd-9-63-2017.

Butler, S. T. and K. A. Small (1963) The excitation of atmospheric oscillations. *Proc. Roy. Soc. Lond. A: Mathematical, Physical and Engineering Sciences*, **274**(1356), 91–121, doi:10.1098/rspa.1963.0116.

Campbell, W. H. and J. M. Young (1963) Auroral zone observations of infrasonic pressure waves related to ionospheric disturbances and geomagnetic activity. *J. Geophys. Res.*, **68**, 5909–5916.

Campus, P. and D. R. Christie (2010) Worldwide observations of infrasonic waves. *In* Le Pichon, A., E. Blanc, and A. Hauchecorne (eds.): *Infrasound Monitoring for Atmospheric Studies*, pp. 185–234. Springer, Dordrecht, the Netherlands. ISBN 978-1-4020-9508-5, doi:10.1007/978-1-4020-9508-5_6.

Cansi, Y. (1995) An automatic seismic event processing for detection and location: The P.M.C.C. Method. *Geophys. Res. Lett.*, **22**(9), 1021–1024, doi:10.1029/95GL00468.

Cecil, D. J. (2015) LIS/OTD Gridded Lightning Climatology Data Collection, Version 2.3.2015 [0.5 Degree High Resolution Monthly Climatology (HRMC)]. Data set, NASA EOSDIS Global Hydrology Resource Center Distributed Active Archive Center, Huntsville, AL, USA, doi:10.5067/LIS/LIS-OTD/DATA311, accessed: 13 August 2018.

Cecil, D. J., D. E. Buechler, and R. J. Blakeslee (2014) Gridded lightning climatology from TRMM-LIS and OTD: Dataset description. *Atmos. Res.*, **135–136**, 404–414, doi:10.1016/j.atmosres.2012.06.028.

Ceranna, L., R. S. Matoza, P. Hupe, A. Le Pichon, and M. Landès (2019) Systematic Array Processing of a Decade of Global IMS Infrasound Data. *In* Le Pichon, A., E. Blanc, and A. Hauchecorne (eds.): *Infrasound Monitoring for Atmospheric Studies — Challenges in Middle-atmosphere Dynamics and Societal Benefits*, pp. 471–482. Springer, Dordrecht, the Netherlands. ISBN 978-3-319-75138-2, doi:10.1007/978-3-319-75140-5_13.

Chanaud, R. C. (1970) Aerodynamic Whistles. *Sci. Amer.*, **222**, 40–47, doi:10.1038/scientificamerican0170-40.

Chapman, S. and R. S. Lindzen (1970) *Atmospheric Tides*. D. Reidel Press, Dordrecht, the Netherlands. 229 pp.

Chapman, S. and K. C. Westfold (1956) A comparison of the annual mean solar and lunar atmospheric tides in barometric pressure, as regards their worldwide distribution of amplitude and phase. *J. Atmos. Terr. Phys.*, **8**(1), 1–23, doi:10.1016/0021-9169(56)90087-3.

Charlton, A. J. and L. M. Polvani (2007) A New Look at Stratospheric Sudden Warmings. Part I: Climatology and Modeling Benchmarks. *J. Climate*, **20**(3), 449–469, doi:10.1175/JCLI3996.1.

Charlton-Perez, A. J., M. P. Baldwin, T. Birner, R. X. Black, A. H. Butler, N. Calvo, N. A. Davis, E. P. Gerber, N. Gillett, S. Hardiman, J. Kim, K. Krüger, Y.-Y. Lee, E. Manzini, B. A. McDaniel, L. Polvani, T. Reichler, T. A. Shaw, M. Sigmond, S.-W. Son, M. Toohey, L. Wilcox, S. Yoden, B. Christiansen, F. Lott, D. Shindell, S. Yukimoto, and S. Watanabe (2013) On the lack of stratospheric dynamical variability in low-top versions of the CMIP5 models. *J. Geophys. Res.*, **118**(6), 2494–2505, doi:10.1002/jgrd.50125.

Chimonas, G. (1977) A Possible Source Mechanism for Mountain-Associated Infrasound. *J. Atmos. Sci.*, **34**(5), 806–811, doi:10.1175/1520-0469(1977)034<0806:APSMFM>2.0.CO;2.

Christie, D. R. and P. Campus (2010) The IMS Infrasound Network: Design and Establishment of Infrasound Stations. *In* Le Pichon, A., E. Blanc, and A. Hauchecorne (eds.): *Infrasound Monitoring for Atmospheric Studies*, pp. 29–75. Springer, Dordrecht, the Netherlands. ISBN 978-1-4020-9508-5, doi:10.1007/978-1-4020-9508-5_2.

Chunchuzov, I. P. (1994) On a Possible Generation Mechanism for Nonstationary Mountain Waves in the Atmosphere. *J. Atmos. Sci.*, **51**(15), 2196–2206, doi:10.1175/1520-0469(1994)051<2196:OAPGMF>2.0.CO;2.

Chunchuzov, I. and S. Kulichkov (2019) Internal Gravity Wave Perturbations and Their Impacts on Infrasound Propagation in the Atmosphere. *In* Le Pichon, A., E. Blanc, and A. Hauchecorne (eds.): *Infrasound Monitoring for Atmospheric Studies — Challenges in Middle-atmosphere Dynamics and Societal Benefits*, pp. 551–590. Springer, Dordrecht, the Netherlands. ISBN 978-3-319-75138-2, doi:10.1007/978-3-319-75140-5_16.

Cook, R. K. (1969) Atmospheric sound propagation. *In* Atlas, D. et al. (eds.): *NAS-NRC Atmospheric Exploration by Remote Probes*, vol. **2**, pp. 633–669. National Academy of Sciences – National Research Council, Panel on Remote Atmospheric Probing, Rockville, MD, USA.

Crocker, M. J. (ed.) (1998) *Handbook of Acoustics*. John Wiley & Sons, Hoboken, NJ, USA. ISBN 978-0-471-25293-1. 1488 pp.

CTBTO PrepCom (2017) 1996: CTBT: A Long-Sought Success. Website. URL: `https://www.ctbto.org/the-treaty/`, last accessed: 23 November 2017.

CTBTO PrepCom (2018) International Monitoring System Infrasound. Website. URL: `https://www.ctbto.org/map`, last accessed: 25 August 2018.

Dai, A. and J. Wang (1999) Diurnal and Semidiurnal Tides in Global Surface Pressure Fields. *J. Atmos. Sci.*, **56**(22), 3874–3891, doi:10.1175/1520-0469(1999)056<3874:DASTIG>2.0.CO;2.

Damiens, F., C. Millet, and F. Lott (2018) An investigation of infrasound propagation over mountain ranges. *J. Acoust. Soc. Am.*, **143**(1), 563–574, doi:10.1121/1.5020783.

Daubechies, I. (1990) Ten Lectures on Wavelets. *In: Ten Lectures on Wavelets*, vol. **61** of *CBMS-NSF Regional Conf. Series in Appl. Math.*, pp. 1–369. Soc. for Industr. and Appl. Math., Philadelphia, PA, USA, doi:10.1137/1.9781611970104.fm.

De Groot-Hedlin, C. D., M. A. H. Hedlin, and D. P. Drob (2010) Atmospheric Variability and Infrasound Monitoring. *In* Le Pichon, A., E. Blanc, and A. Hauchecorne (eds.): *Infrasound Monitoring for Atmospheric Studies*, pp. 475–507. Springer, Dordrecht, the Netherlands. ISBN 978-1-4020-9508-5, doi:10.1007/978-1-4020-9508-5_15.

De Groot-Hedlin, C. D. and M. A. H. Hedlin (2015) A method for detecting and locating geophysical events using groups of arrays. *Geophys. J. Int.*, **203**(2), 960–971, doi:10.1093/gji/ggv345.

De la Torre, A., P. Alexander, R. Hierro, P. Llamedo, A. Rolla, T. Schmidt, and J. Wickert (2012) Large-amplitude gravity waves above the southern Andes, the Drake Passage, and the Antarctic Peninsula. *J. Geophys. Res.*, **117**, D02106, doi:10.1029/2011JD016377.

Dee, D. P., S. M. Uppala, A. J. Simmons, P. Berrisford, P. Poli, S. Kobayashi, U. Andrae, M. A. Balmaseda, G. Balsamo, P. Bauer, P. Bechtold, A. C. M. Beljaars, L. van de Berg, J. Bidlot, N. Bormann, C. Delsol, R. Dragani, M. Fuentes, A. J. Geer, L. Haimberger, S. B. Healy, H. Hersbach, E. V. Hólm, L. Isaksen, P. Kållberg, M. Köhler, M. Matricardi, A. P. McNally, B. M. Monge-Sanz, J.-J. Morcrette, B.-K. Park, C. Peubey, P. de Rosnay, C. Tavolato, J.-N. Thépaut, and F. Vitart (2011) The ERA-Interim reanalysis: configuration and performance of the data assimilation system. *Quart. J. Roy. Meteor. Soc.*, **137**(656), 553–597, doi:10.1002/qj.828.

Díaz-Argandoña, J., A. Ezcurra, J. Sáenz, G. Ibarra-Berastegi, and I. Errasti (2016) Climatology and temporal evolution of the atmospheric semidiurnal tide in present-day reanalyses. *J. Geophys. Res.*, **121**(9), 4614–4626, doi:10.1002/2015JD024513.

Donn, W. L. and D. Rind (1971) Natural infrasound as an atmospheric probe. *Geophys. J. R. Astron. Soc.*, **26**, 111–133.

Donn, W. L. and D. Rind (1972) Microbaroms and the Temperature and Wind of the Upper Atmosphere. *J. Atmos. Sci.*, **29**(1), 156–172, doi:10.1175/1520-0469(1972)029<0156:MATTAW>2.0.CO;2.

Donn, W. L. and B. Naini (1973) Sea wave origin of microbaroms and microseisms. *J. Geophys. Res.*, **78**(21), 4482–4488, doi:10.1029/JC078i021p04482.

Dörnbrack, A., T. Gerz, and U. Schumann (1995) Turbulent breaking of overturning gravity waves below a critical level. *Appl. Sci. Res.*, **54**(3), 163–176, doi:10.1007/bf00849114.

Drob, D. P., J. M. Picone, and M. Garcés (2003) Global morphology of infrasound propagation. *J. Geophys. Res.*, **108**(D21), 4680, doi:10.1029/2002JD003307.

Drob, D. P., J. T. Emmert, G. Crowley, J. M. Picone, G. G. Shepherd, W. Skinner, P. Hays, R. J. Niciejewski, M. Larsen, C. Y. She, J. W. Meriwether, G. Hernandez, M. J. Jarvis, D. P. Sipler, C. A. Tepley, M. S. OBrien, J. R. Bowman, Q. Wu, Y. Murayama, S. Kawamura, I. M. Reid, and R. A. Vincent (2008) An empirical model of the Earth's horizontal wind fields: HWM07. *J. Geophys. Res.*, **113**, A12304, doi:10.1029/2008ja013668.

Drob, D. P., D. Broutman, M. A. Hedlin, N. W. Winslow, and R. G. Gibson (2013) A method for specifying atmospheric gravity wavefields for long-range infrasound propagation calculations. *J. Geophys. Res.*, **118**(10), 3933–3943, doi:10.1029/2012JD018077.

Eckermann, S. D. and P. Preusse (1999) Global Measurements of Stratospheric Mountain Waves from Space. *Science*, **286**(5444), 1534–1537, doi:10.1126/science.286.5444.1534.

ECMWF (2014) Part III: Dynamics and Numerical Procedures. IFS DOCUMENTATION – Cy40r1, ECMWF, Reading, United Kingdom. URL: `https://www.ecmwf.int/sites/default/files/IFS_CY40R1_Part3.pdf`, last accessed: 10 September 2018.

Ehard, B., B. Kaifler, N. Kaifler, and M. Rapp (2015) Evaluation of methods for gravity wave extraction from middle-atmospheric lidar temperature measurements. *Atmos. Meas. Tech.*, **8**(11), 4645–4655, doi:10.5194/amt-8-4645-2015.

Ehard, B., P. Achtert, A. Dörnbrack, S. Gisinger, J. Gumbel, M. Khaplanov, M. Rapp, and J. Wagner (2016) Combination of Lidar and Model Data for Studying Deep Gravity Wave Propagation. *Mon. Weather Rev.*, **144**(1), 77–98, doi:10.1175/MWR-D-14-00405.1.

Ehard, B., B. Kaifler, A. Dörnbrack, P. Preusse, S. D. Eckermann, M. Bramberger, S. Gisinger, N. Kaifler, B. Liley, J. Wagner, and M. Rapp (2017a) Horizontal propagation of large-amplitude mountain waves into the polar night jet. *J. Geophys. Res.*, **122**(3), 1423–1436, doi:10.1002/2016JD025621.

Ehard, B., S. Malardel, A. Dörnbrack, B. Kaifler, N. Kaifler, and N. Wedi (2017b) Comparing ECMWF high-resolution analyses with lidar temperature measurements in the middle atmosphere. *Quart. J. Roy. Meteor. Soc.*, **144**(712), 633–640, doi:10.1002/qj.3206.

Ern, M., P. Preusse, J. C. Gille, C. L. Hepplewhite, M. G. Mlynczak, J. M. Russell, and M. Riese (2011) Implications for atmospheric dynamics derived from global observations of gravity wave momentum flux in stratosphere and mesosphere. *J. Geophys. Res.*, **116**, D19107, doi:10.1029/2011JD015821.

Ern, M., Q. T. Trinh, P. Preusse, J. C. Gille, M. G. Mlynczak, J. M. Russell III, and M. Riese (2018) GRACILE: a comprehensive climatology of atmospheric gravity wave parameters based on satellite limb soundings. *Earth Syst. Sci. Data*, **10**(2), 857–892, doi:10.5194/essd-10-857-2018.

Ern, M., Q. T. Trinh, P. Preusse, J. C. Gille, M. G. Mlynczak, J. M. Russell, and M. Riese (2017) GRACILE: A comprehensive climatology of atmospheric gravity wave parameters based on satellite limb soundings. *PANGAEA*, link to data in netcdf format, doi:10.1594/PANGAEA.879658, supplement to Ern et al. (2018), accessed: 27 July 2018.

Evers, L. G. (2008) *The inaudible symphony: on the detection and source identification of atmospheric infrasound.* Dissertation, Delft University of Technology, Delft, the Netherlands. 160 pp.

Evers, L. G. and P. Siegmund (2009) Infrasonic signature of the 2009 major sudden stratospheric warming. *Geophys. Res. Lett.*, **36**, L23808, doi:10.1029/2009GL041323.

Evers, L. G. and H. W. Haak (2010) The Characteristics of Infrasound, its Propagation and Some Early History. *In* Le Pichon, A., E. Blanc, and A. Hauchecorne (eds.): *Infrasound Monitoring for Atmospheric Studies*, pp. 3–27. Springer, Dordrecht, the Netherlands. ISBN 978-1-4020-9508-5, doi:10.1007/978-1-4020-9508-5_1.

Fetzer, E. J. and J. C. Gille (1994) Gravity Wave Variance in LIMS Temperatures. Part I: Variability and Comparison with Background Winds. *J. Atmos. Sci.*, **51**(17), 2461–2483, doi:10.1175/1520-0469(1994)051<2461:GWVILT>2.0.CO;2.

Fisher, R. A. (1992) Statistical Methods for Research Workers. *In* Kotz, S. and N. L. Johnson (eds.): *Breakthroughs in Statistics: Methodology and Distribution*, pp. 66–70. Springer, New York, NY, USA. ISBN 978-1-4612-4380-9, doi:10.1007/978-1-4612-4380-9_6.

Forbes, J. M. (1984) Middle-atmosphere tides: Recent advances in theory and observation. *Adv. Space Res.*, **4**(4), 87–96, doi:10.1016/0273-1177(84)90268-0.

Forbes, J. M. (1990) Atmospheric tides between 80 km and 120 km. *Adv. Space Res.*, **10**(12), 127–140, doi:10.1016/0273-1177(90)90392-D.

Forbes, J. M. and H. B. Garrett (1979) Solar Tidal Wind Structures and the *E*-Region Dynamo. *J. Geomagn. Geoelec.*, **31**(3), 173–182, doi:10.5636/jgg.31.173.

Forbes, J. M. and D. F. Gillette (1982) Compendium of Theoretical Atmospheric Tidal Structures, Part I: Model Description and Explicit Structures Due to Realistic Thermal and Gravitational Excitation. Project report, Air Force Geophysics Laboratory, Hanscom AFB, MA, USA. URL: `http://www.dtic.mil/dtic/tr/fulltext/u2/a125720.pdf`, last accessed: 18 August 2018. 200 pp.

Forbes, J. M. and D. Wu (2006) Solar Tides as Revealed by Measurements of Mesosphere Temperature by the MLS Experiment on UARS. *J. Atmos. Sci.*, **63**(7), 1776–1797, doi:10.1175/JAS3724.1.

Fritts, D. C. and M. J. Alexander (2003) Gravity wave dynamics and effects in the middle atmosphere. *Rev. Geophys.*, **41**(1), 1003, doi:10.1029/2001RG000106.

Fritts, D. C., R. B. Smith, M. J. Taylor, J. D. Doyle, S. D. Eckermann, A. Dörnbrack, M. Rapp, B. P. Williams, P.-D. Pautet, K. Bossert, N. R. Criddle, C. A. Reynolds, P. A. Reinecke, M. Uddstrom, M. J. Revell, R. Turner, B. Kaifler, J. S. Wagner, T. Mixa, C. G. Kruse, A. D. Nugent, C. D. Watson, S. Gisinger, S. M. Smith, R. S. Lieberman, B. Laughman, J. J. Moore, W. O. Brown, J. A. Haggerty, A. Rockwell, G. J. Stossmeister, S. F. Williams, G. Hernandez, D. J. Murphy, A. R. Klekociuk, I. M. Reid, and J. Ma (2016) The Deep Propagating Gravity Wave Experiment (DEEPWAVE): An Airborne and Ground-Based Exploration of Gravity Wave Propagation and Effects from Their Sources throughout the Lower and Middle Atmosphere. *Bull. Amer. Meteor. Soc.*, **97**(3), 425–453, doi:10.1175/BAMS-D-14-00269.1.

Fritts, D. C., S. B. Vosper, B. P. Williams, K. Bossert, J. M. C. Plane, M. J. Taylor, P.-D. Pautet, S. D. Eckermann, C. G. Kruse, R. B. Smith, A. Dörnbrack, M. Rapp, T. Mixa, I. M. Reid, and D. J. Murphy (2018) Large-Amplitude Mountain Waves in the Mesosphere Accompanying Weak Cross-Mountain Flow During DEEPWAVE Research Flight RF22. *J. Geophys. Res.*, **123**(18), 9992–10022, doi:10.1029/2017JD028250.

Gainville, O., P. Blanc-Benon, E. Blanc, R. Roche, C. Millet, F. Le Piver, B. Despres, and P. F. Piserchia (2010) Misty Picture: A Unique Experiment for the Interpretation of the Infrasound Propagation from Large Explosive Sources. *In* Le Pichon, A., E. Blanc, and A. Hauchecorne (eds.): *Infrasound Monitoring for Atmospheric Studies*, pp. 575–598. Springer, Dordrecht, the Netherlands. ISBN 978-1-4020-9508-5, doi:10.1007/978-1-4020-9508-5_18.

Garcés, M., M. Willis, C. Hetzer, A. Le Pichon, and D. Drob (2004) On using ocean swells for continuous Infrasonic measurements of winds and temperature in the lower, middle, and upper atmosphere. *Geophys. Res. Lett.*, **31**, L23306, doi:10.1029/2004GL020696.

Gavrilov, N. M. (1997) Parametrization of momentum and energy depositions from gravity waves generated by tropospheric hydrodynamic sources. *Ann. Geophys.*, **15**(12), 1570–1580, doi:10.1007/s00585-997-1570-4.

Gelaro, R., W. McCarty, M. J. Suárez, R. Todling, A. Molod, L. Takacs, C. A. Randles, A. Darmenov, M. G. Bosilovich, R. Reichle, K. Wargan, L. Coy, R. Cullather, C. Draper, S. Akella, V. Buchard, A. Conaty, A. M. da Silva, W. Gu, G.-K. Kim, R. Koster, R. Lucchesi, D. Merkova, J. E. Nielsen, G. Partyka, S. Pawson, W. Putman, M. Rienecker, S. D. Schubert, M. Sienkiewicz, and B. Zhao (2017) The Modern-Era Retrospective Analysis for Research and

Applications, Version 2 (MERRA-2). *J. Clim.*, **30**(14), 5419–5454, doi:10.1175/JCLI-D-16-0758.1.

Georges, T. M. (1973) Infrasound from convective storms: Examining the evidence. *Rev. Geophys.*, **11**(3), 571–594, doi:10.1029/RG011i003p00571.

Gibbons, S., T. Kvaerna, and S. Mykkeltveit (2015) Could the IMS Infrasound Stations Support a Global Network of Small Aperture Seismic Arrays? *Seismol. Res. Lett.*, **86**(4), 1148–1159, doi:10.1785/0220150068.

Gill, A. E. (1982) *Atmosphere–Ocean Dynamics*, vol. **30** of *International Geophysics*. Academic Press, San Diego, CA, USA. ISBN 9780080570525. 662 pp.

Global Modeling and Assimilation Office (2015) MERRA-2 tavg3_3d_asm_Nv: 3d, 3-Hourly, Time-Averaged, Model-Level, Assimilation, Assimilated Meteorological Fields V5.12.4. Data set, Goddard Earth Sciences Data and Information Services Center (GES DISC), Greenbelt, MD, USA, doi:10.5067/suoqesm06lpk, accessed: 28 November 2017.

Goerke, V. H. and M. W. Woodward (1966) Infrasound observation of a severe weather system. *Mon. Weather Rev.*, **94**(6), 395–398, doi:10.1175/1520-0493(1966)094<0395:IOOASW>2.3.CO;2.

Gossard, E. E. and W. H. Hooke (1975) *Waves in the Atmosphere: Atmospheric Infrasound and Gravity Waves — Their Generation and Propagation*, vol. **2** of *Developments in Atmospheric Science*. Elsevier Scientific Pub. Co., New York, NY, USA. ISBN 9780444411969.

Green, D. N. and D. Bowers (2010) Estimating the detection capability of the International Monitoring System infrasound network. *J. Geophys. Res.*, **115**, D18116, doi:10.1029/2010JD014017.

Greene, G. E. and J. Howard (1975) Natural Infrasound: A One Year Global Study. Tech. Report 317-WPL-37, NOAA, Boulder, CO, USA.

Hagen, J., A. Murk, R. Rüfenacht, S. Khaykin, A. Hauchecorne, and N. Kämpfer (2018) WIRA-C: A compact 142-GHz-radiometer for continuous middle-atmospheric wind measurements. *Atmos. Meas. Tech.*, **11**, 5007–5024, doi:10.5194/amt-11-5007-2018.

Hann, J. (1918) Untersuchungen über die tägliche Oscillation des Barometers: Die dritteltägige (achtstündige) Luftdruckschwankung. *Denkschr. Akad. Wiss. Wien*, **95**, 1–64. [in German].

Hauchecorne, A. and M.-L. Chanin (1980) Density and temperature profiles obtained by lidar between 35 and 70 km. *Geophys. Res. Lett.*, **7**(8), 565–568, doi:10.1029/GL007i008p00565.

Hauf, T., U. Finke, J. Neisser, G. Bull, and J.-G. Stangenberg (1996) A Ground-Based Network for Atmospheric Pressure Fluctuations. *J. Atmos. Oceanic Technol.*, **13**(5), 1001–1023, doi:10.1175/1520-0426(1996)013<1001:AGBNFA>2.0.CO;2.

Haurwitz, B. (1956) The geographical distribution of the semidiurnal solar pressure oscillation. *N.Y. University Meteor. Papers*, **2**, 3.

Haurwitz, B. (1965) The diurnal surface-pressure oscillation. *Archiv für Meteorologie, Geophysik und Bioklimatologie, Serie A*, **14**(4), 361–379, doi:10.1007/BF02253483.

Haurwitz, B. and A. D. Cowley (1973) The diurnal and semidiurnal barometric oscillations global distribution and annual variation. *Pure Appl. Geophys.*, **102**(1), 193–222, doi:10.1007/BF00876607.

Haurwitz, B. and D. Cowley (1969) The lunar barometric tide, its global distribution and annual variation. *Pure Appl. Geophys.*, **77**(1), 122–150, doi:10.1007/BF00876008.

Hedin, A. E., E. L. Fleming, A. H. Manson, F. J. Schmidlin, S. K. Avery, R. R. Clark, S. J. Franke, G. J. Fraser, T. Tsuda, F. Vial, and R. A. Vincent (1996) Empirical wind model for the upper, middle and lower atmosphere. *J. Atmos. Terr. Phys.*, **58**(13), 1421–1447, doi:10.1016/0021-9169(95)00122-0.

Hedlin, M. A. H. and K. T. Walker (2012) A study of infrasonic anisotropy and multipathing in the atmosphere using seismic networks. *Philosophical Transactions of the Roy. Soc. London A: Mathematical, Physical and Engineering Sciences*, **371**(1984), doi:10.1098/rsta.2011.0542.

Hedlin, M. A. H., B. Alcoverro, and G. D'Spain (2003) Evaluation of rosette infrasonic noise-reducing spatial filters. *J. Acoust. Soc. Am.*, **114**(4), 1807–1820, doi:10.1121/1.1603763.

Hildebrand, J., G. Baumgarten, J. Fiedler, and F.-J. Lübken (2017) Winds and temperatures of the Arctic middle atmosphere during January measured by Doppler lidar. *Atmos. Chem. Phys.*, **17**(21), 13345–13359, doi:10.5194/acp-17-13345-2017.

Hills, M. O. G. and D. R. Durran (2012) Nonstationary Trapped Lee Waves Generated by the Passage of an Isolated Jet. *J. Atmos. Sci.*, **69**(10), 3040–3059, doi:10.1175/JAS-D-12-047.1.

Hoffmann, L., X. Xue, and M. J. Alexander (2013) A global view of stratospheric gravity wave hotspots located with Atmospheric Infrared Sounder observations. *J. Geophys. Res.*, **118**(2), 416–434, doi:10.1029/2012JD018658.

Hoffmann, L., M. J. Alexander, C. Clerbaux, A. W. Grimsdell, C. I. Meyer, T. Rößler, and B. Tournier (2014) Intercomparison of stratospheric gravity wave observations with AIRS and IASI. *Atmos. Meas. Tech.*, **7**(12), 4517–4537, doi:10.5194/amt-7-4517-2014.

Hoffmann, L., A. W. Grimsdell, and M. J. Alexander (2016) Stratospheric gravity waves at Southern Hemisphere orographic hotspots: 2003–2014 AIRS/Aqua observations. *Atmos. Chem. Phys.*, **16**(14), 9381–9397, doi:10.5194/acp-16-9381-2016.

Hoffmann, L., R. Spang, A. Orr, M. J. Alexander, L. A. Holt, and O. Stein (2017) A decadal satellite record of gravity wave activity in the lower stratosphere to study polar stratospheric cloud formation. *Atmos. Chem. Phys.*, **17**(4), 2901–2920, doi:10.5194/acp-17-2901-2017.

Hoinka, K. P. (2007) Semi-diurnal pressure fluctuation in the ERA40 Data. *Meteorol. Z.*, **16**(3), 255–260, doi:10.1127/0941-2948/2007/0213.

Holton, J. R. (1983) The Influence of Gravity Wave Breaking on the General Circulation of the Middle Atmosphere. *J. Atmos. Sci.*, **40**(10), 2497–2507, doi:10.1175/1520-0469(1983)040<2497:TIOGWB>2.0.CO;2.

Hupe, P., L. Ceranna, and C. Pilger (2018) Using barometric time series of the IMS infrasound network for a global analysis of thermally induced atmospheric tides. *Atmos. Meas. Tech.*, **11** (4), 2027–2040, doi:10.5194/amt-11-2027-2018.

Hupe, P., L. Ceranna, C. Pilger, M. De Carlo, A. Le Pichon, B. Kaifler, and M. Rapp (2019) Assessing middle atmosphere weather models using infrasound detections from microbaroms. *Geophys. J. Int.*, **216**(3), 1761–1767, doi:10.1093/gji/ggy520.

Jewtoukoff, V., A. Hertzog, R. Plougonven, A. de la Cámara, and F. Lott (2015) Comparison of Gravity Waves in the Southern Hemisphere Derived from Balloon Observations and the ECMWF Analyses. *J. Atmos. Sci.*, **72**(9), 3449–3468, doi:10.1175/JAS-D-14-0324.1.

Kaifler, B., N. Kaifler, B. Ehard, A. Dörnbrack, M. Rapp, and D. C. Fritts (2015) Influences of source conditions on mountain wave penetration into the stratosphere and mesosphere. *Geophys. Res. Lett.*, **42**, 9488–9494, doi:10.1002/2015GL066465.

Kaifler, B. (2018a) ARISE-2, D2.5: Database on lidar temperature during the campaign in Argentina, and report on future lidar station implementation. Internal report, Deutsches Zentrum für Luft- und Raumfahrt, Oberpfaffenhofen, Germany.

Kaifler, N. and B. Kaifler (2018) Small-scale temperature perturbations in the middle atmosphere. Talk. *In: ARISE2 Final Workshop*, Hamburg, Germany. 14–16 May 2018.

Kaifler, N. (2018b) Personal communication. 28 August 2018.

Kertz, W. (1956) Components of the semidiurnal pressure oscillation. Sci. Rep. No. 4, Dept. of Meteor. and Ocean, New York University, New York, NY, USA.

Koch, K. and C. Pilger (2018) Infrasound observations from the site of past underground nuclear explosions in north korea. *Geophys. J. Int.*, **216**(1), 182–200, doi:10.1093/gji/ggy381.

Kodera, K., H. Mukougawa, and A. Fujii (2013) Influence of the vertical and zonal propagation of stratospheric planetary waves on tropospheric blockings. *J. Geophys. Res.*, **118**(15), 8333–8345, doi:10.1002/jgrd.50650.

Kohyama, T. and J. M. Wallace (2014) Lunar gravitational atmospheric tide, surface to 50 km in a global, gridded data set. *Geophys. Res. Lett.*, **41**(23), 8660–8665, doi:10.1002/2014GL060818.

Kruse, C. G., R. B. Smith, and S. D. Eckermann (2016) The Midlatitude Lower-Stratospheric Mountain Wave "Valve Layer". *J. Atmos. Sci.*, **73**(12), 5081–5100, doi:10.1175/jas-d-16-0173.1.

Kulichkov, S. (2010) On the Prospects for Acoustic Sounding of the Fine Structure of the Middle Atmosphere. *In* Le Pichon, A., E. Blanc, and A. Hauchecorne (eds.): *Infrasound Monitoring for Atmospheric Studies*, pp. 511–540. Springer, Dordrecht, the Netherlands. ISBN 978-1-4020-9508-5, doi:10.1007/978-1-4020-9508-5_16.

Lalande, J.-M., O. Sèbe, M. Landès, P. Blanc-Benon, R. S. Matoza, A. Le Pichon, and E. Blanc (2012) Infrasound data inversion for Atmospheric sounding. *Geophys. J. Int.*, **190**(1), 687–701, doi:10.1111/j.1365-246X.2012.05518.x.

Landès, M., L. Ceranna, A. Le Pichon, and R. S. Matoza (2012) Localization of microbarom sources using the IMS infrasound network. *J. Geophys. Res.*, **117**, D06102, doi:10.1029/2011JD016684.

Landès, M., A. Le Pichon, N. M. Shapiro, G. Hillers, and M. Campillo (2014) Explaining global patterns of microbarom observations with wave action models. *Geophys. J. Int.*, **199**(3), 1328–1337, doi:10.1093/gji/ggu324.

Larson, R. J., L. B. Craine, J. E. Thomas, and C. R. Wilson (1971) Correlation of Winds and Geographic Features with Production of Certain Infrasonic Signals in the Atmosphere. *Geophys. J. Int.*, **26**(1-4), 201–214, doi:10.1111/j.1365-246X.1971.tb03395.x.

Le Pichon, A., E. Blanc, and D. Drob (2005a) Probing high-altitude winds using infrasound. *J. Geophys. Res.*, **110**, D20104, doi:10.1029/2005JD006020.

Le Pichon, A., E. Blanc, D. Drob, S. Lambotte, J. X. Dessa, M. Lardy, P. Bani, and S. Vergniolle (2005b) Infrasound monitoring of volcanoes to probe high-altitude winds. *J. Geophys. Res.*, **110**, D13106, doi:10.1029/2004JD005587.

Le Pichon, A., L. Ceranna, M. Garcés, D. Drob, and C. Millet (2006) On using infrasound from interacting ocean swells for global continuous measurements of winds and temperature in the stratosphere. *J. Geophys. Res.*, **111**, D11106, doi:10.1029/2005JD006690.

Le Pichon, A., J. Vergoz, E. Blanc, J. Guilbert, L. Ceranna, L. Evers, and N. Brachet (2009) Assessing the performance of the International Monitoring System's infrasound network: Geographical coverage and temporal variabilities. *J. Geophys. Res.*, **114**, D08112, doi:10.1029/2008jd010907.

Le Pichon, A., L. Ceranna, and J. Vergoz (2012) Incorporating numerical modeling into estimates of the detection capability of the IMS infrasound network. *J. Geophys. Res.*, **117**, D05121, doi:10.1029/2011JD016670.

Le Pichon, A., J. D. Assink, P. Heinrich, E. Blanc, A. Charlton-Perez, C. F. Lee, P. Keckhut, A. Hauchecorne, R. Rüfenacht, N. Kämpfer, D. P. Drob, P. S. M. Smets, L. G. Evers, L. Ceranna, C. Pilger, O. Ross, and C. Claud (2015) Comparison of co-located independent ground-based middle atmospheric wind and temperature measurements with numerical weather prediction models. *J. Geophys. Res.*, **120**(16), 8318–8331, doi:10.1002/2015JD023273.

Le Pichon, A., L. Ceranna, J. Vergoz, and D. Tailpied (2019) Modeling the Detection Capability of the Global IMS Infrasound Network. *In* Le Pichon, A., E. Blanc, and A. Hauchecorne (eds.): *Infrasound Monitoring for Atmospheric Studies — Challenges in Middle-atmosphere Dynamics and Societal Benefits*, pp. 593–604. Springer, Dordrecht, the Netherlands. ISBN 978-3-319-75138-2, doi:10.1007/978-3-319-75140-5_17.

Le Pichon, A., J. Vergoz, P. Herry, and L. Ceranna (2008) Analyzing the detection capability of infrasound arrays in Central Europe. *J. Geophys. Res.*, **113**, D12115, doi:10.1029/2007JD009509.

Le Pichon, A., R. Matoza, N. Brachet, and Y. Cansi (2010) Recent Enhancements of the PMCC Infrasound Signal Detector. *Inframatics*, **26**, 5–8.

Le Pichon, A., L. Ceranna, C. Pilger, P. Mialle, D. Brown, P. Herry, and N. Brachet (2013) The 2013 Russian fireball largest ever detected by CTBTO infrasound sensors. *Geophys. Res. Lett.*, **40**(14), 3732–3737, doi:10.1002/grl.50619.

Leutbecher, M. and H. Volkert (2000) The Propagation of Mountain Waves into the Stratosphere: Quantitative Evaluation of Three-Dimensional Simulations. *J. Atmos. Sci.*, **57**(18), 3090–3108, doi:10.1175/1520-0469(2000)057<3090:TPOMWI>2.0.CO;2.

Limpasuvan, V., D. W. J. Thompson, and D. L. Hartmann (2004) The Life Cycle of the Northern Hemisphere Sudden Stratospheric Warmings. *Journal of Climate*, **17**(13), 2584–2596, doi:10.1175/1520-0442(2004)017<2584:TLCOTN>2.0.CO;2.

Limpasuvan, V., D. L. Wu, M. J. Alexander, M. Xue, M. Hu, S. Pawson, and J. R. Perkins (2007) Stratospheric gravity wave simulation over Greenland during 24 January 2005. *J. Geophys. Res.*, **112**, D10115, doi:10.1029/2006jd007823.

Lindzen, R. S. and S. Chapman (1969) Atmospheric Tides. *Space Sci. Rev.*, **10**, 3–188.

Lingevitch, J. F., M. D. Collins, D. K. Dacol, D. P. Drob, J. C. W. Rogers, and W. L. Siegmann (2002) A wide angle and high Mach number parabolic equation. *J. Acoust. Soc. Am.*, **111**(2), 729–734, doi:10.1121/1.1430683.

Lomb, N. R. (1976) Least-squares frequency analysis of unequally spaced data. *Astrophys. Space Sci.*, **39**(2), 447–462, doi:10.1007/BF00648343.

Lund, T., D. Fritts, B. Laughman, and H. Liu (2018) High-resolution numerical simulation of breaking gravity waves due to winds over the southern Andes mountains. *In: EGU General Assembly*, vol. **20**. EGU2018-11761.

Manney, G. L., Z. D. Lawrence, M. L. Santee, W. G. Read, N. J. Livesey, A. Lambert, L. Froidevaux, H. C. Pumphrey, and M. J. Schwartz (2015) A minor sudden stratospheric warming with a major impact: Transport and polar processing in the 2014/2015 Arctic winter. *Geophys. Res. Lett.*, **42**(18), 7808–7816, doi:10.1002/2015GL065864.

Margrave, G. F. (2000) New seismic modelling facilities in Matlab. Research Report 12, Consortium for Research in Elastic Wave Exploration Seismology (CREWES), University of Calgary, Alberta, Canada. URL: `https://www.crewes.org/ForOurSponsors/ResearchReports/2000/2000-09.pdf`, last accessed: 27 October 2018.

Marlton, G., A. Charlton-Perez, G. Harrison, and P. Hupe (2018) ARISE-2, D6.4: Database of GW parameter climatologies derived from IMS stations, Radiosondes and LIDAR and accompanying technical document describing the data. Public project report, University of Reading, Reading, United Kingdom.

Marlton, G., A. Charlton-Perez, R. G. Harrison, and C. Lee (2019) Calculating Atmospheric Gravity Wave Parameters from Infrasound Measurements. *In* Le Pichon, A., E. Blanc, and A. Hauchecorne (eds.): *Infrasound Monitoring for Atmospheric Studies — Challenges in Middle-atmosphere Dynamics and Societal Benefits*, pp. 701–718. Springer, Dordrecht, the Netherlands. ISBN 978-3-319-75138-2, doi:10.1007/978-3-319-75140-5_22.

MARTEC (2006) MB2005. Manual Ref. 14643-B, Martec Tekelec Systèmes, Les Ulis, France.

Marty, J. (2019) The IMS Infrasound Network: Current Status and Technological Developments. *In* Le Pichon, A., E. Blanc, and A. Hauchecorne (eds.): *Infrasound Monitoring for Atmospheric Studies — Challenges in Middle-Atmosphere Dynamics and Societal Benefits*, pp. 3–62. Springer, Dordrecht, the Netherlands. ISBN 978-3-319-75138-2, doi:10.1007/978-3-319-75140-5_1.

Marty, J., D. Ponceau, and F. Dalaudier (2010) Using the International Monitoring System infrasound network to study gravity waves. *Geophys. Res. Lett.*, **37**, L19802, doi:10.1029/2010GL044181.

Matoza, R. S. and D. Fee (2018) The Inaudible Rumble of Volcanic Eruptions. *Acoustics Today*, **14**(1), 17–25.

Matoza, R. S., J. Vergoz, A. Le Pichon, L. Ceranna, D. N. Green, L. G. Evers, M. Ripepe, P. Campus, L. Liszka, T. Kvaerna, E. Kvaerna, T., and A. Höskuldsson (2011) Long-range acoustic observations of the Eyjafjallajökull erupation, Iceland, April–May 2010. *Geophys. Res. Lett.*, **38**, L06308, doi:10.1029/2011GL047019.

Matoza, R. S., M. Landès, A. Le Pichon, L. Ceranna, and D. Brown (2013) Coherent ambient infrasound recorded by the International Monitoring System. *Geophys. Res. Lett.*, **40**(2), 429–433, doi:10.1029/2012GL054329.

Matsuno, T. (1971) A Dynamical Model of the Stratospheric Sudden Warming. *J. Atmos. Sci.*, **28**(8), 1479–1494, doi:10.1175/1520-0469(1971)028<1479:ADMOTS>2.0.CO;2.

McKisic, J. M. (1997) Infrasound and the Infrasonic Monitoring of Atmospheric Nuclear Explosions. Research report, Tracor Applied Sciences, Inc., Rockville, MD, USA, 321 pp.

McLandress, C., M. J. Alexander, and D. L. Wu (2000) Microwave Limb Sounder observations of gravity waves in the stratosphere: A climatology and interpretation. *J. Geophys. Res.*, **105** (D9), 11947–11967, doi:10.1029/2000JD900097.

Meecham, W. C. (1971) On aerodynamic infrasound. *J. Atmos. Terr. Phys.*, **33**(2), 149–155, doi:10.1016/0021-9169(71)90193-0.

Meecham, W. C. and G. W. Ford (1958) Acoustic Radiation from Isotropic Turbulence. *J. Acoust. Soc. Am.*, **30**(4), 318–322, doi:10.1121/1.1909583.

Melton, B. S. and L. F. Bailey (1957) Multiple signal correlators. *Geophysics*, **22**(3), 565–588, doi:10.1190/1.1438390.

Mialle, P., D. Brown, and N. Arora (2019) Advances in Operational Processing at the International Data Centre. *In* Le Pichon, A., E. Blanc, and A. Hauchecorne (eds.): *Infrasound Monitoring for Atmospheric Studies — Challenges in Middle-Atmosphere Dynamics and Societal Benefits*, pp. 209–248. Springer, Dordrecht, the Netherlands. ISBN 978-3-319-75138-2, doi:10.1007/978-3-319-75140-5_6.

Moudden, Y. and J. M. Forbes (2013) A decade-long climatology of terdiurnal tides using TIMED/SABER observations. *J. Geophys. Res.*, **118**(7), 4534–4550, doi:10.1002/jgra.50273.

Nappo, C. J. (2012) *An Introduction to Atmospheric Gravity Waves*, vol. **102** of *International Geophysics*. Academic Press, San Diego, CA, USA. ISBN 978-0-12-385223-6, doi:10.1016/B978-0-12-385223-6.00021-5.

Nishida, K., Y. Fukao, S. Watada, N. Kobayashi, M. Tahira, N. Suda, K. Nawa, T. Oi, and T. Kitajima (2005) Array observation of background atmospheric waves in the seismic band from 1 mHz to 0.5 Hz. *Geophys. J. Int.*, **162**(3), 824–840, doi:10.1111/j.1365-246X.2005.02677.x.

Noble, J. M. and A. J. Bedard (2006) Infrasound from tornadoes and other severe storms. *J. Acoust. Soc. Am.*, **120**(5), 3031–3031, doi:10.1121/1.4787148.

Norris, D., R. Gibson, and K. Bongiovanni (2010) Numerical Methods to Model Infrasonic Propagation Through Realistic Specifications of the Atmosphere. *In* Le Pichon, A., E. Blanc, and A. Hauchecorne (eds.): *Infrasound Monitoring for Atmospheric Studies*, pp. 541–573. Springer, Dordrecht, the Netherlands. ISBN 978-1-4020-9508-5, doi:10.1007/978-1-4020-9508-5_17.

Oberheide, J., M. E. Hagan, A. D. Richmond, and J. M. Forbes (2015) Dynamical Meteorology — Atmospheric Tides. *In* North, G. R., J. Pyle, and F. Zhang (eds.): *Encyclopedia of Atmospheric Sciences*, pp. 287–297. Academic Press, Oxford, United Kingdom, 2nd edition. ISBN 978-0-12-382225-3, doi:10.1016/B978-0-12-382225-3.00409-6.

Olson, J. V. (2004) Infrasound signal detection using the Fisher F-statistics. *Inframatics*, **6**, 1–8.

Picone, J. M., A. E. Hedin, D. P. Drob, and A. C. Aikin (2002) NRLMSISE-00 empirical model of the atmosphere: Statistical comparisons and scientific issues. *J. Geophys. Res.*, **107**, A121468, doi:10.1029/2002ja009430.

Pilger, C., L. Ceranna, J. O. Ross, A. Le Pichon, P. Mialle, and M. A. Garcés (2015) CTBT infrasound network performance to detect the 2013 Russian fireball event. *Geophys. Res. Lett.*, **42**(7), 2523–2531, doi:10.1002/2015GL063482.

Pilger, C., L. Ceranna, and C. Bönnemann (eds.) (2017) *Monitoring Compliance with the Comprehensive Nuclear-Test-Ban Treaty (CTBT) – Contributions by the German National Data Center*. Geologisches Jahrbuch Reihe B, Band B 105. Schweizerbart Science Publishers, Stuttgart, Germany. ISBN 978-3-510-96858-9.

Pilger, C., L. Ceranna, J. O. Ross, J. Vergoz, A. Le Pichon, N. Brachet, E. Blanc, J. Kero, L. Liszka, S. Gibbons, T. Kvaerna, S. P. Näsholm, E. Marchetti, M. Ripepe, P. Smets, L. Evers,

D. Ghica, C. Ionescu, T. Sindelarova, Y. Ben Horin, and P. Mialle (2018) The European Infrasound Bulletin. *Pure Appl. Geophys.*, doi:10.1007/s00024-018-1900-3.

Plougonven, R. and F. Zhang (2014) Internal gravity waves from atmospheric jets and fronts. *Rev. Geophys.*, **52**(1), 33–76, doi:10.1002/2012RG000419.

Ponceau, D. and L. Bosca (2010) Low-Noise Broadband Microbarometers. *In* Le Pichon, A., E. Blanc, and A. Hauchecorne (eds.): *Infrasound Monitoring for Atmospheric Studies*, pp. 119–140. Springer, Dordrecht, the Netherlands. ISBN 978-1-4020-9508-5, doi:10.1007/978-1-4020-9508-5_4.

Powers, M. (2018) Why is Tornado Alley So Prone to Tornadoes? Website. URL: `https://www.worldatlas.com/articles/what-is-tornado-alley-where-are-tornadoes-most-likely-to-occur-where-is-the-tornado-belt.html`, last accessed: 27 October 2018.

Pramanik, S. K. (1926) The six-hourly variations of atmospheric pressure and temperature. *Mem. R. Metrol. Soc.*, **1**, 3.

Preusse, P., S. D. Eckermann, and M. Ern (2008) Transparency of the atmosphere to short horizontal wavelength gravity waves. *J. Geophys. Res.*, **113**, D24104, doi:10.1029/2007JD009682.

Rapp, M., A. Dörnbrack, and B. Kaifler (2018) An intercomparison of stratospheric gravity wave potential energy densities from METOP GPS radio occultation measurements and ECMWF model data. *Atmos. Meas. Tech.*, **11**(2), 1031–1048, doi:10.5194/amt-11-1031-2018.

Ray, R. D. and R. M. Ponte (2003) Barometric tides from ECMWF operational analyses. *Ann. Geophys.*, **21**(8), 1897–1910, doi:10.5194/angeo-21-1897-2003.

Ray, R. D. and S. Poulose (2005) Terdiurnal Surface-Pressure Oscillations over the Continental United States. *Mon. Weather Rev.*, **133**(9), 2526–2534, doi:10.1175/MWR2988.1.

Rhines, P. B. (2015) Dynamical Meteorology — Rossby Waves. *In* North, G. R., J. Pyle, and F. Zhang (eds.): *Encyclopedia of Atmospheric Sciences*, pp. 404–416. Academic Press, Oxford, United Kingdom, 2nd edition. ISBN 978-0-12-382225-3, doi:10.1016/B978-0-12-382225-3.00346-7.

Rockway, J. W., G. L. Hower, L. B. Craine, and J. E. Thomas (1974) Applications of Ray-Tracing to Observations of Mountain-Associated Infrasonic Waves. *Geophys. J. R. Astron. Soc.*, **36**(2), 259–266, doi:10.1111/j.1365-246X.1974.tb03637.x.

Rossby, C.-G. (1939) Relation between variations in the intensity of the zonal circulation of the atmosphere and the displacements of the semi-permanent centers of action. *J. Mar. Res.*, **2** (1), 38–55, doi:10.1357/002224039806649023.

Rüfenacht, R., A. Murk, N. Kämpfer, P. Eriksson, and S. A. Buehler (2014) Middle-atmospheric zonal and meridional wind profiles from polar, tropical and midlatitudes with the ground-based microwave Doppler wind radiometer WIRA. *Atmos. Meas. Tech.*, **7**(12), 4491–4505, doi:10.5194/amt-7-4491-2014.

Rüfenacht, R., G. Baumgarten, J. Hildebrand, F. Schranz, V. Matthias, G. Stober, F.-J. Lübken, and N. Kämpfer (2018) Intercomparison of middle-atmospheric wind in observations and models. *Atmos. Meas. Tech.*, **11**(4), 1971–1987, doi:10.5194/amt-11-1971-2018.

Scargle, J. D. (1982) Studies in astronomical time series analysis. II - Statistical aspects of spectral analysis of unevenly spaced data. *Astrophys. J.*, **263**, 835–853, doi:10.1086/160554.

Schindelegger, M. and H. Dobslaw (2016) A global ground truth view of the lunar air pressure tide L2. *J. Geophys. Res.*, **121**(1), 95–110, doi:10.1002/2015JD024243.

Schindelegger, M. and R. D. Ray (2014) Surface Pressure Tide Climatologies Deduced from a Quality-Controlled Network of Barometric Observations. *Mon. Weather Rev.*, **142**(12), 4872–4889, doi:10.1175/MWR-D-14-00217.1.

Schmidt, R. (1986) Multiple emitter location and signal parameter estimation. *IEEE Trans. Antennas Propag.*, **34**(3), 276–280, doi:10.1109/TAP.1986.1143830.

Scorer, R. S. (1949) Theory of waves in the lee of mountains. *Quart. J. Roy. Meteor. Soc.*, **75** (323), 41–56, doi:10.1002/qj.49707532308.

SeismoWave (2014) MB3a. User Guide V2.1, SeismoWave, Lannion, France.

Smets, P. S. M. (2018) *Infrasound and the dynamical stratosphere: a new application for operational weather ad climate prediction*. Dissertation, Delft University of Technology, Delft, the Netherlands. 176 pp.

Smets, P. S. M. and L. G. Evers (2014) The life cycle of a sudden stratospheric warming from infrasonic ambient noise observations. *J. Geophys. Res.*, **119**(21), 12084–12099, doi:10.1002/2014JD021905.

Smith, A., N. Lott, and R. Vose (2011) The Integrated Surface Database: Recent Developments and Partnerships. *Bull. Amer. Meteor. Soc.*, **92**(6), 704–708, doi:10.1175/2011BAMS3015.1.

Stevens, J. L., I. I. Divnov, D. A. Adams, J. R. Murphy, and V. N. Bourchik (2002) Constraints on Infrasound Scaling and Attenuation Relations from Soviet Explosion Data. *Pure Appl. Geophys.*, **159**(5), 1045–1062, doi:10.1007/s00024-002-8672-4.

Sutherland, L. C. and H. E. Bass (2004) Atmospheric absorption in the atmosphere up to 160 km. *J. Acoust. Soc. Am.*, **115**, 1012–1032, doi:10.1121/1.1631937.

Thayaparan, T. (1997) The terdiurnal tide in the mesosphere and lower thermosphere over London, Canada (43°N, 81°W). *J. Geophys. Res.*, **102**(D18), 21695–21708, doi:10.1029/97JD01839.

Thomas, J. E., T. H. Kuckertz, J. D. Logan, T. K. Law, and L. B. Craine (1974) Possible source mechanisms for a frequently occurring infrasonic signal. *J. Acoust. Soc. Am.*, **56**(5), 1391–1397, doi:10.1121/1.1903456.

Thomson, W. (1882) 2. On the Thermodynamic Acceleration of the Earth's Rotation. *Proc. of the Royal Soc. of Edinburgh*, **11**, 396–405, doi:10.1017/s037016460004757x.

Torrence, C. and G. P. Compo (1998) A Practical Guide to Wavelet Analysis. *Bull. Amer. Meteor. Soc.*, **79**(1), 61–78, doi:10.1175/1520-0477(1998)079<0061:APGTWA>2.0.CO;2.

Tripathi, O. P., M. Baldwin, A. Charlton-Perez, M. Charron, S. D. Eckermann, E. Gerber, R. G. Harrison, D. R. Jackson, B.-M. Kim, Y. Kuroda, A. Lang, S. Mahmood, R. Mizuta, G. Roff, M. Sigmond, and S.-W. Son (2014) The predictability of the extratropical stratosphere on monthly time-scales and its impact on the skill of tropospheric forecasts. *Quart. J. Roy. Meteor. Soc.*, **141**(689), 987–1003, doi:10.1002/qj.2432.

Van den Dool, H. M., S. Saha, J. Schemm, and J. Huang (1997) A temporal interpolation method to obtain hourly atmospheric surface pressure tides in Reanalysis 1979–1995. *J. Geophys. Res.*, **102**(D18), 22013–22024, doi:10.1029/97JD01571.

Wagner, J., A. Dörnbrack, M. Rapp, S. Gisinger, B. Ehard, M. Bramberger, B. Witschas, F. Chouza, S. Rahm, C. Mallaun, G. Baumgarten, and P. Hoor (2017) Observed versus simulated mountain waves over Scandinavia – improvement of vertical winds, energy and momentum fluxes by enhanced model resolution? *Atmos. Chem. Phys.*, **17**(6), 4031–4052, doi:10.5194/acp-17-4031-2017.

Waxler, R. and E. K. Gilbert (2006) The radiation of atmospheric microbaroms by ocean waves. *J. Acoust. Soc. Am.*, **119**, 2651–2664, doi:10.1121/1.2191607.

Whitaker, R. W. (1995) Infrasound monitoring. *In: Proceedings of the 17th Annual Seismic Research Symposium*, Scottsdale, AZ, USA.

Whitaker, R. W., T. D. Sandoval, and J. P. Mutschlecner (2003) Recent infrasound analysis. *In: 25th Seismic Research Review – Nuclear Explosion Monitoring: Building the Knowledge Base*, Tucson, AZ, USA. National Nuclear Security Administration.

Whiteman, C. D. and X. Bian (1996) Solar Semidiurnal Tides in the Troposphere: Detection by Radar Profilers. *Bull. Amer. Meteor. Soc.*, **77**(3), 529–542, doi:10.1175/1520-0477(1996)077<0529:SSTITT>2.0.CO;2.

Wilson, C. R., C. A. L. Szuberla, and J. V. Olson (2010) High-latitude Observations of Infrasound from Alaska and Antarctica: Mountain-Associated Waves and Geomagnetic/Auroral Infrasonic Signals. *In* Le Pichon, A., E. Blanc, and A. Hauchecorne (eds.): *Infrasound Monitoring for Atmospheric Studies*, pp. 415–454. Springer, Dordrecht, the Netherlands. ISBN 978-1-4020-9508-5, doi:10.1007/978-1-4020-9508-5_13.

Wilson, D. K. (2003) The sound-speed gradient and refraction in the near-ground atmosphere. *J. Acoust. Soc. Am.*, **113**(2), 750–757, doi:10.1121/1.1532028.

WMO (2014) Measurement of Atmospheric Pressure. vol. **8** of *Guide to Meteorological Instruments and Methods of Observation (CIMO guide), Part I: Measurement of Meteorological Variables*, pp. 89–124. World Meteorological Organization, Geneva, Switzerland.

WMO (2018a) Observation Components of the Global Observing System. Website. URL: `http://www.wmo.int/pages/prog/www/OSY/Gos-components.html#surface`, last accessed: 7 March 2018.

WMO (2018b) Observing Systems Capability Analysis and Review Tool: Surface. Website. URL: `https://oscar.wmo.int/surface`, last accessed: 7 March 2018.

Xiong, J., W. Wan, F. Ding, L. Liu, L. Hu, and C. Yan (2018) Two Day Wave Traveling Westward With Wave Number 1 During the Sudden Stratospheric Warming in January 2017. *J. Geophys. Res.*, **123**(4), 3005–3013, doi:10.1002/2017ja025171.

Zeng, X., X. Xue, X. Dou, C. Liang, and M. Jia (2017) COSMIC GPS observations of topographic gravity waves in the stratosphere around the Tibetan Plateau. *Science China – Earth Sciences*, **60**(1), 188–197, doi:10.1007/s11430-016-0065-6.

Zhao, G., L. Liu, B. Ning, W. Wan, and J. Xiong (2005) The terdiurnal tide in the mesosphere and lower thermosphere over Wuhan (30°N, 114°E). *Earth Planets Space*, **57**(5), 393–398, doi:10.1186/BF03351823.

Acknowledgments

First of all, I thank Markus Rapp (DLR, LMU) for supervising this thesis within the last three years. I highly appreciated the encouraging meetings and fruitful discussions at the DLR. Thank you for supporting me to keep this thesis in time, and for your interest in this topic.

I am also grateful to Alexis Le Pichon (*Commissariat à l'énergie atomique et aux énergies alternatives*, CEA) for assuming the role of the second supervisor. *Merci* for your advice and for sharing your scientific ideas about this topic.

When I joined the BGR in 2015, the research field of infrasound was a great challenge for me as a meteorologist. I am grateful to Lars Ceranna and Christian Bönnemann for offering me the opportunity to conduct research in this field by employing me in the BGR's sub-department B4.3. My thanks go to Christoph Pilger, Ole Roß and my initial office mate, Peter Gaebler, for introducing me into the CTBT-related research in our unit. Thank you, especially Lars, Christoph and Ole, for the scientific discussions and ideas, for supporting my Ph.D. project and for proofreading my thesis.

The research leading to this thesis was performed under the umbrella of the Atmospheric Dynamics Research InfraStructure in Europe (ARISE) project (phase 1: 2012–2015, phase 2: 2015–2018), which received funding from the European Commission's H2020 program (grant agreement 653980). I enjoyed participating in the ARISE2 workshops at several interesting places in Europe. I express the project coordinator, Elisabeth Blanc (CEA), my great respect for her dedication within ARISE.

The collaboration within ARISE2 enabled the lidar campaign at IS26, which allowed me to learn a lot about this instrument and its related research from Natalie and Bernd Kaifler (DLR). Thank you for answering my questions and sharing the high-quality CORAL data.
Thanks again to my involved colleagues from our seismological central observatory unit for supporting Bernd during the installation of the lidar in the Bavarian Forest.

I wish to thank all of my colleagues in B4.3 for the pleasant working atmosphere and multidisciplinary insights. I look forward to continuing research in the CTBT-related field of seismoacoustics in B4.3. Thank you, Lars, for placing your trust in me to finish this thesis in due time.

The CTBTO and the IDC in Vienna, as well as all national station operators, are acknowledged for ensuring the data quality of the IMS infrasound stations. (The views expressed in this thesis are not necessarily the views of the CTBTO.)
I also want to express my gratitude to the providers of the further datasets used in this thesis, including GRACILE (Ern et al., 2017), MERRA-2 (Global Modeling and Assimilation Office, 2015), ECMWF operational HRES analysis produced by the IFS (ECMWF, 2014), HRMC lightning data (Cecil, 2015), modeled wave action data (Ardhuin et al., 2011) and the ALOMAR lidar data, provided by the Leibniz-Institute of Atmospheric Physics via the ARISE data portal (ARISE, 2018).

I owe a big thank to my past colleague at the university, Manuela Sauer, for having an independent look and commenting on parts of this thesis.

And last, but not least, I am very grateful to my family, partner and friends for their patience in the final phase of this thesis, and their continuous support throughout my studies.